

Frontier Materials & Technologies

Founded in 2008

№ 4

2023

16+

Quarterly
Scientific Journal

The Founder is
Togliatti State University

Editor-in-Chief

Mikhail M. Krishtal, DSc (Physics and Mathematics), Professor

Deputy Editor-in-Chief

for Metallurgy and Materials Science

Dmitry L. Merson, DSc (Physics and Mathematics), Professor

Deputy Editor-in-Chief

for Mechanical Engineering and Machine Science

Aleksandr P. Shaikin, DSc (Engineering), Professor

Deputy Editor-in-Chief

for Welding and Allied Processes and Technologies

Aleksandr I. Kovtunov, DSc (Engineering), Associate Professor

Editors:

Petr Yu. Bochkarev, DSc (Engineering), Professor

Boris M. Brzhozovskiy, DSc (Engineering), Professor

Aleksandr F. Denisenko, DSc (Engineering), Professor

Yuri Z. Estrin, DSc (Physics and Mathematics), Professor

Sergey S. Gavryushin, DSc (Engineering), Professor

Gregory Gerstein, DSc (Engineering)

Fedor V. Grechnikov, Academician of the Russian Academy of Sciences, DSc (Engineering), Professor

Mikhail I. Karpov, Corresponding Member of the Russian Academy of Sciences, DSc (Engineering), Professor

Aleksandr V. Katsman, PhD (Physics and Mathematics)

Aleksandr A. Kazakov, DSc (Engineering), Professor

Aleksandr V. Kudrya, DSc (Engineering), Professor

Sergey V. Kuzmin, Corresponding Member of the Russian Academy of Sciences, DSc (Engineering), Professor

Aleksey V. Makarov, Corresponding Member of the Russian Academy of Sciences, DSc (Engineering)

Radik R. Mulyukov, Corresponding Member of the Russian Academy of Sciences, DSc (Physics and Mathematics), Professor

Oleg B. Naimark, DSc (Physics and Mathematics), Professor

Nikolay V. Nosov, DSc (Engineering), Professor

Aleksandr V. Pilinsky, PhD (Engineering), Associate Professor

Aleksey E. Romanov, DSc (Physics and Mathematics), Professor

Vasili V. Rubanik, Corresponding Member of the National Academy of Sciences of Belarus, DSc (Engineering)

Vladimir A. Shishkov, DSc (Engineering)

Rudolf N. Starobinski, DSc (Engineering), Professor

Ramasubbu Sunder, Fellow of the Indian Academy of Sciences, PhD (Engineering)

Vladimir P. Tabakov, DSc (Engineering), Professor

Alexey Yu. Vinogradov, DSc (Engineering), PhD (Physics and Mathematics), Professor

Until December 2021,
the journal was published under
the title
“**Science Vector**
of Togliatti State University”.

Indexed in Scopus.
Included in the List of HAC,
RSCI core, DOAJ, CNKI,
“White List”.
Available in Crossref,
Google Scholar

Registered by the Federal
Service for Supervision
of Communications,
Information Technology
and Mass Media
(Registration Certificate
ПИ No. ФС77-83040
dated March 31, 2022).

Desktop publishing:
Natalya A. Nikitenko

*Responsible/technical
editor:*
Natalya A. Nikitenko

Mailing Address:
14, Belorusskaya St.,
Togliatti,
Russia, 445020
Phone: **(8482) 44-91-74**
E-mail:
vektornaukitgu@yandex.ru

Website:
<https://vektornaukitech.ru>

Passed for printing
29.12.2023.
Published 15.03.2024.
Format 60×84 1/8.
Digital printing.
Conventional printed sheets 15.6.
Circulation is 30 copies.
Order 3-482-23
The price is free.

EDITORIAL BOARD INFORMATION

Editor-in-Chief

Mikhail M. Krishtal, Doctor of Sciences (Physics and Mathematics), Professor, Rector (Togliatti State University, Togliatti, Russia).
Scopus AuthorID: [14634063100](#)
ResearcherID: [AAD-7707-2019](#)
ORCID: <https://orcid.org/0000-0001-7189-0002>

Deputy Editor-in-Chief for Metallurgy and Materials Science

Dmitry L. Merson, Doctor of Sciences (Physics and Mathematics), Professor, Director of the Research and Development Institute of Advanced Technologies (Togliatti State University, Togliatti, Russia).
Scopus AuthorID: [6603449333](#)
ResearcherID: [M-7210-2016](#)
ORCID: <https://orcid.org/0000-0001-5006-4115>

Deputy Editor-in-Chief for Mechanical Engineering and Machine Science

Aleksandr P. Shaikin, Doctor of Sciences (Engineering), Professor, Professor of Chair “Energy-Converting Machines and Control Systems” (Togliatti State University, Togliatti, Russia).
Scopus AuthorID: [6602779899](#)
ORCID: <https://orcid.org/0000-0002-9832-4753>

Deputy Editor-in-Chief for Welding and Allied Processes and Technologies

Aleksandr I. Kovtunov, Doctor of Sciences (Engineering), Associate Professor, Professor of Chair “Welding, Pressure Treatment of Materials and Allied Processes” (Togliatti State University, Togliatti, Russia).
Scopus AuthorID: [36761987000](#)
ResearcherID: [B-4545-2016](#)
ORCID: <https://orcid.org/0000-0002-7705-7377>

Editorial board:

Petr Yu. Bochkarev, Doctor of Sciences (Engineering), Professor, Professor of Chair “Mechanical Engineering Technology and Applied Mechanics” (Kamyshin Technological Institute (Branch) of Volgograd State Technical University, Kamyshin, Russia), Professor of Chair “Technical Support of Agro-Industrial Complex” (Saratov State Vavilov Agrarian University, Saratov, Russia).
Scopus AuthorID: [57189893110](#)

Boris M. Brzhozovskiy, Doctor of Sciences (Engineering), Professor, chief researcher of Laboratory of Theory of Mechanisms and Machine Structure (Institute of Machines Science named after A.A. Blagonravov of the Russian Academy of Sciences, Moscow, Russia).
Scopus AuthorID: [55683317200](#)

Alexander F. Denisenko, Doctor of Sciences (Engineering), Professor, Professor of Chair “Technology of Mechanical Engineering, Machines and Tools” (Samara State Technical University, Samara, Russia).

Scopus AuthorID: [36131150100](#)

Yuri Z. Estrin, Doctor of Sciences (Physics and Mathematics), Professor, Professor of Chair of Engineering Materials (Monash University, Melbourne, Australia).

Scopus AuthorID: [7005031984](#)

Sergey S. Gavryushin, Doctor of Sciences (Engineering), Professor, Head of Chair “Computer Systems of Production Automation”, Head of the Theory & Machines Structure Laboratory (Bauman Moscow State Technical University, Moscow, Russia; Mechanical Engineering Research Institute of the Russian Academy of Sciences, Moscow, Russia).

Scopus AuthorID: [6507067486](#)

ResearcherID: [AAT-8610-2020](#)

ORCID: <https://orcid.org/0000-0002-6547-1351>

Gregory Gerstein, Doctor of Sciences (Engineering), Laboratory Head (Leibniz University Hannover, Hanover, Germany).

Scopus AuthorID: [55001912200](#)

Fedor V. Grechnikov, Academician of the Russian Academy of Sciences, Doctor of Sciences (Engineering), Professor, Head of the Chair of Forming Processes (Samara National Research University, Samara, Russia).

Scopus AuthorID: [6506174877](#)

ResearcherID: [P-2319-2016](#)

ORCID: <https://orcid.org/0000-0002-3767-4004>

Mikhail I. Karpov, Corresponding Member of the Russian Academy of Sciences, Doctor of Sciences (Engineering), Professor, Head of the Laboratory of Materials Science (Institute of Solid State Physics of the Russian Academy of Sciences, Chernogolovka, Russia).

Scopus AuthorID: [7004130343](#)

ResearcherID: [Q-9288-2016](#)

Aleksandr V. Katsman, PhD (Physics and Mathematics), Senior Research Associate (Technion – Israel Institute of Technology, Haifa, Israel).

Scopus AuthorID: [7004225554](#)

Aleksandr A. Kazakov, Doctor of Sciences (Engineering), Professor, Professor of Chair “Metallurgy and Casting Technologies”, Head of the Metallurgy Expertise Laboratory (Peter the Great Saint-Petersburg Polytechnic University, St. Petersburg, Russia).

Scopus AuthorID: [56037035400](#)

ResearcherID: [E-6090-2014](#)

ORCID: <https://orcid.org/0000-0001-6511-1228>

Aleksandr V. Kudrya, Doctor of Sciences (Engineering), Professor, Professor of Chair of Physical Metallurgy and Physics of Strength (National University of Science and Technology MISiS, Moscow, Russia).

Scopus AuthorID: [6603628218](#)

Sergey V. Kuzmin, Corresponding Member of the Russian Academy of Sciences, Doctor of Sciences (Engineering), Professor, First Prorector, Professor of Chair “Equipment and Technology of Welding Production” (Volgograd State Technical University, Volgograd, Russia).

Scopus AuthorID: [57217278342](#)

ResearcherID: [I-7424-2012](#)

ORCID: <https://orcid.org/0000-0003-2802-8497>

Aleksey V. Makarov, Corresponding Member of the Russian Academy of Sciences, Doctor of Sciences (Engineering), Chief Research Associate, Head of Chair of Materials Science, Head of the Laboratory of Mechanical Properties (M.N. Mikheev Institute of Metal Physics of Ural Branch of Russian Academy of Sciences, Ekaterinburg, Russia).

Scopus AuthorID: [36889178900](#)

Scopus AuthorID: [57195590138](#)

ResearcherID: [D-5663-2016](#)

ORCID: <https://orcid.org/0000-0002-2228-0643>

Radik R. Mulyukov, Corresponding Member of the Russian Academy of Sciences, Doctor of Sciences (Physics and Mathematics), Professor, Director (Institute for Metals Superplasticity Problems of the Russian Academy of Sciences, Ufa, Russia).

Scopus AuthorID: [7003520439](#)

ResearcherID: [B-3800-2016](#)

ORCID: <https://orcid.org/0000-0002-0452-3816>

Oleg B. Naimark, Doctor of Sciences (Physics and Mathematics), Professor, Head of the Laboratory of Physical Foundations of Strength (Institute of Continuous Media Mechanics of Ural Branch of Russian Academy of Sciences, Perm, Russia).

Scopus AuthorID: [6701720806](#)

Nikolay V. Nosov, Doctor of Sciences (Engineering), Professor, Professor of Chair “Technology of Mechanical Engineering, Machines and Tools” (Samara State Technical University, Samara, Russia).

Scopus AuthorID: [6602506825](#)

Aleksandr V. Pilinsky, PhD (Engineering), Associate Professor, MSME (Master of Science in Mechanical Engineering), Manager (Raymer Metals, Inc., Los Angeles, USA).

Aleksey E. Romanov, Doctor of Sciences (Physics and Mathematics), Professor, Professor of the Institute of Advanced Data Transfer Systems (ITMO University, St. Petersburg, Russia).

Scopus AuthorID: [7202768874](#)

Vasili V. Rubanik, Corresponding Member of the National Academy of Sciences of Belarus, Doctor of Sciences (Engineering), Head of the Laboratory of Metal Physics (Institute of Technical Acoustics of the National Academy of Sciences of Belarus, Vitebsk, Belarus).

Scopus AuthorID: [57215218253](#)

Vladimir A. Shishkov, Doctor of Sciences (Engineering), Head of the Technical Department (Palladio LLC, Togliatti, Russia).

Rudolf N. Starobinski, Doctor of Sciences (Engineering), Professor, Scientific Consultant (Silencers. Consulting and Engineering, Hamburg, Germany).

Scopus AuthorID: [6602638504](#)

Ramasubbu Sunder, Fellow of the Indian Academy of Sciences, PhD (Engineering), Director (BISS (P) Ltd, Bangalore, India).

Scopus AuthorID: [7003530245](#)

ResearcherID: [H-6740-2016](#)

ORCID: <https://orcid.org/0000-0001-6143-0723>

Vladimir P. Tabakov, Doctor of Sciences (Engineering), Professor, Head of Chair “Innovative Technologies in Mechanical Engineering” (Ulyanovsk State Technical University, Ulyanovsk, Russia).

Scopus AuthorID: [6701501345](#)

ResearcherID: [E-1832-2017](#)

ORCID: <https://orcid.org/0000-0002-2568-9401>

Alexey Yu. Vinogradov, Doctor of Sciences (Engineering), PhD (Physics and Mathematics), Professor, Professor of Faculty of Mechanical and Industrial Engineering (Norwegian University of Science and Technology, Trondheim, Norway).

Scopus AuthorID: [7402889776](#)

ResearcherID: [A-7175-2009](#)

ORCID: <https://orcid.org/0000-0001-9585-2801>

СВЕДЕНИЯ О ЧЛЕНАХ РЕДКОЛЛЕГИИ

Главный редактор

Кристал Михаил Михайлович, доктор физико-математических наук, профессор, ректор (Тольяттинский государственный университет, Тольятти, Россия).

Scopus AuthorID: [14634063100](#)

ResearcherID: [AAD-7707-2019](#)

ORCID: <https://orcid.org/0000-0001-7189-0002>

Заместитель главного редактора по направлению «Металлургия и материаловедение»

Мерсон Дмитрий Львович, доктор физико-математических наук, профессор, директор Научно-исследовательского института перспективных технологий (Тольяттинский государственный университет, Тольятти, Россия).

Scopus AuthorID: [6603449333](#)

ResearcherID: [M-7210-2016](#)

ORCID: <https://orcid.org/0000-0001-5006-4115>

Заместитель главного редактора по направлению «Машиностроение и машиноведение»

Шайкин Александр Петрович, доктор технических наук, профессор, профессор кафедры «Энергетические машины и системы управления» (Тольяттинский государственный университет, Тольятти, Россия).

Scopus AuthorID: [6602779899](#)

ORCID: <https://orcid.org/0000-0002-9832-4753>

Заместитель главного редактора по направлению «Сварка, родственные процессы и технологии»

Ковтунов Александр Иванович, доктор технических наук, доцент, профессор кафедры «Сварка, обработка материалов давлением и родственные процессы» (Тольяттинский государственный университет, Тольятти, Россия).

Scopus AuthorID: [36761987000](#)

ResearcherID: [B-4545-2016](#)

ORCID: <https://orcid.org/0000-0002-7705-7377>

Редакционная коллегия:

Бочкарев Петр Юрьевич, доктор технических наук, профессор, профессор кафедры «Технология машиностроения и прикладная механика» (Камышинский технологический институт (филиал) Волгоградского государственного технического университета, Камышин, Россия), профессор кафедры «Техническое обеспечение АПК» (Саратовский государственный аграрный университет имени Н.И. Вавилова, Саратов, Россия).

Scopus AuthorID: [57189893110](#)

Бржозовский Борис Максавич, доктор технических наук, профессор главный научный сотрудник лаборатории теории механизмов и структуры машин (Институт машиноведения им. А.А. Благонравова РАН, Москва, Россия).

Scopus AuthorID: [55683317200](#)

Виноградов Алексей Юрьевич, доктор технических наук, кандидат физико-математических наук, профессор факультета механической и промышленной инженерии (Норвежский университет науки и технологии, Тронхейм, Норвегия).

Scopus AuthorID: [7402889776](#)

ResearcherID: [A-7175-2009](#)

ORCID: <https://orcid.org/0000-0001-9585-2801>

Гаврюшин Сергей Сергеевич, доктор технических наук, профессор, заведующий кафедрой «Компьютерные системы автоматизации производства», заведующий лабораторией компьютерных систем автоматизации производства и цифровых технологий (Московский государственный технический университет имени Н.Э. Баумана (национальный исследовательский университет), Москва, Россия; Институт машиноведения им. А.А. Благонравова Российской академии наук, Москва, Россия).

Scopus AuthorID: [6507067486](#)

ResearcherID: [AAT-8610-2020](#)

ORCID: <https://orcid.org/0000-0002-6547-1351>

Герштейн Грегори, доктор технических наук, заведующий лабораторией (Ганноверский университет имени Готфрида Вильгельма Лейбница, Ганновер, Германия).

Scopus AuthorID: [55001912200](#)

Гречников Федор Васильевич, академик РАН, доктор технических наук, профессор, заведующий кафедрой обработки металлов давлением (Самарский национальный исследовательский университет имени академика С.П. Королева, Самара, Россия).

Scopus AuthorID: [6506174877](#)

ResearcherID: [P-2319-2016](#)

ORCID: <https://orcid.org/0000-0002-3767-4004>

Денисенко Александр Федорович, доктор технических наук, профессор, профессор кафедры «Технология машиностроения, станки и инструменты» (Самарский государственный технический университет, Самара, Россия).

Scopus AuthorID: [36131150100](#)

Кзаков Александр Анатольевич, доктор технических наук, профессор, профессор кафедры «Металлургические и литейные технологии», руководитель научно-испытательной лаборатории «Металлургическая экспертиза» (Санкт-Петербургский политехнический университет Петра Великого, Санкт-Петербург, Россия).

Scopus AuthorID: [56037035400](#)

ResearcherID: [E-6090-2014](#)

ORCID: <https://orcid.org/0000-0001-6511-1228>

Карпов Михаил Иванович, член-корреспондент РАН, доктор технических наук, профессор, заведующий лабораторией материаловедения (Институт физики твердого тела Российской академии наук, Черноголовка, Россия).

Scopus AuthorID: [7004130343](#)

ResearcherID: [Q-9288-2016](#)

Кацман Александр Владимирович, кандидат физико-математических наук, PhD, старший научный сотрудник (Технион – Израильский технологический институт, Хайфа, Израиль).

Scopus AuthorID: [7004225554](#)

Кудря Александр Викторович, доктор технических наук, профессор, заместитель заведующего кафедрой материаловедения и физики прочности (Национальный исследовательский технологический университет «МИСиС», Москва, Россия).

Scopus AuthorID: [6603628218](#)

Кузьмин Сергей Викторович, член-корреспондент РАН, доктор технических наук, профессор, первый проректор, профессор кафедры «Оборудование и технология сварочного производства» (Волгоградский государственный технический университет, Волгоград, Россия).

Scopus AuthorID: [57217278342](#)

ResearcherID: [I-7424-2012](#)

ORCID: <https://orcid.org/0000-0003-2802-8497>

Макаров Алексей Викторович, член-корреспондент РАН, доктор технических наук, главный научный сотрудник, заведующий отделом материаловедения и лабораторией механических свойств (Институт физики металлов имени М.Н. Михеева Уральского отделения Российской академии наук, Екатеринбург, Россия).

Scopus AuthorID: [36889178900](#)

Scopus AuthorID: [57195590138](#)

ResearcherID: [D-5663-2016](#)

ORCID: <https://orcid.org/0000-0002-2228-0643>

Мулюков Радик Рафикович, член-корреспондент РАН, доктор физико-математических наук, профессор, директор (Институт проблем сверхпластичности металлов Российской академии наук, Уфа, Россия).

Scopus AuthorID: [7003520439](#)

ResearcherID: [B-3800-2016](#)

ORCID: <https://orcid.org/0000-0002-0452-3816>

Наймарк Олег Борисович, доктор физико-математических наук, профессор, заведующий лабораторией «Физические основы прочности» (Институт механики сплошных сред Уральского отделения Российской академии наук, Пермь, Россия).

Scopus AuthorID: [6701720806](#)

Носов Николай Васильевич, доктор технических наук, профессор, профессор кафедры «Технология машиностроения, станки и инструменты» (Самарский государственный технический университет, Самара, Россия).

Scopus AuthorID: [6602506825](#)

Пилинский Александр Вениаминович, кандидат технических наук, доцент, MSME (Master of Science in Mechanical Engineering), менеджер («Реймер Металс Корпорейшн», Лос-Анджелес, США).

Романов Алексей Евгеньевич, доктор физико-математических наук, профессор Института перспективных систем передачи данных, руководитель научно-исследовательского центра перспективных функциональных материалов и лазерных коммуникационных систем (Национальный исследовательский университет ИТМО, Санкт-Петербург, Россия).

Scopus AuthorID: [7202768874](#)

Рубаник Василий Васильевич, член-корреспондент Национальной академии наук Беларуси, доктор технических наук, заведующий лабораторией физики металлов (Институт технической акустики Национальной академии наук Беларуси, Витебск, Республика Беларусь).

Scopus AuthorID: [57215218253](#)

Старобинский Рудольф Натанович, доктор технических наук, профессор, научный консультант (консалтинг-бюро “Prof. Starobinski. Silencers. Consulting and Engineering”, Гамбург, Германия).

Scopus AuthorID: [6602638504](#)

Сундер Рамасуббу, член Индийской академии наук, кандидат технических наук, директор (“BISS (P) Ltd”, Бангалор, Индия).

Scopus AuthorID: [7003530245](#)

ResearcherID: [H-6740-2016](#)

ORCID: <https://orcid.org/0000-0001-6143-0723>

Табачков Владимир Петрович, доктор технических наук, профессор, заведующий кафедрой «Инновационные технологии в машиностроении» (Ульяновский государственный технический университет, Ульяновск, Россия).

Scopus AuthorID: [6701501345](#)

ResearcherID: [E-1832-2017](#)

ORCID: <https://orcid.org/0000-0002-2568-9401>

Шишков Владимир Александрович, доктор технических наук, начальник технического отдела (ООО «Палладио», Тольятти, Россия).

Эстрин Юрий Захарович, доктор физико-математических наук, профессор, профессор кафедры инженерных материалов (Университет им. Монаша, Мельбурн, Австралия).

Scopus AuthorID: [7005031984](#)

CONTENT

The influence of thermal treatment on microstructure and mechanical properties of the Si-rich Al–Mg–Si–Sc–Zr alloy Aryshenskiy E.V., Lapshov M.A., Konovalov S.V., Malkin K.A., Rasposienko D.Yu., Makarov V.V.	9
Sorption properties of layered double hydroxides produced by ultrasonic exposure Golubev R.A., Rubanik V.V., Rubanik V.V. Jr., Kritchenkov I.S., Kritchenkov A.S.	19
Determination of the stress threshold and microstructural factors forming the nonlinear unloading effect of the ZK60 (MA14) magnesium alloy Danyuk A.V., Merson D.L., Brilevskiy A.I., Afanasyev M.A.	31
Thermal stability of a submicrocrystalline structure formed by the pressure shear method in Ni and Ni–2 % Cr alloy Karamyshev K.Yu.	41
Combination of cryogenic deformation and electropulse processing as a way to produce ultrafine-grain metals Markushev M.V., Avtokratova E.V., Valeeva A.Kh., Valeev I.Sh., Ilyasov R.R., Krymskiy S.V., Sitdikov O.Sh.	53
Investigation of phase transformations in a two-layer Ti–Al–C+Y–Al–O coating on a heat-resistant nickel alloy Nazarov A.Yu., Maslov A.A., Nikolaev A.A., Shmakov A.N., Denisov V.V., Ramazanov K.N.	63
Simulation of electrical parameters of a galvanic cell in the process of microarc oxidation Pecherskaya E.A., Semenov A.D., Golubkov P.E.	73
The influence of addition of ZrO₂ nanoparticles to the electrolyte on the structure and anticorrosion properties of oxide layers formed by plasma electrolytic oxidation on the Mg₉₇Y₂Zn₁ alloy Polunina A.O., Polunin A.V., Krishtal M.M.	87
Structure and micromechanical properties of SHS composites with a copper matrix: peculiarities of formation Pugacheva N.B., Bykova T.M., Senaeva E.I.	99
The influence of frictional treatment and liquid carburizing on general corrosion resistance of chromium-nickel austenitic steels Skorynina P.A., Makarov A.V., Savrai R.A.	109
Quantitative analysis of deformation texture and primary recrystallization during angular rolling and annealing of the (Fe₈₃Ga₁₇)₉₉B₁ magnetostrictive alloy Strizhachenko I.R., Gervasyeva I.V., Milyutin V.A., Devyaterikov D.I.	121
OUR AUTHORS	129

СОДЕРЖАНИЕ

Влияние термической обработки на микроструктуру и механические свойства сплава Al–Mg–Si–Sc–Zr с избытком Si Арышенский Е.В., Лапшов М.А., Коновалов С.В., Малкин К.А., Распоиенко Д.Ю., Макаров В.В.	9
Сорбционные свойства слоистых двойных гидроксидов, полученных при ультразвуковом воздействии Голубев Р.А., Рубаник В.В., Рубаник В.В. мл., Критченков И.С., Критченков А.С.	19
Определение порога напряжения и микроструктурных факторов, формирующих эффект нелинейной разгрузки магниевого сплава MA14 (ZK60) Данюк А.В., Мерсон Д.Л., Брилевский А.И., Афанасьев М.А.	31
Термическая стабильность субмикроструктурной структуры, сформированной методом «сдвиг под давлением» в Ni и сплаве Ni–2 % Cr Карамышев К.Ю.	41
Сочетание криогенной деформации и электроимпульсной обработки как способ получения ультрамелкозернистых металлов Маркушев М.В., Автократова Е.В., Валеева А.Х., Валеев И.Ш., Ильясов Р.Р., Крымский С.В., Ситдиков О.Ш.	53
Исследование фазовых превращений в двухслойном жаростойком покрытии Ti–Al–C+Y–Al–O на жаропрочном никелевом сплаве Назаров А.Ю., Маслов А.А., Николаев А.А., Шмаков А.Н., Денисов В.В., Рамазанов К.Н.	63
Моделирование электрических параметров гальванической ячейки в процессе микродугового оксидирования Печерская Е.А., Семёнов А.Д., Голубков П.Е.	73
Влияние добавки наночастиц ZrO₂ в электролит на структуру и антикоррозионные свойства оксидных слоев, формируемых плазменно-электролитическим оксидированием на сплаве Mg₉₇Y₂Zn₁ Полунина А.О., Полунин А.В., Криштал М.М.	87
Структура и микромеханические свойства СВС-композитов с медной матрицей: особенности формирования Пугачева Н.Б., Быкова Т.М., Сенаева Е.И.	99
Влияние фрикционной обработки и жидкостной цементации на сопротивление общей коррозии хромоникелевых аустенитных сталей Скорынина П.А., Макаров А.В., Саврай Р.А.	109
Количественный анализ текстуры деформации и первичной рекристаллизации при угловой прокатке и отжиге магнитоострикционного сплава (Fe₈₃Ga₁₇)₉₉B₁ Стрижаченко И.Р., Гервасьева И.В., Милютин В.А., Девятчиков Д.И.	121
НАШИ АВТОРЫ	129

The influence of thermal treatment on microstructure and mechanical properties of the Si-rich Al–Mg–Si–Sc–Zr alloy

© 2023

Evgeny V. Aryshenskiy*^{1,2,4}, Doctor of Sciences (Engineering), Associate Professor, senior researcher of the Laboratory of Electron Microscopy and Image Processing, leading researcher
Maksim A. Lapshov^{2,5}, engineer

Sergey V. Konovalov^{1,2,6}, Doctor of Sciences (Engineer), Professor, Vice-rector for Science and Innovative Activities, chief researcher

Kirill A. Malkin², laboratory assistant

Dmitry Yu. Rasposienko^{3,7}, PhD (Engineering), senior researcher of the Laboratory of Non-ferrous Alloys
Vladimir V. Makarov^{2,3,8}, researcher of the Laboratory of Non-ferrous Alloys, junior researcher

¹Siberian State Industrial University, Novokuznetsk (Russia)

²Academician S.P. Korolev Samara National Research University, Samara (Russia)

³M.N. Mikheev Institute of Metal Physics of the Ural Branch of RAS, Yekaterinburg (Russia)

*E-mail: ar-evgenii@yandex.ru,
arishenskiy_ev@sibsui.ru

⁴ORCID: <https://orcid.org/0000-0003-3875-7749>

⁵ORCID: <https://orcid.org/0000-0002-1306-4578>

⁶ORCID: <https://orcid.org/0000-0003-4809-8660>

⁷ORCID: <https://orcid.org/0000-0002-7670-9054>

⁸ORCID: <https://orcid.org/0000-0002-7306-3657>

Received 06.10.2023

Accepted 31.10.2023

Abstract: The paper studies the Al–Mg–Si alloy that does not contain scandium and zirconium, as well as the silicon-rich Al–Mg–Si–Sc–Zr alloy. Multistage thermal treatment was carried out for the Al_{0.3}Mg₁Si_{0.3}Sc_{0.15}Zr alloy, which included annealing at a temperature of 440 °C for 8 h, high-temperature annealing at 500 °C for 0.5 h, and artificial aging at a temperature of 180 °C with soaking for 5 h. The Al_{0.3}Mg₁Si alloy was annealed at 550 °C for 8 h, and then artificial aging was carried out similarly to the alloy with Sc and Zr additives. To study the fine structure, transmission electron microscopy was used. In the as-cast condition and after each stage of thermal treatment, the mechanical properties of the alloys were determined. It has been found that in an alloy doped with Sc and Zr, the formation of Al₃Sc particles occurs already at the stage of formation of the cast structure. During subsequent artificial aging, the supersaturated solid solution decomposes with the formation of β" (Mg₅Si₆) particles improving mechanical properties. It has been found that in the scandium-containing alloy, fewer β" (Mg₅Si₆) particles are formed, as a result of which its strength properties are slightly worse than those of the base alloy are. Moreover, these particles are larger than in an alloy that does not contain scandium. This is explained by the fact that complete quenching is impossible for an alloy with scandium additives.

Keywords: Al–Mg–Si–Sc–Zr; excess Si; multistage thermal treatment; artificial aging; TEM; mechanical properties; Al₃Sc; Mg₅Si₆.

Acknowledgements: The study was funded by the Russian Science Foundation grant No. 21-19-00548, <https://rscf.ru/project/21-19-00548/>.

For citation: Aryshenskiy E.V., Lapshov M.A., Konovalov S.V., Malkin K.A., Rasposienko D.Yu., Makarov V.V. The influence of thermal treatment on microstructure and mechanical properties of the Si-rich Al–Mg–Si–Sc–Zr alloy. *Frontier Materials & Technologies*, 2023, no. 4, pp. 9–17. DOI: 10.18323/2782-4039-2023-4-66-1.

INTRODUCTION

Aluminium alloys combine high ductility, acceptable strength, good weldability, and high corrosion resistance, which determines their high demand in various branches of modern industry. Some of the most widely used aluminium alloys are the Al–Mg–Si system alloys. They received the name “Avial” in Russian literature and found their main application in aviation and the automotive industry. These alloys are capable of strengthening during thermal treatment, due to the release of the Mg₂Si strengthening phase. Note that when the ratio Mg/Si < 1.73, there is a silicon excess, and when Mg/Si > 1.73, there is a silicon deficiency [1–3]. A silicon excess accelerates the process of formation of the β" phase (Mg₅Si₆) and contributes to its more even release [4].

Aluminium alloys are often additionally doped with Sc. It has a modifying effect on the cast structure, and increases its strength due to the release of highly dispersed Al₃Sc

particles [5–7]. Usually, zirconium is added together with scandium, which thermally stabilises Al₃Sc particles, and increases the efficiency of the cast structure grinding [8; 9]. At the same time, adding scandium to the Al–Mg–Si system does not always lead to an increase in strength properties. This is caused by the fact that scandium and silicon tend to combine into the Sc₂Si₂Al phase, which is not a strengthening phase. An increase in silicon content leads to an increase in the probability of the formation of this phase [10]. Despite this, strengthening Al₃Sc nanoparticles were discovered even in the Al–Mg–Si system alloys, with a high silicon content [11–13]. However, to simultaneously obtain Al₃Sc and β" (Mg₅Si₆) strengthening particles in alloys with excess silicon, multi-stage thermal treatment is required. The following sequence may be one of its options: annealing at 440 °C to precipitate Al₃Sc, quenching at 500 °C for 30 min for partial Mg and Si dissolution, and ageing at 180 °C for 5 h to form β" (Mg₅Si₆) [14]. At the same time, the influence of this thermal treatment on

the formation of mechanical properties and microstructure in alloys with the $Mg/Si \leq 0.6$ ratio has not been previously studied.

The purpose of the study is to investigate the influence of thermal treatment on the formation of the microstructure and mechanical properties of the Al–Mg–Si alloy with excess silicon and additional alloying with Sc and Zr.

METHODS

The work studied the Al_{0.3}Mg₁Si_{0.3}Sc_{0.15}Zr alloy in the as-cast condition, as well as after various thermal treatments according to the modes given in Table 1. To assess the influence of scandium and zirconium, similar studies were carried out on the base Al_{0.3}Mg₁Si alloy (without Sc and Zr).

The authors carried out casting to a steel mould to ensure the rate of crystallisation and cooling of the cast structure close to real industrial technology. The weight of the cast ingots was 4.5 kg. The following materials were used as a charge for the alloy: A85 aluminium, MG90 magnesium, Al₁₂Si alloy, Al–Sc₂ and Al–Zr₅ alloys. The casting temperature was 720–740 °C. Before pouring the molten metal into the mould, it was refined with carnallite flux, added at the rate of 5 g per 1 kg of charge. After this, scale was removed from the molten metal surface and the metal was poured into a steel mould with a uniform casting time of 40 s. Thermal treatment of the samples was carried out in a muffle electric furnace with water quenching, after which their mechanical properties were determined.

The sizes and morphology of fine particles were studied using transmission electron microscopy (TEM), for the thermal treatment modes given in Table 1. The study was carried out on a Tecnai G2 30 Twin high-resolution microscope equipped with an EDAX energy dispersive X-ray analysis system at an accelerating voltage of 300 kV using standard techniques: light-field, dark-field images and electron microdiffraction. The linear dimensions of the structural elements were determined by direct measurements in the observation plane.

Sample preparation was carried out on Metaserv 250, TenuPol-5, Ultrasonic Disk Cutter, PIPS II devices using instrumental methods.

Mechanical properties were determined on a universal testing machine (Zwick/Roell Z050) according to ISO 6892-1 in the as-cast state, and for each thermal treatment step. The dimensions of the samples were selected in accordance with DIN 50125. The properties obtained

during the tests, such as the yield strength ($\sigma_{0.2}$) and the tensile strength (σ_B) were calculated in accordance with GOST 1497-84 and GOST 11150-84.

RESULTS

In the cast structure of the Al_{0.3}Mg₁Si_{0.3}Sc_{0.15}Zr alloy, the strengthening phase particles were discovered having different morphologies (Fig. 1). At the same time, in some grains, particles were found that had an equiaxial shape, while in others, they were needle-shaped. Equiaxial particles, the average size of which is 30–40 nm, precipitate relatively uniformly in the grain volume (Fig. 1 a). In the structure of grains where needle-shaped particles are present, zones free from precipitation are observed, their width is ~500 nm; i. e., with relatively dense aggregates of needle-shaped particles, the precipitation of equiaxial dispersoids in such zones is completely absent. Moreover, in the single grain volume, as a rule, only one orientation of needle-shaped particles is observed among all crystallographically equivalent ones (Fig. 1 b). From this, one can conclude that for favorable growth of such particles, an appropriate grain orientation (relative to the temperature gradient during crystallisation) is necessary. From the analysis of the TEM results, it follows that all the observed particles were formed during the discontinuous precipitation of a supersaturated scandium solution during the movement of grain boundaries.

Using TEM, Sc-based phases were detected in a sample after annealing the Al_{0.3}Mg₁Si_{0.3}Sc_{0.15}Zr alloy for 8 h at a temperature of 440 °C. They are represented in the form of needle-shaped precipitations with a diameter of up to 40 nm and a length of several microns. Their high volume fraction with a relatively low distribution density should be noted. Moreover, equiaxial particles with a diameter of 20 nm are observed (Fig. 2 c); they are arranged in chains, which, apparently, can be associated with the Al₃Sc phase heterogeneous nucleation on dislocations. Note that needle-shaped precipitations, like equiaxial ones, are apparently previously discovered particles of the Al₃Sc type, released as a result of continuous precipitation during cooling of the cast blank (Fig. 2).

In the Al_{0.3}Mg₁Si_{0.3}Sc_{0.15}Zr alloy after annealing according to the mode (440 °C, 8 h) + (500 °C, 0.5 h) + (180 °C, 5 h) (Fig. 3), rod-like precipitations with a length of 500 nm and a diameter of about 200 nm containing Al, Si, Sc, and Zr are observed. Considering the size and morphology of the particles mentioned above, one

Table 1. Scheme of thermal treatment of alloys
Таблица 1. Схема термической обработки сплавов

Alloy	Thermal treatment
Al _{0.3} Mg ₁ Si _{0.3} Sc _{0.15} Zr	440 °C, 8 h
	(440 °C, 8 h) + (500 °C, 0.5 h)
	(440 °C, 8 h) + (500 °C, 0.5 h) + (180 °C, 5 h)
Al _{0.3} Mg ₁ Si	(550 °C, 8 h) + (180 °C, 5 h)

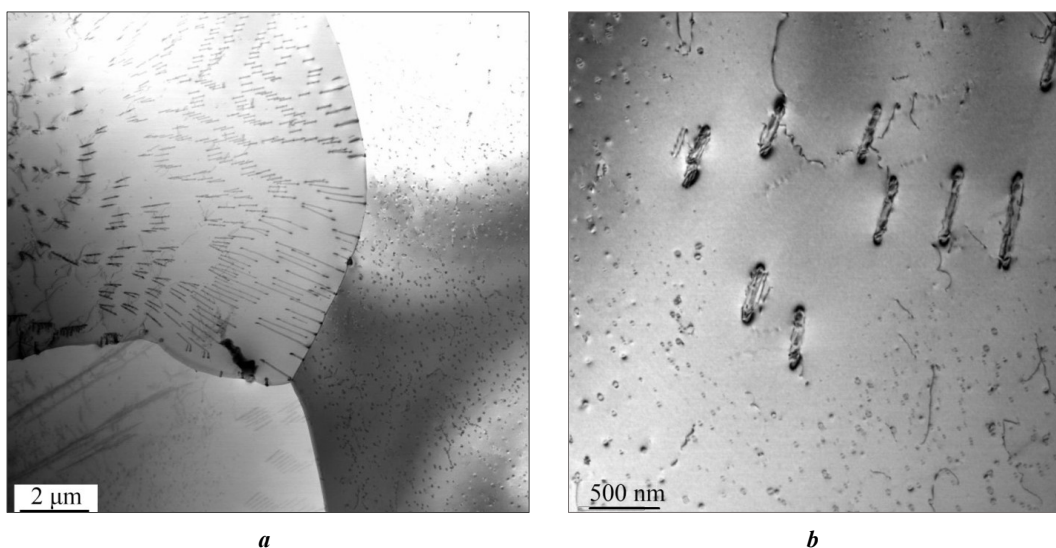


Fig. 1. Electron microscopic images of the microstructure of the $Al_{0.3}Mg_1Si_{0.3}Sc_{0.15}Zr$ alloy in the as-cast condition:
a, b – light-field images

Рис. 1. Электронно-микроскопические изображения микроструктуры сплава $Al_{0.3}Mg_1Si_{0.3}Sc_{0.15}Zr$ в литом состоянии:
a, b – светлопольные изображения

could assume that these particles represent an equilibrium Sc_2Si_2Al phase, which is apparently capable of partially dissolving zirconium. Evidently, even short-term heating at a temperature of 500 °C is enough for its formation. Particles released during discontinuous precipitation after casting, are observed along the grain boundaries (Fig. 3 a, 3 b).

After artificial ageing at 180 °C for 5 h, the β'' phase (Mg_5Si_6) becomes the main strengthening phase for an alloy of this composition, which precipitates in the form of rods up to 70 nm long (Fig. 4 a). The quite high volume fraction and the size of β'' particle should be noted, as indicated by the pronounced reflexes of this phase in the corresponding electron diffraction patterns (Fig. 4 b). Moreover, despite the rather large sizes of the β'' precipitates, they retain their coherence with the aluminium matrix.

In the $Al_{0.3}Mg_1Si$ alloy, the precipitation of Si-based phases is observed in the form of irregular-shape polygons, with dimensions up to 300 nm, which are apparently formed during the process of heating for quenching (Fig. 5 a). During artificial ageing at 180 °C for 5 h, highly dispersed needle-shaped precipitations of the Guinier – Preston zone and β'' phase are formed (Fig. 5 b, 6 a). In general, the pattern is similar to the $Al_{0.3}Mg_1Si_{0.3}Sc_{0.15}Zr$ alloy after three-stage thermal treatment; however, one should note that in the base alloy, more Mg_5Si_6 strengthening particles were found.

Fig. 7 represents the mechanical properties of the alloys under consideration in the as-cast state and after thermal treatment. In the as-cast condition, scandium and zirconium additives can significantly increase the properties of the alloy: yield strength by 32 MPa, tensile strength by 60 MPa. Annealing of $Al_{0.3}Mg_1Si_{0.3}Sc_{0.15}Zr$ alloy at 440 °C for 8 h does not lead to a significant change in the yield strength and causes a decrease in the tensile strength by 32 MPa. Three-stage annealing of an alloy doped with Sc and Zr according to the route (440 °C, 8 h) +

(500 °C, 0.5 h) + (180 °C, 5 h), increases the yield strength by 8 MPa and the tensile strength by 17 MPa relative to the as-cast state. However, the base alloy after heating for quenching followed by artificial ageing (550 °C, 8 h) + (180 °C, 5 h) has significantly higher indicators – the yield strength increased by 106 MPa, the tensile strength increased by 70 MPa.

DISCUSSION

It has been found that the $Al_{0.3}Mg_1Si_{0.3}Sc_{0.15}Zr$ alloy in the as-cast state has higher strength indicators, which is primarily due to the appearance of the Al_3Sc type particles, both semi-coherent and fully coherent to the aluminium matrix. Note that silicon significantly accelerates discontinuous precipitation, and actually makes the appearance of such particles inevitable [7].

Further annealing (440 °C, 8 h) does not lead to a significant change in the yield strength, and causes a decrease in the tensile strength. This is firstly related to the fact that the essential part of scandium precipitates from the supersaturated solid solution, when the ingot cools during the casting process, after which new strengthening particles are no longer formed. A decrease in strength properties can be caused as well by the release of magnesium in the form of Mg_2Si particles from a supersaturated solid solution, which, according to calculations represented in [15], begins at temperatures below 500 °C.

After final artificial ageing, the strength indicators in the alloy with scandium additives increase slightly, primarily due to the formation of β'' particles (Mg_5Si_6), the presence of which is confirmed by TEM data. At the same time, the increase in strength caused by them is small in comparison with the base alloy, and the reason for this is the large size of these particles. In the base alloy, a larger number of β'' particles (Mg_5Si_6) are formed, during ageing compared

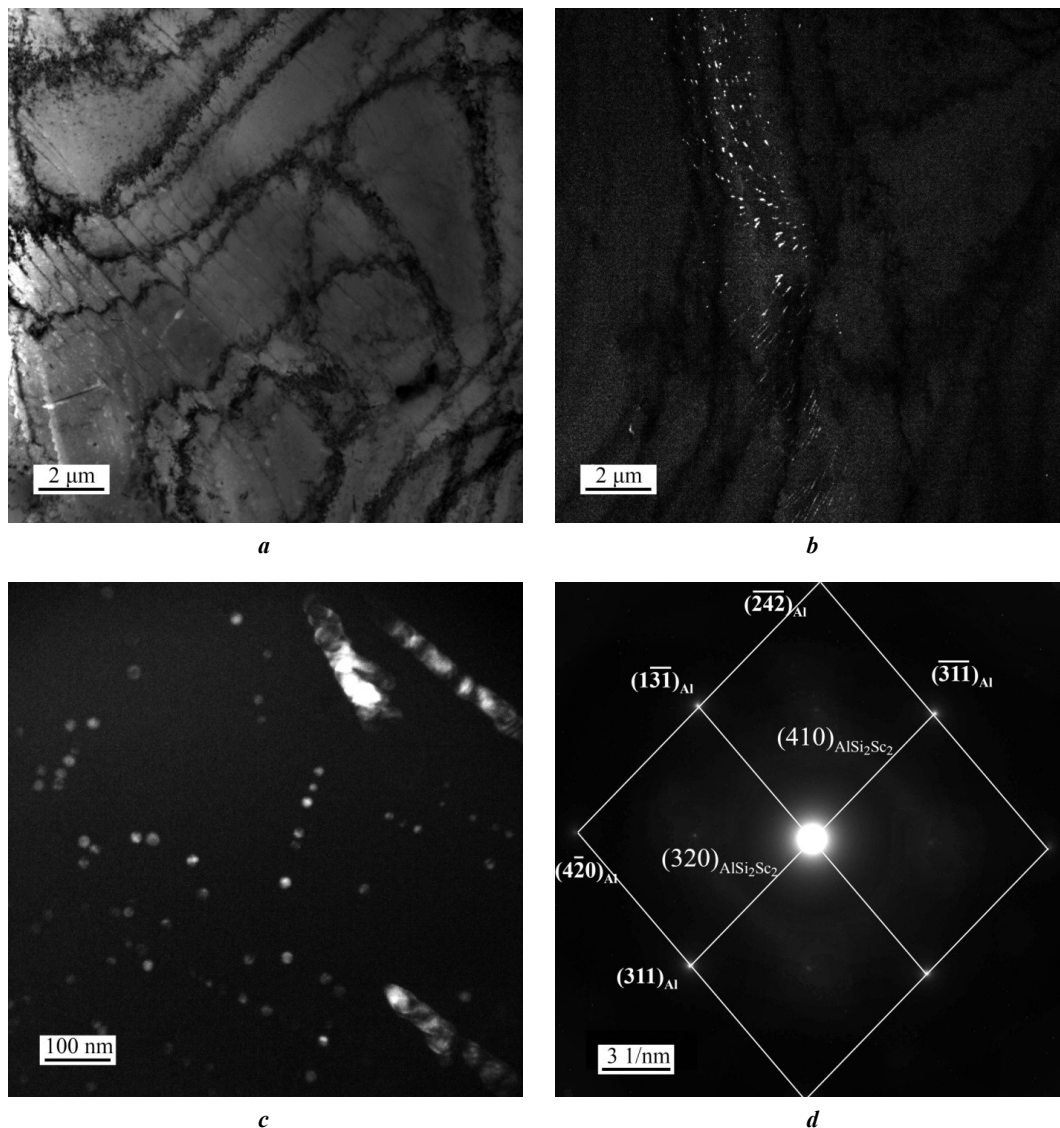


Fig. 2. Electron microscopic images of the microstructure of the $Al_{0.3}Mg_1Si_{0.3}Sc_{0.15}Zr$ alloy after annealing at 440 °C for 8 h:

- a* – light-field image;
b, c – dark-field images in reflex $(110)_{Al_3Sc}$;
d – microelectronogram (zone axis $[2\bar{7}5]_{Al}$)

Рис. 2. Электронно-микроскопические изображения микроструктуры сплава $Al_{0.3}Mg_1Si_{0.3}Sc_{0.15}Zr$ после отжига при 440 °C в течение 8 ч:

- a* – светлопольное изображение;
b, c – темнопольные изображения в рефлекс $(110)_{Al_3Sc}$;
d – микроэлектронограмма (ось зоны) $[2\bar{7}5]_{Al}$

to an alloy containing scandium, which causes a more significant increase in strength. This is related to the fact that in the base alloy, it is possible to carry out complete quenching at a temperature of 550 °C and holding for 8 h. This mode allows magnesium to dissolve and thereby contributes to the release of a much larger number of β'' particles (Mg_5Si_6).

At the same time, it is impossible to carry out full quenching in an alloy containing scandium, since it will completely neutralise the strengthening effect of Al_3Sc particles. This is explained by the fact that when heating to

a temperature of 550 °C and holding for 8 h, coagulation of particles occurs resulting in that the strengthening effect they cause is completely lost. Thus, scandium additives to Al–Mg–Si alloys cause a significant increase in strength, only in the as-cast state at the stage of the supersaturated solid solution decomposition. Subsequent stages of thermal treatment do not allow precipitating fully both types of strengthening particles. As a result, the mechanical properties of the base alloy are higher than the properties of the alloy containing scandium.

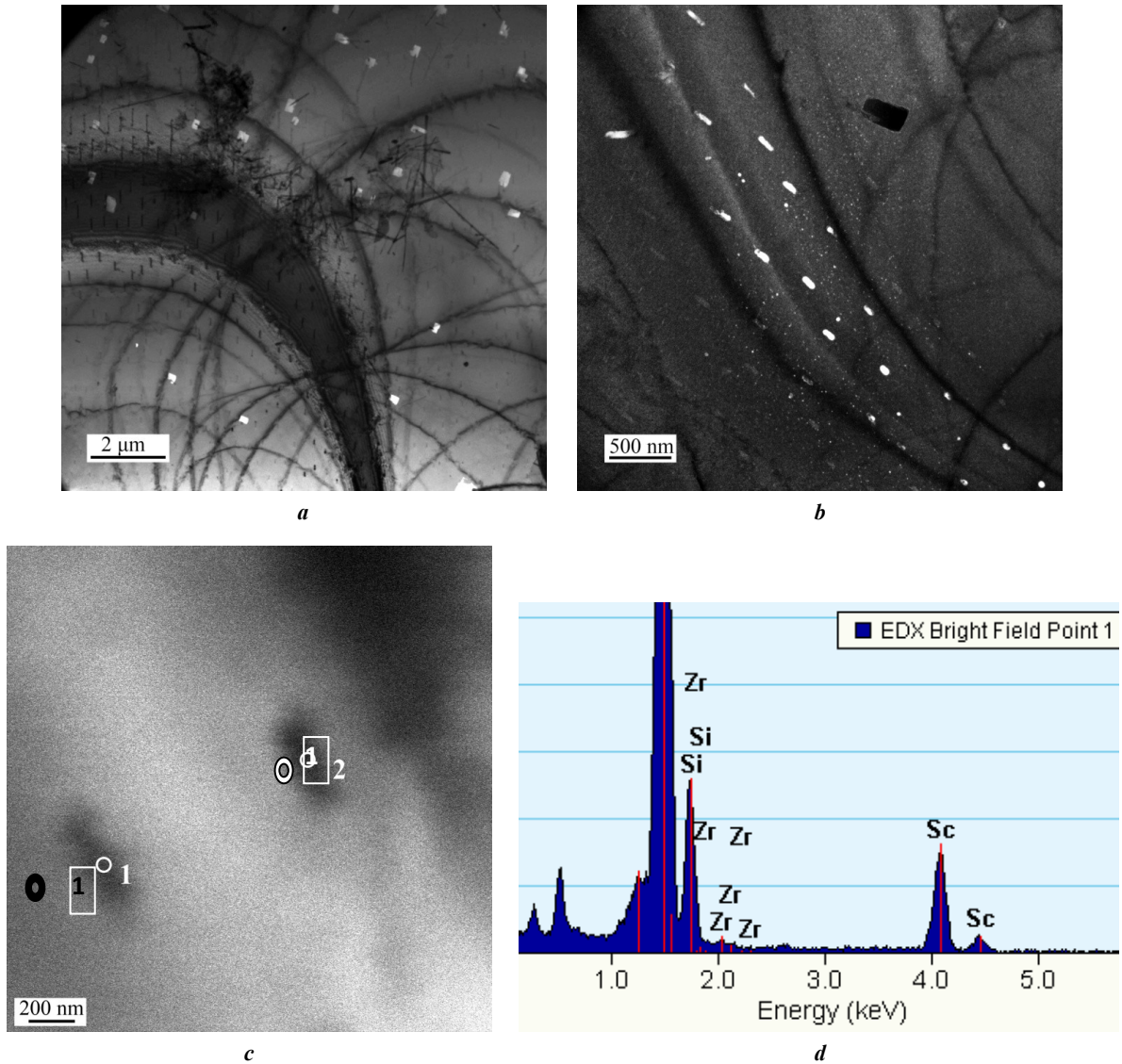


Fig. 3. Electron microscopic images of the $Al_{0.3}Mg_1Si_{0.3}Sc_{0.15}Zr$ alloy microstructure after annealing at $(440\text{ }^{\circ}C, 8\text{ h}) + (500\text{ }^{\circ}C, 0.5\text{ h}) + (180\text{ }^{\circ}C, 5\text{ h})$:

a – light-field image;

b – dark-field image in the $(100)Al_3(Sc,Zr)$ phase reflex;

c – light-field image in transmission scanning mode (STEM);

d – spectrum of characteristic radiation at point 1 in Fig. 3 c

Рис. 3. Электронно-микроскопические изображения микроструктуры сплава $Al_{0.3}Mg_1Si_{0.3}Sc_{0.15}Zr$ после отжига по режиму $(440\text{ }^{\circ}C, 8\text{ ч}) + (500\text{ }^{\circ}C, 0,5\text{ ч}) + (180\text{ }^{\circ}C, 5\text{ ч})$:

a – светлопольное изображение;

b – темнопольное изображение в рефлексе фазы $(100)Al_3(Sc,Zr)$;

c – светлопольное изображение в режиме сканирования на просвет (STEM);

d – спектр характеристического излучения в точке 1 на рис. 3 c

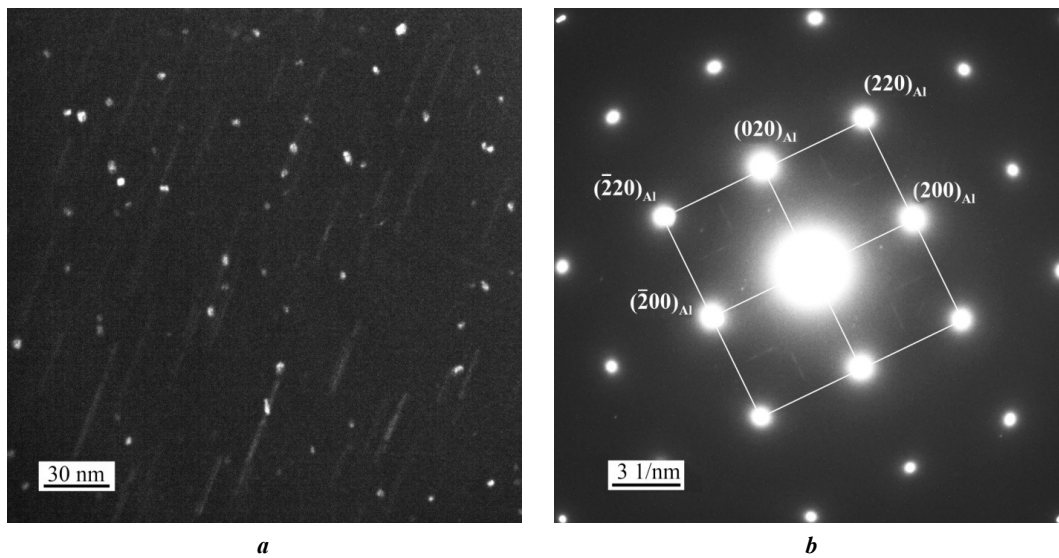


Fig. 4. Electron microscopic images of the $Al_{0.3}Mg_1Si_{0.3}Sc_{0.15}Zr$ alloy microstructure after annealing at $(440\text{ }^{\circ}C, 8\text{ h}) + (500\text{ }^{\circ}C, 0.5\text{ h}) + (180\text{ }^{\circ}C, 5\text{ h})$:

a – dark-field image in phase reflexes;

b – microelectronogram, zone axis $[001]_{Al}$

Рис. 4. Электронно-микроскопические изображения микроструктуры сплава $Al_{0.3}Mg_1Si_{0.3}Sc_{0.15}Zr$ после отжига по режиму $(440\text{ }^{\circ}C, 8\text{ ч}) + (500\text{ }^{\circ}C, 0,5\text{ ч}) + (180\text{ }^{\circ}C, 5\text{ ч})$:

a – темнопольное изображение в рефлексах фаз;

b – микроэлектронограмма, ось зоны $[001]_{Al}$

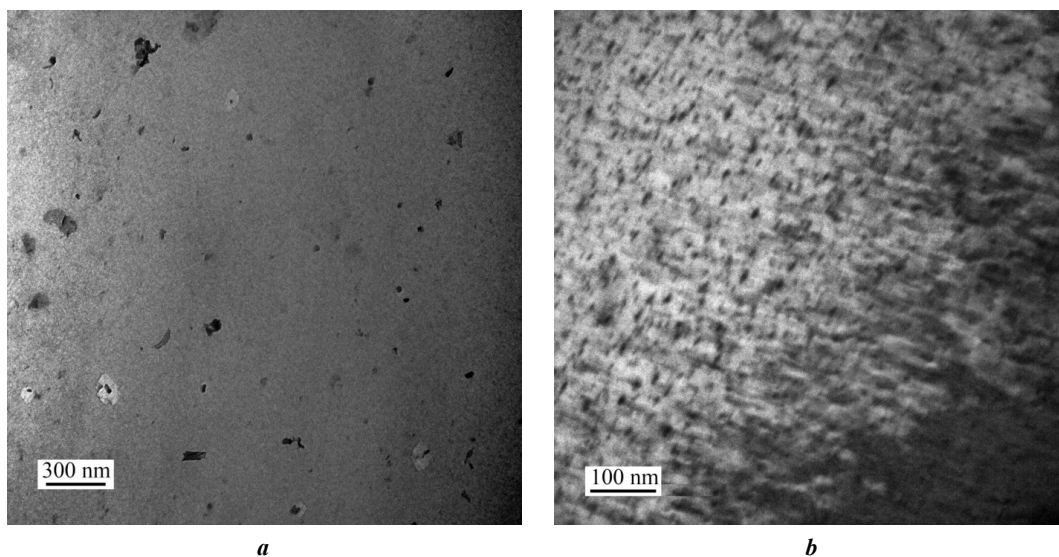


Fig. 5. Electron microscopic images of the $Al_{0.3}Mg_1Si$ alloy microstructure after annealing at $(550\text{ }^{\circ}C, 8\text{ h}) + (180\text{ }^{\circ}C, 5\text{ h})$:

a, b – light-field images

Рис. 5. Электронно-микроскопические изображения микроструктуры сплава $Al_{0.3}Mg_1Si$ после отжига по режиму $(550\text{ }^{\circ}C, 8\text{ ч}) + (180\text{ }^{\circ}C, 5\text{ ч})$:

a, b – светлопольные изображения

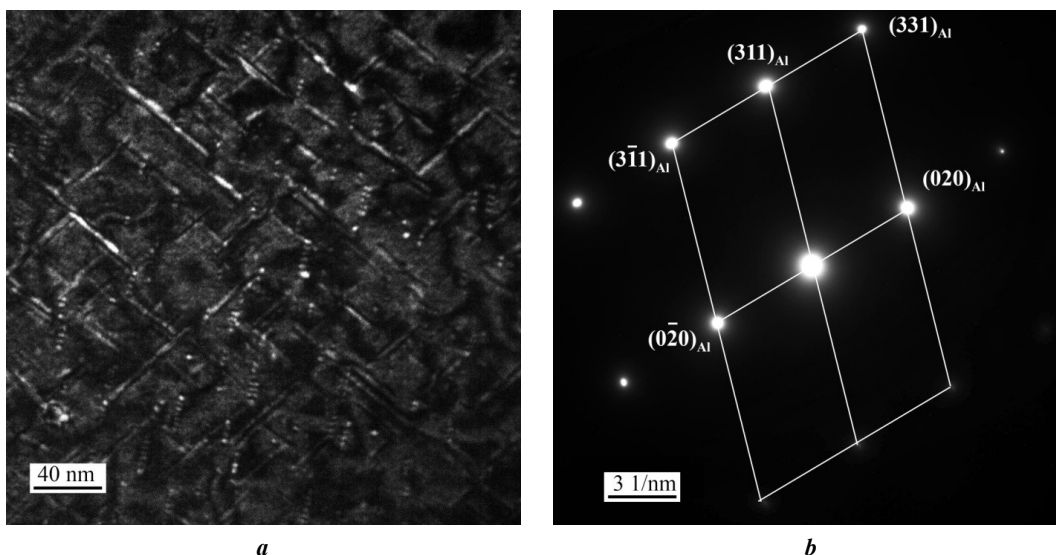


Fig. 6. Electron microscopic images of the $Al_{0.3}Mg_1Si$ alloy microstructure after annealing at $(550\text{ }^{\circ}C, 8\text{ h}) + (180\text{ }^{\circ}C, 5\text{ h})$:

a – dark-field image in phase reflexes; **b** – microelectronogram

Рис. 6. Электронно-микроскопические изображения микроструктуры сплава $Al_{0.3}Mg_1Si$ после отжига по режиму $(550\text{ }^{\circ}C, 8\text{ ч}) + (180\text{ }^{\circ}C, 5\text{ ч})$:

a – темнопольное изображение в рефлексах фаз; **b** – микроэлектронограмма

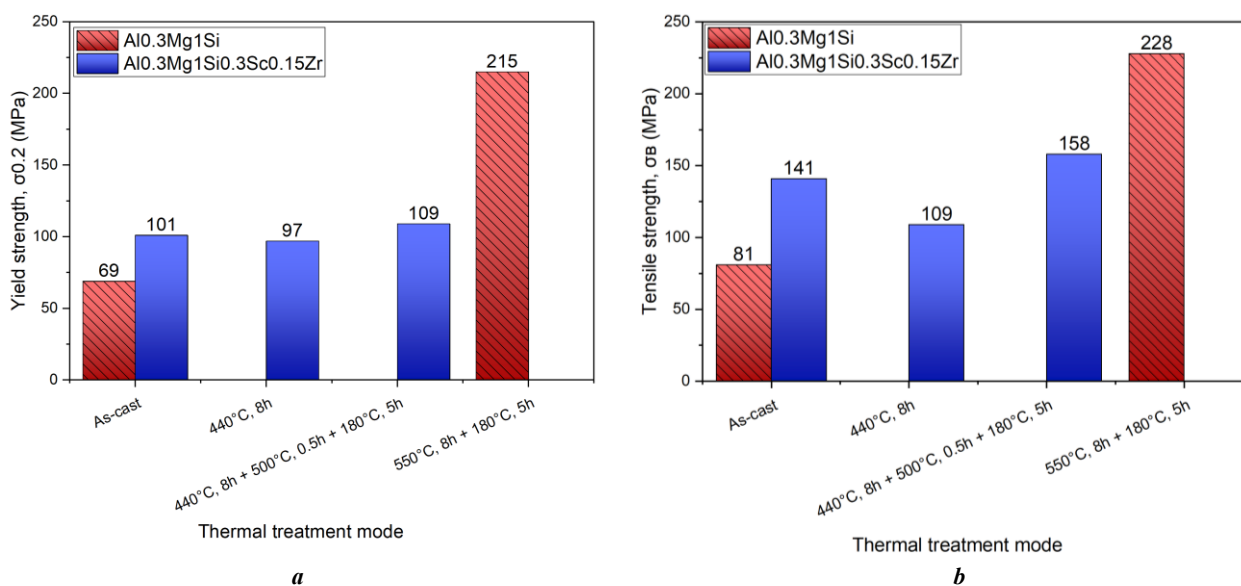


Fig. 7. Mechanical properties of the alloys under consideration after thermal treatment:

a – yield strength; **b** – tensile strength

Рис. 7. Механические свойства рассматриваемых сплавов после термической обработки:

a – предел текучести; **b** – предел прочности

CONCLUSIONS

1. In Al–Mg–Si series alloys with additional Sc and Zr alloying, improved mechanical properties are observed in the as-cast state compared to the base alloy. The main reason for this is the formation of strengthening Al_3Sc type particles precipitated during the cooling process of the cast structure. Solid solution strengthening with scandium and zirconium also contributes to improving mechanical properties.

2. Annealing at $440\text{ }^{\circ}C$ does not lead to a significant increase in the number of Al_3Sc particles. This is related to

the fact that the precipitation of the bulk of scandium from the solid solution occurs at the stage of cooling the ingot. The yield strength at this stage of thermal treatment does not change, but the tensile strength decreases. The decrease in this indicator is associated, primarily, with the magnesium release from the supersaturated solid solution.

3. Artificial ageing at $180\text{ }^{\circ}C$ for 5 h leads to the formation of strengthening β'' particles (Mg_2Si_6), which significantly increase the mechanical properties in both types of alloy. However, in the base alloy, the number of these particles is larger, and the strengthening effect they cause is

higher. This is primarily related to the fact that for an alloy without Sc and Zr, complete hardening is possible (550 °C, 8 h) promoting the dissolution of Mg and Si.

REFERENCES

1. Edwards G.A., Stiller K., Dunlop G.L., Couper M.J. The precipitation sequence in Al–Mg–Si alloys. *Acta Materialia*, 1998, vol. 46, no. 11, pp. 3893–3904. DOI: [10.1016/S1359-6454\(98\)00059-7](https://doi.org/10.1016/S1359-6454(98)00059-7).
2. Murayama M., Hono K. Pre-precipitate clusters and precipitation processes in Al–Mg–Si alloys. *Acta Materialia*, 1999, vol. 47, no. 5, pp. 1537–1548. DOI: [10.1016/S1359-6454\(99\)00033-6](https://doi.org/10.1016/S1359-6454(99)00033-6).
3. Meyruey G., Massadier V., Lefebvre W., Perez M. Over-ageing of an Al–Mg–Si alloy with silicon excess. *Materials Science and Engineering: A*, 2018, vol. 730, pp. 92–105. DOI: [10.1016/j.msea.2018.05.094](https://doi.org/10.1016/j.msea.2018.05.094).
4. Matsuda K., Ikeno S., Terayama K., Matsui H., Sato T., Uetani Ya. Comparison of precipitates between excess Si-type and balanced-type Al–Mg–Si alloys during continuous heating. *Metallurgical and materials transactions*, 2005, vol. 36, no. 8, pp. 2007–2012. DOI: [10.1007/s11661-005-0321-y](https://doi.org/10.1007/s11661-005-0321-y).
5. Elagin V.I., Zakharov V.V., Rostova T.D. Prospects for alloying aluminum alloys with scandium. *Tsvetnye metally*, 1982, no. 2, pp. 96–99.
6. Dorin T., Ramajayam M., Vahid A., Langan T. Aluminium scandium alloys. *Fundamentals of aluminium metallurgy*, 2018, pp. 439–494. DOI: [10.1016/B978-0-08-102063-0.00012-6](https://doi.org/10.1016/B978-0-08-102063-0.00012-6).
7. Röyset J., Ryum N. Scandium in aluminium alloys. *International Materials Reviews*, 2005, vol. 50, no. 1, pp. 19–44. DOI: [10.1179/174328005X14311](https://doi.org/10.1179/174328005X14311).
8. Lityńska-Dobrzyńska L. Effect of heat treatment on the sequence of phases formation in Al–Mg–Si alloy with Sc and Zr additions. *Archives of Metallurgy and Materials*, 2006, vol. 51, no. 4, pp. 555–560.
9. Mikhaylovskaya A.V., Mochugovskiy A.G., Levchenko V.S., Tabachkova N.Yu., Mufalo W., Portnoy K. Precipitation behavior of L₁₂ Al₃Zr phase in Al–Mg–Zr alloy. *Materials Characterization*, 2018, vol. 139, pp. 30–37. DOI: [10.1016/j.matchar.2018.02.030](https://doi.org/10.1016/j.matchar.2018.02.030).
10. Rokhlin L.L., Bochvar N.R., Tabachkova N.Yu., Sukhanov A.V. The Effect of Scandium on Kinetics and Strengthening of Al–Mg₂Si System Alloys in the Case of Ageing. *Tekhnologiya legkikh splavov*, 2015, no. 2, pp. 53–62. EDN: [VKABCF](https://www.edn.ru/VKABCF).
11. Vlach M., Smola B., Stulíková I., Očenášek V. Microstructure and mechanical properties of the AA6082 aluminium alloy with small additions of Sc and Zr. *International journal of materials research*, 2009, vol. 100, no. 3, pp. 420–423. DOI: [10.3139/146.110022](https://doi.org/10.3139/146.110022).
12. Jiang Shengyu, Wang Ruihong. Grain size-dependent Mg/Si ratio effect on the microstructure and mechanical/electrical properties of Al–Mg–Si–Sc alloys. *Journal of Materials Science & Technology*, 2019, vol. 35, no. 7, pp. 1354–1363. DOI: [10.1016/j.jmst.2019.03.011](https://doi.org/10.1016/j.jmst.2019.03.011).
13. Cabibbo M., Evangelista E. A TEM study of the combined effect of severe plastic deformation and (Zr),(Sc+Zr)-containing dispersoids on an Al–Mg–Si alloy. *Journal of materials science*, 2006, vol. 41, pp. 5329–5338. DOI: [10.1007/s10853-006-0306-2](https://doi.org/10.1007/s10853-006-0306-2).
14. Gao Y.H., Kuang J., Zhang Jinyu, Liu G., Sun J. Tailoring precipitation strategy to optimize microstructural evolution, aging hardening and creep resistance in an Al–Cu–Sc alloy by isochronal aging. *Materials Science and Engineering: A*, 2020, vol. 795, article number 139943. DOI: [10.1016/j.msea.2020.139943](https://doi.org/10.1016/j.msea.2020.139943).
15. Aryshenskii E., Lapshov M., Hirsh J., Kononov S., Bazhenov V., Drits A., Zaitsev D. Influence of the small Sc and Zr additions on the as-cast microstructure of Al–Mg–Si alloys with excess silicon. *Metals*, 2021, vol. 11, no. 11, article number 1797. DOI: [10.3390/met11111797](https://doi.org/10.3390/met11111797).

СПИСОК ЛИТЕРАТУРЫ

1. Edwards G.A., Stiller K., Dunlop G.L., Couper M.J. The precipitation sequence in Al–Mg–Si alloys // *Acta Materialia*. 1998. Vol. 46. № 11. P. 3893–3904. DOI: [10.1016/S1359-6454\(98\)00059-7](https://doi.org/10.1016/S1359-6454(98)00059-7).
2. Murayama M., Hono K. Pre-precipitate clusters and precipitation processes in Al–Mg–Si alloys // *Acta Materialia*. 1999. Vol. 47. № 5. P. 1537–1548. DOI: [10.1016/S1359-6454\(99\)00033-6](https://doi.org/10.1016/S1359-6454(99)00033-6).
3. Meyruey G., Massadier V., Lefebvre W., Perez M. Over-ageing of an Al–Mg–Si alloy with silicon excess // *Materials Science and Engineering: A*. 2018. Vol. 730. P. 92–105. DOI: [10.1016/j.msea.2018.05.094](https://doi.org/10.1016/j.msea.2018.05.094).
4. Matsuda K., Ikeno S., Terayama K., Matsui H., Sato T., Uetani Ya. Comparison of precipitates between excess Si-type and balanced-type Al–Mg–Si alloys during continuous heating // *Metallurgical and materials transactions*. 2005. Vol. 36. № 8. P. 2007–2012. DOI: [10.1007/s11661-005-0321-y](https://doi.org/10.1007/s11661-005-0321-y).
5. Елагин В.И., Захаров В.В., Ростова Т.Д. Перспективы легирования алюминиевых сплавов скандием // *Цветные металлы*. 1982. № 2. С. 96–99.
6. Dorin T., Ramajayam M., Vahid A., Langan T. Aluminium scandium alloys // *Fundamentals of aluminium metallurgy*. 2018. P. 439–494. DOI: [10.1016/B978-0-08-102063-0.00012-6](https://doi.org/10.1016/B978-0-08-102063-0.00012-6).
7. Röyset J., Ryum N. Scandium in aluminium alloys // *International Materials Reviews*. 2005. Vol. 50. № 1. P. 19–44. DOI: [10.1179/174328005X14311](https://doi.org/10.1179/174328005X14311).
8. Lityńska-Dobrzyńska L. Effect of heat treatment on the sequence of phases formation in Al–Mg–Si alloy with Sc and Zr additions // *Archives of Metallurgy and Materials*. 2006. Vol. 51. № 4. P. 555–560.
9. Mikhaylovskaya A.V., Mochugovskiy A.G., Levchenko V.S., Tabachkova N.Yu., Mufalo W., Portnoy K. Precipitation behavior of L₁₂ Al₃Zr phase in Al–Mg–Zr alloy // *Materials Characterization*. 2018. Vol. 139. P. 30–37. DOI: [10.1016/j.matchar.2018.02.030](https://doi.org/10.1016/j.matchar.2018.02.030).
10. Рохлин Л.Л., Бочвар Н.Р., Табачкова Н.Ю., Суханов А.В. Влияние скандия на кинетику и упрочнение при старении сплавов системы Al–Mg₂Si // *Технология легких сплавов*. 2015. № 2. С. 53–62. EDN: [VKABCF](https://www.edn.ru/VKABCF).
11. Vlach M., Smola B., Stulíková I., Očenášek V. Microstructure and mechanical properties of the AA6082 aluminium alloy with small additions of Sc and Zr // *International journal of materials research*. 2009. Vol. 100. № 3. P. 420–423. DOI: [10.3139/146.110022](https://doi.org/10.3139/146.110022).
12. Jiang Shengyu, Wang Ruihong. Grain size-dependent Mg/Si ratio effect on the microstructure and mechanical/electrical properties of Al–Mg–Si–Sc alloys // *Journal of Materials Science & Technology*. 2019. Vol. 35. № 7. P. 1354–1363. DOI: [10.1016/j.jmst.2019.03.011](https://doi.org/10.1016/j.jmst.2019.03.011).

13. Cabibbo M., Evangelista E. A TEM study of the combined effect of severe plastic deformation and (Zr),(Sc+Zr)-containing dispersoids on an Al–Mg–Si alloy // Journal of materials science. 2006. Vol. 41. P. 5329–5338. DOI: [10.1007/s10853-006-0306-2](https://doi.org/10.1007/s10853-006-0306-2).
14. Gao Y.H., Kuang J., Zhang Jinyu, Liu G., Sun J. Tailoring precipitation strategy to optimize microstructural evolution, aging hardening and creep resistance in an Al–Cu–Sc alloy by isochronal aging // Materials Science and Engineering: A. 2020. Vol. 795. Article number 139943. DOI: [10.1016/j.msea.2020.139943](https://doi.org/10.1016/j.msea.2020.139943).
15. Aryshenskii E., Lapshov M., Hirsh J., Konovalov S., Bazhenov V., Drits A., Zaitsev D. Influence of the small Sc and Zr additions on the as-cast microstructure of Al–Mg–Si alloys with excess silicon // Metals. 2021. Vol. 11. № 11. Article number 1797. DOI: [10.3390/met11111797](https://doi.org/10.3390/met11111797).

Влияние термической обработки на микроструктуру и механические свойства сплава Al–Mg–Si–Sc–Zr с избытком Si

© 2023

Арышенский Евгений Владимирович^{*1,2,4}, доктор технических наук, доцент, старший научный сотрудник лаборатории электронной микроскопии и обработки изображений, ведущий научный сотрудник

Лапшов Максим Александрович^{2,5}, инженер

Коновалов Сергей Валерьевич^{1,2,6}, доктор технических наук, профессор, проректор по научной и инновационной деятельности, главный научный сотрудник

Малкин Кирилл Александрович², лаборант

Распосиенко Дмитрий Юрьевич^{3,7}, кандидат технических наук, старший научный сотрудник лаборатории цветных сплавов

Макаров Владимир Викторович^{2,3,8}, научный сотрудник лаборатории цветных сплавов, младший научный сотрудник

¹Сибирский государственный индустриальный университет, Новокузнецк (Россия)

²Самарский национальный исследовательский университет имени академика С.П. Королева, Самара (Россия)

³Институт физики металлов имени М.Н. Михеева Уральского отделения РАН, Екатеринбург (Россия)

*E-mail: ar-evgenii@yandex.ru,
arishenskiy_ev@sibsiu.ru

⁴ORCID: <https://orcid.org/0000-0003-3875-7749>

⁵ORCID: <https://orcid.org/0000-0002-1306-4578>

⁶ORCID: <https://orcid.org/0000-0003-4809-8660>

⁷ORCID: <https://orcid.org/0000-0002-7670-9054>

⁸ORCID: <https://orcid.org/0000-0002-7306-3657>

Поступила в редакцию 06.10.2023

Принята к публикации 31.10.2023

Аннотация: В работе исследовался сплав Al–Mg–Si, не содержащий скандия и циркония, а также сплав Al–Mg–Si–Sc–Zr с избытком кремния. Для сплава Al_{0,3}Mg₁Si_{0,3}Sc_{0,15}Zr была проведена многоступенчатая термическая обработка, включающая в себя отжиг при температуре 440 °С в течение 8 ч, высокотемпературный отжиг при 500 °С в течение 0,5 ч и искусственное старение при температуре 180 °С с выдержкой 5 ч. Сплав Al_{0,3}Mg₁Si подвергался отжигу при 550 °С в течение 8 ч, затем проводилось искусственное старение аналогично сплаву с добавками Sc и Zr. Для изучения тонкой структуры проводилось исследование при помощи просвечивающей электронной микроскопии. В литом состоянии и после каждой стадии термической обработки определялись механические свойства сплавов. Установлено, что в сплаве, легированном Sc и Zr, уже на стадии формирования литой структуры происходит образование частиц Al₃Sc. При последующем искусственном старении происходит распад пересыщенного твердого раствора с образованием частиц β" (Mg₅Si₆), улучшающих механические свойства. Установлено, что в сплаве с содержанием скандия формируется меньше частиц β" (Mg₅Si₆), в результате его прочностные свойства несколько хуже, чем у базового сплава. Кроме того, данные частицы крупнее, чем в сплаве, не содержащем скандий. Это объясняется тем, что для сплава со скандиевыми добавками невозможно проведение полноценной закалки.

Ключевые слова: Al–Mg–Si–Sc–Zr; избыток Si; многоступенчатая термическая обработка; искусственное старение; ПЭМ; механические свойства; Al₃Sc; Mg₅Si₆.

Благодарности: Исследование выполнено за счет гранта РФФИ № 21-19-00548, <https://rscf.ru/project/21-19-00548/>.

Для цитирования: Арышенский Е.В., Лапшов М.А., Коновалов С.В., Малкин К.А., Распосиенко Д.Ю., Макаров В.В. Влияние термической обработки на микроструктуру и механические свойства сплава Al–Mg–Si–Sc–Zr с избытком Si // Frontier Materials & Technologies. 2023. № 4. С. 9–17. DOI: 10.18323/2782-4039-2023-4-66-1.

Sorption properties of layered double hydroxides produced by ultrasonic exposure

© 2023

Roman A. Golubev*^{1,2}, junior researcher, postgraduate student

Vasily V. Rubanik^{1,4}, Doctor of Sciences (Engineering),
corresponding member of the National Academy of Sciences of Belarus,
Associate Professor, Head of Laboratory of Metal Physics

Vasily V. Rubanik Jr.^{1,5}, Doctor of Sciences (Engineering), Associate Professor, Director

Ilya S. Kritchenkov^{1,3,6}, PhD (Chemistry), senior researcher

Andrey S. Kritchenkov^{1,2,7}, Doctor of Sciences (Chemistry), leading researcher

¹*Institute of Technical Acoustics of the National Academy of Sciences of Belarus, Vitebsk (Republic of Belarus)*

²*RUDN University (Peoples' Friendship University of Russia), Moscow (Russia)*

³*St. Petersburg State University, St. Petersburg (Russia)*

*E-mail: ita@vitebsk.by,
asfdss.asdasf@yandex.ru

⁴ORCID: <https://orcid.org/0000-0002-0350-1180>

⁵ORCID: <https://orcid.org/0000-0002-9268-0167>

⁶ORCID: <https://orcid.org/0000-0003-0108-0690>

⁷ORCID: <https://orcid.org/0000-0002-6411-5988>

Received 03.07.2023

Accepted 12.11.2023

Abstract: Layered double hydroxides (LDH) can be classified as promising materials due to the ease of synthesis, as well as their wide scope of application. However, the process of LDH synthesis, depending on the LDH chemical composition, can take from tens of hours to several days. It was previously identified that ultrasound exposure during the LDH production significantly reduces the synthesis time, and LDHs produced in this way are interesting in relation to the study of their physicochemical properties and sorption capacity. In this work, the authors produced Mg/Fe LDHs in nitrate form by the traditional method and by the combined action of ultrasound and increased hydrostatic pressure. The resulting samples are characterized by a complex of physicochemical methods of analysis, including scanning electron microscopy (SEM), infrared spectroscopy (IR), X-ray phase analysis (XRD), and thermal gravimetric analysis (TGA) with differential scanning calorimetry (DSC). Experiments were carried out to study the sorption capacity of the obtained Fe/Mg LDH samples in relation to chromate ions under normal conditions and under the influence of ultrasound, including in combination with increased hydrostatic pressure. A photoelectric photometer was used to obtain and analyze data with quantitative values of the sorption process. Data of comprehensive analysis of the finished product indicate that the synthesized material is a Mg/Fe layered double hydroxide. X-ray phase analysis identified that the LDH synthesis using ultrasound and pressure increases the crystallinity degree of the finished product. It has been found that the sorption properties of LDHs produced by the conventional method and LDHs produced under the influence of ultrasound and pressure are different. In Mg/Fe LDHs synthesized by the conventional method, chromate sorption proceeds better than in samples synthesized using ultrasonic treatment in combination with increased hydrostatic pressure. The study shows that the sorption process of the examined LDH samples is described by different mathematical models.

Keywords: layered double hydroxides; Mg/Fe; ultrasonic synthesis; sorption properties; chromate ions.

Acknowledgments: The work was supported by the Belarusian Republican Foundation for Fundamental Research (project No. H21RM-081).

The authors express gratitude to the Individual Project for Fundamental and Applied Research “Ultrasonic Synthesis of Medical-Purpose Layered Double Hydroxides”.

The authors express their gratitude to Scientific Park of St. Petersburg State University (Interdisciplinary Resource Center “Nanotechnology” and Resource Center for Chemical Analysis and Materials Research) for their assistance in studying the microstructure (SEM) and IR-spectra of synthesized LDH samples. In commemoration of the 300th anniversary of St. Petersburg State University’s founding.

The paper was written on the reports of the participants of the XI International School of Physical Materials Science (SPM-2023), Togliatti, September 11–15, 2023.

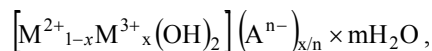
For citation: Golubev R.A., Rubanik V.V., Rubanik V.V. Jr., Kritchenkov I.S., Kritchenkov A.S. Sorption properties of layered double hydroxides produced by ultrasonic exposure. *Frontier Materials & Technologies*, 2023, no. 4, pp. 19–30. DOI: 10.18323/2782-4039-2023-4-66-2.

INTRODUCTION

Layered double hydroxides (LDHs) are considered a promising class of compounds for the creation of catalytic systems [1], biomedical materials [2], and adsorbents [3]. An LDH can be used both as a separate sorbent [4], and as an element of a composite sorbent [5]. Recently, there has

been a growing number of publications on the study of the LDH ability to sorb substances polluting wastewater, i. e., pollutants. This includes substances containing heavy metals [6] or chromates [7]. In an environmental context, studies on the sorption properties of LDHs containing metals with low water environment toxicity – Mg, Al, Fe are the most interesting [8; 9].

LDHs can be used as sorbents due to their physico-chemical properties. LDHs are inorganic frameworks consisting of two positively charged layers, formed by metal ions and hydroxide ions, between which mobile anions and water molecules are located [10]. In their structure and properties, they are similar to anionic clays consisting of brucite-like layers [11]. The LDH composition is expressed by the general formula:



where M^{2+} and M^{3+} are cations of divalent and trivalent metals, respectively;

A^{n-} is an interlayer anion;

x is the molar ratio of trivalent cation to divalent cation;

n and m are the amount of interlayer water.

Due to their layered structure and electrostatic nature, layered double hydroxides can be intercalated with anions or anionic complexes of various sizes and nature, which determines the possibility of their use as promising sorption materials [12–14].

The LDH synthesis does not require complex laboratory equipment, and the synthesis process itself consists of two key stages: coprecipitation and crystallisation. The crystallisation stage, in accordance with the classical LDH synthesis method, is carried out by heating and takes from 10 h to several days [15; 16]. Relatively recently, in the literature, works have appeared on the use of ultrasound in the LDH synthesis. These works state that the ultrasound effect on the reaction mixture reduces the crystallisation stage to several tens of minutes [17–19]. The sorption properties of LDH produced in this way may differ from the sorption properties of LDH produced by the classical method. It should be noted that the LDH synthesis under the influence of ultrasound in combination with increased hydrostatic pressure, and therefore the sorption properties of such LDH, are not described at all in the literature.

The purpose of this work is to investigate the possibility of synthesising layered double hydroxides under the influence of ultrasound and pressure, as well as to study their sorption properties in relation to the CrO_4^{2-} chromate anion, compared to LDHs produced by the conventional method.

METHODS

The authors used analytically pure magnesium (II) nitrate 6-water, analytically pure iron (III) nitrate 9-water (JSC "Base of chemical reagents No. 1"), sodium hydroxide, sodium nitrate (JSC "Vekton"), potassium chromate (Sigma-Aldrich). Other chemicals, solvents, and materials were received from commercial sources and used without additional purification.

The Mg(II)/Fe(III)- NO_3^- LDH synthesis was carried out by coprecipitation. A solution of sodium hydroxide and sodium nitrate (2 and 0.25 eq., respectively) was added drop-by-drop to a solution of magnesium (II) nitrate hexahydrate, and iron (III) nitrate nonahydrate (0.75 and 0.25 eq., respectively). Further processing of the reaction mixture was carried out using one of the following methods:

1) the reaction mixture was kept at 75 °C for 72 h;

2) the reaction mixture was processed with ultrasound at a frequency of 22 kHz with an applied hydrostatic pressure of 2 atm for 1 h.

The resulting precipitate was washed with distilled water until pH=7, centrifuged (5000 rpm for 5 min), and then stored under a layer of water or dried to constant weight at 30 °C for 24 h.

The resulting samples were examined for their ability to sorption of chromate ions.

To determine the time of sorption equilibrium onset, 0.084 g of LDH, 45–47 g of water, 1 g of 0.1000 N K_2CrO_4 solution, and 0.001 g of sodium hydroxide were placed in a conical flat-bottomed flask, after that, the mixture weight was made up to 50 g by adding distilled water. The resulting suspension was stirred for 1–10 min or exposed to ultrasound, or ultrasound in combination with increased hydrostatic pressure of 2 atm. The equilibrium concentration of potassium chromate in the suspension was determined photometrically using the calibration curve method. Experimental solutions and a control solution were photometered against distilled water at a wavelength of 410 nm.

Experiments to study the sorption of LDH were carried out at a temperature of 18 °C. An LDH (0.084 g), 45–47 g of water, 0.1000 N solution of K_2CrO_4 (0.5, 1, 2, and 3 g), 0.001 g of sodium hydroxide were placed in a conical flat-bottomed flask, after that, the mixture weight was made up to 50 g by adding distilled water. The resulting suspension, was stirred for 10 min. The potassium chromate concentration in the suspension was determined photometrically, using the calibration curve method. Experimental solutions, and a control solution were photometered against distilled water at a wavelength of 410 nm. When photometering experimental solutions, the equilibrium absorbance A_e was determined, followed by the calculation of the equilibrium concentration of potassium chromate C_e .

X-ray diffraction analysis (XRF) was performed on a DRON-7 diffractometer, 2θ angular interval from 7 to 80° with a scanning step of $\Delta 2\theta=0.02^\circ$ and exposure time of 7 s per point. The authors used Cu- $K\alpha$ radiation (Ni-filter), which was subsequently decomposed into components $K\alpha_1$ and $K\alpha_2$, when processing the spectra.

Thermal gravimetric analysis (TGA) was carried out on a NETZSCH STA 449 F3 Jupiter device, using a heating rate of 10 °C/min in a temperature range of 30 to 600 °C.

The microstructure study (SEM) was carried out at the Interdisciplinary Resource Centre for Nanotechnology of the Research Park of St. Petersburg State University on a Carl Zeiss Merlin scanning microscope (Carl Zeiss AG, Oberkochen, Germany) at 10 kV, SE2 detector, working distance of 6.4 mm, pressure of $9.4 \cdot 10^{-7}$ mbar. Graphite was deposited by a Gatan PECS Model 682 device; deposition layer of 10 nm. Infrared (IR) spectra were recorded on a Shimadzu IRPrestige-21 spectrometer (Japan). Photometric studies were carried out using a KFK-3 photoelectric photometer.

RESULTS

Synthesis conditions, physical form, and codenames of the obtained LDHs are given in Table 1.

An image of powder LDH taken using a scanning electron microscope (Fig. 1) clearly shows "flakes", which are a consequence of its layered structure. Fig. 2 shows

an example of the LDH IR spectrum. IR spectra were recorded in the range of 4000–400 cm^{-1} . The IR spectrum contains two intense absorption bands (broad one with a maximum at 3447 cm^{-1} and narrow one with a maximum at 1340 cm^{-1}), two broadened low-intensity bands at 1642 and 750 cm^{-1} , and a band of medium intensity at 549 cm^{-1} .

The diffraction patterns of the produced LDHs demonstrate the presence of peaks characteristic of the LDH crystal lattice (Fig. 3). Fig. 3 b also contains an additional peak in the region of $2\theta=40^\circ$, indicating the presence of an additional phase in the compound.

The TGA and DSC dependences for all produced LDHs are of the same type; an example of a typical thermogram is shown in Fig. 4. The thermogram shows that the thermal decomposition of the sample, goes through the stages of interlayer water removal, degradation of hydroxide layers to oxide layers, and removal of interlayer anions, respectively.

The data obtained from the experiment on the chromate sorption of Mg/Fe LDH are given in Table 2. The experimental data obtained from studying the influence of chromate weight on the sorption process are given in Table 3. Fig. 5 shows the adsorption isotherms obtained from these experimental data.

To select the most appropriate adsorption model, Langmuir (Fig. 6) and Freundlich (Fig. 7) isotherms were plotted in inverse and logarithmic coordinates, respectively.

Langmuir adsorption is described by the equation

$$\frac{c_e}{q_e} = \frac{1}{Q_m K_L} + \frac{c_e}{Q_m},$$

where q_e is the weight of adsorbed potassium chromate per LDH adsorbent unit weight, mg/g;

Table 1. Synthesis conditions, physical form, and codenames of LDHs

Таблица 1. Условия синтеза, физическая форма и кодовые наименования СДГ

Code	Synthesis conditions			Physical form
	Temperature 75 °C, 72 h in water bath	Ultrasound treatment at 22 kHz	Ultrasound treatment at 22 kHz with pressure of 2 atm	
1i	+			Powder
1ii	+			Suspension
2i		+	+	Powder
2ii		+	+	Suspension

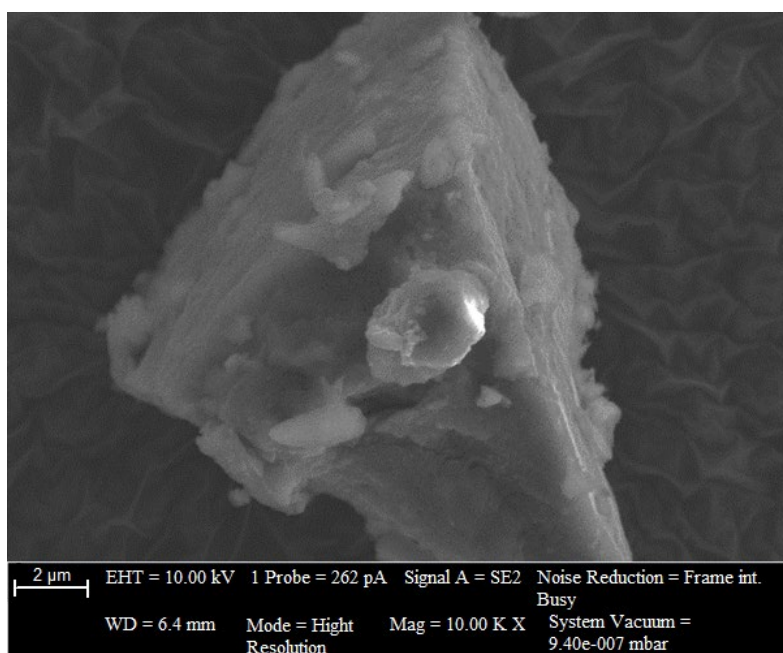


Fig. 1. A scanning electron microscope image of the Mg(II)/Fe(III)–NO₃[−] layered double hydroxide

Рис. 1. Снимок Mg(II)/Fe(III)–NO₃[−] слоистого двойного гидроксида, сделанный на сканирующем электронном микроскопе

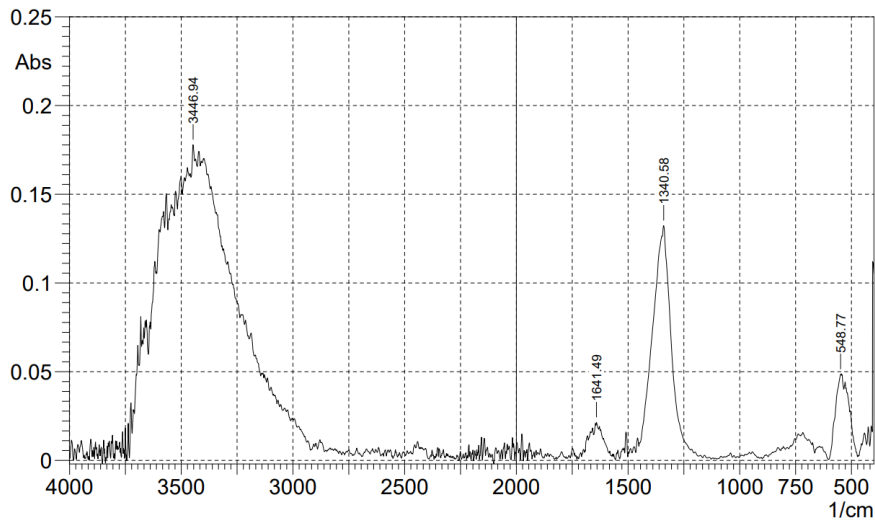


Fig. 2. Infrared spectra of the Mg(II)/Fe(III)-NO₃⁻ layered double hydroxide
Рис. 2. Инфракрасные спектры Mg(II)/Fe(III)-NO₃⁻ слоистого двойного гидроксида

C_e is an equilibrium concentration of potassium chromate calculated from photometric data, mg/l;

K_L is an adsorption free energy constant (otherwise – Langmuir affinity constant), l/mg;

Q_m is a monolayer adsorption power, mg/g.

Within the framework of Langmuir adsorption theory, it is expected that all adsorption centres are energetically equivalent, and each such centre can hold only one adsorbent particle. Therefore, the adsorbent centre has a finite capacity to adsorb an adsorbate.

Based on the graphically represented experimental data (Fig. 6), the K_L and Q_m parameters were calculated

(Table 4). The Langmuir approach can be used to predict the affinity force between adsorbate and adsorbent using the dimensionless partition coefficient (R_L) (Table 3), which was determined by the equation

$$R_L = \frac{1}{(1 + K_L c_0)}$$

At partition coefficient values $0 < R_L < 1$, adsorption predominates, at $R_L > 1$, desorption predominates, while at $R_L = 1$, so-called linear adsorption is observed, and adsorption is irreversible at $R_L = 0$.

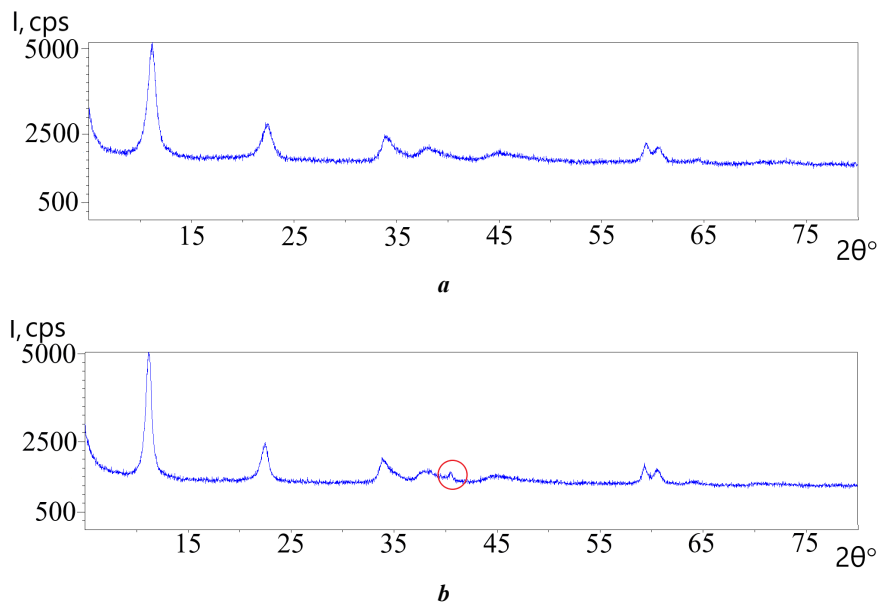


Fig. 3. Diffraction patterns of the Mg(II)/Fe(III)-NO₃⁻ layered double hydroxides synthesized by the 1i (a) and 2i (b) method. The marked area is an additional peak indicating the presence of an extra phase in the compound

Рис. 3. Диффрактограммы Mg(II)/Fe(III)-NO₃⁻ слоистых двойных гидроксидов, синтезированных способом 1i (a) и 2i (b). Выделенная область – дополнительный пик, говорящий о наличии в соединении дополнительной фазы

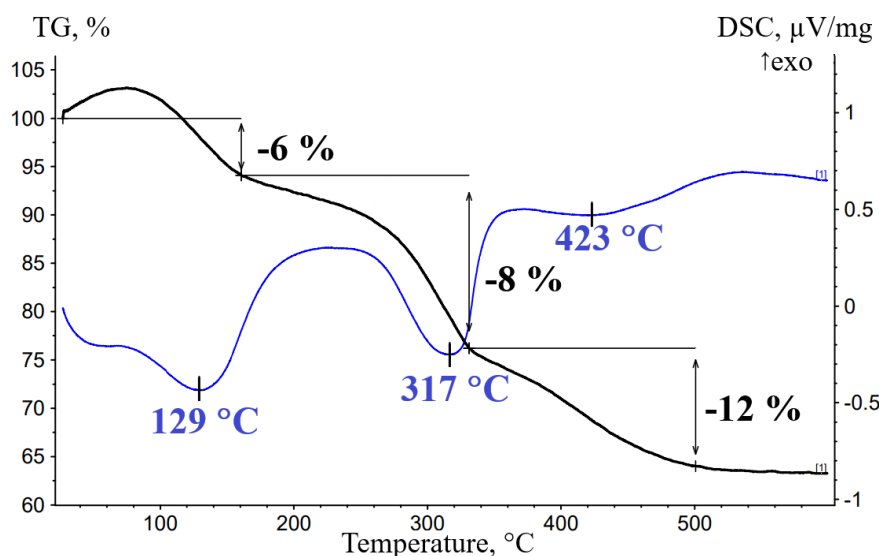


Fig. 4. Stages of thermal decomposition of the Mg(II)/Fe(III)-NO₃⁻ layered double hydroxide
Рис. 4. Стадии термического разложения Mg(II)/Fe(III)-NO₃⁻ слоистого двойного гидроксида

According to Freundlich, adsorption is described by the empirical equation

$$\lg q_e = \lg K_F + \frac{1}{n} \lg c_e,$$

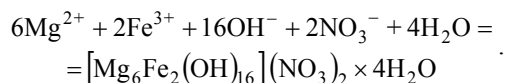
where q_e is the weight of adsorbed potassium chromate per LDH adsorbent unit weight, mg/g;
 K_F is a Freundlich constant, mg/g;
 $1/n$ is the adsorption intensity.

Based on the graphically represented experimental data (Fig. 7), the K_F and $1/n$ parameters, as well as the partition coefficient (Table 4), were calculated.

To determine the more likely adsorption mechanism, the correlation coefficient r^2 (Table 4) for the experimental data was calculated using the Langmuir (Fig. 6) and Freundlich (Fig. 7) adsorption plots.

DISCUSSION

Chemical processes proceeding during LDH synthesis can be expressed by the following equation:



The SEM image of LDHs (Fig. 1) clearly demonstrates the flaky microstructure of the synthesised powder LDHs, which, in turn, is a consequence of their layered organisation. The data obtained using SEM are consistent with literature data [20–22] on other LDHs, as well as their natural analogues – cationic clays, which also have a flaky structure due to their layered morphology.

The presented IR spectra (Fig. 2) contain absorption bands that prove the presence of chemical bonds characteristic of magnesium-iron LDHs: a wide intense absorption band at 3750–3200 cm⁻¹ corresponds to OH stretching vi-

brations of water molecules and hydroxyl groups. The presence of a broadened low-intensity absorption band at 1641 cm⁻¹ is caused by bending vibrations of water molecules. Absorption bands at 1340 and 750 cm⁻¹ of high and low intensity, respectively, relate to nitrate anion vibrations, while the presence of a medium-intensity band at 549 cm⁻¹ is caused by covalent metal-oxygen coordination bonds.

The diffraction patterns of the resulting LDHs are almost identical (Fig. 3) and contain a set of basal reflections typical for LDHs with a hydrotalcite structure. All samples are characterised by a hexagonal crystal system. These facts indicate a layered structure of the produced LDHs and allow attributing the resulting LDHs to the hydrotalcite crystallographic type. In addition, calculations using the obtained experimental data indicate that the crystallinity of the samples is maximum for 2i and 2ii. Moreover, in the case of 2i and 2ii samples, an extra layer line appears in the diffraction patterns in the region of $2\theta=40.50^\circ$ ($d=2.225 \text{ \AA}$).

TGA/DSC analysis of LDH samples (Fig. 4) showed that, in general, the thermal decomposition of the samples proceeds in three stages. At the first stage, a loss of inter-layer water occurs, which is accompanied by a pronounced endo-effect (weight loss is about 6%). At the second stage, also accompanied by a visible endo-effect, the hydrotalcite-like hydroxide layers are destroyed, accompanied by their transformation into predominantly oxide-type layered structures. At the second stage, the NO₃⁻ anion also decomposes. The weight loss at the second stage is about 18%. The third stage is accompanied by a weakly expressed, barely noticeable endo-effect; the final decomposition of residual hydroxides and the NO₂⁻ anion occurs. As a result, a mixture of iron (III) and magnesium (II) oxides is formed, and the weight loss is about 12%.

The data obtained when studying the LDH sorption properties in relation to chromate ions (Table 2) indicate that with normal stirring, sorption equilibrium is achieved within 5 min after the experiment onset (Table 2, No. 1, 4, 7). However, the maximum sorption is observed after 1 min.

Table 2. Comparison of sorption efficiency under various conditions
Таблица 2. Сравнение эффективности сорбции в различных условиях

No.	Sorption conditions		Optical density of control solution A_0	Optical density of experimental solution A_e	Optical density difference ΔA
	Treatment*	Time, min			
1	18 °C, stirring (1i)	1	0.339	0.210	0.129
2	18 °C, stirring (2ii)	1	0.339	0.229	0.110
3	18 °C, stirring (1ii)	5	0.339	0.220	0.119
4	18 °C, stirring (1i)	5	0.337	0.236	0.101
5	18 °C, stirring (2ii)	5	0.339	0.241	0.098
6	18 °C, stirring (2i)	5	0.339	0.267	0.072
7	18 °C, stirring (1i)	10	0.378	0.276	0.102
8	US 22 kHz (1ii)	5	0.338	0.211	0.127
9	US 22 kHz (2ii)	5	0.338	0.222	0.116
10	US 22 kHz, $p=2$ atm (1ii)	5	0.351	0.199	0.152
11	US 22 kHz, $p=2$ atm (2ii)	5	0.351	0.223	0.128
12	US 22 kHz, $p=2$ atm (1ii)	0.5	0.343	0.228	0.115
13	US 22 kHz, $p=2$ atm (2ii)	0.5	0.337	0.246	0.091
14	US 22 kHz, $p=2$ atm (1i)	0.5	0.337	0.233	0.104
15	US 22 kHz, $p=2$ atm (2i)	0.5	0.337	0.234	0.103
16	US 22 kHz (1ii)	0.5	0.348	0.200	0.148
17	US 22 kHz (2ii)	0.5	0.348	0.219	0.129

Note. * LHD code is given in brackets (see Table 1).

Примечание. * В скобках указан код СДГ (см. таблицу 1).

Table 3. Adsorption at constant LDH weight and different chromate weight
Таблица 3. Адсорбция при постоянной массе СДГ и разной массе хромата

m_0 0.1000 N of K_2CrO_4 solution, g	Concentration in the initial solution C_0 , mg/l	Optical density A_e	Weight of sorbate chromate m_e K_2CrO_4 , mg	Concentration of sorbate chromate C_e , mg/l	Adsorption value q_e , mg/g	LDH m , mg
for 1i LDH						
0.500	64.7	0.126	2.20	44.0	12.4	0.0840
1.00	129	0.276	4.82	96.5	19.7	0.0840
2.00	258	0.581	10.2	203	33.3	0.0840
3.00	388	0.898	15.7	314	44.5	0.0840
for 2i LDH						
0.500	64.7	0.096	1.80	36	17.22	0.0840
1.00	129	0.256	4.81	96.2	19.68	0.0840
2.00	258	0.578	10.87	217.4	24.36	0.0840
3.00	388	0.906	17.03	340.6	28.44	0.0840

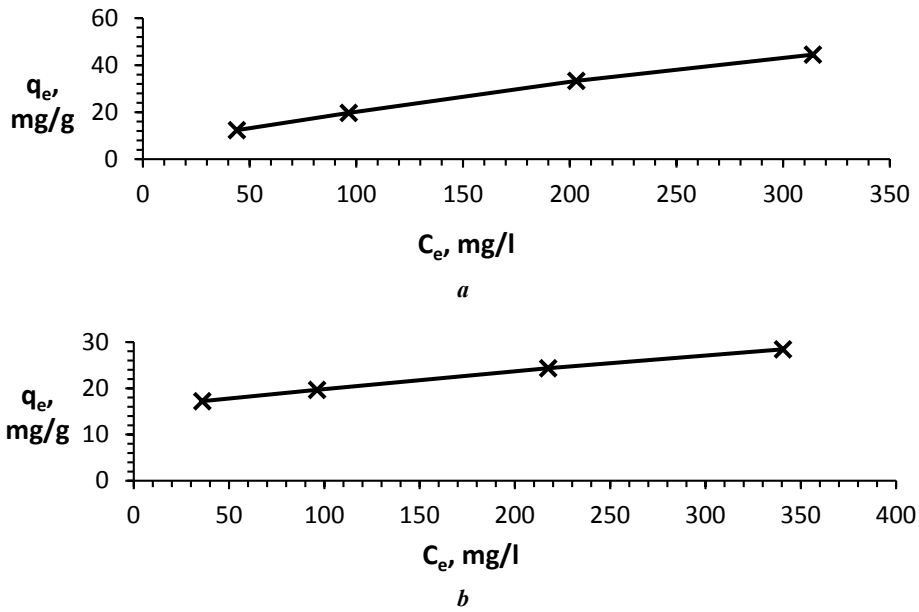


Fig. 5. Adsorption isotherm of potassium chromate for 1i (a) and 2i (b)
 Рус. 5. Изотерма адсорбции хромата калия для 1i (a) и 2i (b)

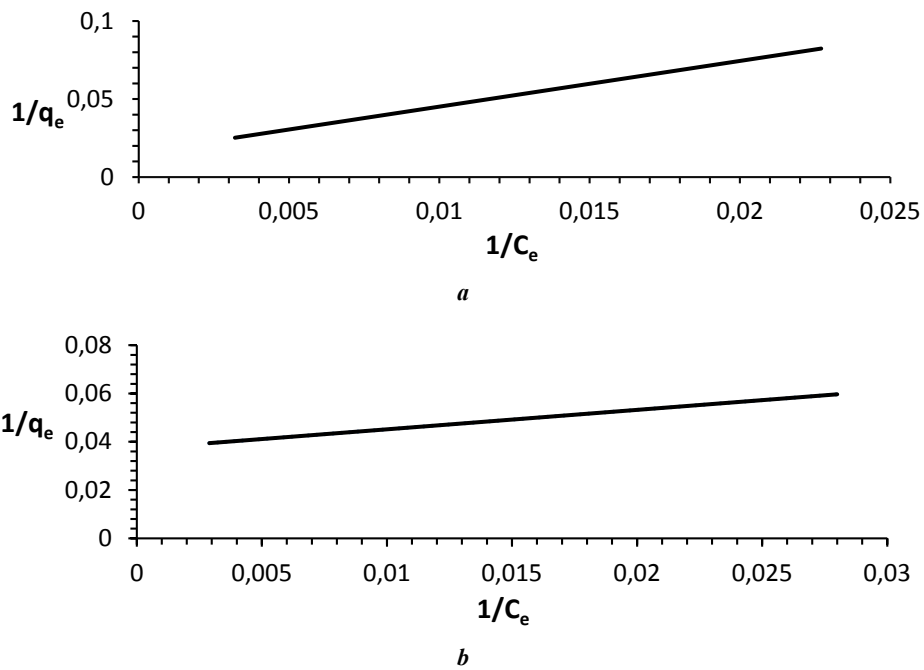


Fig. 6. Langmuir adsorption isotherm for 1i (a) and 2i (b)
 Рус. 6. Изотерма адсорбции для 1i (a) и 2i (b) по Ленгмюру

One should note that the use of the suspension LDH allows achieving slightly better sorption results than the use of the powder form (Table 2, No. 3 and 4, 5 and 6).

Experimental data (Table 2) indicate that when using the same hydroxide forms as sorbents, sorption improves for the same time when the system is exposed to ultrasound, and even greater when ultrasound is applied in combination with increased hydrostatic pressure (Table 2, No. 3, 8, 10 or 5, 9, 11).

In the case of ultrasonic treatment of sorption systems, the maximum sorption is observed in 0.5 min, and by 5 min of exposure, partial desorption of chromate ions occurs (Table 2, No. 8 and 16, 9 and 17). In the case of simultaneous action of ultrasound and pressure, the amount of sorbate chromate increases with an increase in sorption time from 0.5 to 5 min by approximately 30 % (Table 2, No. 10 and 12, 11 and 13). To determine accurately the time of maximum sorption, additional experiments are required.

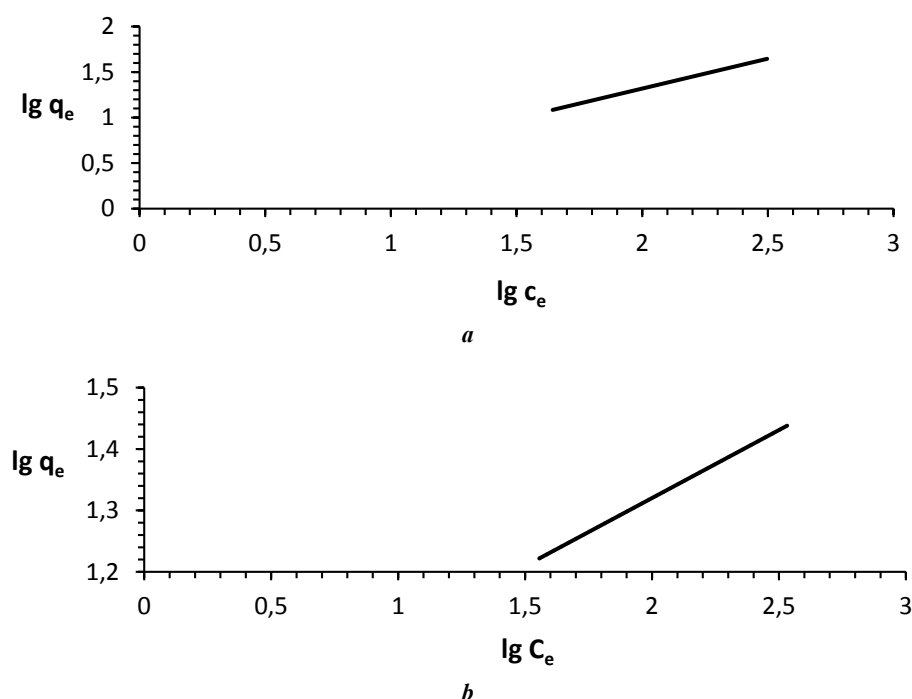


Fig. 7. Freundlich adsorption isotherm for 1i (a) and 2i (b)
 Рис. 7. Изотерма адсорбции для 1i (a) и 2i (b) по Фрейндлиху

Table 4. Comparison of Langmuir and Freundlich adsorption parameters
 Таблица 4. Сравнение параметров адсорбции по Ленгмюру и Фрейндлиху

According to Langmuir				According to Freundlich			
K_L	Q_m	R_L	r^2_L	K_F	$1/n$	R_L	r^2_F
for 1i LDH							
0.0032	62.50	0.7073	0.99275	1.01	0.656	0.0076	0.99927
for 2i LDH							
0.028	27.03	0.2168	0.8200	–	–	–	–

It is important to note that, as a rule, 1i and 1ii LDHs produced by the conventional method, demonstrate better sorption results than 2i and 2ii LDHs produced under the influence of ultrasound and pressure (Table 2, ΔA values for No. 3 and 5, 4 and 6, 8 and 9, 10 and 11, 12 and 13, 16 and 17).

The adsorption of LDH chromate ions obtained by the classical method (1i) is well described by both the Langmuir and Freundlich models. Although the correlation coefficients represented in Table 4 are very close, the slightly larger correlation coefficient r^2_F indicates that the adsorption of chromate ions by 1i LDH is somewhat more consistent with the Freundlich equation. In the case of an LDH produced by treating the reaction mixture with ultrasound at elevated pressure (2i), the adsorption of chromate ions is well described by the Langmuir model and cannot be described by the Freundlich equation. This is because, according to the Freundlich model, the straight

isotherm line must intersect the ordinate axis in the region of negative values, which does not agree with the experimental data. Thus, it seems possible to compare the efficiency of 1i and 2i samples only within the framework of the Langmuir model. Within the framework of this model, the adsorption power of LDH produced by the classical method (1i) is almost 2 times higher than the power of LDH produced under the influence of ultrasound in combination with pressure (2i), as evidenced by the Q_m values (Table 4). Moreover, the values of the Langmuir constant K_L given in Table 4 indicate that the affinity of chromate ions for 1i LDH is greater than for 2i. Thus, the Langmuir model indicates a higher sorption efficiency of 1i LDH, which is consistent with the data represented in Table 2.

The structure, and therefore the sorption properties in relation to chromate ions for LDHs produced by the classical method (1i and 1ii) and LDHs produced under the influence of ultrasound and pressure (2i and 2ii) differ.

Chromate ion has a greater affinity for LDHs of *1i* and *1ii* types, which may be interesting for the creation of purification systems. The lower affinity of the chromate ion for LDHs of *2i* and *2ii* types may be useful for the development of delivery systems and oxidative microoperators, where both the sorption of the chromate ion and its release, i. e., desorption are necessary. Thus, both LDH types are of interest from a practical point of view.

CONCLUSIONS

1. Ultrasound in combination with high pressure intensifies the interaction of magnesium (II) and iron (III) nitrates with alkali, which can be used successfully to produce layered double hydroxides (LDH).

2. The use of ultrasound in combination with increased pressure allows increasing the crystallinity of the resulting LDHs.

3. The resulting LDHs are sorbents of chromate ions. The sorption properties of LDH produced by the conventional method are more pronounced than those of LDH obtained under the influence of ultrasound and pressure.

4. For LDHs produced by the conventional method, sorption is better described by the Freundlich model, and for LDHs produced under the influence of ultrasound and pressure – by the Langmuir model.

5. The experimental results indicate that when using the same forms of hydroxide as sorbents, for the same time, sorption improves when exposing the system to ultrasound, and even more when ultrasound is applied in combination with increased hydrostatic pressure.

REFERENCES

- Aflak N., El Mersly L., Ben El Ayouchia H., Rafqah S., Anane H., Julve M., Stiriba S.E. A new Cu₃Al-layered double hydroxide heterogeneous catalyst for azide-alkyne [3 + 2] cycloaddition reaction in water. *Journal of Coordination Chemistry*, 2022, vol. 75, no. 17-18, pp. 2346–2358. DOI: [10.1080/00958972.2022.2105701](https://doi.org/10.1080/00958972.2022.2105701).
- Seung Yu Seungjin, Piao Huiyan, Rejinold N. Sanoj, Lee Hanna, Choi Goeun, Choy Jin-Ho. pH-Responsive Inorganic/Organic Nanohybrids System for Controlled Nicotinic Acid Drug Release. *Molecules*, 2022, vol. 27, no. 19, article number 6439. DOI: [10.3390/molecules27196439](https://doi.org/10.3390/molecules27196439).
- de Souza dos Santos G.E., dos Santos Lins P.V., Oliveira L.M.T.M., Oliveira da Silva E., Anastopoulos I., Erto A., Giannakoudakis D.A., Almeida A.R.F., Duarte J.L., Meili L. Layered double hydroxides/biochar composites as adsorbents for water remediation applications: recent trends and perspectives. *Journal of Cleaner Production*, 2020, vol. 284, article number 124755. DOI: [10.1016/j.jclepro.2020.124755](https://doi.org/10.1016/j.jclepro.2020.124755).
- Johnston A.-L., Lester E., Williams O., Gomes R. Understanding Layered Double Hydroxide properties as sorbent materials for removing organic pollutants from environmental waters. *Journal of Environmental Chemical Engineering*, 2021, vol. 9, no. 4, article number 105197. DOI: [10.1016/j.jece.2021.105197](https://doi.org/10.1016/j.jece.2021.105197).
- Matusik J., Rybka K. Removal of chromates and sulphates by Mg/Fe LDH and heterostructured LDH/halloysite materials: Efficiency, selectivity, and stability of adsorbents in single- and multi-element systems. *Materials*, 2019, vol. 12, no. 9, article number 1373. DOI: [10.3390/ma12091373](https://doi.org/10.3390/ma12091373).
- Shafiq M., Alazba A.A., Amin M.T. Preparation of ZnMgAl-Layered Double Hydroxide and Rice Husk Biochar Composites for Cu(II) and Pb(II) Ions Removal from Synthetic Wastewater. *Water (Switzerland)*, 2023, vol. 15, no. 12, article number 2207. DOI: [10.3390/w15122207](https://doi.org/10.3390/w15122207).
- Roy S.C., Rahman M.A., Celik A. et al. Efficient removal of chromium(VI) ions by hexagonal nanosheets of CoAl–MoS₄ layered double hydroxide. *Journal of Coordination Chemistry*, 2022, vol. 75, no. 11-14, pp. 1581–1595. DOI: [10.1080/00958972.2022.2101103](https://doi.org/10.1080/00958972.2022.2101103).
- Ma Lijiao, Islam S.M., Liu Hongyun, Zhao Jing, Sun Genban, Li Huifeng, Ma Shulan, Kanatzidis M.G. Selective and Efficient Removal of Toxic Oxoanions of As(III), As(V), and Cr(VI) by Layered Double Hydroxide Intercalated with MoS₄²⁻. *Chemistry of Materials*, 2017, vol. 29, no. 7, pp. 3274–3284. DOI: [10.1021/acs.chemmater.7b00618](https://doi.org/10.1021/acs.chemmater.7b00618).
- Sankaranarayanan S., Gupta M. Emergence of God's favorite metallic element: Magnesium based materials for engineering and biomedical applications. *Materials Today: Proceedings*, 2021, vol. 39, pp. 311–316. DOI: [10.1016/j.matpr.2020.07.220](https://doi.org/10.1016/j.matpr.2020.07.220).
- Williams G.R., O'Hare D. Towards Understanding, Control and Application of Layered Double Hydroxide Chemistry. *Cheminform*, 2006, vol. 37, no. 45. DOI: [10.1002/chin.200645266](https://doi.org/10.1002/chin.200645266).
- Evans D.G., Slade R.C.T. Structural Aspects of Layered Double Hydroxides. *Layered Double Hydroxides*. Berlin, Springer Berlin Heidelberg Publ., 2006, pp. 1–87. DOI: [10.1007/430_005](https://doi.org/10.1007/430_005).
- Srilakshmi Ch., Thirunavukkarasu Th. Enhanced adsorption of Congo red on microwave synthesized layered Zn–Al double hydroxides and its adsorption behaviour using mixture of dyes from aqueous solution. *Inorganic Chemistry Communications*, 2019, vol. 100, pp. 107–117. DOI: [10.1016/j.inoche.2018.12.027](https://doi.org/10.1016/j.inoche.2018.12.027).
- Go Goh Kok-Hui, Lim Teik Thye, Dong Zhili. Application of layered double hydroxides for removal of oxyanions: A review. *Water Research*, 2008, vol. 42, no. 6-7, pp. 1343–1368. DOI: [10.1016/j.watres.2007.10.043](https://doi.org/10.1016/j.watres.2007.10.043).
- Huang Weiya, Yu Xiang, Li Dan. Adsorption removal of Congo red over flower-like porous microspheres derived from Ni/Al layered double hydroxide. *RSC Advances*, 2015, vol. 5, no. 103, pp. 84937–84946. DOI: [10.1039/C5RA13922H](https://doi.org/10.1039/C5RA13922H).
- Ibrahimova K.A. The Synthesis Methods and Applications of Layered Double Hydroxides – a Brief Review. *NNC RK Bulletin*, 2022, no. 4, pp. 16–29. DOI: [10.52676/1729-7885-2022-4-17-29](https://doi.org/10.52676/1729-7885-2022-4-17-29).
- Olanrewaju J., Newalkar B.L., Mancino C., Komarneni S. Simplified synthesis of nitrate form of layered double hydroxide. *Materials Letters*, 2000, vol. 45, no. 6, pp. 307–310. DOI: [10.1016/S0167-577X\(00\)00123-3](https://doi.org/10.1016/S0167-577X(00)00123-3).
- Li Yanlin, Wang Jun, Li Zhanshuang, Liu Qi, Liu Jingyuan, Liu Lianhe, Zhang Xiaofei, Yu Jing. Ultrasound assisted synthesis of Ca–Al hydrotalcite for U (VI) and Cr (VI) adsorption. *Chemical Engineering Journal*, 2013, vol. 218, pp. 295–302. DOI: [10.1016/j.cej.2012.12.051](https://doi.org/10.1016/j.cej.2012.12.051).

18. Salak A.N., Vieira D.E.L., Lukienko I.M. et al. High-Power Ultrasonic Synthesis and Magnetic-Field-Assisted Arrangement of Nanosized Crystallites of Cobalt-Containing Layered Double Hydroxides. *Chem-Engineering*, 2019, vol. 3, no. 3, article number 62. DOI: [10.3390/chemengineering3030062](https://doi.org/10.3390/chemengineering3030062).
19. Sokol D., Vieira D.E.L., Zarkov A., Ferreira M.G.S., Beganskiene A., Rubanik V.V., Shilin A.D., Kareiva A., Salak A.N. Sonication accelerated formation of Mg–Al-phosphate layered double hydroxide via sol-gel prepared mixed metal oxides. *Scientific Reports*, 2019, vol. 9, no. 1, article number 10419. DOI: [10.1038/s41598-019-46910-5](https://doi.org/10.1038/s41598-019-46910-5).
20. Abdel Aziz S.A.A., Gadelhak Y., Mohamed M.B.E.D., Mahmoud R. Antimicrobial properties of promising Zn–Fe based layered double hydroxides for the disinfection of real dairy wastewater effluents. *Scientific Reports*, 2023, vol. 13, no. 1, article number 7601. DOI: [10.1038/s41598-023-34488-y](https://doi.org/10.1038/s41598-023-34488-y).
21. Abdel-Hady E.E., Mohamed H.F.M., Hafez S.H.M., Fahmy A.M.M., Magdy A., Mohamed A.S., Ali E.O., Abdelhamed H.R., Mahmoud O.M. Textural properties and adsorption behavior of Zn–Mg–Al layered double hydroxide upon crystal violet dye removal as a low cost, effective, and recyclable adsorbent. *Scientific Reports*, 2023, vol. 13, no. 1, article number 6435. DOI: [10.1038/s41598-023-33142-x](https://doi.org/10.1038/s41598-023-33142-x).
22. Ghanbari N., Ghafuri H. Preparation of novel Zn–Al layered double hydroxide composite as adsorbent for removal of organophosphorus insecticides from water. *Scientific Reports*, 2023, vol. 13, no. 1, article number 10215. DOI: [10.1038/s41598-023-37070-8](https://doi.org/10.1038/s41598-023-37070-8).
5. Matusik J., Rybka K. Removal of chromates and sulphates by Mg/Fe LDH and heterostructured LDH/halloysite materials: Efficiency, selectivity, and stability of adsorbents in single- and multi-element systems // *Materials*. 2019. Vol. 12. № 9. Article number 1373. DOI: [10.3390/ma12091373](https://doi.org/10.3390/ma12091373).
6. Shafiq M., Alazba A.A., Amin M.T. Preparation of ZnMgAl-Layered Double Hydroxide and Rice Husk Biochar Composites for Cu(II) and Pb(II) Ions Removal from Synthetic Wastewater // *Water (Switzerland)*. 2023. Vol. 15. № 12. Article number 2207. DOI: [10.3390/w15122207](https://doi.org/10.3390/w15122207).
7. Roy S.C., Rahman M.A., Celik A. et al. Efficient removal of chromium(VI) ions by hexagonal nanosheets of CoAl–MoS₄ layered double hydroxide // *Journal of Coordination Chemistry*. 2022. Vol. 75. № 11–14. P. 1581–1595. DOI: [10.1080/00958972.2022.2101103](https://doi.org/10.1080/00958972.2022.2101103).
8. Ma Lijiao, Islam S.M., Liu Hongyun, Zhao Jing, Sun Genban, Li Huifeng, Ma Shulan, Kanatzidis M.G. Selective and Efficient Removal of Toxic Oxoanions of As(III), As(V), and Cr(VI) by Layered Double Hydroxide Intercalated with MoS₄²⁻ // *Chemistry of Materials*. 2017. Vol. 29. № 7. P. 3274–3284. DOI: [10.1021/acs.chemmater.7b00618](https://doi.org/10.1021/acs.chemmater.7b00618).
9. Sankaranarayanan S., Gupta M. Emergence of God's favorite metallic element: Magnesium based materials for engineering and biomedical applications // *Materials Today: Proceedings*. 2021. Vol. 39. P. 311–316. DOI: [10.1016/j.matpr.2020.07.220](https://doi.org/10.1016/j.matpr.2020.07.220).
10. Williams G.R., O'Hare D. Towards Understanding, Control and Application of Layered Double Hydroxide Chemistry // *Cheminform*. 2006. Vol. 37. № 45. DOI: [10.1002/chin.200645266](https://doi.org/10.1002/chin.200645266).
11. Evans D.G., Slade R.C.T. Structural Aspects of Layered Double Hydroxides // *Layered Double Hydroxides*. Berlin: Springer Berlin Heidelberg, 2006. P. 1–87. DOI: [10.1007/430_005](https://doi.org/10.1007/430_005).
12. Srilakshmi Ch., Thirunavukkarasu Th. Enhanced adsorption of Congo red on microwave synthesized layered Zn–Al double hydroxides and its adsorption behaviour using mixture of dyes from aqueous solution // *Inorganic Chemistry Communications*. 2019. Vol. 100. P. 107–117. DOI: [10.1016/j.inoche.2018.12.027](https://doi.org/10.1016/j.inoche.2018.12.027).
13. Goh Kok-Hui, Lim Teik Thye, Dong Zhili. Application of layered double hydroxides for removal of oxyanions: A review // *Water Research*. 2008. Vol. 42. № 6–7. P. 1343–1368. DOI: [10.1016/j.watres.2007.10.043](https://doi.org/10.1016/j.watres.2007.10.043).
14. Huang Weiya, Yu Xiang, Li Dan. Adsorption removal of Congo red over flower-like porous microspheres derived from Ni/Al layered double hydroxide // *RSC Advances*. 2015. Vol. 5. № 103. P. 84937–84946. DOI: [10.1039/C5RA13922H](https://doi.org/10.1039/C5RA13922H).
15. Ibrahimova K.A. The Synthesis Methods and Applications of Layered Double Hydroxides – a Brief Review // *NNC RK Bulletin*. 2022. № 4. P. 16–29. DOI: [10.52676/1729-7885-2022-4-17-29](https://doi.org/10.52676/1729-7885-2022-4-17-29).
16. Olanrewaju J., Newalkar B.L., Mancino C., Komarneni S. Simplified synthesis of nitrate form of layered double hydroxide // *Materials Letters*. 2000. Vol. 45. № 6. P. 307–310. DOI: [10.1016/S0167-577X\(00\)00123-3](https://doi.org/10.1016/S0167-577X(00)00123-3).
17. Li Yanlin, Wang Jun, Li Zhanshuang, Liu Qi, Liu Jingyuan, Liu Lianhe, Zhang Xiaofei, Yu Jing.

СПИСОК ЛИТЕРАТУРЫ

1. Aflak N., El Mersly L., Ben El Ayouchia H., Rafqah S., Anane H., Julve M., Stiriba S.E. A new Cu₃Al-layered double hydroxide heterogeneous catalyst for azide-alkyne [3 + 2] cycloaddition reaction in water // *Journal of Coordination Chemistry*. 2022. Vol. 75. № 17–18. P. 2346–2358. DOI: [10.1080/00958972.2022.2105701](https://doi.org/10.1080/00958972.2022.2105701).
2. Yu Seungjin, Piao Huiyan, Rejinold N. Sanoj, Lee Hanna, Choi Goeun, Choy Jin-Ho. pH-Responsive Inorganic/Organic Nanohybrids System for Controlled Nicotinic Acid Drug Release // *Molecules*. 2022. Vol. 27. № 19. Article number 6439. DOI: [10.3390/molecules27196439](https://doi.org/10.3390/molecules27196439).
3. de Souza dos Santos G.E., dos Santos Lins P.V., Oliveira L.M.T.M., Oliveira da Silva E., Anastopoulos I., Erto A., Giannakoudakis D.A., Almeida A.R.F., Duarte J.L., Meili L. Layered double hydroxides/biochar composites as adsorbents for water remediation applications: recent trends and perspectives // *Journal of Cleaner Production*. 2020. Vol. 284. Article number 124755. DOI: [10.1016/j.jclepro.2020.124755](https://doi.org/10.1016/j.jclepro.2020.124755).
4. Johnston A.-L., Lester E., Williams O., Gomes R. Understanding Layered Double Hydroxide properties as sorbent materials for removing organic pollutants from environmental waters // *Journal of Environmental Chemical Engineering*. 2021. Vol. 9. № 4. Article number 105197. DOI: [10.1016/j.jece.2021.105197](https://doi.org/10.1016/j.jece.2021.105197).

- Ultrasound assisted synthesis of Ca–Al hydrotalcite for U (VI) and Cr (VI) adsorption // *Chemical Engineering Journal*. 2013. Vol. 218. P. 295–302. DOI: [10.1016/j.ccej.2012.12.051](https://doi.org/10.1016/j.ccej.2012.12.051).
18. Salak A.N., Vieira D.E.L., Lukienko I.M. et al. High-Power Ultrasonic Synthesis and Magnetic-Field-Assisted Arrangement of Nanosized Crystallites of Cobalt-Containing Layered Double Hydroxides // *Chemical Engineering*. 2019. Vol. 3. № 3. Article number 62. DOI: [10.3390/chemengineering3030062](https://doi.org/10.3390/chemengineering3030062).
 19. Sokol D., Vieira D.E.L., Zarkov A., Ferreira M.G.S., Beganskiene A., Rubanik V.V., Shilin A.D., Kareiva A., Salak A.N. Sonication accelerated formation of Mg–Al-phosphate layered double hydroxide via sol-gel prepared mixed metal oxides // *Scientific Reports*. 2019. Vol. 9. № 1. Article number 10419. DOI: [10.1038/s41598-019-46910-5](https://doi.org/10.1038/s41598-019-46910-5).
 20. Abdel Aziz S.A.A., Gadelhak Y., Mohamed M.B.E.D., Mahmoud R. Antimicrobial properties of promising Zn–Fe based layered double hydroxides for the disinfection of real dairy wastewater effluents // *Scientific Reports*. 2023. Vol. 13. № 1. Article number 7601. DOI: [10.1038/s41598-023-34488-y](https://doi.org/10.1038/s41598-023-34488-y).
 21. Abdel-Hady E.E., Mohamed H.F.M., Hafez S.H.M., Fahmy A.M.M., Magdy A., Mohamed A.S., Ali E.O., Abdelhamed H.R., Mahmoud O.M. Textural properties and adsorption behavior of Zn–Mg–Al layered double hydroxide upon crystal violet dye removal as a low cost, effective, and recyclable adsorbent // *Scientific Reports*. 2023. Vol. 13. № 1. Article number 6435. DOI: [10.1038/s41598-023-33142-x](https://doi.org/10.1038/s41598-023-33142-x).
 22. Ghanbari N., Ghafuri H. Preparation of novel Zn–Al layered double hydroxide composite as adsorbent for removal of organophosphorus insecticides from water // *Scientific Reports*. 2023. Vol. 13. № 1. Article number 10215. DOI: [10.1038/s41598-023-37070-8](https://doi.org/10.1038/s41598-023-37070-8).

Сорбционные свойства слоистых двойных гидроксидов, полученных при ультразвуковом воздействии

© 2023

Голубев Роман Александрович^{*1,2}, младший научный сотрудник, аспирант
Рубаник Василий Васильевич^{1,4}, доктор технических наук,
член-корреспондент Национальной академии наук Беларуси,
доцент, заведующий лабораторией физики металлов

Рубаник Василий Васильевич мл.^{1,5}, доктор технических наук, доцент, директор
Критченков Илья Сергеевич^{1,3,6}, кандидат химических наук, старший научный сотрудник
Критченков Андрей Сергеевич^{1,2,7}, доктор химических наук, ведущий научный сотрудник

¹*Институт технической акустики Национальной академии наук Беларуси, Витебск (Республика Беларусь)*²*Российский университет дружбы народов, Москва (Россия)*³*Санкт-Петербургский государственный университет, Санкт-Петербург (Россия)**E-mail: ita@vitebsk.by,
asfdss.asdasf@yandex.ru⁴ORCID: <https://orcid.org/0000-0002-0350-1180>⁵ORCID: <https://orcid.org/0000-0002-9268-0167>⁶ORCID: <https://orcid.org/0000-0003-0108-0690>⁷ORCID: <https://orcid.org/0000-0002-6411-5988>

Поступила в редакцию 03.07.2023

Принята к публикации 12.11.2023

Аннотация: Слоистые двойные гидроксиды (СДГ) можно отнести к классу перспективных материалов благодаря простоте синтеза, а также обширной сфере их применения. Однако процесс синтеза СДГ в зависимости от их химического состава может занимать от десятков часов до нескольких суток. Ранее было установлено, что воздействие ультразвуком в процессе получения СДГ значительно сокращает время синтеза, а полученные таким способом СДГ интересны в отношении изучения их физико-химических свойств, а также сорбционной способности. В работе получены Mg/Fe СДГ в нитратной форме традиционным методом, а также при совместном действии ультразвука и повышенного гидростатического давления. Полученные образцы охарактеризованы с помощью комплекса физико-химических методов анализа, включающих сканирующую электронную микроскопию (СЭМ), инфракрасную спектроскопию (ИК), рентгенофазовый анализ (РФА), термогравиметрический анализ (ТГА) с дифференциальной сканирующей калориметрией (ДСК). Проведены эксперименты по исследованию сорбционной способности полученных образцов Fe/Mg СДГ по отношению к хромат-ионам в нормальных условиях, а также при действии ультразвука, в т. ч. в сочетании с повышенным гидростатическим давлением. На фотоэлектрическом фотометре были получены и проанализированы данные с количественными значениями процесса сорбции. Данные, полученные в ходе комплексного анализа готового продукта, указывают на то, что синтезированный материал является Mg/Fe слоистым двойным гидроксидом. При проведении рентгенофазового анализа выявлено, что синтез СДГ с применением ультразвука и давления повышает степень кристалличности конечного продукта. Установлено, что сорбционные свойства СДГ, полученных традиционным способом, и СДГ, полученных под действием ультразвука и давления, отличаются. У Mg/Fe СДГ, синтезированных традиционным методом, сорбция хромата протекает лучше, чем у образцов, синтезированных при помощи ультразвуковой обработки в сочетании с повышенным гидростатическим давлением. Показано, что процесс сорбции исследованных образцов СДГ описывается разными математическими моделями.

Ключевые слова: слоистые двойные гидроксиды; Mg/Fe; ультразвуковой синтез; сорбционные свойства; хромат-анионы.

Благодарности: Работа выполнена при поддержке БРФФИ (проект № X21PM-081).

Авторы выражают благодарность Отдельному проекту фундаментальных и прикладных научных исследований «Ультразвуковой синтез слоистых двойных гидроксидов медицинского назначения».

Авторы выражают признательность научному парку Санкт-Петербургского государственного университета (Междисциплинарный ресурсный центр по направлению «Нанотехнологии» и ресурсный центр «Методы анализа состава вещества») за оказанную помощь в исследовании микроструктуры (СЭМ) и измерении ИК-спектров синтезированных образцов СДГ. Посвящается 300-летию юбилею основания Санкт-Петербургского государственного университета.

Статья подготовлена по материалам докладов участников XI Международной школы «Физическое материаловедение» (ШФМ-2023), Тольятти, 11–15 сентября 2023 года.

Для цитирования: Голубев Р.А., Рубаник В.В., Рубаник В.В. мл., Критченков И.С., Критченков А.С. Сорбционные свойства слоистых двойных гидроксидов, полученных при ультразвуковом воздействии // Frontier Materials & Technologies. 2023. № 4. С. 19–30. DOI: 10.18323/2782-4039-2023-4-66-2.

Determination of the stress threshold and microstructural factors forming the nonlinear unloading effect of the ZK60 (MA14) magnesium alloy

© 2023

*Aleksey V. Danyuk**¹, PhD (Physics and Mathematics),

senior researcher of the Research Institute of Advanced Technologies

*Dmitry L. Merson*², Doctor of Sciences (Physics and Mathematics), Professor,

Director of the Research Institute of Advanced Technologies

*Aleksandr I. Brilevskiy*³, junior researcher of the Research Institute of Advanced Technologies

Maksim A. Afanasyev, researcher of the Research Institute of Advanced Technologies

Togliatti State University, Togliatti (Russia)

*E-mail: A.Danyuk@tltu.ru,
Alexey.Danyuk@gmail.com

¹ORCID: <https://orcid.org/0000-0002-7352-9947>

²ORCID: <https://orcid.org/0000-0001-5006-4115>

³ORCID: <https://orcid.org/0000-0002-5780-6094>

Received 14.12.2022

Accepted 01.09.2023

Abstract: Magnesium alloys are an ideal material for creating lightweight and durable modern transport systems, but their widespread use is limited due to some physical and chemical properties. This paper considers the effect of nonlinear elastic unloading of the MA14 (ZK60, Mg–5.4Zn–0.5Zr) magnesium alloy in a coarse-grained state after recrystallisation annealing. The study found that the nonlinearity of the unloading characteristic, is formed when reaching a certain threshold stress level. It is expected that the effect under the study is associated with the deformation behavior of the alloy, during which the twin structure formation according to the tensile twinning mechanism is observed. The sample material microstructure was determined, by scanning electron microscopy using electron backscattered diffraction analysis. Determination of the threshold stress, for the formation of unloading nonlinearity was carried out by two methods: 1) by the value of the loop area formed by the nonlinearity of the unloading mechanical characteristics and the repeated loading (mechanical hysteresis) characteristics, and 2) by analysing the acoustic emission recorded during failure strain. A comparison of the results obtained, allows suggesting that the unloading nonlinearity is caused by twinning in grains, in which an unfavorable configuration (low Schmidt factor), for dislocation slip is observed. Rotating the twinned crystal at an angle close to 90° does not contribute to an increase in the Schmidt factor and activation of dislocation slip systems to secure the deformed structure through the dislocation strengthening mechanism. With a subsequent decrease in the external stress, detwinning and partial restoration of the crystal lattice configuration occur.

Keywords: magnesium; magnesium alloy; ZK60 (Mg–5.4Zn–0.5Zr); nonlinear unloading; stress threshold; elasticity; twinning; detwinning; deformation behavior.

Acknowledgements: The research was financially supported by the Russian Science Foundation within the scientific project No. 22-23-01169.

For citation: Danyuk A.V., Merson D.L., Brilevskiy A.I., Afanasyev M.A. Determination of the stress threshold and microstructural factors forming the nonlinear unloading effect of the ZK60 (MA14) magnesium alloy. *Frontier Materials & Technologies*, 2023, no. 4, pp. 31–39. DOI: 10.18323/2782-4039-2023-4-66-3.

INTRODUCTION

Lightweight magnesium alloys have a high strength-to-weight ratio, which makes them extremely attractive for application in vehicle construction. Currently, magnesium alloys are used primarily for casting into moulds or manufacturing elements using turning and milling from rolled products (plates, sheets, rods, and pipes). Elastic forging, and other methods of pressure metal treatment (PMT) of magnesium alloys are significantly limited or require the application of alloys with relatively high doping with expensive elements, which significantly reduces the attractiveness of magnesium for widespread use. The problems of pressure metal treatment of magnesium alloys, especially in the cast or coarse-grained state, are associated with the peculiarities of their deformation behaviour manifested in the form of: asymmetry of the mechanical response to the application of tensile, and compressive loads; highly limited plasticity, even at elevated

shaping temperatures; nonlinear characteristics of elastic behaviour (unloading) [1–6].

The peculiarities of magnesium hardening and plasticity are associated with its hexagonal close-packed (hcp) crystal lattice, which is the cause of strong anisotropy of elastic and deformation properties. It is quite difficult to get rid of the anisotropy manifestation, so many authors are forced to study magnesium alloys, including after hardening deformation treatment, in several directions. For example, for rolling (forging), three directions are selected (normal, longitudinal, transverse), for extrusion – two (normal, transverse) [7].

When a magnesium alloy is compressed and tensioned, pronounced strain anisotropy and deformation behaviour asymmetry are observed, manifested in a significant difference in the yield strengths during tension and compression [8–10], and the initial hardening may be a reason for the material asymmetric behaviour [11]. In the above works, one can note the nonlinear behaviour of the unload-

ing characteristics of magnesium alloys, but the authors do not specify the reasons and parameters for the formation of such an effect.

The purpose of this work is to determine the conditions and reasons for the formation of nonlinear elastic behaviour, during unloading of the MA14 magnesium alloy.

METHODS

The chemical composition of magnesium alloy samples was pre-studied according to the GOST 7728-79 method, using a Thermo Fisher Scientific ARL 4460 optical emission spectrometer. Table 1 gives the chemical composition of the studied material; the element content values correspond to the requirements for the MA14 grade according to GOST 14957-76.

The material under study has a coarse-grained structure with a grain size of 60...120 μm and a texture corresponding to homogenising recrystallisation annealing (not textured). Fig. 1 shows an image of the alloy structure obtained on a Zeiss Sigma scanning electron microscope, using electron backscattered diffraction analysis (SEM+EBS), as well as histograms of the grain size distribution, and the crystal lattice misorientation at the grain boundaries. Determination of the mechanical characteristics of the alloy, under cyclic loading, and monotonic tensioning until failure was carried out on flat samples with blades for grippers, sample working section 4×4 mm, length 4 mm. The samples were cut using the electroerosive method on a numerically controlled machine, which makes it possible to obtain samples of identical geometry without hardening the surface layer.

The test specimens were prepared in the same initial state (after homogenising annealing), and were not subjected to initial deformation or hardening, before both compression and tensile testing, and when installing the specimens in the grips of the testing machine, the procedure for protecting the specimen from loading prior to testing was followed.

To study the reasons forming the nonlinearity of elastic behaviour and unloading, the authors performed a series of tests with a loading–unloading cycle with a maximum stress point below, near and above the yield strength at engineering stress of $\sigma_{\text{eng}} \approx 50, 90, \text{ and } 145 \text{ MPa}$, respectively, and the active grip displacement rate corresponded to a strain rate of $1 \cdot 10^{-4} \text{ s}^{-1}$. To measure small deformations in the elastic loading area, an HBM MX440 strain-gauge complex with strain-elements glued directly to the sample surface was used. Magnesium and its alloys are prone to creep [12] and long intervals of relaxation of elas-

tic stresses [13], therefore, to reduce the influence of the viscous-dynamic component of plasticity, the sample was statically kept under load for a long time relative to the loading interval, and after unloading – until the activity of deformation processes decreased. The activity of deformation processes was monitored by the acoustic emission (AE) signals. Mechanical twinning, during deformation of magnesium alloys, generates discrete high-amplitude acoustic pulses [14], therefore, when the AE activity decreased to less than one signal/s, the authors considered activity of the deformation process during relaxation insignificant and proceeded to the next stage of the loading–unloading cycle. AE was recorded on the PAC PCI-2 equipment, in a wideband mode of 20 kHz – 1 MHz, with a sampling frequency of 2 MHz, gain of +60 dB, the amplitude detector threshold was 27 dB at a noise level of 25 dB. After testing, the sample material from the deformed area was re-examined using scanning electron microscopy with structure analysis.

To test the assumption that the peculiarities of the “dislocation sliding” and “twinning”, deformation mechanisms may be the reasons for the nonlinear elastic behaviour formation, the same sample was tested for tension to failure at a strain rate of $1 \cdot 10^{-3} \text{ s}^{-1}$. During the stretching process, the AE signal was recorded in a continuous (threshold-free) mode, synchronised with the stress/strain parameters. To assess the staging, the authors used the spectral-energy parameters of AE signals [15; 16]: in this case, for the recorded signal, the change in two parameters of the spectral characteristic resulting from the applied mechanical stress was assessed: 1) power – the integral of the signal power spectral density and 2) median frequency – the median of the signal power spectral density calculated according to the method described in [17].

RESULTS

The tests of cyclic tension and compression without changing the deformation direction relative to the original direction are shown in Fig. 2, which presents three loading cycles separately for compression and tension. The first loading up to a stress of 50 MPa demonstrates elastic loading, and a linear return of the material to its original state, and the slope of the linear loading and unloading section corresponds to an elastic modulus of 42...44 GPa. In the second (90 MPa) and third (145 MPa) loading cycles, the elastic section nonlinearity is observed, which can be estimated according to the area of the hysteresis loop formed by the loading and unloading lines.

*Table 1. Chemical composition of the studied alloy
Таблица 1. Химический состав исследуемого сплава*

Materials	Element weight content, %								
	Mg	Zn	Zr	Al	Fe	Cu	Ni	Mn	Si
Studied material	Base	5.4	0.47	0.002	0.001	0.002	0.001	0.005	0.003
MA14 according to GOST 14957-76	Base	5.0–6.0	0.3–0.9	≤0.05	≤0.03	≤0.05	≤0.005	≤0.1	≤0.05

For each loop, the authors recorded the stress at the top of the loop and the energy volumetric density of the material viscoelastic behaviour – the area of the loop formed by the loading and unloading characteristics, the measurement results of which are shown in Fig. 3.

To determine the twinning activation stress, the authors processed AE recorded during monotonic tensioning of the sample; the loading characteristic is shown in Fig. 4. Calculation of the AE signal spectral parameters was carried out by post-processing, using spectral clustering algorithms [16].

The results of studying the microstructure, using scanning electron microscopy after deformation show the presence of twins, which are formed simultaneously with nonlinear elastic behaviour and, therefore, may be the cause of it. Fig. 5 shows the structure of the samples after compression and tensile testing up to a residual deformation of 1.5 %.

DISCUSSION

A quantitative comparison of the obtained elastic modulus of 42...44 GPa is fully consistent, with data from literature sources for the MA14 (ZK60) alloy – 42...45 GPa [18;

19]. When the alloy is loaded to a stress of 90 MPa, at which a microplastic deformation of 0.05 % is formed, the elastic modulus retains its value, but the material unloading occurs along a curved downward characteristic, forming a hysteresis of the "loading – unloading" characteristic. During tensile twinning, lattice rotation is observed, and the rotation directions may correspond to the maximum anisotropy of the elastic constants of the material, $E(0001)=50.8$ GPa, $E(-1-120) (-1100)=45.5$ GPa [20], but the influence of the anisotropy factor only is quite small, or insignificant, since repeated loading occurs along a curved upward trajectory.

During loading of more than 100 MPa, a transition to the mode of active plastic deformation occurs: in the experiment, this is observed after the third loading cycle, which was stopped when the stress reached 145 MPa, and the residual deformation was 0.29 and 0.22 % for compression and tension, respectively. The difference in the magnitude of plastic compressive, and tensile deformation when applying the same magnitude of stress is described in [8–11], and is a manifestation of the asymmetry in the deformation behaviour of magnesium, and some other metals and alloys.

A feature of the unloading stage after applying a stress of 145 MPa is strong nonlinearity, in which the divergence

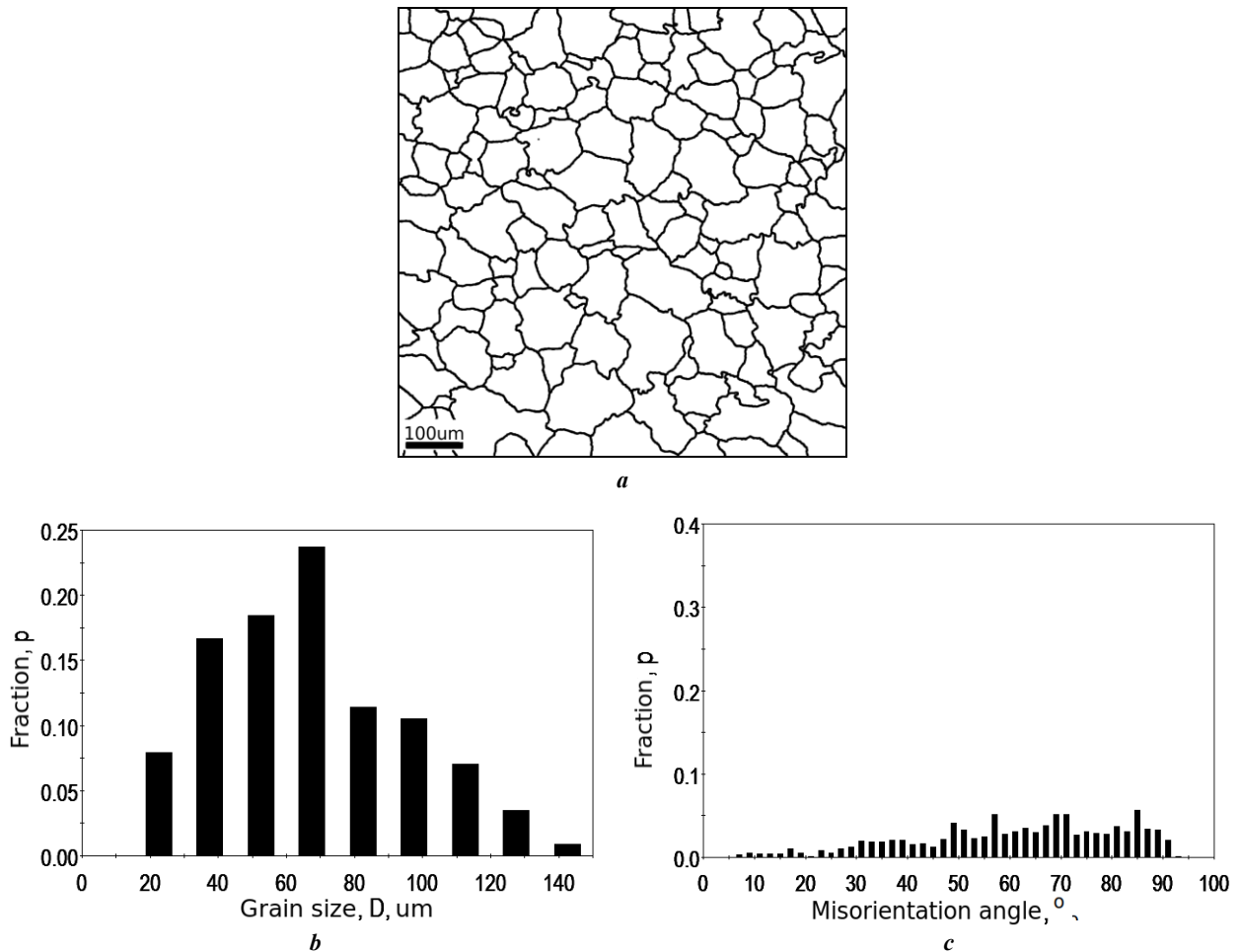


Fig. 1. The initial structure of the MA14 alloy (a), histograms of the grain size distribution (b) and the crystal lattice misorientation at the grain boundaries (c)
Рис. 1. Исходная структура сплава MA14 (a), гистограммы распределений размера зерна (b) и углов разориентировки кристаллической решетки на границах зерен (c)

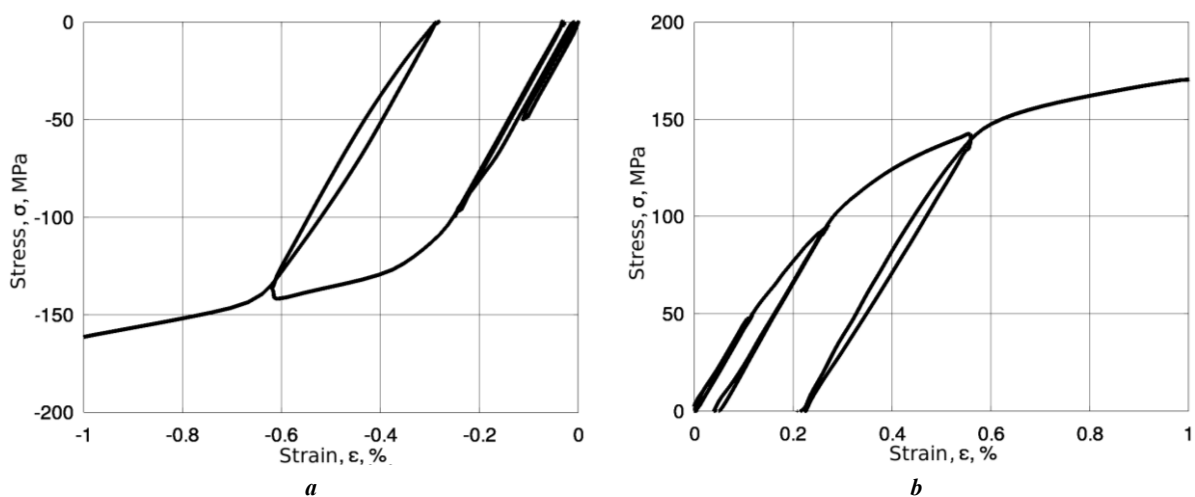


Fig. 2. Loading – unloading diagrams of the MA14 alloy.
Under compression, strain and stress have a negative sign (a),
under tension – a positive sign (b)

Рис. 2. Диаграммы нагружения – разгрузки сплава MA14.
При сжатии деформация и напряжение имеют отрицательный знак (a),
при растяжении – положительный знак (b)

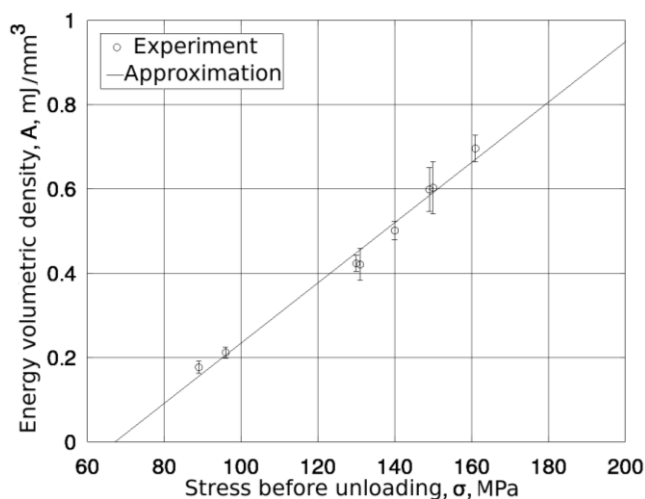


Fig. 3. Energy volumetric density of the material viscoelastic behaviour
Рис. 3. Объемная плотность энергии вязкоупругого поведения материала

of the loading and unloading trajectories increases forming a visually symmetrical mechanical hysteresis loop. Similar descriptions of the behaviour of the MA14 (ZK60) alloy are given in [1; 4; 6; 7].

Approximation of experimental values of the energy volumetric density, which forms the nonlinear elasticity behaviour, and interpolation towards the stress axis in Fig. 3 show that the nonlinear unloading effect appears, when the stress reaches a value in the range of 65...70 MPa.

It was shown in [13] and [16] that analysis of AE signal parameters and signal clustering according to the power spectral density distribution make it possible to accurately monitor twinning activity. The operation of deformation twinning systems is accompanied by high-amplitude AE pulses with a sharp leading edge and relaxation decay, and

the spectral characteristic has a low median frequency. AE generated by dislocation slip is characterised by small amplitudes and a wide spectrum.

In this case, it is worth paying attention to the nature of changes in the power parameters, and median frequency of the AE signal, which are shown in Fig. 4. Acoustic emission exhibits intermittence when twinning is activated, while the measured signal parameters respond proportionally to the intensity of the process by increasing energy (amplitude), and median frequency in the mechanical stress range of 70...140 MPa, it is in this stress range that the material is most actively deformed by the twinning mechanism.

It is obvious that the stress "threshold" of 65...70 MPa corresponds to the physical yield strength of the material

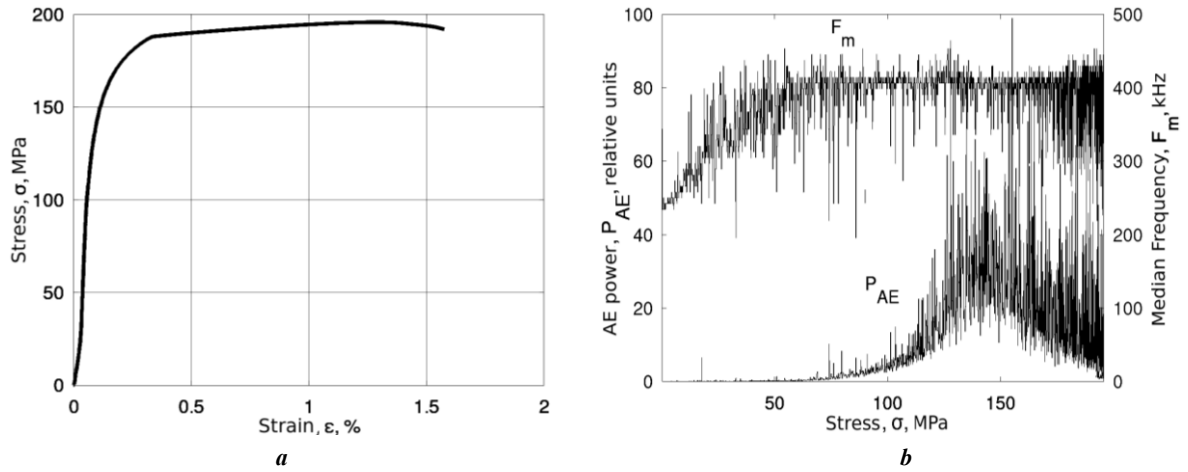


Fig. 4. Loading diagram of the MA14 alloy sample (a) and acoustic emission parameters depending on the stress (b)
Рис. 4. Диаграмма нагружения образца сплава MA14 (a) и параметры акустической эмиссии в зависимости от напряжения (b)

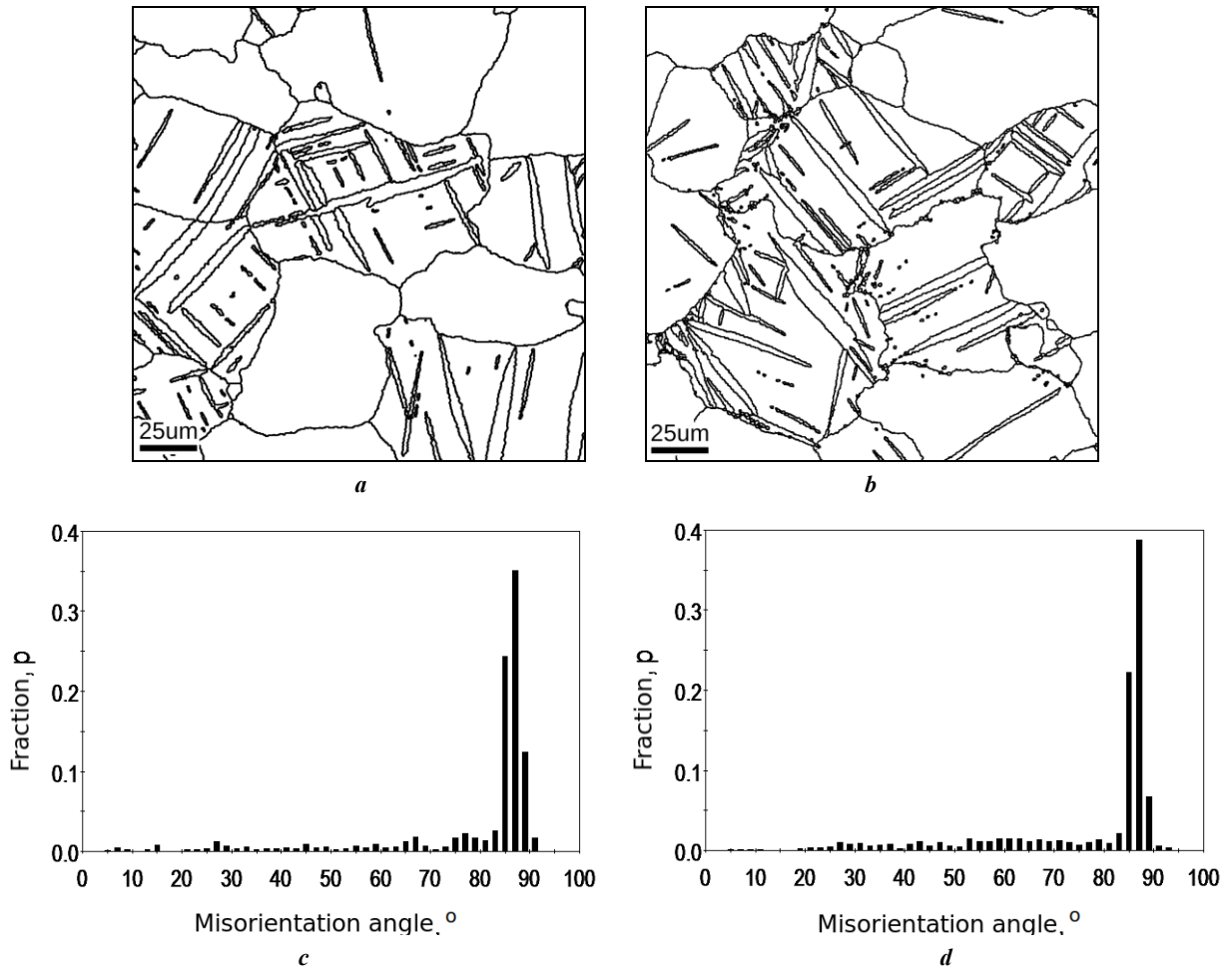


Fig. 5. MA14 alloy structure after compression (a) and tensile (b) tests, histograms of the crystal lattice misorientation angles at the grain boundaries after compression (c) and tensile (d) tests
Рис. 5. Структура сплава MA14 после испытания на сжатие (a) и на растяжение (b), гистограммы распределений углов разориентировки кристаллической решетки на границах зерен после испытания на сжатие (c) и на растяжение (d)

being tested: at this stress, strain hardening and the manifestation of the relaxation properties of the strain mechanisms, slip and, to a greater extent, twinning creating powerful AE begin.

The structural state of the samples tested in compression and tension was similar. The deformed structures contain signs of activity of dislocation slip systems forming a sub-grain structure, with small grain-boundary angles ($3...5^\circ$) and tensile twins with crystal lattice grain-boundary angles of about 86° . The type of active strain mechanisms in adjacent grains may be different, since the activation of a specific deformation system occurs only after a certain critical shear stress is exceeded: the basal plane slip systems have the lowest values of the critical shear stress; the prismatic slip and tensile twinning systems are the next as the critical shear stress increases [13; 21], and it is these systems that can be identified at the small deformations observed in this study. The critical shear stress is primarily achieved in crystals (grains) that are favourably oriented with respect to external stress, and is numerically determined by the Schmidt factor [22; 23]. The heterogeneity of activation of deformation systems forms a stress state that is uneven throughout the volume of the material, and elastic stress gradients can inhibit the twin propagation inside the grain, and then, when the external stress decreases under the influence of elastic forces, the reverse detwinning process can occur [24; 25].

CONCLUSIONS

The most likely mechanism forming the nonlinear unloading characteristic, and nonlinear elastic behaviour of the MA14 alloy is the twinning–detwinning mechanism in the “twinning – tension” systems. The twin formation in a grain is associated with an insufficient number of active easy slip systems in the basal and prismatic planes, which are orthogonal to each other. At the same time, “twinning – tension”, with a crystal lattice rotation of 86° does not create more favorable conditions for the activation of easy slide systems. As a consequence, in magnesium, the conditions for the formation of a twin are observed in an unstrengthened lattice (with short lengths of sections of pinned dislocations), while after the twin formation, its pinning (strengthening) by active slip is not observed. Thus, apparently, unrelaxed elastic stresses are formed both at the periphery of the twin inside the grain and along the grain perimeter, and it is these stresses that lead to detwinning when removing the external stress. The mechanism of operation of an unpinned (unstrengthened “elastic” twin) is similar to the behaviour of a curved elastic beam between two supports, which has the possibility of elastic deflection and two deformation “paths” depending on the direction: increasing or decreasing stress, while the sign of loading has no effect.

REFERENCES

1. Yu Hai Yan, Wu Hangyu, Wang Lin. Inelastic strain recovery of magnesium alloys and a new elastic modulus model. *IOP Conference Series: Materials Science and Engineering*, 2020, vol. 967, article number 012046. DOI: [10.1088/1757-899X/967/1/012046](https://doi.org/10.1088/1757-899X/967/1/012046).
2. Xiong Ying, Yu Qin, Jiang Yanyao. Deformation of extruded ZK60 magnesium alloy under uniaxial loading in different material orientations. *Materials Science and Engineering: A*, 2018, vol. 710, pp. 206–213. DOI: [10.1016/j.msea.2017.10.059](https://doi.org/10.1016/j.msea.2017.10.059).
3. Shiraishi K., Mayama T., Yamasaki M., Kawamura Y. Enhanced non-linearity during unloading by LPSO phase in as-cast Mg–Zn–Y alloys and slip-dominated non-linear unloading mechanism. *Materials Science and Engineering: A*, 2020, vol. 790, article number 139679. DOI: [10.1016/j.msea.2020.139679](https://doi.org/10.1016/j.msea.2020.139679).
4. Hama T., Matsudai R., Kuchinomachi Y., Fujimoto H., Takuda H. Non-linear Deformation behavior during unloading in various metal sheets. *ISIJ International*, 2015, vol. 55, no. 5, pp. 1067–1075. DOI: [10.2355/isijinternational.55.1067](https://doi.org/10.2355/isijinternational.55.1067).
5. Wang Lifei, Huang Guangsheng, Quan Quan, Bassani P., Mostaed E., Vadani M., Pan Fusheng. The effect of twinning and detwinning on the mechanical property of AZ31 extruded magnesium alloy during strain-path changes. *Material & Design*, 2014, vol. 63, pp. 177–184. DOI: [10.1016/j.matdes.2014.05.056](https://doi.org/10.1016/j.matdes.2014.05.056).
6. Frydrych K., Libura T., Kowalewski Z., Maj M., Kowalczyk-Gajewska K. On the role of slip, twinning and detwinning in magnesium alloy AZ31B sheet. *Materials Science and Engineering: A*, 2021, vol. 813, article number 141152. DOI: [10.1016/j.msea.2021.141152](https://doi.org/10.1016/j.msea.2021.141152).
7. Tang Weigin, Lee Jeong Yeon, Wang Huamiao, Steglich D., Li Dayong, Peng Yinghong, Wu Peidong. Unloading behaviors of the rare-earth magnesium alloy ZE10 sheet. *Journal of Magnesium and Alloys*, 2021, vol. 9, no. 3, pp. 927–936. DOI: [10.1016/j.jma.2020.02.023](https://doi.org/10.1016/j.jma.2020.02.023).
8. Shi Baodong, Yang Chong, Peng Yan, Zhang Fucheng, Pan Fusheng. Anisotropy of wrought magnesium alloys: A focused overview. *Journal of Magnesium and Alloys*, 2022, vol. 10, no. 6, pp. 1476–1510. DOI: [10.1016/j.jma.2022.03.006](https://doi.org/10.1016/j.jma.2022.03.006).
9. Chen Hongbing, Liu Tianmo, Zhang Yin, Song Bo, Hou Dewen, Pan Fusheng. The yield asymmetry and precipitation behavior of pre-twinned ZK60 alloy. *Materials Science and Engineering: A*, 2016, vol. 652, pp. 167–174. DOI: [10.1016/j.msea.2015.11.092](https://doi.org/10.1016/j.msea.2015.11.092).
10. Zhao Lingyu, Chen Wenhao, Zhou Beian, He Cong, Yan Changjian, Jin Zhaoyang, Yu Huihui, Xin Yunchang. Quantative study on the tension-compression yield asymmetry of a Mg–3Al–1Zn alloy with bimodal texture components. *Journal of Magnesium and Alloys*, 2022, vol. 10, no. 6, pp. 1680–1693. DOI: [10.1016/j.jma.2022.03.002](https://doi.org/10.1016/j.jma.2022.03.002).
11. Vinogradov A., Vasilev E., Linderov M., Merson D. Evolution of Mechanical Twinning during Cyclic Deformation of Mg–Zn–Ca Alloys. *Metals*, 2016, vol. 6, no. 12, article number 304. DOI: [10.3390/met6120304](https://doi.org/10.3390/met6120304).
12. Wang Yang-Yang, Jia Chen, Tayebi M., Hamawandi B. Microstructural Evolution during Accelerated Tensile Creep Test of ZK60/SiCp Composite after KoBo Extrusion. *Materials*, 2022, vol. 15, no. 18, article number 6428. DOI: [10.3390/ma15186428](https://doi.org/10.3390/ma15186428).
13. Trojanova Z., Drozd Z., Lukac P., Dzugan J. Stress Relaxation Tests: Modeling Issues and Applications in Magnesium Alloys and Composites. *Journal*

- of Materials Engineering and Performance*, 2023, vol. 32, pp. 2766–2783. DOI: [10.1007/s11665-022-06951-w](https://doi.org/10.1007/s11665-022-06951-w).
14. Vinogradov A., Orlov D., Danyuk A., Estrin Y. Effect of grain size on the mechanisms of plastic deformation in wrought Mg–Zn–Zr alloy revealed by acoustic emission measurements. *Acta Materialia*, 2013, vol. 61, no. 6, pp. 2044–2056. DOI: [10.1016/j.actamat.2012.12.024](https://doi.org/10.1016/j.actamat.2012.12.024).
 15. Capek J., Knapek M., Minarik P., Dittrich J., Mathis K. Characterization of Deformation Mechanisms in Mg Alloys by Advanced Acoustic Emission Methods. *Metals*, 2018, vol. 8, no. 8, article number 644. DOI: [10.3390/met8080644](https://doi.org/10.3390/met8080644).
 16. Vinogradov A., Orlov D., Danyuk A., Estrin Y. Deformation mechanisms underlying tension–compression asymmetry in magnesium alloy ZK60 revealed by acoustic emission monitoring. *Materials Science and Engineering: A*, 2015, vol. 621, pp. 243–251. DOI: [10.1016/j.msea.2014.10.081](https://doi.org/10.1016/j.msea.2014.10.081).
 17. Vinogradov A., Nadtochiy M., Hashimoto S., Miura S. Acoustic Emission Spectrum and Its Orientation Dependence in Copper Single Crystals. *Materials Transactions, JIM*, 1995, vol. 36, no. 4, pp. 496–503. DOI: [10.2320/matertrans1989.36.496](https://doi.org/10.2320/matertrans1989.36.496).
 18. Tromans D. Elastic anisotropy of HCP metal crystals and polycrystals. *IJRRAS*, 2011, vol. 6, no. 4, pp. 462–483.
 19. Pahlevanpour A.H., Karparvarfard S.M.H., Shaha S.K., Behraves S.B., Adibnazari S., Jahed H. Anisotropy in the Quasi-static and Cyclic Behavior of ZK60 Extrusion: Characterization and Fatigue Modeling. *Material & Design*, 2018, vol. 160, pp. 936–948. DOI: [10.1016/j.matdes.2018.10.026](https://doi.org/10.1016/j.matdes.2018.10.026).
 20. Russell W.D., Bratton N.R., Paudel Y. et al. In Situ Characterization of the Effect of Twin-Microstructure Interactions on {1 0 1 2} Tension and {1 0 1 1} Contraction Twin Nucleation, Growth and Damage in Magnesium. *Metals*, 2020, vol. 10, no. 11, article number 1403. DOI: [10.3390/met10111403](https://doi.org/10.3390/met10111403).
 21. Agnew S.R. Deformation mechanisms of magnesium alloys. *Advances in Wrought Magnesium Alloys. Fundamentals of Processing, Properties and Applications*, 2012, pp. 63–104. DOI: [10.1533/9780857093844.1.63](https://doi.org/10.1533/9780857093844.1.63).
 22. Wang Jingya, Chen Yiwen, Chen Zhe, Llorca J., Zeng Xiaogin. Deformation mechanisms of Mg–Ca–Zn alloys studied by means of micropillar compression tests. *Acta Materialia*, 2021, vol. 217, article number 117151. DOI: [10.1016/j.actamat.2021.117151](https://doi.org/10.1016/j.actamat.2021.117151).
 23. Li Lichao, Kim Chunjoong, Kim Young-Min. Identification of Active Slip Mode and Calculation of Schmid Factors in Magnesium Alloy. *Metals*, 2022, vol. 12, no. 10, article number 1604. DOI: [10.3390/met12101604](https://doi.org/10.3390/met12101604).
 24. Kosevich A.M., Boyko V.S. Dislocation theory of the elastic twinning of crystals. *Uspekhi fizicheskikh nauk*, 1971, vol. 104, no. 2, pp. 201–254. DOI: [10.3367/UFNr.0104.197106b.0201](https://doi.org/10.3367/UFNr.0104.197106b.0201).
 25. Yu Qin, Wang Jian, Jiang Yanyao, McCabe R.J., Li Nan, Tomé C.N. Twin–twin interactions in magnesium. *Acta Materialia*, 2014, vol. 77, pp. 28–42. DOI: [10.1016/j.actamat.2014.05.030](https://doi.org/10.1016/j.actamat.2014.05.030).
- ### СПИСОК ЛІТЕРАТУРИ
1. Yu Hai Yan, Wu Hangyu, Wang Lin. Inelastic strain recovery of magnesium alloys and a new elastic modulus model // IOP Conference Series: Materials Science and Engineering. 2020. Vol. 967. Article number 012046. DOI: [10.1088/1757-899X/967/1/012046](https://doi.org/10.1088/1757-899X/967/1/012046).
 2. Xiong Ying, Yu Qin, Jiang Yanyao. Deformation of extruded ZK60 magnesium alloy under uniaxial loading in different material orientations // Materials Science and Engineering: A. 2018. Vol. 710. P. 206–213. DOI: [10.1016/j.msea.2017.10.059](https://doi.org/10.1016/j.msea.2017.10.059).
 3. Shiraiishi K., Mayama T., Yamasaki M., Kawamura Y. Enhanced non-linearity during unloading by LPSO phase in as-cast Mg–Zn–Y alloys and slip-dominated non-linear unloading mechanism // Materials Science and Engineering: A. 2020. Vol. 790. Article number 139679. DOI: [10.1016/j.msea.2020.139679](https://doi.org/10.1016/j.msea.2020.139679).
 4. Hama T., Matsudai R., Kuchinomachi Y., Fujimoto H., Takuda H. Non-linear Deformation behavior during unloading in various metal sheets // ISIJ International. 2015. Vol. 55. № 5. P. 1067–1075. DOI: [10.2355/isijinternational.55.1067](https://doi.org/10.2355/isijinternational.55.1067).
 5. Wang Lifei, Huang Guangsheng, Quan Quan, Bassani P., Mostaed E., Vadani M., Pan Fusheng. The effect of twinning and detwinning on the mechanical property of AZ31 extruded magnesium alloy during strain-path changes // Material & Design. 2014. Vol. 63. P. 177–184. DOI: [10.1016/j.matdes.2014.05.056](https://doi.org/10.1016/j.matdes.2014.05.056).
 6. Frydrych K., Libura T., Kowalewski Z., Maj M., Kowalczyk-Gajewska K. On the role of slip, twinning and detwinning in magnesium alloy AZ31B sheet // Materials Science and Engineering: A. 2021. Vol. 813. Article number 141152. DOI: [10.1016/j.msea.2021.141152](https://doi.org/10.1016/j.msea.2021.141152).
 7. Tang Weigin, Lee Jeong Yeon, Wang Huamiao, Steglich D., Li Dayong, Peng Yinghong, Wu Peidong. Unloading behaviors of the rare-earth magnesium alloy ZE10 sheet // Journal of Magnesium and Alloys. 2021. Vol. 9. № 3. P. 927–936. DOI: [10.1016/j.jma.2020.02.023](https://doi.org/10.1016/j.jma.2020.02.023).
 8. Shi Baodong, Yang Chong, Peng Yan, Zhang Fucheng, Pan Fusheng. Anisotropy of wrought magnesium alloys: A focused overview // Journal of Magnesium and Alloys. 2022. Vol. 10. № 6. P. 1476–1510. DOI: [10.1016/j.jma.2022.03.006](https://doi.org/10.1016/j.jma.2022.03.006).
 9. Chen Hongbing, Liu Tianmo, Zhang Yin, Song Bo, Hou Dewen, Pan Fusheng. The yield asymmetry and precipitation behavior of pre-twinned ZK60 alloy // Materials Science and Engineering: A. 2016. Vol. 652. P. 167–174. DOI: [10.1016/j.msea.2015.11.092](https://doi.org/10.1016/j.msea.2015.11.092).
 10. Zhao Lingyu, Chen Wenhao, Zhou Beian, He Cong, Yan Changjian, Jin Zhaoyang, Yu Huihui, Xin Yunchang. Quantative study on the tension-compression yield asymmetry of a Mg–3Al–1Zn alloy with bimodal texture components // Journal of Magnesium and Alloys. 2022. Vol. 10. № 6. P. 1680–1693. DOI: [10.1016/j.jma.2022.03.002](https://doi.org/10.1016/j.jma.2022.03.002).
 11. Vinogradov A., Vasilev E., Linderov M., Merson D. Evolution of Mechanical Twinning during Cyclic Deformation of Mg–Zn–Ca Alloys // Metals. 2016. Vol. 6. № 12. Article number 304. DOI: [10.3390/met6120304](https://doi.org/10.3390/met6120304).
 12. Wang Yang-Yang, Jia Chen, Tayebi M., Hamawandi B. Microstructural Evolution during Accelerated Tensile

- Creep Test of ZK60/SiCp Composite after KoBo Extrusion // *Materials*. 2022. Vol. 15. № 18. Article number 6428. DOI: [10.3390/ma15186428](https://doi.org/10.3390/ma15186428).
13. Trojanova Z., Drozd Z., Lukac P., Dzugan J. Stress Relaxation Tests: Modeling Issues and Applications in Magnesium Alloys and Composites // *Journal of Materials Engineering and Performance*. 2023. Vol. 32. P. 2766–2783. DOI: [10.1007/s11665-022-06951-w](https://doi.org/10.1007/s11665-022-06951-w).
 14. Vinogradov A., Orlov D., Danyuk A., Estrin Y. Effect of grain size on the mechanisms of plastic deformation in wrought Mg–Zn–Zr alloy revealed by acoustic emission measurements // *Acta Materialia*. 2013. Vol. 61. № 6. P. 2044–2056. DOI: [10.1016/j.actamat.2012.12.024](https://doi.org/10.1016/j.actamat.2012.12.024).
 15. Capek J., Knapek M., Minarik P., Dittrich J., Mathis K. Characterization of Deformation Mechanisms in Mg Alloys by Advanced Acoustic Emission Methods // *Metals*. 2018. Vol. 8. № 8. Article number 644. DOI: [10.3390/met8080644](https://doi.org/10.3390/met8080644).
 16. Vinogradov A., Orlov D., Danyuk A., Estrin Y. Deformation mechanisms underlying tension–compression asymmetry in magnesium alloy ZK60 revealed by acoustic emission monitoring // *Materials Science and Engineering: A*. 2015. Vol. 621. P. 243–251. DOI: [10.1016/j.msea.2014.10.081](https://doi.org/10.1016/j.msea.2014.10.081).
 17. Vinogradov A., Nadtochiy M., Hashimoto S., Miura S. Acoustic Emission Spectrum and Its Orientation Dependence in Copper Single Crystals // *Materials Transactions, JIM*. 1995. Vol. 36. № 4. P. 496–503. DOI: [10.2320/matertrans1989.36.496](https://doi.org/10.2320/matertrans1989.36.496).
 18. Tromans D. Elastic anisotropy of HCP metal crystals and polycrystals // *IJRRAS*. 2011. Vol. 6. № 4. P. 462–483.
 19. Pahlevanpour A.H., Karpavarfard S.M.H., Shaha S.K., Behraves S.B., Adibnazari S., Jahed H. Anisotropy in the Quasi-static and Cyclic Behavior of ZK60 Extrusion: Characterization and Fatigue Modeling // *Material & Design*. 2018. Vol. 160. P. 936–948. DOI: [10.1016/j.matdes.2018.10.026](https://doi.org/10.1016/j.matdes.2018.10.026).
 20. Russell W.D., Bratton N.R., Paudel Y. et al. In Situ Characterization of the Effect of Twin-Microstructure Interactions on {1 0 1 2} Tension and {1 0 1 1} Contraction Twin Nucleation, Growth and Damage in Magnesium // *Metals*. 2020. Vol. 10. № 11. Article number 1403. DOI: [10.3390/met10111403](https://doi.org/10.3390/met10111403).
 21. Agnew S.R. Deformation mechanisms of magnesium alloys. *Advances in Wrought Magnesium Alloys // Advances in Wrought Magnesium Alloys. Fundamentals of Processing, Properties and Applications*. 2012. P. 63–104. DOI: [10.1533/9780857093844.1.63](https://doi.org/10.1533/9780857093844.1.63).
 22. Wang Jingya, Chen Yiwen, Chen Zhe, Llorca J., Zeng Xiaogin. Deformation mechanisms of Mg–Ca–Zn alloys studied by means of micropillar compression tests // *Acta Materialia*. 2021. Vol. 217. Article number 117151. DOI: [10.1016/j.actamat.2021.117151](https://doi.org/10.1016/j.actamat.2021.117151).
 23. Li Lichao, Kim Chunjoong, Kim Young-Min. Identification of Active Slip Mode and Calculation of Schmid Factors in Magnesium Alloy // *Metals*. 2022. Vol. 12. № 10. Article number 1604. DOI: [10.3390/met12101604](https://doi.org/10.3390/met12101604).
 24. Косевич А.М., Бойко В.С. Дислокационная теория упругого двойникования кристаллов // *Успехи физических наук*. 1971. Т. 104. № 2. С. 201–254. DOI: [10.3367/UFNr.0104.197106b.0201](https://doi.org/10.3367/UFNr.0104.197106b.0201).
 25. Yu Qin, Wang Jian, Jiang Yanyao, McCabe R.J., Li Nan, Tomé C.N. Twin–twin interactions in magnesium // *Acta Materialia*. 2014. Vol. 77. P. 28–42. DOI: [10.1016/j.actamat.2014.05.030](https://doi.org/10.1016/j.actamat.2014.05.030).

Определение порога напряжения и микроструктурных факторов, формирующих эффект нелинейной разгрузки магниевого сплава MA14 (ZK60)

© 2023

Данюк Алексей Валериевич^{*1}, кандидат физико-математических наук, старший научный сотрудник НИИ прогрессивных технологий
*Мерсон Дмитрий Львович*², доктор физико-математических наук, профессор, директор НИИ прогрессивных технологий

*Брилевский Александр Игоревич*³, младший научный сотрудник НИИ прогрессивных технологий
Афанасьев Максим Анатольевич, научный сотрудник НИИ прогрессивных технологий

Тольяттинский государственный университет, Тольятти (Россия)

*E-mail: A.Danyuk@tltso.ru,
Alexey.Danyuk@gmail.com

¹ORCID: <https://orcid.org/0000-0002-7352-9947>

²ORCID: <https://orcid.org/0000-0001-5006-4115>

³ORCID: <https://orcid.org/0000-0002-5780-6094>

Поступила в редакцию 14.12.2022

Принята к публикации 01.09.2023

Аннотация: Магниевого сплавы – идеальный материал для создания легких и прочных современных транспортных систем, однако его широкое применение ограничено из-за некоторых физико-химических свойств. В работе рассмотрен эффект нелинейной упругой разгрузки магниевого сплава MA14 (ZK60, Mg–5,4Zn–0,5Zr) в крупнозернистом состоянии после рекристаллизационного отжига. Установлено, что нелинейность характеристики разгрузки формируется после достижения определенного порогового уровня напряжения. Предполагается, что изучаемый эффект связан с деформационным поведением сплава, при котором наблюдается формирование двойниковой структуры по механизму двойникования растяжения. Микроструктура материала образцов была определена методами растровой электронной микроскопии с применением анализа дифракции обратно рассеянных электронов. Определение порогового напряжения формирования нелинейности разгрузки было проведено двумя ме-

тодами: 1) по величине площади петли, образуемой нелинейностью механической характеристики разгрузки и характеристики повторного нагружения (механический гистерезис), и 2) по анализу акустической эмиссии, зарегистрированной при растяжении до разрушения. Сопоставление полученных результатов позволяет предположить, что нелинейность разгрузки обусловлена двойникованием в зернах, в которых наблюдается невыгодная конфигурация (низкий фактор Шмидта) для дислокационного скольжения. Разворот продвойниковавшего кристалла на угол, близкий к 90° , не способствует повышению фактора Шмидта и активации систем скольжения дислокаций для закрепления деформированной структуры по механизму дислокационного упрочнения. При последующем снижении величины внешнего напряжения происходит раздвойникование и частичное восстановление конфигурации кристаллической решетки.

Ключевые слова: магний; магниевый сплав; MA14 (ZK60, Mg–5,4Zn–0,5Zr); нелинейная разгрузка; порог напряжения; упругость; двойникование; раздвойникование; деформационное поведение.

Благодарности: Исследование выполнено при финансовой поддержке Российского научного фонда в рамках реализации научного проекта № 22-23-01169.

Для цитирования: Данюк А.В., Мерсон Д.Л., Брилевский А.И., Афанасьев М.А. Определение порога напряжения и микроструктурных факторов, формирующих эффект нелинейной разгрузки магниевое сплава MA14 (ZK60) // Frontier Materials & Technologies. 2023. № 4. С. 31–39. DOI: 10.18323/2782-4039-2023-4-66-3.

Thermal stability of a submicrocrystalline structure formed by high-pressure torsion in Ni and Ni–2 % Cr alloy

© 2023

Konstantin Yu. Karamyshev, engineer of the Laboratory of Precision Alloys and Intermetallic Compounds

M.N. Mikheev Institute of Metal Physics of the Ural Branch of RAS, Yekaterinburg (Russia)

E-mail: karamyshev.imp@mail.ru

ORCID: <https://orcid.org/0009-0000-1752-2284>

Received 23.06.2023

Accepted 21.11.2023

Abstract: The main problem of submicrocrystalline (SMC) materials formed as a result of severe plastic deformation is their thermal stability. The large stored energy and the formation of strongly disordered microcrystallites in the structure lead to a decrease in the recrystallization onset temperature and, therefore, possibly decrease the structure stability. In the work, severe plastic deformation by high-pressure torsion and annealing of pure nickel and an alloy containing 2 at. % chromium were carried out. The structure of both deformed and annealed material was studied by scanning and transmission electron microscopy. The dependence of hardness on the square root of true strain and structure evolution were analyzed to identify the boundaries of the stages of structural states. The energy stored during deformation was estimated using differential scanning calorimetry by the amount of absorbed heat energy. The author studied the behaviour of materials during annealing depending on the stored strain energy at the SMC structure stage. Three stages of structural states were identified in pure nickel: cellular, mixed, and SMC structure, while in the alloy containing 2 at. % chromium, a cellular structure stage was not detected. A decrease in the stored strain energy was found at the stage of the SMC structure for both materials. Alloying nickel with 2 at. % chromium increases its thermal stability, which increases the temperature when the grain growth becomes intensive by 150 °C. The amount of stored strain energy affects grain growth in the alloy containing 2 at. % chromium, whereas in pure nickel no effect was detected. In the Ni–Cr alloy, greater stored energy corresponds to larger recrystallized grain size.

Keywords: nickel; Ni–Cr alloy; high-pressure torsion; submicrocrystalline structure; stored strain energy.

Acknowledgements: The work was carried out within the state assignment of the Ministry of Education and Science of Russia (topic “Pressure”, No. 122021000032-5).

The author expresses gratitude to the employees of M.N. Mikheev Institute of Metal Physics of the UB of RAS: V.P. Pilyugin, PhD (Physics and Mathematics), Head of the High Pressure Physics Laboratory, for carrying out the deformation, and M.V. Degtyarev, Doctor of Sciences (Engineering), Head of the Department of Precision Metallurgy and Pressure Processing Technologies, for discussion of the results.

The research was carried out using the equipment of the Collaborative Access Center “Testing Center of Nanotechnology and Advanced Materials” of the IMP UB RAS.

The paper was written on the reports of the participants of the XI International School of Physical Materials Science (SPM-2023), Togliatti, September 11–15, 2023.

For citation: Karamyshev K.Yu. Thermal stability of a submicrocrystalline structure formed by high-pressure torsion in Ni and Ni–2 % Cr alloy. *Frontier Materials & Technologies*, 2023, no. 4, pp. 41–51. DOI: 10.18323/2782-4039-2023-4-66-4.

INTRODUCTION

Industrial development requires the creation of new materials with unique physical and mechanical properties. One of the approaches to achieve these properties is the formation of submicrocrystalline (SMC) and nanocrystalline (NC), structural states in these materials, for which severe plastic deformation (SPD) can be used [1; 2], in particular, high-pressure torsion (HPT) [3; 4]. The structure formation directly depends on the stacking fault energy (SFE) of the studied materials. Thus, in materials with a medium SFE during deformation at room temperature, the structure evolution appears to be three successive stages: cellular, mixed, and SMC structure [1; 5; 6]. The cellular-type structure is formed due to the movement of dislocations. At the second stage, along with the dislocation mechanism, rotational modes of deformation appear leading to the formation of individual microcrystal-

lites [7]. Such a structure contains both high- and low-angle boundaries; it is usually called a mixed structure [8]. Finally, at the last stage, the structure consists of microcrystallites only – this is the SMC structure stage. In materials with high SFE during HPT, the cellular structure stage is not registered; after small angles of anvil rotation, a mixed structure appears [9].

The presence of an SMC structure leads to a significant (by about 150 °C) decrease in the recrystallization temperature, which may be associated with a decrease in the thermal stability of the structure [10]. On the other hand, in [11–13] it is shown that grinding the structural elements below a certain critical size, leads to an increase in thermal stability. In the works [14; 15], it was found that the formation of a honeycomb-type structure as a result of SMC structure recrystallization gives the material high thermal stability. The SMC structure can be obtained in the material surface layer by frictional processing [16]. This treatment

of martensitic and austenitic steels delays the softening (by 200–300 °C) of the material surface layer [17].

Another characteristic of thermal stability is the grain growth rate during recrystallization. It is possible to reduce the grain growth rate by alloying to form a solid solution. It is important to limit the content of the alloying element to prevent such a decrease in the SFE, that would lead to a change in the strain mechanism.

The stored strain energy also affects recrystallization [18]. In a number of materials, SPD can lead to the development of relaxation processes, such as dynamic recovery and dynamic recrystallization [3; 5; 19]. As a result of these processes, with an increase in true strain, a decrease in the stored strain energy can be observed, and, consequently, a decrease in the recrystallization driving force.

The purpose of this work is to study the influence of alloying Ni-2 at. % Cr on the SMC structure formation, the amount of stored energy during HPT deformation, as well as on the thermal stability of the resulting structure upon heating.

METHODS

To carry out the study, single-crystalline nickel (99.98 wt. % Ni) and a polycrystalline single-phase Ni-Cr alloy, with a chromium content of 2 at. % (Ni-2Cr) were selected. The samples had a diameter of 5 mm and a thickness of 0.3 mm. They were deformed by HPT in Bridgman anvils at room temperature under a pressure of 8 GPa by upsetting and with anvil rotation: for Ni – from 15° to 7 revolutions, and for Ni-2Cr – from 15° to 10 revolutions. The true strain was calculated using the formula

$$e = \ln \left(1 + \left(\frac{\varphi r}{h_i} \right)^2 \right)^{\frac{1}{2}} + \ln \left(\frac{h_0}{h_i} \right),$$

where φ is the angle of anvil rotation, rad.;

r_i is the radius from the center of the sample, mm;

h_0 is the sample thickness before deformation, mm;

h_i is the thickness of the sample after deformation at the i -radius, mm.

The hardness of the studied materials was measured after deformation, using a METOLAB 502 device under a load of 0.5 N along two mutually perpendicular diameters of the sample with a step of 0.25 mm. Hardness values were averaged over true strain intervals $\Delta e=0.4$. The boundaries of the deformation stages were determined by the inflection points in the hardness dependence on the square root of true strain $H=f(e^{1/2})$ in accordance with the technique described in [20]. To assess the mechanical properties of nano- and submicrocrystalline materials, hardness values were used as flow stress, as substantiated in [21]. Before measuring hardness, the samples were ground and electropolished.

Calorimetric studies were carried out using a STA 449 F3 thermal analyser, with a heating rate of 20 °C/min in the temperature range of 25–1000 °C. Two successive heatings were carried out in the same temperature range with the sample being cooled to room temperature after each heating. During the first heating, heat release peaks were recorded on the curves. The peak temperatures were determined by the secant method, and the amount of released

thermal energy was determined as the area under the peak. This energy was then associated with the stored strain energy [22]. Reheating was carried out to ensure that the heat release process was irreversible. The error, when determining the amount of energy released during calorimetric measurements did not exceed 2.5 %.

The samples were annealed in a vacuum furnace at the following temperatures: for Ni – 200–350 °C with a step of 50 °C for 1 h; for Ni-2Cr – 200–400 °C with a step of 100 °C for 1 h. Samples with the maximum stored energy (for Ni – $e=7.0$ and for Ni-2Cr – $e=9.3$, which corresponds to the anvil rotation by 2 and 10 revolutions), and SMC structure samples, where the maximum stored energy has not been reached (for pure nickel – with the anvil rotation by 7 revolutions ($e=8.3$), and for Ni-2Cr – by 5 revolutions ($e=8.5$)), were selected for annealing.

The resulting structures were assessed using QUANTA 200 and TESCAN MIRA scanning electron microscopes, and a JEM200CX transmission electron microscope. Using scanning electron microscopy (SEM), the structure was examined at a distance of 1.0 mm from the centre of the samples. Based on the SEM results, the spectra of grain-boundary angles, and grain sizes were determined. Using transmission electron microscopy, the structure was examined at the distances of 1.5 mm from the centre of the samples. The sizes of structural elements (dislocation cells, microcrystallites, and recrystallized grains) were determined from bright-field images, as well as from dark-field images in the {111} type reflection, based on the results of more than 400 measurements, which ensured an error of less than 10 %.

The results were processed using the STATISTICA software.

RESULTS

Fig. 1 shows a diagram of the hardness dependence on the true strain of the studied materials. It can be seen that alloying with 2 % of Cr only slightly influences the strain, hardening of Ni in the region of relatively small strains (up to $e=6$). At $e>6$, alloying, ensures an increase in the hardness growth coefficient; in Ni, hardness stabilisation is registered after $e=5$.

To identify the stages of deformation in the studied materials, the dependences shown in Fig. 2 were obtained. For pure Ni, three stages were identified, their change occurs at $e=0.8$ and $e=5$. For the alloy containing 2 % of Cr, only two stages were obtained; the transition from one stage to another in Ni-2Cr occurred at $e=8.5$.

Fig. 3 shows the structures of pure Ni and the Ni-2Cr alloy deformed in this work. It can be seen that the evolution of the pure nickel structure goes through three stages. First, a cellular-type structure is formed up to $e=0.8$ (Fig. 3 a). In the interval $0.8<e<5$, individual microcrystallites with high-angle boundaries are formed in the structure, which is a sign of a mixed-type structure (Fig. 3 b). Moreover, after $e=5$, the structure contains only microcrystallites, which is a sign that the SMC structure has been achieved (Fig. 3 c). Unlike pure nickel, in Ni-2Cr, the cellular structure stage was not registered, therefore, only one boundary is identified in this alloy, at which the mixed structure is replaced by the SMC structure at $e=8.5$ (Fig. 3 d, 3 e).

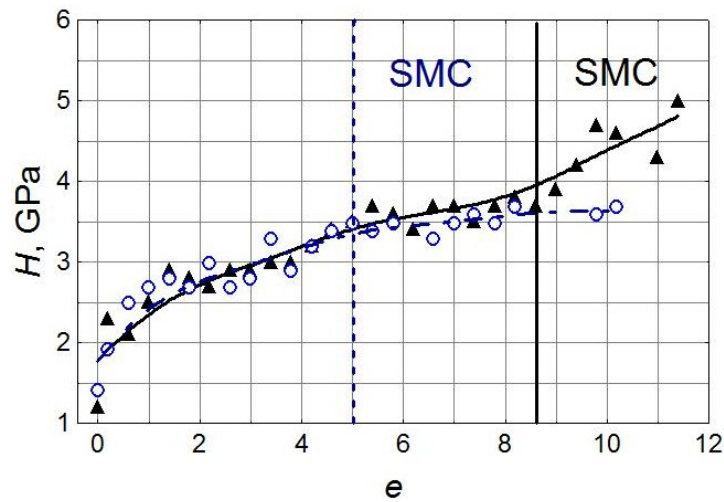


Fig. 1. Microhardness dependence on true strain: \circ – pure Ni; \blacktriangle – Ni-2Cr alloy
Рис. 1. Зависимость твердости от истинной деформации: \circ – чистый Ni; \blacktriangle – сплав Ni-2Cr

Fig. 4 shows the dependence of the average size of structural elements on true strain. It has been found that alloying with chromium in an amount of 2 % does not lead to a decrease in the size of microcrystallites in the single-phase Ni-2Cr alloy compared to pure nickel: after $e=9$, the average size of microcrystallites in both cases is $(0.14 \pm 0.01) \mu\text{m}$. It can be seen that the output of the dependencies shown in Fig. 4 to saturation in grinding is typical for both studied materials.

Fig. 5 shows that the stored energy (E) in the studied materials continuously increases with increasing deformation up to $e=7$ in pure Ni and $e=9$ in Ni-2Cr, and with continued deformation at the SMC structure stage it decreases in both materials. Thus, the maximum stored energy was recorded after deformation $e=7.0$ for Ni and $e=9.3$ for Ni-2Cr, which corresponds to the anvil rotations for 2 and 10 revolutions.

Fig. 6 gives images of the pure nickel structure after deformation and annealing. Annealing pure nickel at 150°C leads to the recrystallization onset (Fig. 6 a). The average

size of structural elements is $0.2 \mu\text{m}$. Increasing the annealing temperature to 200°C leads to the recrystallization completion (Fig. 6 b). The average size of recrystallized grains is $6 \mu\text{m}$, while the maximum size of recrystallized grains is about $40 \mu\text{m}$. After annealing at 300°C , a decrease in the average size of recrystallized grains to $5.5 \mu\text{m}$ is observed, apparently due to the appearance of nuclei through the thermal activation mechanism (Fig. 6 c). At the annealing temperature of 350°C , the grain growth rate becomes greater than the rate of nucleation of new recrystallization centres (Fig. 6 d), and the average grain size increases again.

Fig. 7 shows that in nickel, the average grain size obtained through annealing the material with the maximum (2 revolutions) and lower (7 revolutions) stored strain energy is almost the same. The temperature when rapid grain growth begins also does not depend on the strain amount (stored energy). Thus, no effect of the difference in the stored strain energy on recrystallization in pure nickel with an SMC structure was detected.

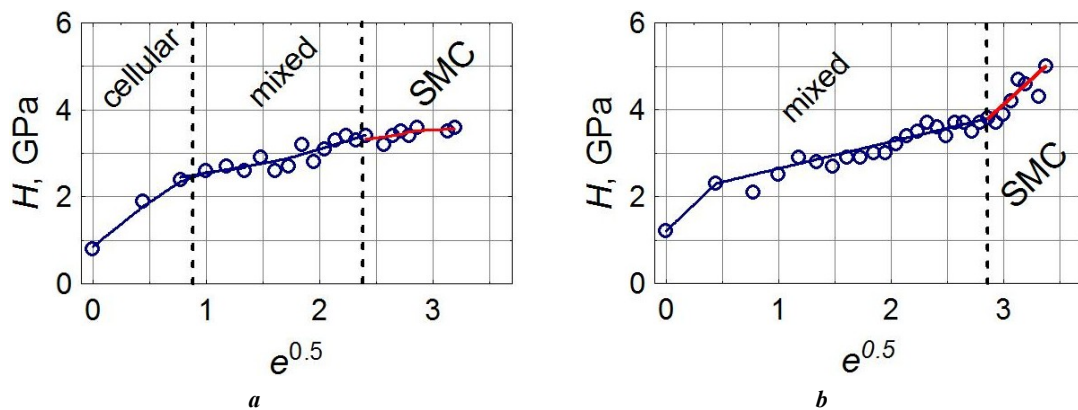


Fig. 2. Diagram of microhardness dependence on the square root of true strain: **a** – pure Ni; **b** – Ni-2Cr alloy
Рис. 2. График зависимости твердости от квадратного корня из истинной деформации: **a** – чистый Ni; **b** – сплав Ni-2Cr

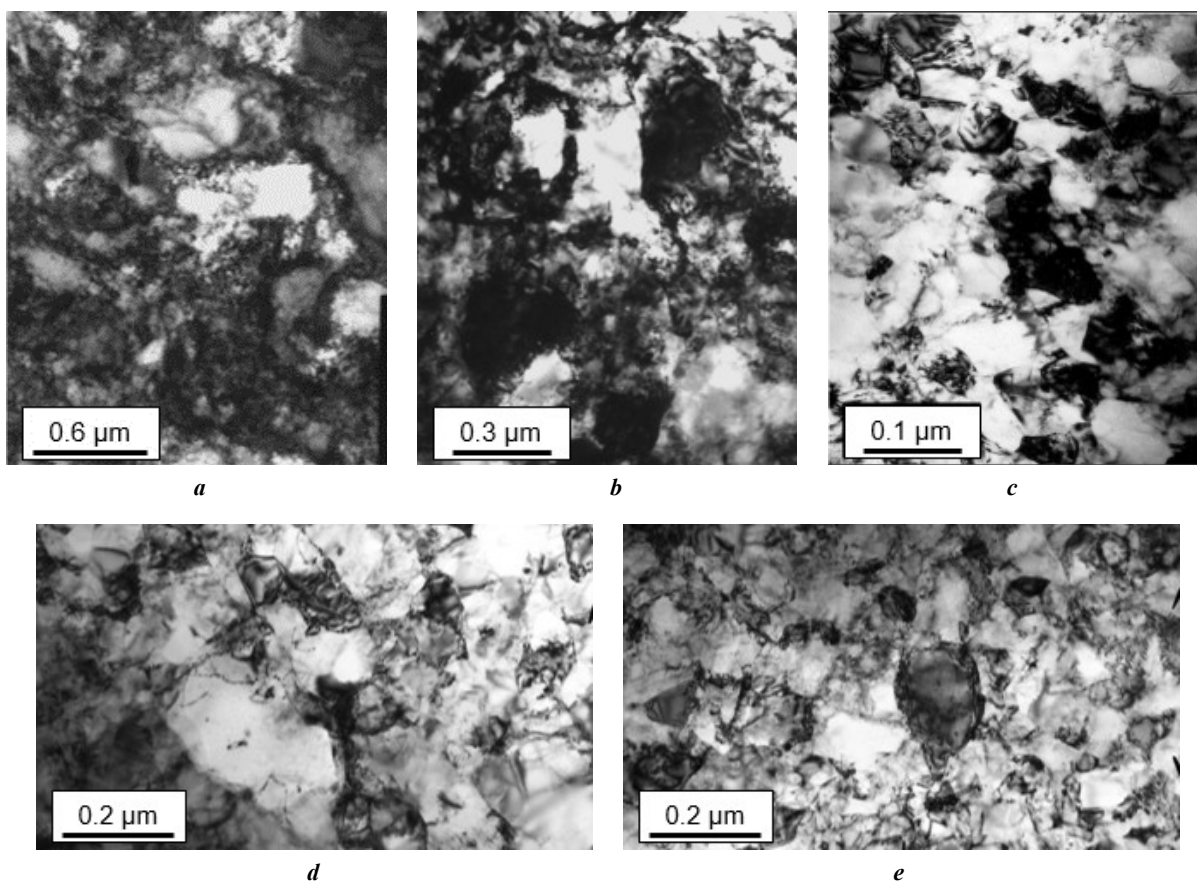


Fig. 3. Fine structure of pure nickel and Ni-2Cr alloy deformed by high-pressure torsion:
a – Ni, $e=0.3$; **b** – Ni, $e=4.2$; **c** – Ni, $e=6.9$; **d** – Ni-2Cr, $e=4.0$; **e** – Ni-2Cr, $e=8.6$
Рис. 3. Тонкая структура чистого никеля и сплава Ni-2Cr, деформированных СПД:
a – Ni, $e=0.3$; **b** – Ni, $e=4.2$; **c** – Ni, $e=6.9$; **d** – Ni-2Cr, $e=4.0$; **e** – Ni-2Cr, $e=8.6$

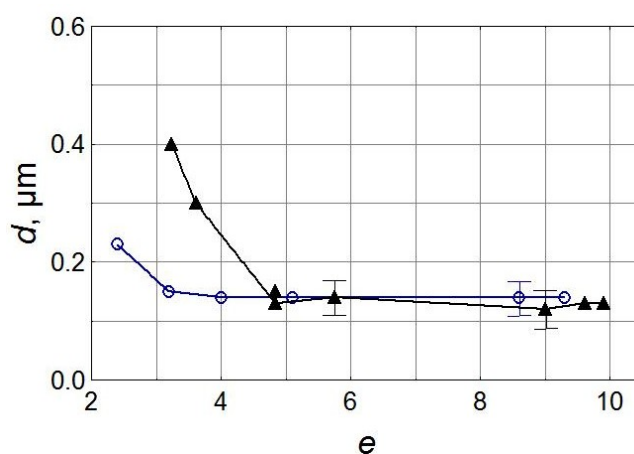


Fig. 4. Dependence of average size of structural elements on true strain:
 ○ – pure Ni; ▲ – Ni-2Cr alloy
Рис. 4. Зависимость среднего размера элементов структуры от истинной деформации:
 ○ – чистый Ni; ▲ – сплав Ni-2Cr

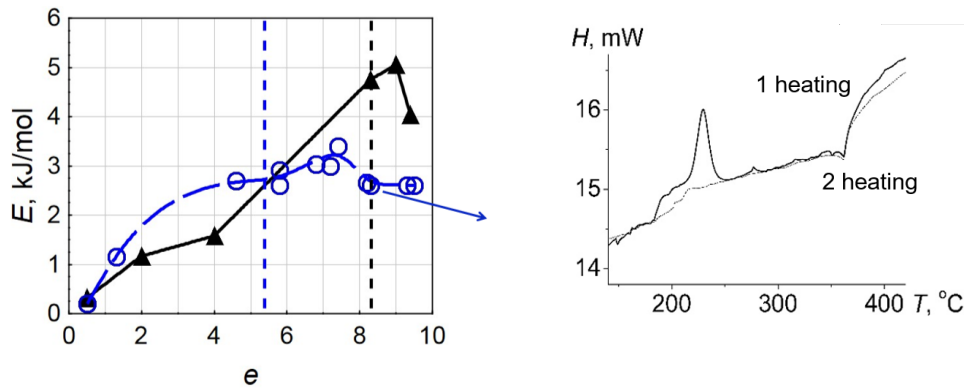


Fig. 5. Dependence of stored strain energy on true strain: \circ – pure Ni; \blacktriangle – Ni-2Cr alloy; the inset shows an example of a DSC (differential scanning calorimetry) curve for Ni deformed by 5 anvil revolutions
Рис. 5. Зависимость запасенной энергии деформации от истинной деформации: \circ – чистый Ni; \blacktriangle – сплав Ni-2Cr; на вставке пример ДСК (дифференциальной сканирующей калориметрии) кривой для Ni, деформированного на 5 оборотов наковальни

There are individual recrystallized grains with a size of about 0.7 μm in the Ni-2Cr alloy after annealing at 200 $^{\circ}\text{C}$ (Fig. 8 a, 8 b). The average size of the structural elements did not change much, relative to the size of the microcrystallites in the deformed state. It amounts $(0.16 \pm 0.03) \mu\text{m}$. This shows that the number of recrystallized grains is small. Thus, recrystallization in this material just begins at a temperature of 200 $^{\circ}\text{C}$.

In turn, annealing at 300 $^{\circ}\text{C}$ shows that in the Ni-2Cr alloy, recrystallization occurs more completely after deformation with $e=9.3$ (10 anvil revolutions, Fig. 8 c). In this case, in the sample that was deformed by HPT for 5 revolutions, a large fraction of the non-recrystallized matrix is retained (Fig. 8 d). The structure contains large deformed structure areas, as well as individual grains larger

than 1 μm in size, which do not contain dislocations. SEM images demonstrate that annealing led to the bimodal structure formation (Fig. 9). The average size of the structural elements for both treatments is close: 1.2 μm after deformation with $e=8.5$ and 0.8 μm with $e=9.3$, while the maximum size differs by a factor of 2 and is 5 and 9 μm , respectively.

Increasing the annealing temperature to 400 $^{\circ}\text{C}$ increases the dimensional heterogeneity of the structure of the alloy with 2 % of Cr deformed by both 5 and 10 anvil revolutions (Fig. 10); along with large grains, small crystallites are observed. It can be seen that after deformation by 10 revolutions, and annealing at 400 $^{\circ}\text{C}$, individual coarse grains larger than 50 μm in size appeared (Fig. 10 a), the average grain size is approximately 8 μm . After

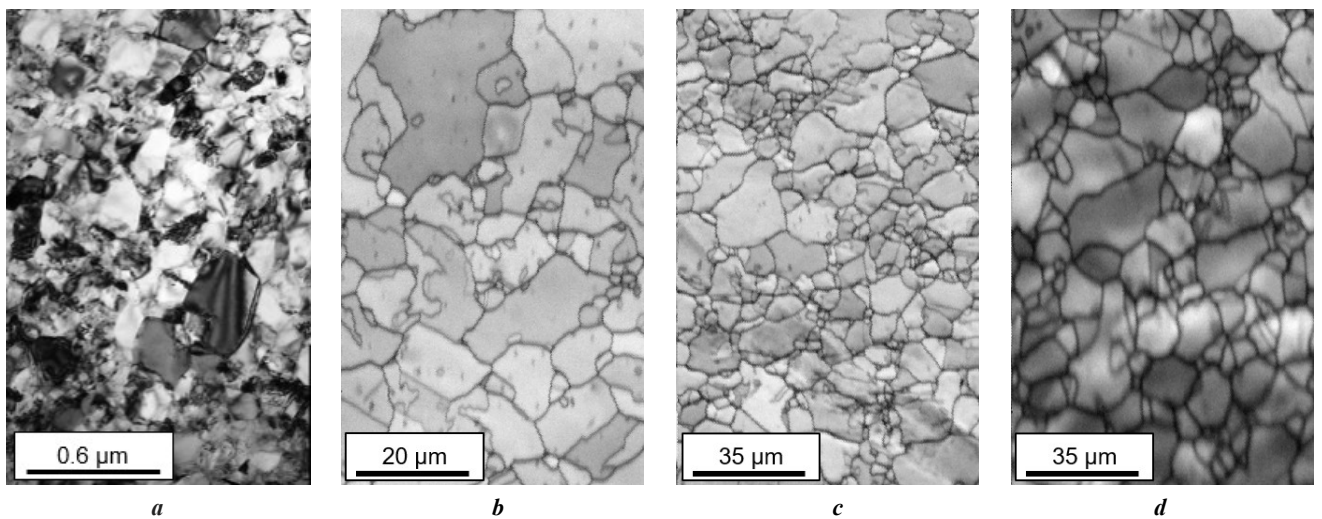


Fig. 6. Electron microscope images of the structure of pure nickel deformed with $e=7$ (2 anvil revolutions) and following annealing at:
 a – 150 $^{\circ}\text{C}$; b – 200 $^{\circ}\text{C}$; c – 300 $^{\circ}\text{C}$; d – 350 $^{\circ}\text{C}$

Рис. 6. Электронно-микроскопические изображения структуры чистого никеля, деформированного с $e=7$ (2 оборота наковальни), и последующего отжига при:
 a – 150 $^{\circ}\text{C}$; b – 200 $^{\circ}\text{C}$; c – 300 $^{\circ}\text{C}$; d – 350 $^{\circ}\text{C}$

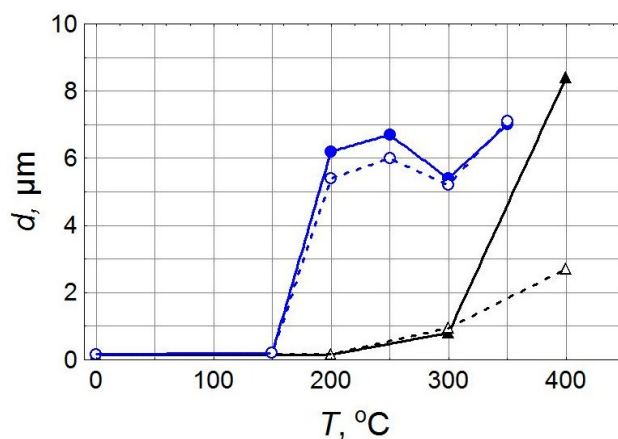


Fig. 7. Dependence of average size of structural elements on annealing temperature:

● – pure Ni; ▲ – Ni-2Cr alloy;

filled markers correspond to the deformation when the stored energy is maximum according to DSC data

Рис. 7. Зависимость среднего размера элементов структуры от температуры отжига:

● – чистый Ni; ▲ – сплав Ni-2Cr;

закрашенные маркеры соответствуют деформации, при которой запасенная энергия максимальна, согласно данным ДСК

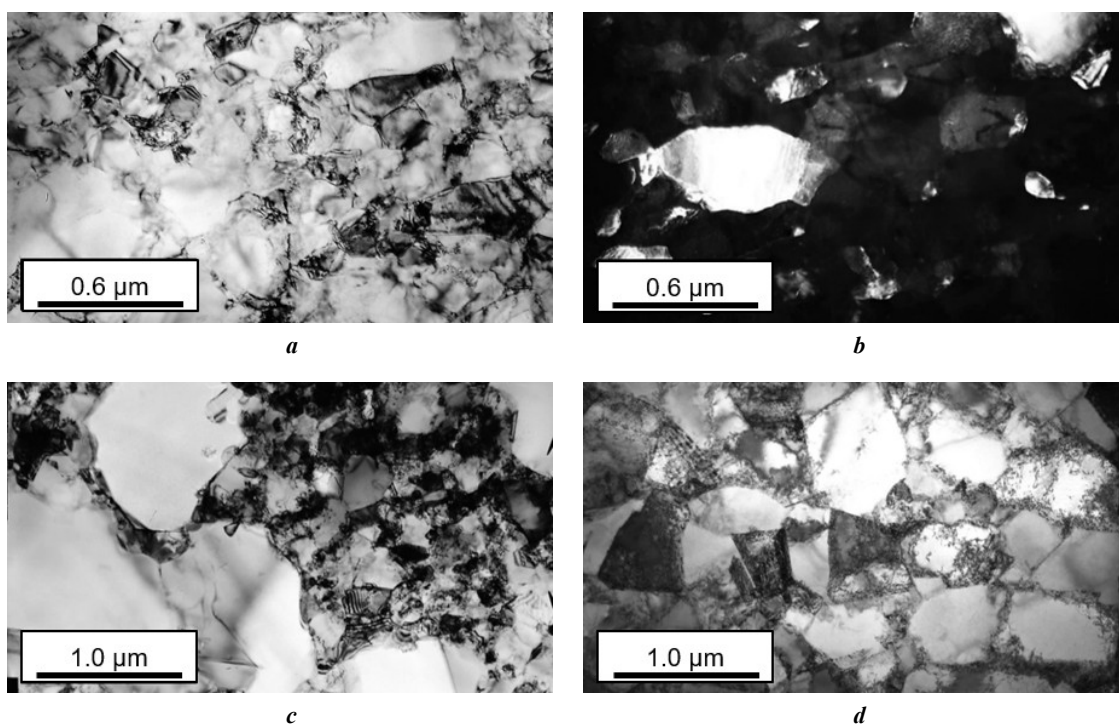


Fig. 8. Microstructure of the Ni-2Cr alloy after deformation and subsequent annealing at 200 (a, b) and 300 °C (c, d):

a – bright-field image, $e=8.5$; b – dark-field image, $e=8.5$; c – bright-field image, $e=9.3$; d – bright-field image, $e=8.5$

Рис. 8. Микроструктура сплава Ni-2Cr после деформации и последующего отжига при 200 (a, b) и 300 °C (c, d):

a – светлопольное изображение, $e=8,5$; b – темнопольное изображение, $e=8,5$;

c – светлопольное изображение, $e=9,3$; d – светлопольное изображение, $e=8,5$

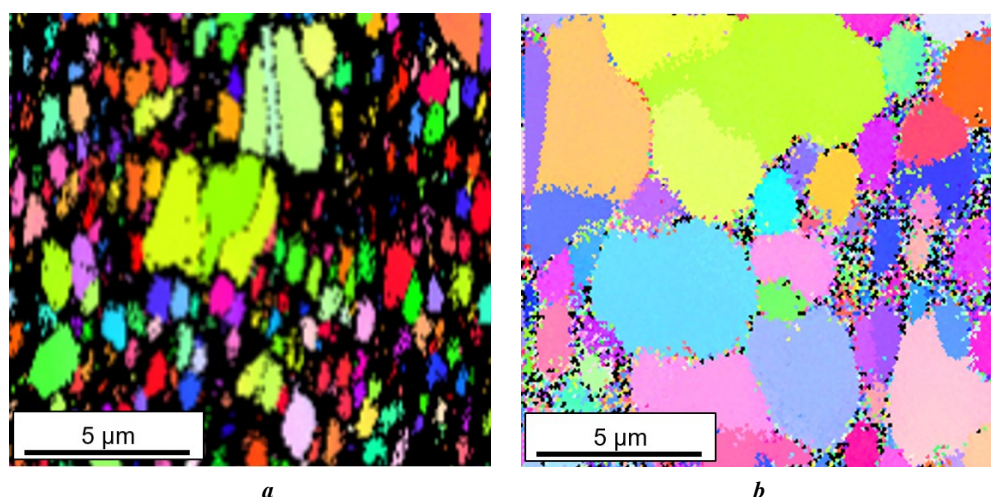


Fig. 9. Orientation map in colours of the inverse pole figure of the Ni-2Cr alloy after deformation and subsequent annealing at 300 °C: **a** – $e=8.5$; **b** – $e=9.3$

Рис. 9. Ориентационная карта в цветах обратной полюсной фигуры сплава Ni-2Cr после деформации и последующего отжига при 300 °C: **a** – $e=8.5$; **b** – $e=9.3$

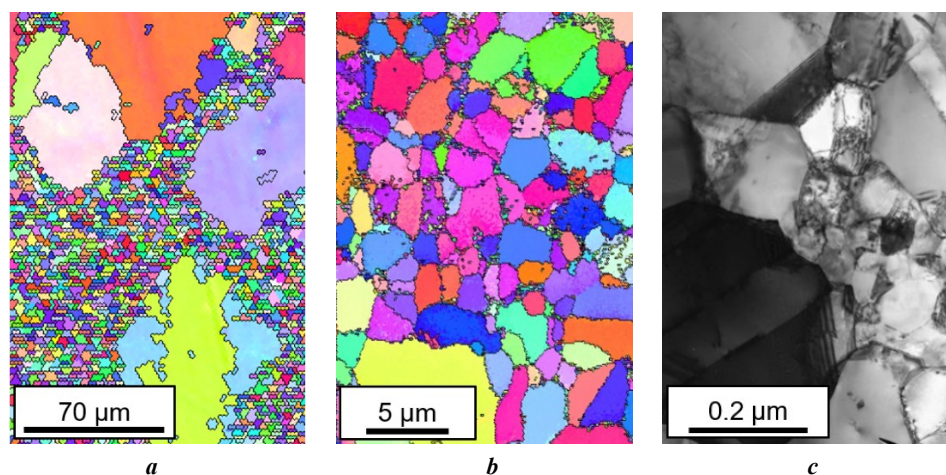


Fig. 10. Orientation map in colours of the inverse pole figure and fine structure of the Ni-2Cr alloy after deformation and subsequent annealing at 400 °C: **a** – $e=9.3$; **b**, **c** – $e=8.5$; **a**, **b** – SEM; **c** – TEM

Рис. 10. Ориентационная карта в цветах обратной полюсной фигуры и тонкая структура сплава Ni-2Cr после деформации и последующего отжига при 400 °C: **a** – $e=9.3$; **b**, **c** – $e=8.5$; **a**, **b** – СЭМ; **c** – ПЭМ

deformation by 5 revolutions and annealing at 400 °C, relatively large grains up to 8 μm in size and small areas of non-recrystallized structure are also observed (Fig. 10 b, 10 c), but the average grain size is several times smaller – 2.5 μm. Thus, in this alloy, primary recrystallization does not complete even at 400 °C. For the Ni-2Cr alloy, the dependences of the average size of structural elements on the annealing temperature obtained by SEM and TEM methods are shown in Fig. 7.

DISCUSSION

Pure nickel deformation at the SMC structure stage does not lead to a change in hardness (Fig. 1). At the same time, the dimensions of the nickel structural elements also remain constant (Fig. 4), and calorimetric studies show a decrease in the stored strain energy (Fig. 5). Based on these results,

one can conclude that in nickel deformed by HPD at the SMC structure stage, the dominant structure-forming process is dynamic recovery. This is consistent with data known from the literature [23].

The results of the work confirmed that alloying with a small amount of chromium did not cause a change in the strain mechanism, which is observed, for example, in the Ni-20Cr alloy [24]. In this work, the author managed to identify the influence of solid solution strengthening on the formation of the structure of the studied materials during deformation and subsequent annealing. In the Ni-2Cr alloy, the SMC structure is formed at a significantly higher true strain ($e=8.5$) than in pure Ni ($e=5$). In this case, deformation at the SMC structure stage does not lead to stabilisation of the alloy hardness value. However, the average size of the SMC structure elements, just as in nickel, does not change (Fig. 1 and 2). Despite the stabilisation of sizes

in Ni–2Cr, according to calorimetric studies, the stored energy changes: it increases to $e=9.3$ (10 anvil revolutions), and then decreases. Consequently, the structure continues to change. A decrease in the stored strain energy, at the SMC structure stage indicates the occurrence of dynamic recovery in the alloy (Fig. 5). However, the increase in hardness shows that in this case, dynamic recovery is not the dominant process.

Annealing of SMC nickel showed that recrystallization begins at 150 °C (Fig. 6 a) and proceeds as the growth of individual centres. This leads to strong grain heterogeneity: a small number of large grains are located in a fine-grained matrix. Recrystallization is completed at 200 °C (Fig. 6 b). After annealing at 300 °C, a decrease in the average size of recrystallized grains is observed (Fig. 6 c). A similar effect was recorded in [15] as a result of annealing the iron SMC structure. In the latter case, the decrease in size was associated with the appearance of thermally activated recrystallization nuclei. A further increase in the annealing temperature of nickel shows a tendency towards grain structure coarsening (Fig. 6 d).

Nickel alloying with 2 at. % of chromium increases the temperature of the recrystallization onset from 150 to 200 °C, and the temperature of the beginning of intensive grain growth – from 150 to 300 °C (Fig. 7 and 8). Therefore, one can conclude that solid solution strengthening increased the thermal stability of the SMC structure. Just like in Ni, in the Ni–2Cr alloy, recrystallization occurs according to the mechanism of accelerated growth of individual centres, which does not allow obtaining a homogeneous submicrogranular recrystallized structure, as, for example, in iron [14; 15]. In this work, it was not possible to determine the temperature of the end of recrystallization in the Ni–2Cr alloy.

In pure nickel, a change in the stored strain energy at the SMC structure stage does not affect recrystallization, while in Ni–2Cr the stored strain energy affects the size of the recrystallized grain: greater stored energy corresponds to a larger recrystallized grain size (Fig. 7).

CONCLUSIONS

1. During high-pressure torsion deformation, in the Ni–2Cr alloy, in contrast to pure nickel, a continuous increase in hardness is observed throughout the entire studied deformation range. Alloying with chromium significantly inhibits the transition to the SMC structure stage: in the Ni–2Cr alloy, the transition to the submicrocrystalline structure stage occurs at a true strain $e=8.5\pm 0.3$ – higher than for pure nickel ($e=5.3$).

2. Nickel alloying with chromium in an amount of 2 at. % does not lead to an increase in the submicrocrystalline structure dispersion; in both cases, after deformation with $e=9$, the microcrystallite size is (0.14 ± 0.01) μm .

3. Alloying with chromium affects the recrystallization temperature of nickel. The temperature, when the recrystallization of nickel with a submicrocrystalline structure begins, is 150 °C, and that of the Ni–2Cr alloy is 200 °C. The temperature of the intensive grain growth onset increases from 150 °C in pure nickel, to 300 °C in the Ni–2Cr alloy.

4. In the Ni–2Cr alloy, preliminary high-pressure torsion deformation and the energy stored during this, influ-

ence the recrystallized grain size. As a result of annealing of the Ni–2Cr alloy, in which the maximum energy was accumulated during deformation, the largest recrystallized grains, and high dimensional heterogeneity of the structure are observed, whereas in pure nickel, the dependence was not detected.

5. In both studied materials, submicrocrystalline structure recrystallization occurs through the accelerated growth of individual centres. This makes it impossible to obtain a submicrogranular recrystallized structure uniform in size.

REFERENCES

1. Valiev R.Z., Islamgaliev R.K., Alexandrov I.V. Bulk Nanostructured Materials from Severe Plastic Deformation. *Progress in Materials Science*, 2000, vol. 45, no. 2, pp. 103–189. DOI: [10.1016/S0079-6425\(99\)00007-9](https://doi.org/10.1016/S0079-6425(99)00007-9).
2. Valiev R.Z., Estrin Yu., Horita Z., Langdon T.G., Zehetbauer M.J., Zhu Yuntian. Producing Bulk Ultrafine-Grained Materials by Severe Plastic Deformation: Ten Years Later. *JOM*, 2016, vol. 68, pp. 1216–1226. DOI: [10.1007/s11837-016-1820-6](https://doi.org/10.1007/s11837-016-1820-6).
3. Cao Yang, Ni Song, Liao Xiaozhou, Song Min, Zhu Yuntian. Structural evolutions of metallic materials processed by severe plastic deformation. *Materials Science and Engineering: R: Reports*, 2018, vol. 133, pp. 1–59. DOI: [10.1016/j.mser.2018.06.001](https://doi.org/10.1016/j.mser.2018.06.001).
4. Valiev R.Z., Straumal B., Langdon T.G. Using Severe Plastic Deformation to Produce Nanostructured Materials with Superior Properties. *Annual Review of Materials Research*, 2022, vol. 52, pp. 357–382. DOI: [10.1146/annurev-matsci-081720-123248](https://doi.org/10.1146/annurev-matsci-081720-123248).
5. Zhilyaev A.P., Langdon T.G. Using High-Pressure Torsion for Metal Processing: Fundamentals and Applications. *Progress in Materials Science*, 2008, vol. 53, no. 6, pp. 893–979. DOI: [10.1016/j.pmatsci.2008.03.002](https://doi.org/10.1016/j.pmatsci.2008.03.002).
6. Degtyarev M., Chashchukhina T., Voronova L., Gaponseva T., Levit V. Evolution of microstructure and microtexture upon recrystallization of submicrocrystalline niobium. *International Journal of Refractory Metals and Hard Materials*, 2020, vol. 86, article number 105117. DOI: [10.1016/j.ijrmhm.2019.105117](https://doi.org/10.1016/j.ijrmhm.2019.105117).
7. Smirnova N.A., Levit V.I., Pilyugin V.P., Kuznetsov R.I., Davydova L.S., Sazonova V.A. Evolution of the structure of F.C.C. single crystals under high plastic deformations. *Fizika metallov i metallovedenie*, 1986, vol. 61, no. 6, pp. 1170–1177. EDN: [UCKEJT](https://www.edn.net/UCKEJT).
8. Gaponseva T.M., Degtyarev M.V., Pilyugin V.P., Chashchukhina T.I., Voronova L.M., Patselov A.M. Effect of temperature of HPT deformation and the initial orientation on the structural evolution in single-crystal niobium. *The Physics of Metals and Metallography*, 2016, vol. 117, no. 4, pp. 336–347. DOI: [10.1134/S0031918X16040062](https://doi.org/10.1134/S0031918X16040062).
9. Voronova L.M., Chashchukhina T.I., Gaponseva T.M., Patselov A.M., Pilyugin V.P., Degtyarev M.V. Effect of single-crystal orientation on the molybdenum structure and hardness upon high pressure torsion. *International Journal of Refractory Metals and Hard Materials*, 2022, vol. 103, article number 105754. DOI: [10.1016/j.ijrmhm.2021.105754](https://doi.org/10.1016/j.ijrmhm.2021.105754).

10. Chuvildeev V.N., Kopylov V.I., Nokhrin A.V., Makarov I.M., Gryaznov M.Yu. Recrystallization in microcrystalline copper and nickel produced by equal-channel angular pressing: III. Abnormal grain growth: a model. *The Physics of Metals and Metallography*, 2004, vol. 97, no. 1, pp. 1–6. EDN: [LIRFML](#).
11. Zhou Xin, Li Xiuyan, Lu Ke. Stabilizing nanograins in metals with grain boundary relaxation. *Scripta Materialia*, 2020, vol. 187, pp. 345–349. DOI: [10.1016/j.scriptamat.2020.06.047](#).
12. Zhou Xin, Li Xiuyan, Lu Ke. 70 nm: The most unstable grain size in Cu prepared by surface mechanical grinding treatment. *Nano Materials Science*, 2020, vol. 2, no. 1, pp. 32–38. DOI: [10.1016/j.nanoms.2020.01.001](#).
13. Zhou Xin, Li Xiuyan, Lu Ke. Enhanced thermal stability of nanograined metals below a critical grain size. *Science*, 2018, vol. 360, no. 6388, pp. 526–530. DOI: [10.1126/science.aar6941](#).
14. Degtyarev M.V., Voronova L.M., Gubernatorov V.V., Chashchukhina T.I. On the thermal stability of the microcrystalline structure in single-phase metallic materials. *Doklady Physics*, 2002, vol. 47, no. 9, pp. 647–650. DOI: [10.1134/1.1512627](#).
15. Voronova L.M., Degtyarev M.V., Chashchukhina T.I. Recrystallization of the ultradispersed structure of pure iron formed at different stages of the deformation-induced strain hardening. *The Physics of Metals and Metallography*, 2007, vol. 104, no. 3, pp. 262–273. DOI: [10.1134/S0031918X07090086](#).
16. Guo X.K., Luo Z.P., Li X.Y., Lu K. Plastic deformation induced extremely fine nano-grains in nickel. *Materials Science and Engineering: A*, 2021, vol. 802, article number 140664. DOI: [10.1016/j.msea.2020.140664](#).
17. Makarov A.V., Korshunov L.G. Metallophysical foundations of nanostructuring frictional treatment of steels. *The Physics of Metals and Metallography*, 2019, vol. 120, no. 3, pp. 303–311. DOI: [10.1134/S0031918X18120128](#).
18. Haessner F. *Recrystallization of Metallic Materials*. Stuttgart, Riederer-Verlag Publ., 1978. 293 p.
19. Degtyarev M.V., Pilyugin V.P., Chashchukhina T.I., Voronova L.M. Structure of iron deformed at 250°C by torsion under a pressure. *The Physics of Metals and Metallography*, 2019, vol. 120, no. 12, pp. 1193–1199. DOI: [10.1134/S0031918X19120044](#).
20. Trefilov V.I., Moiseev V.F., Pechkovskiy E.P., Gornaya I.D., Vasilev A.D. *Deformatsionnoe uprochnenie i razrushenie polikristallicheskih metallov* [Work Hardening and Fracture of Polycrystalline Metals]. Kiev, Naukova dumka Publ., 1987. 248 p.
21. Lee Seungwon, Horita Z. High-Pressure Torsion for Pure Chromium and Niobium. *Materials Transactions*, 2012, vol. 53, no. 1, pp. 38–45. DOI: [10.2320/matertrans.MD201131](#).
22. Zhang Yubin, Mishin O.V. Stored energy and recrystallized microstructures in nickel processed by accumulative roll bonding to different strains. *Materials Characterization*, 2017, vol. 129, pp. 323–328. DOI: [10.1016/j.matchar.2017.05.024](#).
23. Langdon T.G. Twenty-five years of ultrafine-grained materials: Achieving exceptional properties through grain refinement. *Acta Materialia*, 2013, vol. 61, no. 19, pp. 7035–7059. DOI: [10.1016/j.actamat.2013.08.018](#).
24. Dudova N., Belyakov A., Kaibyshev R. Recrystallization behavior of a Ni–20%Cr alloy subjected to severe plastic deformation. *Materials Science and Engineering: A*, 2012, vol. 543, pp. 164–172. DOI: [10.1016/j.msea.2012.02.067](#).

СПИСОК ЛИТЕРАТУРЫ

1. Valiev R.Z., Islamgaliev R.K., Alexandrov I.V. Bulk Nanostructured Materials from Severe Plastic Deformation // *Progress in Materials Science*. 2000. Vol. 45. № 2. P. 103–189. DOI: [10.1016/S0079-6425\(99\)00007-9](#).
2. Valiev R.Z., Estrin Yu., Horita Z., Langdon T.G., Zehetbauer M.J., Zhu Yuntian. Producing Bulk Ultrafine-Grained Materials by Severe Plastic Deformation: Ten Years Later // *JOM*. 2016. Vol. 68. P. 1216–1226. DOI: [10.1007/s11837-016-1820-6](#).
3. Cao Yang, Ni Song, Liao Xiaozhou, Song Min, Zhu Yuntian. Structural evolutions of metallic materials processed by severe plastic deformation // *Materials Science and Engineering: R: Reports*. 2018. Vol. 133. P. 1–59. DOI: [10.1016/j.mser.2018.06.001](#).
4. Valiev R.Z., Straumal B., Langdon T.G. Using Severe Plastic Deformation to Produce Nanostructured Materials with Superior Properties // *Annual Review of Materials Research*. 2022. Vol. 52. P. 357–382. DOI: [10.1146/annurev-matsci-081720-123248](#).
5. Zhilyaev A.P., Langdon T.G. Using High-Pressure Torsion for Metal Processing: Fundamentals and Applications // *Progress in Materials Science*. 2008. Vol. 53. № 6. P. 893–979. DOI: [10.1016/j.pmatsci.2008.03.002](#).
6. Degtyarev M., Chashchukhina T., Voronova L., Gapontseva T., Levit V. Evolution of microstructure and microtexture upon recrystallization of submicrocrystalline niobium // *International Journal of Refractory Metals and Hard Materials*. 2020. Vol. 86. Article number 105117. DOI: [10.1016/j.ijrmhm.2019.105117](#).
7. Смирнова Н.А., Левит В.И., Пилюгин В.П., Кузнецов Р.И., Давыдова Л.С., Сазонова В.А. Эволюция структуры ГЦК монокристаллов при больших пластических деформациях // *Физика металлов и металловедение*. 1986. Т. 61. № 6. С. 1170–1177. EDN: [UCKEJT](#).
8. Гапонцева Т.М., Дегтярев М.В., Пилюгин П.В., Чащухина Т.И., Воронова Л.М., Пацелов А.М. Влияние температуры деформации в наковальнях Бриджмена и исходной ориентировки на эволюцию структуры монокристаллического ниобия // *Физика металлов и металловедение*. 2016. Т. 117. № 4. С. 349–361. DOI: [10.7868/S0015323016040069](#).
9. Voronova L.M., Chashchukhina T.I., Gapontseva T.M., Patselov A.M., Pilyugin V.P., Degtyarev M.V. Effect of single-crystal orientation on the molybdenum structure and hardness upon high pressure torsion // *International Journal of Refractory Metals and Hard Materials*. 2022. Vol. 103. Article number 105754. DOI: [10.1016/j.ijrmhm.2021.105754](#).
10. Чувильдеев В.Н., Копылов В.И., Нохрин А.В., Макаров И.М., Грязнов М.Ю. Рекристаллизация в микрокристаллических меди и никеле, полученных методами РКУ-прессования. III. Аномальный рост зерен. Модель // *Физика металлов и металловедение*. 2004. Т. 97. № 1. С. 3–8. EDN: [OXKNZJ](#).

11. Zhou Xin, Li Xiuyan, Lu Ke. Stabilizing nanograins in metals with grain boundary relaxation // Scripta Materialia. 2020. Vol. 187. P. 345–349. DOI: [10.1016/j.scriptamat.2020.06.047](https://doi.org/10.1016/j.scriptamat.2020.06.047).
12. Zhou Xin, Li Xiuyan, Lu Ke. 70 nm: The most unstable grain size in Cu prepared by surface mechanical grinding treatment // Nano Materials Science. 2020. Vol. 2. № 1. P. 32–38. DOI: [10.1016/j.nanoms.2020.01.001](https://doi.org/10.1016/j.nanoms.2020.01.001).
13. Zhou Xin, Li Xiuyan, Lu Ke. Enhanced thermal stability of nanograined metals below a critical grain size // Science. 2018. Vol. 360. № 6388. P. 526–530. DOI: [10.1126/science.aar6941](https://doi.org/10.1126/science.aar6941).
14. Дегтярев М.В., Воронова Л.М., Губернаторов В.В., Чашухина Т.И. О термической стабильности микрокристаллической структуры в однофазных металлических материалах // Доклады Академии наук. 2002. Т. 386. № 2. С. 180–183. EDN: [MPLCLS](https://www.edn.net/MPLCLS).
15. Воронова Л.М., Дегтярев М.В., Чашухина Т.И. Рекристаллизация ультрадисперсной структуры чистого железа, сформированной на разных стадиях деформационного наклепа // Физика металлов и металловедение. 2007. Т. 104. № 3. С. 275–286. EDN: [IASANZ](https://www.edn.net/IASANZ).
16. Guo X.K., Luo Z.P., Li X.Y., Lu K. Plastic deformation induced extremely fine nano-grains in nickel // Materials Science and Engineering: A. 2021. Vol. 802. Article number 140664. DOI: [10.1016/j.msea.2020.140664](https://doi.org/10.1016/j.msea.2020.140664).
17. Макаров А.В., Коршунов Л.Г. Металлофизические основы наноструктурирующей фрикционной обработки сталей // Физика металлов и металловедение. 2019. Т. 120. № 3. С. 327–336. DOI: [10.1134/S0015323018120124](https://doi.org/10.1134/S0015323018120124).
18. Haessner F. Recrystallization of Metallic Materials. Stuttgart: Riederer-Verlag, 1978. 293 p.
19. Дегтярев М.В., Пилюгин В.П., Чашухина Т.И., Воронова Л.М. Структура железа, деформированного кручением под давлением при 250°C // Физика металлов и металловедение. 2019. Т. 120. № 12. С. 1292–1298. DOI: [10.1134/S0015323019120040](https://doi.org/10.1134/S0015323019120040).
20. Трефилов В.И., Моисеев В.Ф., Печковский Э.П., Горная И.Д., Васильев А.Д. Деформационное упрочнение и разрушение поликристаллических металлов. Киев: Наукова думка, 1987. 248 с.
21. Lee Seungwon, Horita Z. High-Pressure Torsion for Pure Chromium and Niobium // Materials Transactions. 2012. Vol. 53. № 1. P. 38–45. DOI: [10.2320/matertrans.MD201131](https://doi.org/10.2320/matertrans.MD201131).
22. Zhang Yubin, Mishin O.V. Stored energy and recrystallized microstructures in nickel processed by accumulative roll bonding to different strains // Materials Characterization. 2017. Vol. 129. P. 323–328. DOI: [10.1016/j.matchar.2017.05.024](https://doi.org/10.1016/j.matchar.2017.05.024).
23. Langdon T.G. Twenty-five years of ultrafine-grained materials: Achieving exceptional properties through grain refinement // Acta Materialia. 2013. Vol. 61. № 19. P. 7035–7059. DOI: [10.1016/j.actamat.2013.08.018](https://doi.org/10.1016/j.actamat.2013.08.018).
24. Dudova N., Belyakov A., Kaibyshev R. Recrystallization behavior of a Ni–20%Cr alloy subjected to severe plastic deformation // Materials Science and Engineering: A. 2012. Vol. 543. P. 164–172. DOI: [10.1016/j.msea.2012.02.067](https://doi.org/10.1016/j.msea.2012.02.067).

Термическая стабильность субмикрокристаллической структуры, сформированной методом «сдвиг под давлением» в Ni и сплаве Ni–2 % Cr

© 2023

Карамышев Константин Юрьевич, инженер лаборатории прецизионных сплавов и интерметаллидов
Институт физики металлов имени М.Н. Михеева Уральского отделения РАН, Екатеринбург (Россия)

E-mail: karamyshev.imp@mail.ruORCID: <https://orcid.org/0009-0000-1752-2284>

Поступила в редакцию 23.06.2023

Принята к публикации 21.11.2023

Аннотация: Основной проблемой субмикрокристаллических (СМК) материалов, сформированных в результате большой пластической деформации, является их термическая стабильность. Большая запасенная энергия и формирование в структуре сильно разориентированных микрокристаллитов ведет к уменьшению температуры начала рекристаллизации и, как следствие, возможно, к снижению стабильности структуры. В работе проведена большая пластическая деформация методом «сдвиг под давлением», а также отжиг чистого никеля и его сплава, содержащего 2 ат. % хрома. Исследование структуры как деформированного, так и отожженного материала осуществляли методами сканирующей и просвечивающей электронной микроскопии. Анализ зависимости твердости от квадратного корня из истинной деформации совместно с анализом структурных изменений позволил выделить границы стадий структурных состояний. Запасенную при деформации энергию оценивали с помощью дифференциально-сканирующей калориметрии по количеству поглощенной тепловой энергии. Исследовано поведение материалов при отжиге в зависимости от запасенной энергии деформации на стадии СМК-структуры. В чистом никеле выделены три стадии структурных состояний: ячеистой, смешанной и СМК-структуры, тогда как в сплаве, содержащем 2 ат. % Cr, стадия ячеистой структуры не зафиксирована. Обнаружено снижение запасенной энергии деформации на стадии СМК-структуры для обоих материалов. Легирование никеля 2 ат. % хрома повышает термическую стабильность, что проявляется в повышении температуры начала интенсивного роста зерна на 150 °С. Величина запасенной энергии деформации оказывает влияние на рост зерна в сплаве с содержанием хрома 2 ат. %, тогда как в чистом никеле влияние не зафиксировано. В сплаве Ni–Cr большая запасенная энергия соответствует большему размеру рекристаллизованного зерна.

Ключевые слова: никель; сплав Ni–Cr; сдвиг под давлением; субмикрокристаллическая структура; запасенная энергия деформации.

Благодарности: Работа выполнена в рамках государственного задания Минобрнауки России (тема «Давление», № 122021000032-5).

Автор благодарит сотрудников Института физики металлов имени М.Н. Михеева УрО РАН: кандидата физико-математических наук, заведующего лабораторией физики высоких давлений В.П. Пилюгина за проведение деформации, а также доктора технических наук, заведующего отделом прецизионной металлургии и технологий обработки давлением М.В. Дегтярева за обсуждения результатов.

Работа выполнена с использованием оборудования ЦКП «Испытательный центр нанотехнологий и перспективных материалов» ИФМ УрО РАН.

Статья подготовлена по материалам докладов участников XI Международной школы «Физическое материаловедение» (ШФМ-2023), Тольятти, 11–15 сентября 2023 года.

Для цитирования: Карамышев К.Ю. Термическая стабильность субмикроструктурной структуры, сформированной методом «сдвиг под давлением» в Ni и сплаве Ni-2 % Cr // Frontier Materials & Technologies. 2023. № 4. С. 41–51. DOI: 10.18323/2782-4039-2023-4-66-4.

Combination of cryogenic deformation and electropulse processing as a way to produce ultrafine-grain metals

© 2023

*Mikhail V. Markushev**, Doctor of Sciences (Engineering), senior researcher, Head of laboratory

Elena V. Avtokratova, PhD (Engineering), senior researcher

*Aigul Kh. Valeeva*¹, PhD (Engineering), researcher

*Irshat Sh. Valeev*², PhD (Engineering), researcher

*Rafis R. Ilyasov*³, junior researcher

*Stanislav V. Krymsky*⁴, PhD (Engineering), Head of laboratory

Oleg Sh. Sitdikov, PhD (Physics and Mathematics), senior researcher

Institute for Metals Superplasticity Problems of RAS, Ufa (Russia)

*E-mail: mvmark@imsp.ru

¹ORCID: <https://orcid.org/0000-0003-4305-4538>

²ORCID: <https://orcid.org/0009-0002-5162-7324>

³ORCID: <https://orcid.org/0000-0003-0195-1206>

⁴ORCID: <https://orcid.org/0000-0002-1534-3239>

Received 15.08.2023

Accepted 01.12.2023

Abstract: The data of a comparative analysis of the structure and hardness of pure metals with a face-centered cubic lattice – aluminum, nickel and copper, subjected to complex thermomechanical treatment (TMT), including isothermal cryogenic rolling at liquid nitrogen temperature and subsequent high-density electropulse treatment (EPT) were presented. The main stages, features and advantages of TMT, which first ensure strong work hardening of the processed material due to deformation at low temperatures and then its ultra-fast contact electropulse heating up to a specified temperature, were considered. A multi-level analysis of the metals structure evolution due to TMT was carried out using modern methods of scanning electron microscopy and X-ray diffractometry, recording a wide range of its linear and angular parameters. The kinetics and nature of the processes of the metals structure evolution under cryogenic rolling and EPT, their driving forces and controlling factors, as well as general patterns and temperature intervals of activation of the deformation structure recovery and recrystallization influenced by an electric pulse are identified and discussed. Based on the results of the analysis of the structural and mechanical behaviour of metals, it was concluded that the combination of severe plastic cryogenic deformation and a single-step treatment with ultrashort alternating current pulses is an effective way to obtain semi-finished products with controlled parameters of their structure and properties, including high-strength ultrafine-grain rolled products. At that the phenomenology and nature of the strengthening/softening of metals during cryogenic rolling and subsequent electropulsing are similar to those observed under cold rolling and furnace annealing.

Keywords: FCC metals; cryogenic deformation; cryogenic rolling; electric pulse treatment; ultrafine-grain structure.

Acknowledgments: The work was carried out within the framework of the state assignment of the Federal State Budgetary Institution of Science Institute for Metals Superplasticity Problems of the Russian Academy of Sciences.

Experimental studies were carried out on the base of the Collaborative Access Centre “Structural, Physical and Mechanical Studies of Materials” of the RAS.

For citation: Markushev M.V., Avtokratova E.V., Valeeva A.Kh., Valeev I.Sh., Ilyasov R.R., Krymsky S.V., Sitdikov O.Sh. Combination of cryogenic deformation and electropulse processing as a way to produce ultrafine-grain metals. *Frontier Materials & Technologies*, 2023, no. 4, pp. 53–62. DOI: 10.18323/2782-4039-2023-4-66-5.

INTRODUCTION

The development of effective industrial methods for increasing the service properties of metals and alloys, through the controlled strain and thermal effects on them leading, among other things, to a decrease in the size of crystallites (grains and subgrains) to nanosizes [1–3] is an urgent task of modern materials science. Among these methods are thermomechanical treatment (TMT) based on a combination of cryogenic rolling (CR) and subsequent electric pulse treatment (EPT) [4–6] and ensuring at least the formation of an ultrafine-grained (UFG) structure (with a grain size of less than 10 μm) in the processed material.

Currently, the effect of temperature decrease during the transition from cold (at room temperature) to cryogenic (at temperatures below 120 K) deformation on the structure

and mechanical behaviour of metallic materials has been studied quite well. Generally, it is described as their extra strengthening due to the suppression of dynamic recovery, and an increase in the dislocation density [7–9]. Moreover, in a number of studies, for example in [9–11], strengthening is also associated with crystallite refinement.

At the same time, the effect of electric current on the deformation structure of metals and alloys has been studied to a much lesser extent, especially when using short-time high-density current pulses [12], and in relation to cryodeformed materials. Most investigations in this area connected with direct current, and with its long-term (up to several hours) exposure [13; 14]. Carrying out such experiments was primarily caused by the needs to study the peculiarities of the influence of contact electric heating on the structural and mechanical behaviour of objects during their direct deformation

processing, as well as by the search for a less expensive alternative to their non-contact (furnace, induction) heating. The main result of these studies includes a convincing demonstration of high efficiency when using electric heating of blanks for deformation and post-deformation heat treatment [13; 14]. The papers [15–17] describe the so-called electroplastic effect, which “facilitates” the process of metal plastic flow, when directly exposed to electric current, and propose options for interpreting its nature.

As a result of a few studies, where short-time electric pulse exposure was implemented, it was found that the activation of the recovery, polygonization and recrystallization processes [18] in pre-strained metal materials, improves a number of their technological properties [15; 19; 20]. The reason is obvious – a decrease in strength, and an increase in ductility due to a decrease in the structure defectiveness and an increase in its dispersity [2; 18]. However, there is some literature data with an opposite trends in structure changes, indicating the multidirectionality of the EPT effect on the structure and properties of materials. For example, in [21] it was noted the suppression of recrystallization in steels during EPT.

There is a belief that the softening of work-hardened material during electro-induced heating is accompanied by the so-called “electron wind” effect [22] contributing to an increase in the mobility of dislocations, and the accelerated formation of recrystallization centres. While the latter phenomenon can be explained within the framework of classical ideas on the influence of heating rate on nuclei formation during recrystallization [18], the nature of the former still does not have a clear physical interpretation. Another EPT character feature is the skin-effect [20; 22]. It is caused by the uneven distribution of electric and heat flows inside and on the surface of the blank (conductor) under the electrical impulse action. As a result, the structure formed on the surface may differ significantly from the structure inside the blank. In this case, the degree of grain size nonhomogeneity, and the depth of the subsurface layer directly depend on the nature of the material being processed, the shape and cross-sectional area of the conductor, as well as on the EPT parameters, in particular on the pulse energy [20; 22].

From general point of view, TMT based on a combination of CR and EPT should be the most popular and effective for pure metals and solid solutions. The reason is that in such objects, there are no dispersed particles of second phases, which act as the main factor in controlling the structure and strength of alloys through limiting the rearrangement of dislocations in them and the growth (migration of boundaries) of crystallites [18]. During TMT of metals and solid solutions, their structuring is controlled by dislocation reactions, which are often determined by stacking fault energy (SFE). In our previous works [23–26], we have already analysed and partially published data on the phenomenology and nature of the structural-mechanical behaviour of various pure fcc metals, subjected to rolling up to high strains at liquid nitrogen temperature, and subsequent single-step EPT with different integral current densities. At the same time, in the papers mentioned, the analysis of the data obtained was carried out separately for each metal, and the overall picture of changes in their structure and properties occurring during TMT was not presented.

The purpose of this work is to supplement the published data, identify common patterns, and discuss the nature of

the structural and mechanical behaviour of three fcc metals – Al, Cu and Ni during cryogenic rolling, and subsequent electric pulse treatment, taking into account the differences in their melting temperature and stacking fault energy value.

METHODS

Al (99.99 %), Ni (99.5 %), and Cu (99.99 %) were used as research materials. Plates cut from forged and annealed coarse-grained billets, were subjected to cryogenic deformation to a total strain of 90 % ($\epsilon=2.3$) on a laboratory isothermal six-roll mill with a removable work rolls diameter of 64 mm. Isothermal rolling conditions were ensured by pre-cooling the work rolls and blanks in a bath of liquid nitrogen for 1 h. The deformed blanks were cooled after each pass and the rolls – after 4–5 passes. The absence of nitrogen boiling was the criterion for achieving the required temperature. The deformation temperature of Ni, Cu and Al was about 0.05, 0.06 and 0.08 of their melting point, consequently. The strain per pass did not exceed 7 % at a rolling speed of about 100 mm/s. The rolled strips were stored in a freezer at a temperature of -18 °C. The duration of their room temperature annealing during the subsequent TMT stage, as well as during the objects fabrication and analysis of the structure and properties of metals, was recorded to control the degree of their softening.

Using a MIU-20 device, EPT was carried out on flat samples with a gauge part of 3×4 mm cut on an electric spark machine from cryo-rolled strips 0.4 mm thick along the direction of their rolling. The selected thickness guaranteed the absence of skin effect in the working area of samples, made of all metals and the uniform distribution of thermal and electrical flows over their cross section. The samples were fixed in clamps served as current conductors during the discharge of the capacitor bank. The current pulse was recorded using a Rogowski coil, and an AKTAKOM ASK-3107 storage oscilloscope. As the pulse energy criterion, the integral current density K_j was taken, which was calculated using the following equation [22]:

$$K_j = \int_0^\tau j^2 \partial\tau = \frac{k^2}{S^2} \cdot \frac{A_1^3}{A_2} \cdot \frac{\tau}{4 \ln(A_1 / A_3)},$$

where j is the current density;

τ is the pulse duration;

k is the Rogowski coil coefficient;

S is the cross-sectional area of the sample;

A_1 , A_2 and A_3 are the first, second, and third amplitudes of the damped pulse, respectively.

During EPT, the sample was heated according to the Joule – Lenz law. Due to pulsed thermoelectric action of about $\sim 10^{-4}$ s, reliable measurement of sample heating temperature (T_h) was a difficult technical point. In this regard, as recommended in [22], this temperature was determined by the calculation method, assuming that

$$\frac{j^2}{\sigma_e} = \rho c \frac{\partial T}{\partial t},$$

where ρ , c , σ_e are the density, heat capacity and electrical conductivity of the metal being processed, respectively.

By integrating this equation, the authors obtained the dependences of the heating temperature of metals on the integral pulse current density.

The microstructure of metals was analysed in the rolling plane by the EBSD method using a TESCAN MIRA 3 LMH scanning electron microscope, and the HKL Channel 5 software package. Diffraction patterns were indexed by 6 Kikuchi lines with a scanning step of no more than 0.5 μm . A grain-boundary angle of 15° was used as a criterion for dividing into low- and high-angle boundaries (LABs and HABs). The sizes of grains and subgrains (d_g and d_{sg}) were determined by the equivalent diameter method. The average grain-boundary angle of intercrystalline boundaries (Θ_{av}) and the fraction of high-angle and twin boundaries (F_{hab} and F_{Σ}) were determined from the grain-boundary angle spectra. In this case, boundaries with $\Theta < 2^\circ$ were not taken into account. The fraction of recrystallized grains (F_{rec}) was determined as the ratio of the area they occupy to the area of the map.

X-ray diffraction analysis (XRD) was carried out on a DRON-4-07 diffractometer in Cu-K α radiation at a voltage of 40 kV and a current of 30 mA with a wavelength of $\lambda = 1.54418 \text{ \AA}$. The scanning was carried out with a rotating sample, a step of 0.1° and an exposure time of 4 s, using a graphite monochromator on a diffracted beam. The root-mean-square microstrain of the crystal lattice ($\langle \epsilon^2 \rangle^{1/2}$) and the size of coherent domain size (D) were calculated by full-profile analysis in the MAUD software package. The dislocation density (ρ) was determined as

$$\rho = \frac{2\sqrt{3}\langle \epsilon^2 \rangle^{1/2}}{D \times b},$$

where b is the Burgers vector.

The strength of metals was assessed by the microhardness level determined by the Vickers method using 10 measurements on an MVDM 8 AFFRY hardness tester at loads of 1 and 0.5 N and duration of their application of 10 s in the central part of the rolled strips and samples subjected to EPT.

Structure analysis and assessment of the hardness of metals were carried out in laboratory conditions. In this case, the total duration of cryo-rolled samples at room temperature required for preparation of objects (samples for EPT) and their structural and mechanical analysis did not exceed 24 h.

RESULTS

Tables 1 and 2 show the results of assessing the linear and angular parameters of the structure of Al, Cu, and Ni, as well as their hardness recorded after cryogenic rolling and EPT with different integral current densities. Even a cursory glance at these data allows concluding that the implemented TMT scheme makes it possible to effectively control the processes of deformation structure transformations of all studied metals, to comparatively easy change its type and parameters, and most importantly, to ensure the achievement of its main goal. In particular, to obtain sheets in three main structural states: 1) with a developed dislocation-cellular structure with nanosized cells; 2) with

a homogeneous UFG structure with a grain size of 1–3 μm ; 3) with an “intermediate” composite structure with controlled dislocation density and ratios of the main components, as well as low- and high-angle boundaries.

As should be expected, due to the lowest melting temperature (the highest homologous CR temperature), the least dispersed (with the largest crystallite sizes) structure of all types was recorded in aluminium (Table 1). Such a result was caused by the formation during cryogenic rolling of coarsest and the least developed cellular structure with an integral dislocation density almost an order of magnitude lower than in other metals (Table 2). Another fact that attracted attention was that with an increase in the pulse energy (heating temperature) during EPT, the hardness of cryo-rolled metals noticeably decreased. At the same time, the almost twofold softening observed in the studied range of integral current densities was caused primarily by the activation of recrystallization processes (see changes in F_{rec} and F_{hab} in Table 1 and dislocation densities in Table 2).

Despite the differences in the structure types and parameters and in the level of strength of metals recorded at various TMT stages, there was a similarity in their behaviour during EPT. Thus, the dependences of the hardness of all cryo-rolled metals on the homologous temperature of their heating turned out to be qualitatively similar (Fig. 1). These dependences consist of three characteristic temperature regions indicating a similar nature and kinetics of the development of thermally activated processes under electric pulsing. In the first region, the deformation structures were relatively stable and retained the maximum strengthening effect recorded after rolling. In the second and third regions, the metals became softer. In the second region, intensive softening was occurred in a narrow temperature range. In the third region, on the opposite, it was observed weak softening, leading to an almost complete loss of deformation and structural (due to grain refinement) hardening by cryorolled metals.

It is noteworthy that for all three metals, the boundaries between the marked regions were quite close, although the parameters of their deformation structure and the level of stacking fault energy were different. Thus, the deformation structure of Ni was retained after EPT up to the temperature of heating the sample to 0.33 T_m with its SFE of about 90 mJ/m^2 , Cu – up to 0.38 T_m with the SFE of about 70 mJ/m^2 , and Al – up to 0.42 T_m at SFE of about 200 mJ/m^2 . To define more exactly, the SFE values of metals are given based on the averaged values published in [27–29]. Intense softening of Ni was completed at 0.36 T_m , Cu and Al – at 0.42–0.45 T_m . At first glance, these data indicated the absence of SFE influence on the structural and mechanical behaviour of metals during TMT. However, in reality, this effect took place in the form of structural manifestations of the processes of accumulation of internal stresses during rolling and their relaxation during EPT. Thus, when rolling aluminium, its highest SFE level contributed to the least accumulation of dislocations and lattice distortions among the metals studied due to the easiest dynamic recovery. During EPT, the same factor ensured the development of polygonization in aluminium, which preceded recrystallization. Meanwhile in copper and nickel there were observed an active twinning, resulting in new a smaller size of recrystallized grains due to the lower mobility of twin boundaries.

Table 1. EBSD data on metals structure parameters after cryorolling to 90 % and further single electropulsing with different energies
Таблица 1. Параметры структуры криокатанных до 90 % и подвергнутых однократной ЭИО с различной энергией импульса металлов по данным EBSD-анализа

Metal	State	K_j , $10^4 \text{ A}^2/\text{mm}^4$	T_h , K	T_h/T_m	d_{sg} , μm	d_g , μm	F_{rec} , %	Θ_{av} , deg	F_{hab} , %	F_{Σ} , %
Al	CR	–	293	0.31	2.0±0.3	4.0±0.4	3	7	11	–
	EPT	1.0	398	0.42	2.0±0.4	4.0±0.8	6	16	23	–
		1.2	423	0.45	5.0±0.3	19.0±1.1	66	31	76	–
		2.9	623	0.67	14.0±0.5	53.0±1.3	76	32	74	–
Ni	CR	–	293	0.17	0.2±0.1	2.5±0.5	3	7	7	<1
	EPT	1.0	573	0.33	1.3±0.2	1.9±0.4	5	5	4	44
		1.1	593	0.34	2.8±0.6	3.2±0.6	92	47	92	42
		1.6	943	0.55	4.4±1.0	4.7±0.9	95	48	92	41
Cu	CR	–	293	0.20	0.3±0.1	0.7±0.2	15	17	33	2
	EPT	3.5	513	0.38	0.4±0.1	0.9±0.1	37	21	42	5
		3.8	573	0.42	0.8±0.2	1.0±0.2	86	39	79	22
		6.8	923	0.68	1.2±0.2	1.3±0.3	96	43	88	30

Note. K_j is integral current density;
 T_h/T_m is heating/melting temperature;
 d_g and d_{sg} are grain and subgrain size, respectively;
 F_{rec} , F_{hab} and F_{Σ} are fraction of recrystallized grains, high-angle boundaries and twin boundaries, respectively;

Θ_{av} is average angle of grain boundary misorientation.

Примечание. K_j – интегральная плотность тока;

T_h/T_m – температура нагрева/плавления;

d_g и d_{sg} – размер зерна и субзерна соответственно;

F_{rec} , F_{hab} и F_{Σ} – доля рекристаллизованных зерен, высокоугловых границ и двойниковых границ соответственно;

Θ_{av} – средний угол разориентировки межкристаллитных границ.

Data in Table 2 also follow that the maximum strain energy was stored in nickel, the homologous rolling temperature of which was the lowest, and the SFE level was close to copper. Therefore, to activate recrystallization in nickel, processing with the minimum pulse energy for three metals was required. As a result, after EPT, even with an energy of only $K_j=1.1 \times 10^4 \text{ A}^2/\text{mm}^4$, it was possible to fix in nickel a grain structure close in degree of dispersion to copper, and treated with a current pulse with an integral density almost 4 times higher (Table 1). At the same time, it should be noted that EPT of copper with $K_j=3.5 \times 10^4 \text{ A}^2/\text{mm}^4$ did not lead to significant changes in the linear parameters of the structure and hardness with a simultaneous increase in the proportion of HABs and recrystallized grains against the background of a twofold decrease in internal lattice distortions. At the same time, the homologous rolling temperature of copper was slightly higher, and occupied an intermediate position among the metals studied, and its SFE was slightly lower than in nickel. Structural changes during EPT detected in copper were caused by the greater intensity of the processes of static recovery and recrystallization,

leading to a more significant increase in the structure equilibrium, and to a significant compensation of the softening effect by the strengthening one, caused by the formation of submicron-sized grains. In other words, probably the more active formation and improvement of the structure of ultrafine crystallites, and their boundaries were the reason for the less intensive softening of cryorolled copper in this EPT area. When increasing current density to $K_j=3.8 \times 10^4 \text{ A}^2/\text{mm}^4$, the stored deformation energy (and hardness) of copper, similar to nickel and aluminium, sharply decreased due to the transformation of the subgrain structure into a partially recrystallized one with significantly larger subgrains (Table 1). This structure was also characterized by almost complete levelling of lattice microdistortions, due to a decrease in the dislocation density to an equilibrium level (Table 2). A further increase in the pulse energy upon transition to the third EPT temperature range, led to the recrystallization in the full volume of the processed materials accompanied by subsequent normal growth of recrystallized grains (Table 1), which was able to occur even with an extremely short time of exposure of electric current.

Table 2. XRD data on structure parameters and hardness of metals after cryorolling to 90 % and further single electropulsing with different energies

Таблица 2. Параметры структуры по данным РСА и твердость криокатаных до 90 % и подвергнутых однократной ЭИО с различной энергией импульса металлов

Metal	State	K_j , $10^4 \text{ A}^2\text{s}/\text{mm}^4$	T_h , К	T_h/T_m	ρ , 10^{14} m^{-2}	$\langle \varepsilon^2 \rangle^{1/2}$, %	D , nm	HV
Al	CR	–	293	0.31	0.5	0.060±0.001	340±4	49±5
	EPT	1.0	398	0.42	<0.01	0.001±0.001	156±2	49±4
		1.2	423	0.45			96±3	31±4
		2.9	623	0.67			123±4	26±5
Ni	CR	–	293	0.17	3.5	0.165±0.002	68±4	246±8
	EPT	1.0	573	0.33	<0.01	0.001±0.001	75±3	242±7
		1.1	593	0.34			129±2	101±8
		1.6	943	0.55			141±2	91±9
Cu	CR	–	293	0.20	4.5	0.186±0.004	57±2	152±7
	EPT	3.5	513	0.38	<0.1	0.001±0.001	48±2	143±8
		3.8	573	0.42			67±4	96±7
		6.8	923	0.68			100±4	81±8

Note. K_j is integral current density; T_h/T_m is heating/melting temperature; ρ is dislocation density; $\langle \varepsilon^2 \rangle^{1/2}$ is root-mean-square microstrain of crystal lattice; D is coherent domain size.

Примечание. K_j – интегральная плотность тока; T_h/T_m – температура нагрева/плавления; ρ – плотность дислокаций; $\langle \varepsilon^2 \rangle^{1/2}$ – среднеквадратичная микродеформация кристаллической решетки; D – размер областей когерентного рассеяния.

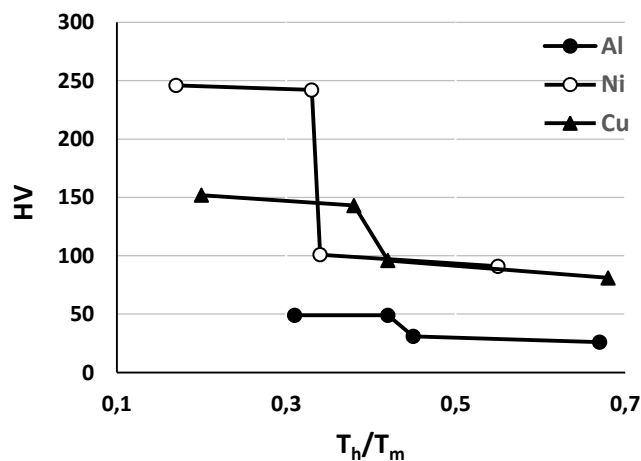


Fig. 1. Changes in hardness of cryorolled metals after room temperature annealing and further heating to a T_h temperature due to electropulsing
Рис. 1. Изменения твердости криокатаных металлов, вызванные отжигом при комнатной температуре и ЭИО с нагревом до температуры T_h

DISCUSSION

The generalized character of behaviour of cryodeformed metals during EPT can be represented as follows. In the first temperature range, the main mechanism for their structure transformation was static recovery, which led to a decrease in the defectiveness of the deformation structure and its improvement. Along with the recovery, static recrystallization developed locally, and prevailed in the second temperature range. As a result, when heating nonequilibrium work-hardened metals within this range, their predominant dislocation-cellular structure was almost completely replaced by an equilibrium grain-type one, which was accompanied by a decrease in their strength almost to the level of undeformed metal. In the third range there was occurred normal grain growth, which led to further softening of metals due to the loss of the Hall–Petch effect caused by the refinement of recrystallized grains [18].

Compared to the continuous static recrystallization, observed during furnace annealing of metals highly deformed at room temperature [2; 18], during EPT in the range of 0.3–0.4 T_m , the main process of transforming the deformation structure of cryorolled metals, was a transition process of the structure improvement by the *in situ* type, controlled by a recovery, to normal grain growth. A sharp drop in hardness at the boundary of the first and second temperature ranges in Fig. 1 was caused by two main reasons. On the one hand, the growth of individual nanosized crystallites formed during rolling, which could potentially serve as recrystallization centres, intensified. On the other hand, due to the structural heterogeneity inherent in the deformed state and the different recrystallization kinetics in each individual grain, grains formed *in situ* in the deformed structure acquired the potential for accelerated growth. When the pulse energy/heating temperature, during EPT, reached a certain “threshold” level, some grains were “freed” from defects, which activated their growth, while neighbouring grains still “occupied” with high-densities of dislocations and, could undergo polygonization or twinning. The grain growth was the result of migration of their boundaries, which occurred under the influence of driving forces caused by previous deformation. The migrated boundaries of growing grains absorbed the crystal structure defects (vacancies, dislocations and other boundaries) [18], which led to a decrease in the internal energy of the system and, as a consequence, to a decrease in the metal strength level achieved due to rolling.

It should also be noted, that the boundaries of new grains formed as a result of severe low-temperature deformation had increased specific energy, and accordingly, the ability to migrate more quickly during EPT. In contrast to such boundaries, low-energy low-angle boundaries of both dynamically and statically formed cells had less mobility. As a result, at low heating energies/temperatures, migration of the boundaries of recrystallized grains predominantly took place towards the deformed matrix. At higher energies, in particular, after the deformed structure disappearance (the end of the transition from the polygonization and recrystallization processes to normal grain growth), grain boundaries continued to migrate under the influence of a driving force, caused by a decrease in

the local radius of their curvature. This process was accompanied by an increase in grain sizes due to their normal growth [18].

Based on the above, and considering the results of few investigations [5; 10; 18; 26], one can conclude that the processes occurring during EPT of cryorolled fcc metals are close to the ones occurring at static annealing of cold-strained materials: static recovery, continuous static recrystallization, and grain growth. At that, the short duration (pulse nature) of the thermal effect on the deformed metal during EPT was compensated by the high applied energy. Since recovery and static recrystallization are controlled by self-diffusion [18; 30], then, according to the Arrhenius law, even a slight increase in the EPT temperature/energy should lead to a noticeable increase in the rate of these processes, and consequently, to a decrease in the time of their completion, which is what we observed in the experiments.

Thus, the data obtained cannot testify for either the presence or absence of the “electron wind” effect, which could have a noticeable impact on the structural and mechanical behaviour of cryorolled fcc metals during high-density electropulsing. All experimental results found and discussed can be explained from the well-known, classical positions developed for conventionally work-hardened materials, subjected to annealing without exposure to electric current.

CONCLUSIONS

1. Thermomechanical treatment based on a combination of severe plastic deformation at cryogenic temperatures, and subsequent high-density electric pulsing, is an effective way to produce sheets of pure fcc metals with controlled structure, and strength parameters, including those with homogeneous UFG recrystallized structure with a grain size of 1–3 μm , and a developed dislocation-cellular structure with nanosized cells.

2. The processes of softening of cryorolled fcc metals under electric pulse exposure to high-density currents, are similar in nature and kinetics and are characterized by the presence of clearly defined three energy/heating temperature intervals. In the first of them, EPT has virtually no effect on the level of metal hardness after cryogenic rolling to high strains. In the second one, starting from a certain “threshold” value of the integral current density K_j , corresponding to the calculated temperature equal to 0.33 T_m for nickel, 0.38 T_m for copper and 0.42 T_m for aluminium, their hardness is significantly reduced, due to the activation of static recrystallization of the deformation structure. When the heating temperature exceeded the values equal to 0.36 T_m for nickel, and 0.42–0.45 T_m for copper and aluminium, the third EPT region is observed, which accompanied by low hardness loss to the values corresponding to the original undeformed states, caused by the recrystallized grain growth.

3. The processes of transformation of a highly work-hardened structures during EPT of cryorolled fcc metals, are close to the processes occurring during static annealing of cold-deformed materials – static recovery, continuous static recrystallization and grain growth.

REFERENCES

- Estrin Y., Vinogradov A. Extreme grain refinement by severe plastic deformation: A wealth of challenging science. *Acta Materialia*, 2013, vol. 61, no. 3, pp. 782–817. DOI: [10.1016/j.actamat.2012.10.038](https://doi.org/10.1016/j.actamat.2012.10.038).
- Zhilyaev A.P., Pshenichnyuk A.I., Utyashev F.Z., Raab G.I. *Superplasticity and Grain Boundaries in Ultrafine-Grained Materials*. Amsterdam, Elsevier Publ., 2020. 416 p.
- Edalati K., Bachmaier A., Beloshenko V.A., Beygelzimer Y., Blank V.D., Botta W.J. Nanomaterials by severe plastic deformation: review of historical developments and recent advances. *Materials Research Letters*, 2022, vol. 10, no. 4, pp. 163–256. DOI: [10.1080/21663831.2022.2029779](https://doi.org/10.1080/21663831.2022.2029779).
- Pan Dong, Zhao Yuguang, Xu Xiaofeng, Wang Yitong, Jiang Wenqiang, Ju Hong. Effect of High-Energy and Instantaneous Electropulsing Treatment on Microstructure and Properties of 42CrMo Steel. *Acta Metall Sin*, 2018, vol. 54, no. 9, pp. 1245–1252. DOI: [10.11900/0412.1961.2017.00562](https://doi.org/10.11900/0412.1961.2017.00562).
- Konkova T., Valeev I., Mironov S., Korznikov A., Myshlyaev M.M., Semiatin S.L. Effect of electric-current pulses on grain-structure evolution in cryogenically rolled copper. *Journal of Materials Research*, 2014, vol. 29, no. 22, pp. 2727–2737. DOI: [10.1557/jmr.2014.299](https://doi.org/10.1557/jmr.2014.299).
- Konkova T., Valeev I., Mironov S., Korznikov A., Korznikova G., Myshlyaev M.M., Semiatin S.L. Microstructure response of cryogenically-rolled Cu–30Zn brass to electric-current pulsing. *Journal of Alloys and Compounds*, 2016, vol. 659, pp. 184–192. DOI: [10.1016/j.jallcom.2015.11.059](https://doi.org/10.1016/j.jallcom.2015.11.059).
- Khaymovich P.A. Cryodeformation of metals under all-around compression (Review Article). *Fizika nizkikh temperatur*, 2018, vol. 44, no. 5, pp. 463–490. EDN: [YTJSLG](https://www.edn.net/YTJSLG).
- Panigrahi S.K., Jayaganthan R. A Study on the Combined Treatment of Cryorolling, Short-Annealing, and Aging for the Development of Ultrafine-Grained Al 6063 Alloy with Enhanced Strength and Ductility. *Metalurgical and Materials Transactions: A*, 2010, vol. 41, pp. 2675–2690. DOI: [10.1007/s11661-010-0328-x](https://doi.org/10.1007/s11661-010-0328-x).
- Magalhães D.C.C., Kliauga A.M., Ferrante M., Sordi V.L. Plastic deformation of FCC alloys at cryogenic temperature: the effect of stacking-fault energy on microstructure and tensile behavior. *Journal of Materials Science*, 2017, vol. 52, pp. 7466–7478. DOI: [10.1007/s10853-017-0979-8](https://doi.org/10.1007/s10853-017-0979-8).
- Ma E. Eight Routes to Improve the Tensile Ductility of Bulk Nanostructured Metals and Alloys. *JOM*, 2006, vol. 58, no. 4, pp. 49–53. DOI: [10.1007/s11837-006-0215-5](https://doi.org/10.1007/s11837-006-0215-5).
- Krymskiy S., Sitdikov O., Avtokratova E., Markushev M. 2024 aluminum alloy ultrahigh-strength sheet due to two-level nanostructuring under cryorolling and heat treatment. *Transactions of Nonferrous Metals Society of China*, 2020, vol. 30, no. 1, pp. 14–26. DOI: [10.1016/S1003-6326\(19\)65176-9](https://doi.org/10.1016/S1003-6326(19)65176-9).
- Sheng Yinying, Hua Youlu, Wang Xiaojian, Zhao Xueyang, Chen Lianxi, Zhou Hanyu, Wang James, Berndt Ch.C., Li Wei. Application of High-Density Electropulsing to Improve the Performance of Metallic Materials: Mechanisms, Microstructure and Properties. *Materials*, 2018, vol. 11, no. 2, article number 185. DOI: [10.3390/ma11020185](https://doi.org/10.3390/ma11020185).
- Kang Kaijiao, Li Dayong, Wang Ao, Shi Dequan, Gao Guili, Xu Zhenyu. Experimental investigation on aging treatment of 7050 alloy assisted by electric pulse. *Results in Physics*, 2020, vol. 3, article number 103016. DOI: [10.1016/j.rinp.2020.103016](https://doi.org/10.1016/j.rinp.2020.103016).
- Xua Hong, Liu Meng, Wang Yu-peng, Ma Pin-kui, Bai Ming, Jiang Bo, Guo Zhi-peng, Zou Yu-jie. Refined microstructure and dispersed precipitates in a gradient rolled AZ91 alloy under pulsed current. *Materialia*, 2021, vol. 20, article number 101245. DOI: [10.1016/j.mtla.2021.101245](https://doi.org/10.1016/j.mtla.2021.101245).
- Xu Zhutian, Jiang Tianhao, Huang Jihui, Peng Linfa, Lai Xinmin, Fu M.W. Electroplasticity in electrically-assisted forming: Process phenomena, performances and modeling. *International Journal of Machine Tools and Manufacture*, 2022, vol. 175, article number 103871. DOI: [10.1016/j.ijmachtools.2022.103871](https://doi.org/10.1016/j.ijmachtools.2022.103871).
- Kim Moon-Jo, Yoon Sangmoon, Park S. et al. Elucidating the origin of electroplasticity in metallic materials. *Applied Materials Today*, 2020, vol. 21, article number 100874. DOI: [10.1016/j.apmt.2020.100874](https://doi.org/10.1016/j.apmt.2020.100874).
- Ruszkiewicz B.J., Mears L., Roth J.T. Investigation of Heterogeneous Joule Heating as the Explanation for the Transient Electroplastic Stress Drop in Pulsed Tension of 7075-T6 Aluminum. *Journal of Manufacturing Science and Engineering*, 2018, vol. 140, no. 9, article number 091014. DOI: [10.1115/1.4040349](https://doi.org/10.1115/1.4040349).
- Humphreys F.J., Hatherly M. *Recrystallization and Related Annealing Phenomena*. 2nd ed. Amsterdam, Elsevier Publ., 2004. 658 p.

СПИСОК ЛИТЕРАТУРЫ

- Estrin Y., Vinogradov A. Extreme grain refinement by severe plastic deformation: A wealth of challenging science // *Acta Materialia*. 2013. Vol. 61. № 3. P. 782–817. DOI: [10.1016/j.actamat.2012.10.038](https://doi.org/10.1016/j.actamat.2012.10.038).
- Zhilyaev A.P., Pshenichnyuk A.I., Utyashev F.Z., Raab G.I. *Superplasticity and Grain Boundaries in Ultrafine-Grained Materials*. Amsterdam: Elsevier, 2020. 416 p.
- Edalati K., Bachmaier A., Beloshenko V.A., Beygelzimer Y., Blank V.D., Botta W.J. Nanomaterials by severe plastic deformation: review of historical developments and recent advances // *Materials Research Letters*. 2022. Vol. 10. № 4. P. 163–256. DOI: [10.1080/21663831.2022.2029779](https://doi.org/10.1080/21663831.2022.2029779).
- Pan Dong, Zhao Yuguang, Xu Xiaofeng, Wang Yitong, Jiang Wenqiang, Ju Hong. Effect of High-Energy and

- Instantaneous Electropulsing Treatment on Microstructure and Properties of 42CrMo Steel // *Acta Metall Sin.* 2018. Vol. 54. № 9. P. 1245–1252. DOI: [10.11900/0412.1961.2017.00562](https://doi.org/10.11900/0412.1961.2017.00562).
5. Konkova T., Valeev I., Mironov S., Korznikov A., Myshlyaev M.M., Semiatin S.L. Effect of electric-current pulses on grain-structure evolution in cryogenically rolled copper // *Journal of Materials Research.* 2014. Vol. 29. № 22. P. 2727–2737. DOI: [10.1557/jmr.2014.299](https://doi.org/10.1557/jmr.2014.299).
6. Konkova T., Valeev I., Mironov S., Korznikov A., Korznikova G., Myshlyaev M.M., Semiatin S.L. Microstructure response of cryogenically-rolled Cu–30Zn brass to electric-current pulsing // *Journal of Alloys and Compounds.* 2016. Vol. 659. P. 184–192. DOI: [10.1016/j.jallcom.2015.11.059](https://doi.org/10.1016/j.jallcom.2015.11.059).
7. Хаймович П.А. Криодеформирование металлов в условиях всестороннего сжатия (обзор) // *Физика низких температур.* 2018. Т. 44. № 5. С. 463–490. EDN: [YTJSLG](https://www.elibrary.ru/ytjslug).
8. Panigrahi S.K., Jayaganthan R. A Study on the Combined Treatment of Cryorolling, Short-Annealing, and Aging for the Development of Ultrafine-Grained Al 6063 Alloy with Enhanced Strength and Ductility // *Metallurgical and Materials Transactions A.* 2010. Vol. 41. P. 2675–2690. DOI: [10.1007/s11661-010-0328-x](https://doi.org/10.1007/s11661-010-0328-x).
9. Magalhães D.C.C., Kliauga A.M., Ferrante M., Sordi V.L. Plastic deformation of FCC alloys at cryogenic temperature: the effect of stacking-fault energy on microstructure and tensile behaviour // *Journal of Materials Science.* 2017. Vol. 52. P. 7466–7478. DOI: [10.1007/s10853-017-0979-8](https://doi.org/10.1007/s10853-017-0979-8).
10. Ma E. Eight Routes to Improve the Tensile Ductility of Bulk Nanostructured Metals and Alloys // *JOM.* 2006. Vol. 58. № 4. P. 49–53. DOI: [10.1007/s11837-006-0215-5](https://doi.org/10.1007/s11837-006-0215-5).
11. Krymskiy S., Sitdikov O., Avtokratova E., Markushev M. 2024 aluminum alloy ultrahigh-strength sheet due to two-level nanostructuring under cryorolling and heat treatment // *Transactions of Nonferrous Metals Society of China.* 2020. Vol. 30. № 1. P. 14–26. DOI: [10.1016/S1003-6326\(19\)65176-9](https://doi.org/10.1016/S1003-6326(19)65176-9).
12. Sheng Yinying, Hua Youlu, Wang Xiaojian, Zhao Xueyang, Chen Lianxi, Zhou Hanyu, Wang James, Berndt Ch.C., Li Wei. Application of High-Density Electropulsing to Improve the Performance of Metallic Materials: Mechanisms, Microstructure and Properties // *Materials.* 2018. Vol. 11. № 2. Article number 185. DOI: [10.3390/ma11020185](https://doi.org/10.3390/ma11020185).
13. Kang Kaijiao, Li Dayong, Wang Ao, Shi Dequan, Gao Guili, Xu Zhenyu. Experimental investigation on aging treatment of 7050 alloy assisted by electric pulse // *Results in Physics.* 2020. Vol. 3. Article number 103016. DOI: [10.1016/j.rinp.2020.103016](https://doi.org/10.1016/j.rinp.2020.103016).
14. Xua Hong, Liu Meng, Wang Yu-peng, Ma Pin-kui, Bai Ming, Jiang Bo, Guo Zhi-peng, Zou Yu-jie. Refined microstructure and dispersed precipitates in a gradient rolled AZ91 alloy under pulsed current // *Materialia.* 2021. Vol. 20. Article number 101245. DOI: [10.1016/j.mtla.2021.101245](https://doi.org/10.1016/j.mtla.2021.101245).
15. Xu Zhutian, Jiang Tianhao, Huang Jihui, Peng Linfa, Lai Xinmin, Fu M.W. Electroplasticity in electrically-assisted forming: Process phenomena, performances and modelling // *International Journal of Machine Tools and Manufacture.* 2022. Vol. 175. Article number 103871. DOI: [10.1016/j.ijmachtools.2022.103871](https://doi.org/10.1016/j.ijmachtools.2022.103871).
16. Kim Moon-Jo, Yoon Sangmoon, Park S. et al. Elucidating the origin of electroplasticity in metallic materials // *Applied Materials Today.* 2020. Vol. 21. Article number 100874. DOI: [10.1016/j.apmt.2020.100874](https://doi.org/10.1016/j.apmt.2020.100874).
17. Ruszkiewicz B.J., Mears L., Roth J.T. Investigation of Heterogeneous Joule Heating as the Explanation for the Transient Electroplastic Stress Drop in Pulsed Tension of 7075-T6 Aluminum // *Journal of Manufacturing Science and Engineering.* 2018. Vol. 140. № 9. Article number 091014. DOI: [10.1115/1.4040349](https://doi.org/10.1115/1.4040349).
18. Humphreys F.J., Hatherly M. Recrystallization and Related Annealing Phenomena. 2nd ed. Amsterdam: Elsevier, 2004. 658 p.
19. Conrad H. Electroplasticity in metals and ceramics // *Materials Science and Engineering: A.* 2000. Vol. 287. № 2. P. 276–287. DOI: [10.1016/S0921-5093\(00\)00786-3](https://doi.org/10.1016/S0921-5093(00)00786-3).
20. Grimm T.J., Mears L.M. Skin effects in electrically assisted manufacturing // *Manufacturing Letters.* 2022. Vol. 34. P. 67–70. DOI: [10.1016/j.mfglet.2022.09.006](https://doi.org/10.1016/j.mfglet.2022.09.006).
21. He Changshu, Zhang Yudong, Wang Y.N., Zhao Xingyong, Zuo Liang, Esling C. Texture and microstructure development in cold-rolled interstitial free (IF) steel sheet during electric field annealing // *Scripta Materialia.* 2003. Vol. 48. № 6. P. 737–742. DOI: [10.1016/S1359-6462\(02\)00552-3](https://doi.org/10.1016/S1359-6462(02)00552-3).
22. Shneerson G.A., Dolotenko M.I., Krivosheev S.I. Strong and Superstrong Pulsed Magnetic Fields Generation. Berlin: De Gruyter, 2014. 439 p. DOI: [10.1515/9783110252576](https://doi.org/10.1515/9783110252576).
23. Валеев И.Ш., Валеева А.Х., Ильясов Р.Р., Автократова Е.В., Крымский С.В., Ситдиков О.Ш., Маркушев М.В. Влияние электроимпульсной обработки на структуру и твердость криопрокатаного алюминия // *Письма о материалах.* 2021. Т. 11. № 3. С. 351–356. DOI: [10.22226/2410-3535-2021-3-351-356](https://doi.org/10.22226/2410-3535-2021-3-351-356).
24. Маркушев М.В., Ильясов Р.Р., Крымский С.В., Валеев И.Ш., Ситдиков О.Ш. Структура и прочность мелкозернистой меди после криопрокатки и однократной электроимпульсной обработки различной мощности // *Письма о материалах.* 2021. Т. 11. № 4. С. 491–496. DOI: [10.22226/2410-3535-2021-4-491-496](https://doi.org/10.22226/2410-3535-2021-4-491-496).
25. Markushev M., Valeev I., Valeeva A., Ilyasov R., Avtokratova E., Krymskiy S., Sitdikov O. Effect of electric pulsing on the structure, texture and hardness of cryorolled fine-grain copper // *Facta Universitatis. Series: Mechanical Engineering.* 2022. P. 1–12.

26. Markushev M.V., Valeev I.Sh., Avtokratova E.V., Ilyasov R.R., Valeeva A.K., Krimsky S.V., Sitdikov O.S. Effect of high-dense electropulsing with different energies on the structure and strength of nickel cryorolled to different strains // Letters on Materials. 2023. Vol. 13. № 2. P. 126–131. DOI: [10.22226/2410-3535-2023-2-126-131](https://doi.org/10.22226/2410-3535-2023-2-126-131).
27. Danyuk A., Merson D., Yasnikov I., Agletdinov E., Afanasyev M., Vinogradov A. The effect of stacking fault energy on acoustic emission in pure metals with face-centered crystal lattice // Letters on Materials. 2017. Vol. 7. № 4. P. 437–441. DOI: [10.22226/2410-3535-2017-4-437-441](https://doi.org/10.22226/2410-3535-2017-4-437-441).
28. Sarma V.S., Wang Jun, Jian W.W., Kauffmann A., Conrad H., Freudenberger J., Zhu Yuntian T. Role of stacking fault energy in strengthening due to cryo-deformation of FCC metals // Materials Science and Engineering: A. 2010. Vol. 527. № 29–30. P. 7624–7630. DOI: [10.1016/j.msea.2010.08.015](https://doi.org/10.1016/j.msea.2010.08.015).
29. Zhao Yonghao, Liao X.Z., Zhu Yuntian, Horita Z., Langdon T.G. Influence of stacking fault energy on nanostructure under high pressure torsion // Materials Science and Engineering: A. 2005. Vol. 410–411. P. 188–193. DOI: [10.1016/j.msea.2005.08.074](https://doi.org/10.1016/j.msea.2005.08.074).
30. Belyakov A., Sakai T., Miura H., Kaibyshev R., Tszuzaki K. Continuous recrystallization in austenitic stainless steel after large strain deformation // Acta Materialia. 2002. Vol. 50. № 6. P. 1547–1557. DOI: [10.1016/S1359-6454\(02\)00013-7](https://doi.org/10.1016/S1359-6454(02)00013-7).

Сочетание криогенной деформации и электроимпульсной обработки как способ получения ультрамелкозернистых металлов

© 2023

Маркушев Михаил Вячеславович*, доктор технических наук, старший научный сотрудник, заведующий лабораторией

Автokratова Елена Викторовна, кандидат технических наук, старший научный сотрудник

Валеева Айгуль Хамматовна¹, кандидат технических наук, научный сотрудник

Валеев Иршат Шамилович², кандидат технических наук, научный сотрудник

Ильясов Рафис Раисович³, младший научный сотрудник

Крымский Станислав Вацлавович⁴, кандидат технических наук, заведующий лабораторией

Ситдииков Олег Шамилович, кандидат физико-математических наук, старший научный сотрудник

Институт проблем сверхпластичности металлов РАН, Уфа (Россия)

*E-mail: mvmark@imsp.ru

¹ORCID: <https://orcid.org/0000-0003-4305-4538>

²ORCID: <https://orcid.org/0009-0002-5162-7324>

³ORCID: <https://orcid.org/0000-0003-0195-1206>

⁴ORCID: <https://orcid.org/0000-0002-1534-3239>

Поступила в редакцию 15.08.2023

Принята к публикации 01.12.2023

Аннотация: Проведен сравнительный анализ структуры и твердости чистых металлов с гранцентрированной кубической решеткой – алюминия, никеля и меди, подвергнутых комплексной термомеханической обработке (ТМО), включавшей изотермическую криогенную прокатку при температуре жидкого азота и последующую электроимпульсную обработку (ЭИО) токами высокой плотности. Рассмотрены основные этапы, особенности и преимущества ТМО, обеспечивающие сначала сильный наклеп обрабатываемого материала за счет деформации при отрицательных температурах, а затем его сверхбыстрый контактный электроимпульсный нагрев до заданной температуры. С использованием современных методов сканирующей электронной микроскопии и рентгеноструктурного анализа проведено многоуровневое исследование структуры металлов после основных этапов ТМО с фиксацией широкого спектра ее линейных и угловых параметров. Выявлены кинетика и природа процессов трансформации структуры металлов при криопротатке и ЭИО, их движущая сила и контролируемые факторы, а также общие закономерности и температурные интервалы активации возврата и рекристаллизации деформационной структуры под воздействием электроимпульса. На основе результатов анализа структурно-механического поведения металлов сделан вывод о том, что сочетание большой пластической криогенной деформации с последующей однократной обработкой ультракороткими импульсами переменного тока является эффективным способом получения полуфабрикатов с регламентированными параметрами их структуры и свойств, в т. ч. высокопрочного ультрамелкозернистого проката. При этом феноменология и природа упрочнения/разупрочнения металлов при криогенной прокатке и последующей обработке импульсами тока аналогичны наблюдающимся при холодной прокатке и печном отжиге.

Ключевые слова: ГЦК-металлы; криогенная деформация; криогенная прокатка; электроимпульсная обработка; ультрамелкозернистая структура.

Благодарности: Работа выполнена в рамках государственного задания федерального государственного бюджетного учреждения науки «Институт проблем сверхпластичности металлов Российской академии наук».

Экспериментальные исследования были выполнены на базе Центра коллективного пользования ИПСМ РАН «Структурные и физико-механические исследования материалов».

Для цитирования: Маркушев М.В., Автократова Е.В., Валеева А.Х., Валеев И.Ш., Ильясов Р.Р., Крымский С.В., Ситдиков О.Ш. Сочетание криогенной деформации и электроимпульсной обработки как способ получения ультрамелкозернистых металлов // Frontier Materials & Technologies. 2023. № 4. С. 53–62. DOI: 10.18323/2782-4039-2023-4-66-5.

Investigation of phase transformations in a two-layer Ti–Al–C+Y–Al–O coating on a heat-resistant nickel alloy

© 2023

*Almaz Yu. Nazarov**^{1,4}, PhD (Engineering),
assistant professor of Chair of Mechanical Engineering
Aleksey A. Maslov^{1,5}, laboratory assistant of Chair of Mechanical Engineering
*Aleksey A. Nikolaev*¹, assistant of Chair of Mechanical Engineering
Aleksandr N. Shmakov^{2,3}, leading researcher
*Vladimir V. Denisov*³, PhD (Engineering),
Head of Laboratory of Beam-Plasma Surface Engineering
*Kamil N. Ramazanov*¹, Doctor of Sciences (Engineering),
Head of Chair of Mechanical Engineering

¹Ufa University of Science and Technology, Ufa (Russia)

²Federal Research Center Boreskov Institute of Catalysis SB of RAS, Novosibirsk (Russia)

³Institute of High Current Electronics SB of RAS, Tomsk (Russia)

*E-mail: nazarov_almaz15@mail.ru,
nazarov.ayu@ugatu.su

⁴ORCID: <https://orcid.org/0000-0002-4711-4721>

⁵ORCID: <https://orcid.org/0000-0002-2568-1784>

Received 03.07.2023

Accepted 17.11.2023

Abstract: Currently, an active increase in requirements for fuel efficiency and specific gravity of aircraft turbojet engines is observed. Existing coatings based on zirconium dioxide intended for protecting engine parts are largely outdated and have exhausted their development potential, so new ceramic systems for the production of protective coatings based on them are an area of research. The authors carried out a study of a heat-resistant two-layer coating based on the Y–Al–O system (outer layer) and the Ti₂AlC MAX phase of the Ti–Al–C system (sublayer) produced using vacuum-arc deposition on the Inconel 738 heat-resistant nickel alloy and molybdenum by alternate deposition of layers based on Ti–Al–C and a Y–Al–O layer. Using synchrotron radiation, phase transformations in the coating were examined when samples were heated to 1400 °C in a vacuum and to 1100 °C in the atmosphere to study the process of oxidation and coating formation in the presence of oxygen. Using scanning electron microscopy, the authors studied the microstructure and chemical composition of the coating. The study identified that heating the coating in a vacuum and in the atmosphere causes various phase transformations in it, but in both cases, the formation of a mixture of oxides of the Y–Al–O group and destabilization of the Ti–Al–C-based sublayer are observed. After heating the coating in the atmosphere without preliminary heat treatment, the coating was destroyed upon cooling, which was not observed when the coating was heated in a vacuum.

Keywords: heat-resistant coating; ceramic coating; MAX phase; yttrium oxide; vacuum-arc deposition; synchrotron radiation.

Acknowledgments: The work was financially supported by the Ministry of Science and Higher Education of the Russian Federation (Project No. 075-15-2021-1348).

The paper was written on the reports of the participants of the XI International School of Physical Materials Science (SPM-2023), Togliatti, September 11–15, 2023.

For citation: Nazarov A.Yu., Maslov A.A., Nikolaev A.A., Shmakov A.N., Denisov V.V., Ramazanov K.N. Investigation of phase transformations in a two-layer Ti–Al–C+Y–Al–O coating on a heat-resistant nickel alloy. *Frontier Materials & Technologies*, 2023, no. 4, pp. 63–71. DOI: 10.18323/2782-4039-2023-4-66-6.

INTRODUCTION

In modern aircraft engine building, there is a constant search for ways to improve the efficiency of gas turbine engines, due to the growing requirements of aviation regulators. It is known that to improve the efficiency and specific power of engines, the main task is to increase the operating temperature in the combustion chamber, and turbine, which leads to increased requirements for the materials used. Nickel alloys traditionally used in turbines are capable of operating at temperatures up to 1050 °C at the alloy surface; however, this is not enough to operate in modern engines. Therefore, to protect the blades of gas turbine engines, industry applies multilayer heat-barrier and heat-resistant coatings consisting of a sublayer based on

MeCrAlY or the Ni–Al–Pt system, and an external columnar thermal barrier layer based on zirconium dioxide, stabilised with ZrO₂·Y₂O₃ (6...8 wt. %) yttrium oxide. The sublayer based on MeCrAlY, or the Ni–Al–Pt system during operation creates an oxide film layer that prevents oxygen diffusion to the substrate material [1–3]. This protective coating architecture allows the blades to operate at ambient temperatures up to 1300 °C by creating a temperature gradient, between the layer surface and the inner part of the cooled blade [4–6]. However, the mentioned combination of coatings is rapidly becoming obsolete, and is not suitable for the next generation of gas turbine engines, whose operating temperature exceeds 1500 °C in the turbine [7–9]. The reasons for such obsolescence, were the phase transformations occurring in the ceramic layer

at temperatures above 1300 °C on the coating surface, the ceramic layer sintering, a sharp increase in thermal conductivity, and degradation of the heat-resistant sublayer. This leads to the impossibility of further increasing the operating temperature of gas turbine engines without a catastrophic drop in the service life of the blades [10–12].

The listed factors actualise the search for new heat-resistant and heat-barrier coatings to protect the engine blades of the next generations. One of the promising candidates for replacing the traditional ZrO₂–Y₂O₃ coating is the Y–Al–O system including stable Y₃Al₅O₁₂, YAlO₃ and Y₄Al₂O₉ compounds, which demonstrate promising high-temperature characteristics, such as oxidation resistance, and a relatively high thermal expansion coefficient [13–15]. One of the promising candidates for replacing the MCrAlY (Ni–Al–Pt) sublayer can be a coating consisting of the M_{n+1}AX_n phase of Ti₂AlC. The M_{n+1}AX_n phase of Ti₂AlC has high heat resistance due to the formation of a strong α-Al₂O₃ oxide film, and a relatively high thermal expansion coefficient, that allows creating a transition oxidation-resistant sublayer under the Y–Al–O ceramic coating [16–18].

Another important task is the study of the structure and phase transformations in a combined coating, during heating to understand the processes occurring in the coating.

The purpose of this work is to study structural and phase transformations, in a combined Y–Al–O+Ti–Al–C coating when heating the sample in a vacuum, to a temperature of 1400 °C in real time using synchrotron radiation.

METHODS

The coatings of the Ti–Al–C system and the Y–Al–O system were deposited using a modernised NNV-6.6-II installation. The coating was applied to the Inconel 738 alloy and commercially pure (99.96 %) molybdenum. To study the qualitative phase composition, and phase transformations in the coating in real time, when heating the sample to 1400 and 1100 °C, the authors used the following equipment: VEPP-3 synchrotron radiation source of the Institute of Nuclear Physics of the Siberian Branch of the Russian Academy of Sciences, an Anton Paar HTK-2000 high-temperature X-ray camera, OD-3M-350 position-sensitive single-axis detector, and Origin software for data processing.

Due to the peculiarities of the imaging technique using synchrotron radiation with heating in the atmosphere, the maximum test temperature was limited and amounted to 1100 °C. All diffraction patterns are presented in the angle scale corresponding to CuKα radiation (0.15406 nm). To estimate the quantitative content of phases, a method of shooting without a standard was used, based on assessing the ratio of the intensity of the desired phase reflexes to the total intensity of oxide reflexes in the diffraction pattern. The coating structure was studied using a JEOL JSM-6390 scanning electron microscope. Secondary electron mode was used to obtain images of the polished section surface. The coating chemical composition was assessed using the INCA Energy system for energy dispersive microanalysis.

The Ti–Al–C coating was applied by the vacuum-arc method, assisted by a plasma source with an incandescent cathode, through which a mixture of acetylene and argon was supplied in a ratio of 1:4. The discharge current was 10 A. The current on the arc evaporators was 50 and 80 A for titanium and aluminium, respectively, the pressure

in the chamber was 0.3 Pa. Coating deposition time was 2 h. After coating deposition, vacuum heat treatment was carried out at a temperature of 800 °C for 2 h.

The Y–Al–O coating was applied using the vacuum-arc method. A mixture of oxygen and argon was supplied to the chamber in a ratio of 54.5 l/h of argon to 42.7 l/h of oxygen. The discharge current was 55 A. The current on the arc evaporators was 60 and 80 A for yttrium and aluminium, respectively, the pressure in the chamber was 0.3 Pa. Coating deposition time was 2 h.

RESULTS

The study of phase transformations in a Ti–Al–C+Y–Al–O coating when heating in a vacuum

Fig. 1 demonstrates a series of X-ray photographs of the process of heating a coated molybdenum sample in a vacuum, in the form of a projection of the intensity of reflexes, onto the “diffraction angle – temperature” plane. The first frames show that in the initial state, the coating is an amorphous structure – the X-ray diffraction pattern shows a smooth increase in the diffracted intensity, with a maximum in the region of angles of 2θ ~29...31°. Individual reflexes belonging to yttrium and aluminium are recorded. No reflexes of titanium or phases containing titanium and carbon are observed in the diffraction pattern of the initial sample (before heating).

When the sample is heated in a vacuum to 1400 °C, a series of X-ray diffraction patterns shows a change in the phase composition of the coating, which begins at a temperature of ~1200 °C. The amorphous component disappears, and predominantly phases of YAlO₃ mixed oxide and Y₂O₃ yttrium oxide appear. Reflexes related to phases containing titanium or carbon are still not observed. There are no further changes in the coating phase composition when keeping the sample at a temperature of 1400 °C. Fig. 2 presents the final diffraction pattern of a sample with a Ti–Al–C+Y–Al–O coating on molybdenum after cooling to room temperature.

The study of phase transformations in a Ti–Al–C+Y–Al–O coating when heating in the atmosphere

Fig. 3 shows a series of X-ray diffraction patterns of the process of heating a coated Inconel 738 alloy sample in the atmosphere in the form of a projection of the reflex intensity onto the “diffraction angle – temperature” plane. The first frames show that in the initial state, the coating has an amorphous structure with separate yttrium and aluminium reflexes. During heating at a temperature of ~890...910 °C, the broad maximum associated with the amorphous component begins to disappear, and reflexes begin to appear. Their identity is difficult to be accurately determined due to thermal expansion. At the same time, the reflexes of the Y₂O₃, YAlO₃ and Y₄Al₂O₉ oxides appear. Reflexes related to titanium or carbon-containing phases are still not observed. With further exposure of the sample at a temperature of 1100 °C for 1 h, the coating phase composition practically does not change, except for the disappearance of reflexes of aluminium and phase transformations, at the beginning of exposure, which is associated with the diffusion processes, and the formation of oxides in the coating. When cooling the sample after exposure, at

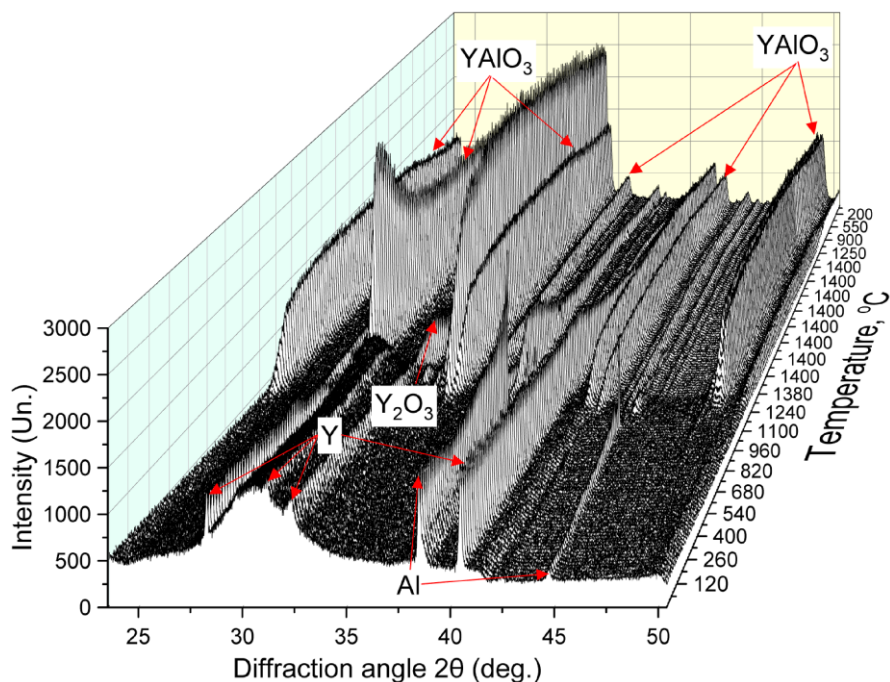


Fig. 1. Series of diffraction patterns of the process of heating a sample with a combined Ti–Al–C+Y–Al–O coating on molybdenum in a vacuum in the form of a set of reflexes in the “diffraction angle – intensity – temperature” coordinates
Рис. 1. Серия дифрактограмм процесса нагрева образца с комбинированным покрытием Ti–Al–C+Y–Al–O на молибдене в вакууме в виде набора рефлексов в координатах «угол дифракции – интенсивность – температура»

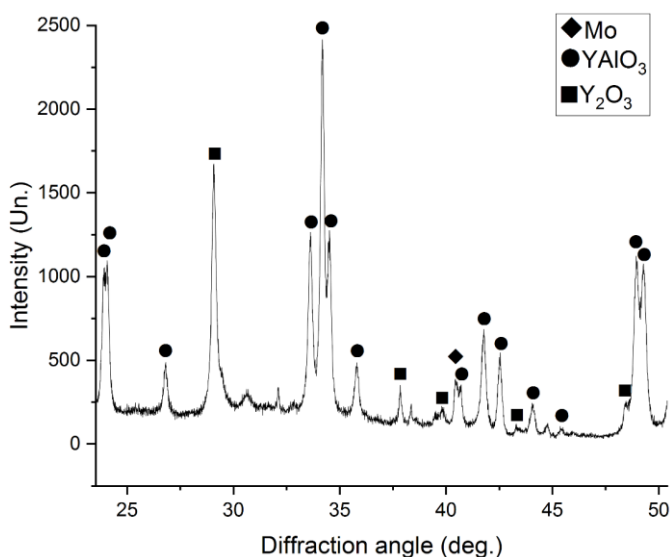


Fig. 2. Diffraction pattern of a sample with a combined Ti–Al–C+Y–Al–O coating on molybdenum after heating and cooling in a vacuum
Рис. 2. Дифрактограмма образца с комбинированным покрытием Ti–Al–C+Y–Al–O на молибдене после прогрева и остывания в вакууме

a temperature of ~420 °C, partial coating destruction and peeling occurs, as well as a change in the optical scheme of the experiment, so the final coating composition could not be determined with sufficient accuracy. Therefore, the belonging of reflexes indicated in Fig. 3 and 4 is a matter of judgment. Unlike the previous heating experiment, a complex $Y_4Al_2O_9$ oxide with a monoclinic structure was formed in

this coating. The high intensity of chromium reflexes present in the Inconel 738 alloy is worth noting. The appearance of chromium reflexes indicates a loss of coating continuity and beam penetration to the substrate layer.

Fig. 4 shows the final diffraction pattern of a sample coated with Ti–Al–C+Y–Al–O on the Inconel 738 alloy after cooling to room temperature.

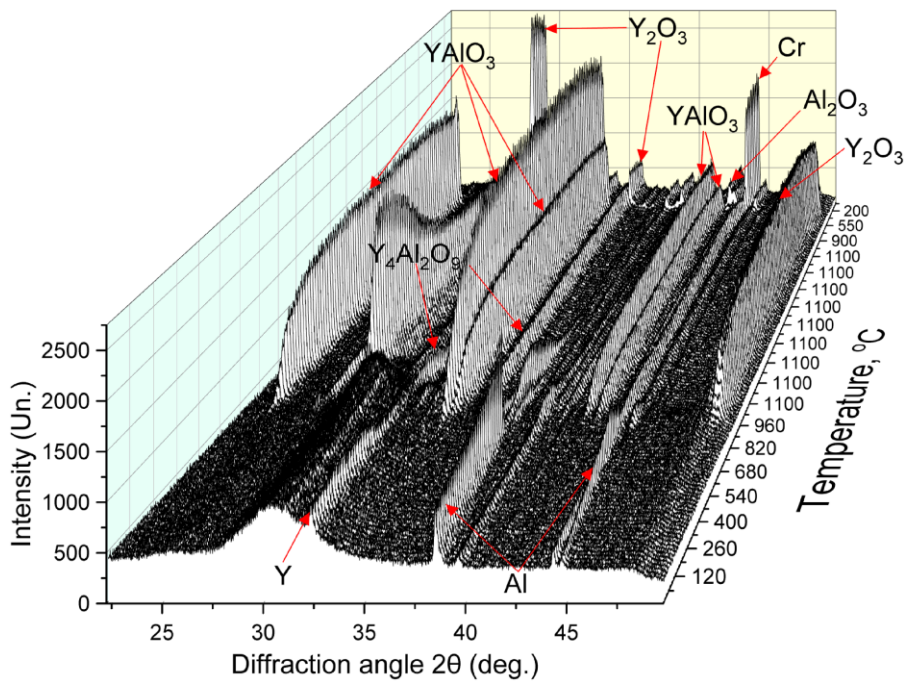


Fig. 3. Series of diffraction patterns of the process of heating a sample with a combined Ti–Al–C+Y–Al–O coating on the Inconel 738 alloy in the atmosphere in the form of a set of reflexes in the “diffraction angle – intensity – temperature” coordinates
Рис. 3. Серия дифрактограмм процесса нагрева образца с комбинированным покрытием Ti–Al–C+Y–Al–O на сплаве Inconel 738 в атмосфере в виде набора рефлексов в координатах «угол дифракции – интенсивность – температура»

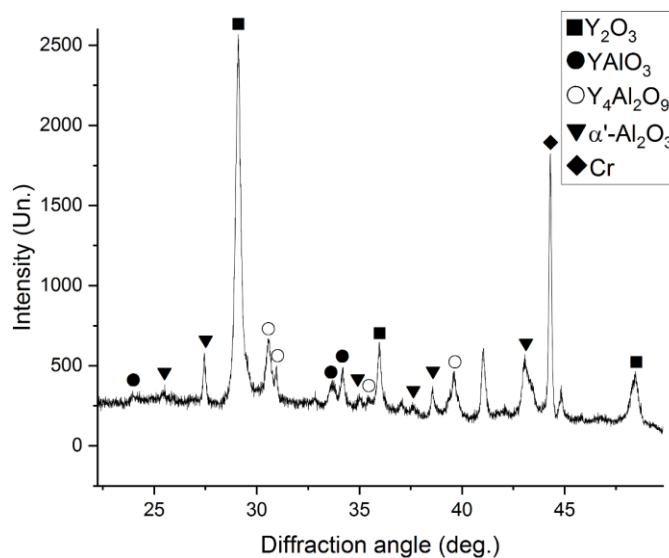


Fig. 4. Diffraction pattern of a sample with a combined Ti–Al–C+Y–Al–O coating on the Inconel 738 alloy after heating and cooling in the atmosphere
Рис. 4. Дифрактограмма образца с комбинированным покрытием Ti–Al–C+Y–Al–O на сплаве Inconel 738 после прогрева и остывания в атмосфере

The study of the coating structure and chemical composition

Fig. 5 and 6 present the results of scanning electron microscopy of samples, with a Ti–Al–C+Y–Al–O coating deposited on the Inconel 738 alloy. Analysis of the images shows the formation of 2 regions: on the outer surface of

the sample there is a Y–Al–O coating, demonstrating a rather non-continuous layered structure (without vacuum heat treatment), underneath there is a Ti–Al–C sublayer (subjected to vacuum heat treatment), which retains its continuity and adhesion to the surface. In the Ti–Al–C layer, an increased nickel content is observed (up to 57 wt. %).

No diffusion is observed between the Y–Al–O and Ti–Al–C layers. Under the coating, two characteristic diffusion zones saturated with aluminium are observed in the alloy.

Table 1 presents a set of points for spectral elemental analysis of coatings. Diffusion zone I (Fig. 5) is located from the boundary of the Ti–Al–C coating deep into the nickel alloy, and has a thickness of $\sim 11 \mu\text{m}$. According to elemental analysis, the zone covered by spectra 9 and 11 consists of intermetallic compounds of the Ni–Al system (spectra 9–11 in Fig. 6 and in Table 1) and possibly contains the δ -phase of the Ni_2Al_3 intermetallic compound, which is stoichiometrically appropriate. This zone also contains an increased content of chromium, which is released along the δ -phase boundaries in the form of finely dispersed particles less than $1 \mu\text{m}$ in size. Diffusion zone II (Fig. 5) is located under diffusion zone I, and has a thickness of $7 \mu\text{m}$. The structure of this zone is characterized by needle-like precipitates of excess phases based on chromium and cobalt.

DISCUSSION

The presented results showed that immediately after deposition, the Y–Al–O coating has an amorphous structure, which was also observed in the works of other authors [15; 21]. To crystallise the YAlO_3 phase, it is necessary to exceed a certain energy level, and maintain the required temperature. Moreover, the cooling rate must be low enough to complete the rearrangement of atoms, and the formation of long-range order [15]. Such conditions can be implemented under conditions of vacuum-arc coating deposition using additional heating sources. However, in this case, due to the non-stationary conditions of deposition at each point of the vacuum chamber, and the sputtering of more low-melting elements during additional heating,

a shift from the stoichiometrically required phase composition and the formation of secondary phases will occur. Therefore, to form the required phase composition, it is rational to carry out subsequent heat treatment of the coating.

The results of studying changes in the phase composition, during vacuum heating of the Y–Al–O coating (Fig. 1), showed that for its complete crystallisation and decomposition of secondary phases, the required annealing temperature is 1200°C . In this case, the coating phase composition will be represented predominantly by the required YAlO_3 phase with a small content of the Y_2O_3 phase. Semi-quantitative analysis based on assessing the ratio of the intensity of the YAlO_3 phase reflexes to the total intensity of all oxide reflexes of the diffraction pattern (Fig. 2), showed that the content of the required phase in the coating is $\sim 85\%$. The formation of the Y_2O_3 phase is caused by the high yttrium content in the coating – up to 60 wt. % (Table 1, spectra 1–5). It follows from this that to form a homogeneous YAlO_3 coating, it is necessary to increase the aluminium component content.

In the work [22], it was noted that the Y_2O_3 phase increases the coating adhesion and has a thermal expansion coefficient similar to the YAlO_3 and Al_2O_3 phases. When the coating is heated in air (Fig. 3), coating crystallisation occurs at lower temperatures. The formation of oxide phases occurs already at a temperature of 890°C . Presumably, this is related to the fact that due to the excess concentration of oxygen from the atmosphere, the surface oxidation occurs, and specified reflexes represent the phase composition of the surface layer, and not the coating as a whole. In this case, during the cooling process, coating peeling occurred, which is associated with stresses and cracks that appeared immediately after deposition (Fig. 5), as well as with a high oxidation rate compared to vacuum heating. The formation

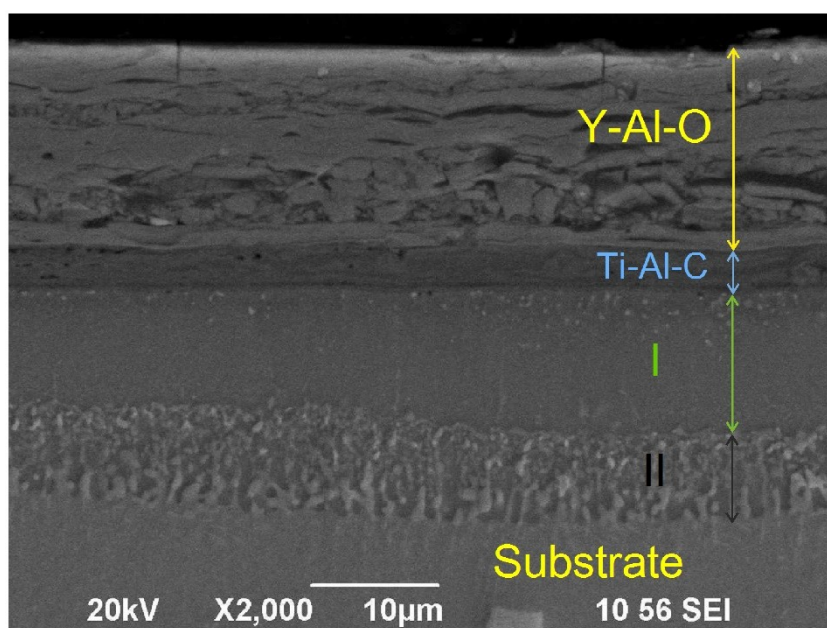


Fig. 5. The structure of the combined Y–Al–O+Ti–Al–C coating on the Inconel 738 alloy after deposition
 Рус. 5. Структура комбинированного покрытия Y–Al–O+Ti–Al–C на сплаве Inconel 738 после осаждения

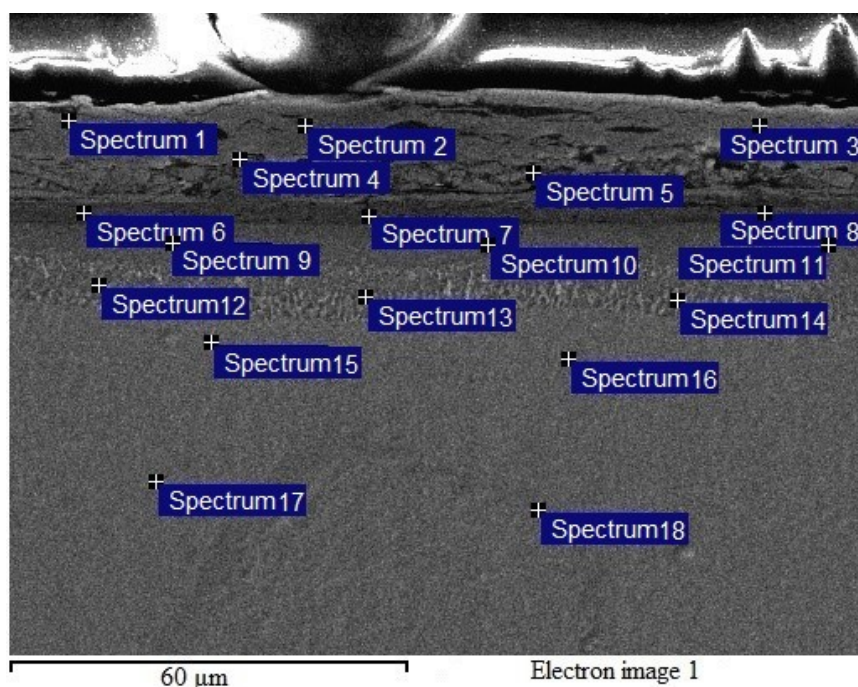


Fig. 6. Set of points for spectral analysis
Рис. 6. Набор точек для спектрального анализа

Table 1. Results of spectral analysis by points
Таблица 1. Результаты спектрального анализа по точкам

Spectrum	O	Al	Ti	Cr	Co	Ni	Y
Spectrum 1	22.34	17.67	0.00	0.00	0.00	0.00	59.99
Spectrum 2	26.01	16.05	0.00	0.00	0.00	0.00	57.95
Spectrum 3	25.25	16.28	0.00	0.36	0.00	0.00	58.11
Spectrum 4	20.84	20.13	0.33	0.00	0.00	0.00	58.70
Spectrum 5	17.77	29.22	5.72	0.00	0.00	1.95	45.34
Spectrum 6	7.17	16.04	51.39	1.60	2.19	21.61	0.00
Spectrum 7	0.00	24.48	6.99	4.36	6.68	57.49	0.00
Spectrum 8	0.00	26.30	16.73	2.88	4.92	49.18	0.00
Spectrum 9	0.00	20.64	4.11	6.00	7.32	61.93	0.00
Spectrum 10	3.53	11.13	4.33	36.93	6.48	37.61	0.00
Spectrum 11	0.00	19.99	4.96	7.23	7.83	59.99	0.00
Spectrum 12	0.00	14.08	4.87	10.92	9.44	60.68	0.00
Spectrum 13	4.29	9.53	4.20	22.24	10.36	49.39	0.00
Spectrum 14	0.00	6.10	5.72	16.24	9.12	62.82	0.00
Spectrum 15	2.83	3.74	3.19	19.74	10.37	60.12	0.00
Spectrum 16	0.00	5.08	3.75	15.54	7.78	67.86	0.00
Spectrum 17	0.00	2.60	2.89	23.18	11.49	59.85	0.00
Spectrum 18	3.54	2.50	2.11	22.20	10.87	58.77	0.00

of cracks is apparently caused by the occurrence of unwanted stresses in the coating due to the discrepancy between the physical and mechanical properties of the Ti₂AlC phase and the Y–Al–O layer. For an exact explanation, additional study and determination of the optimal parameters for the Y–Al–O coating deposition are required.

CONCLUSIONS

In this work, using synchrotron radiation, the authors studied real-time phase transformations in a two-layer Ti–Al–C+Y–Al–O coating. During heating in a vacuum to a temperature of 1400 °C, the coating crystallises with the formation of predominantly YAlO₃ yttrium orthoaluminate and Y₂O₃ yttrium oxide. After heating in the atmosphere, the coating crystallises with the formation of a mixture of YAlO₃, Y₂O₃, and Y₄Al₂O₉ oxides; however, if heated in the atmosphere, the coating is destroyed upon cooling.

REFERENCES

- Mondal K., Nunez L., Lii C.M., Downey I.J., Rooyen I.J. Thermal barrier coatings overview: Design, manufacturing, and applications in high-temperature industries. *Industrial & Engineering Chemistry Research*, 2021, vol. 60, no. 17, pp. 6061–6077. DOI: [10.1021/acs.iecr.1c00788](https://doi.org/10.1021/acs.iecr.1c00788).
- Liu Bin, Liu Yuchen, Zhu Changhua, Xiang Huimin, Chen Hongfei, Sun Luchao, Gao Yanfeng, Zhou Yanchun. Advances on strategies for searching for next generation thermal barrier coating materials. *Journal of Materials Science & Technology*, 2019, vol. 35, no. 5, pp. 833–851. DOI: [10.1016/j.jmst.2018.11.016](https://doi.org/10.1016/j.jmst.2018.11.016).
- Vaßen R., Bakan E., Mack D.E., Guillon O. A perspective on thermally sprayed thermal barrier coatings: current status and trends. *Journal of Thermal Spray Technology*, 2022, vol. 31, no. 4, pp. 685–698. DOI: [10.1007/s11666-022-01330-2](https://doi.org/10.1007/s11666-022-01330-2).
- Lashmi P.G., Ananthapadmanabhan P.V., Unnikrishnan G., Aruna S.T. Present status and future prospects of plasma sprayed multilayered thermal barrier coating systems. *Journal of the European Ceramic Society*, 2020, vol. 40, no. 8, pp. 2731–2745. DOI: [10.1016/j.jeurceramsoc.2020.03.016](https://doi.org/10.1016/j.jeurceramsoc.2020.03.016).
- Thakare J.G., Pandey Ch., Mahapatra M.M., Mulik R.S. Thermal barrier coatings – A state of the art review. *Metals and Materials International*, 2021, vol. 27, pp. 1947–1968. DOI: [10.1007/s12540-020-00705-w](https://doi.org/10.1007/s12540-020-00705-w).
- Cernuschi F., Bison P. Thirty Years of Thermal Barrier Coatings (TBC), Photothermal and thermographic techniques: Best practices and lessons learned. *Journal of Thermal Spray Technology*, 2022, vol. 31, no. 4, pp. 716–744. DOI: [10.1007/s11666-022-01344-w](https://doi.org/10.1007/s11666-022-01344-w).
- Tejero-Martin D., Bennett C., Hussain T. A review on environmental barrier coatings: History, current state of the art and future developments. *Journal of the European Ceramic Society*, 2021, vol. 41, no. 3, pp. 1747–1768. DOI: [10.1016/j.jeurceramsoc.2020.10.057](https://doi.org/10.1016/j.jeurceramsoc.2020.10.057).
- Liu Yuchen, Zhang Wei, Wang Banghui, Sun Luchao, Li Fangzhi, Xue Zhenhai, Zhou Guohong, Liu Bin, Nian Hanggiang. Theoretical and experimental investigations on high temperature mechanical and thermal properties of BaZrO₃. *Ceramics International*, 2018, vol. 44, no. 14, pp. 16475–16482. DOI: [10.1016/j.ceramint.2018.06.064](https://doi.org/10.1016/j.ceramint.2018.06.064).
- Jarligo M.O., Mack D.E., Vassen R., Stover D. Application of plasma-sprayed complex perovskites as thermal barrier coatings. *Journal of Thermal Spray Technology*, 2009, vol. 18, pp. 187–193. DOI: [10.1007/s11666-009-9302-9](https://doi.org/10.1007/s11666-009-9302-9).
- Guo Hongbo, Zhang Hongju, Ma Guohui, Gong Shengkai. Thermo-physical and thermal cycling properties of plasma-sprayed BaLa₂Ti₃O₁₀ coating as potential thermal barrier materials. *Surface and Coatings Technology*, 2009, vol. 204, no. 5, pp. 691–696. DOI: [10.1016/j.surfcoat.2009.09.009](https://doi.org/10.1016/j.surfcoat.2009.09.009).
- Yuan Jieyan, Sun Junbin, Wang Jinshuang, Zhang Hao, Dong Shujuan, Jiang Jianing, Deng Longhui, Zhou Xin, Cao Xueqiang. SrCeO₃ as a novel thermal barrier coating candidate for high-temperature applications. *Journal of Alloys and Compounds*, 2018, vol. 740, pp. 519–528. DOI: [10.1016/j.jallcom.2018.01.021](https://doi.org/10.1016/j.jallcom.2018.01.021).
- Li Enbo, Ma Wen, Zhang Peng, Zhang Chennan, Bai Yu, Liu Hongxia, Yan Shufang, Dong Hongying, Meng Xiangfeng. The effect of Al³⁺ doping on the infrared radiation and thermophysical properties of SrZrO₃ perovskites as potential low thermal infrared material. *Acta Materialia*, 2021, vol. 209, article number 116795. DOI: [10.1016/j.actamat.2021.116795](https://doi.org/10.1016/j.actamat.2021.116795).
- Plaza A.V., Krause A.R. Mitigating CMAS Attack in Model YAlO₃ Environmental Barrier Coatings: Effect of YAlO₃ Crystal Orientation on Apatite Nucleation. *Coatings*, 2022, vol. 12, no. 10, article number 1604. DOI: [10.3390/coatings12101604](https://doi.org/10.3390/coatings12101604).
- Turcer L.R., Krause A.R., Garces H.F., Lin Zhang, Padture N.P. Environmental-barrier coating ceramics for resistance against attack by molten calcia-magnesia-aluminosilicate (CMAS) glass: Part I, YAlO₃ and γ -Y₂Si₂O₇. *Journal of the European Ceramic Society*, 2018, vol. 38, no. 11, pp. 3905–3913. DOI: [10.1016/j.jeurceramsoc.2018.03.021](https://doi.org/10.1016/j.jeurceramsoc.2018.03.021).
- Gatzen C., Mack D.E., Guillon O., Vaben R. YAlO₃ – a novel environmental barrier coating for Al₂O₃/Al₂O₃–ceramic matrix composites. *Coatings*, 2019, vol. 9, no. 10, article number 609. DOI: [10.3390/coatings9100609](https://doi.org/10.3390/coatings9100609).
- Haftani M., Heydari M.S., Baharvandi H.R., Ehsani N. Studying the oxidation of Ti₂AlC MAX phase in atmosphere: A review. *International Journal of Refractory Metals and Hard Materials*, 2016, vol. 61, pp. 51–60. DOI: [10.1016/j.jrmhm.2016.07.006](https://doi.org/10.1016/j.jrmhm.2016.07.006).
- Badie S., Sebold D., Vaben R., Guillon O., Gonzalez-Julian J. Mechanism for breakaway oxidation of the Ti₂AlC MAX phase. *Acta Materialia*, 2021, vol. 215, article number 117025. DOI: [10.1016/j.actamat.2021.117025](https://doi.org/10.1016/j.actamat.2021.117025).
- Eklund P., Rosen J., Persson P.O. Layered ternary M_{n+1}AX_n phases and their 2D derivative MXene: an overview from a thin-film perspective. *Journal of Physics D: Applied Physics*, 2017, vol. 50, no. 11, article number 113001. DOI: [10.1088/1361-6463/aa57bc](https://doi.org/10.1088/1361-6463/aa57bc).
- Garkas W., Leyens C., Flores-Renteria A. Synthesis and characterization of Ti₂AlC and Ti₂AlN MAX phase coatings manufactured in an industrial-size coater.

- Advanced Materials Research*, 2010, vol. 89, pp. 208–213. DOI: [10.4028/www.scientific.net/AMR.89-91.208](https://doi.org/10.4028/www.scientific.net/AMR.89-91.208).
20. Tang C., Klimenkov M., Jaentsch U., Leiste H., Rinke M., Ulrich S., Steinbruck M., Saifert H.J., Stueber M. Synthesis and characterization of Ti₂AlC coatings by magnetron sputtering from three elemental targets and ex-situ annealing. *Surface and Coatings Technology*, 2017, vol. 309, pp. 445–455. DOI: [10.1016/j.surfcoat.2016.11.090](https://doi.org/10.1016/j.surfcoat.2016.11.090).
 21. Weyant C.M., Faber K.T. Processing–microstructure relationships for plasma-sprayed yttrium aluminum garnet. *Surface and Coatings Technology*, 2008, vol. 202, no. 24, pp. 6081–6089. DOI: [10.1016/j.surfcoat.2008.07.008](https://doi.org/10.1016/j.surfcoat.2008.07.008).
 22. Mechnich P., Braue W. Air plasma-sprayed Y₂O₃ coatings for Al₂O₃/Al₂O₃ ceramic matrix composites. *Journal of the European Ceramic Society*, 2013, vol. 33, no. 13-14, pp. 2645–2653. DOI: [10.1016/j.jeurceramsoc.2013.03.034](https://doi.org/10.1016/j.jeurceramsoc.2013.03.034).
- ### СПИСОК ЛИТЕРАТУРЫ
1. Mondal K., Nunez L., Lii C.M., Downey I.J., Rooyen I.J. Thermal barrier coatings overview: Design, manufacturing, and applications in high-temperature industries // *Industrial & Engineering Chemistry Research*. 2021. Vol. 60. № 17. P. 6061–6077. DOI: [10.1021/acs.iecr.1c00788](https://doi.org/10.1021/acs.iecr.1c00788).
 2. Liu Bin, Liu Yuchen, Zhu Changhua, Xiang Huimin, Chen Hongfei, Sun Luchao, Gao Yanfeng, Zhou Yanchun. Advances on strategies for searching for next generation thermal barrier coating materials // *Journal of Materials Science & Technology*. 2019. Vol. 35. № 5. P. 833–851. DOI: [10.1016/j.jmst.2018.11.016](https://doi.org/10.1016/j.jmst.2018.11.016).
 3. Vaßen R., Bakan E., Mack D.E., Guillon O. A perspective on thermally sprayed thermal barrier coatings: current status and trends // *Journal of Thermal Spray Technology*. 2022. Vol. 31. № 4. P. 685–698. DOI: [10.1007/s11666-022-01330-2](https://doi.org/10.1007/s11666-022-01330-2).
 4. Lashmi P.G., Ananthapadmanabhan P.V., Unnikrishnan G., Aruna S.T. Present status and future prospects of plasma sprayed multilayered thermal barrier coating systems // *Journal of the European Ceramic Society*. 2020. Vol. 40. № 8. P. 2731–2745. DOI: [10.1016/j.jeurceramsoc.2020.03.016](https://doi.org/10.1016/j.jeurceramsoc.2020.03.016).
 5. Thakare J.G., Pandey Ch., Mahapatra M.M., Mulik R.S. Thermal barrier coatings – A state of the art review // *Metals and Materials International*. 2021. Vol. 27. P. 1947–1968. DOI: [10.1007/s12540-020-00705-w](https://doi.org/10.1007/s12540-020-00705-w).
 6. Cernuschi F., Bison P. Thirty Years of Thermal Barrier Coatings (TBC), Photothermal and thermographic techniques: Best practices and lessons learned // *Journal of Thermal Spray Technology*. 2022. Vol. 31. № 4. P. 716–744. DOI: [10.1007/s11666-022-01344-w](https://doi.org/10.1007/s11666-022-01344-w).
 7. Tejero-Martin D., Bennett C., Hussain T. A review on environmental barrier coatings: History, current state of the art and future developments // *Journal of the European Ceramic Society*. 2021. Vol. 41. № 3. P. 1747–1768. DOI: [10.1016/j.jeurceramsoc.2020.10.057](https://doi.org/10.1016/j.jeurceramsoc.2020.10.057).
 8. Liu Yuchen, Zhang Wei, Wang Banghui, Sun Luchao, Li Fangzhi, Xue Zhenhai, Zhou Guohong, Liu Bin, Nian Hanggiang. Theoretical and experimental investigations on high temperature mechanical and thermal properties of BaZrO₃ // *Ceramics International*. 2018. Vol. 44. № 14. P. 16475–16482. DOI: [10.1016/j.ceramint.2018.06.064](https://doi.org/10.1016/j.ceramint.2018.06.064).
 9. Jarligo M.O., Mack D.E., Vassen R., Stover D. Application of plasma-sprayed complex perovskites as thermal barrier coatings // *Journal of Thermal Spray Technology*. 2009. Vol. 18. P. 187–193. DOI: [10.1007/s11666-009-9302-9](https://doi.org/10.1007/s11666-009-9302-9).
 10. Guo Hongbo, Zhang Hongju, Ma Guohui, Gong Shengkai. Thermo-physical and thermal cycling properties of plasma-sprayed BaLa₂Ti₃O₁₀ coating as potential thermal barrier materials // *Surface and Coatings Technology*. 2009. Vol. 204. № 5. P. 691–696. DOI: [10.1016/j.surfcoat.2009.09.009](https://doi.org/10.1016/j.surfcoat.2009.09.009).
 11. Yuan Jieyan, Sun Junbin, Wang Jinshuang, Zhang Hao, Dong Shujuan, Jiang Jianing, Deng Longhui, Zhou Xin, Cao Xueqiang. SrCeO₃ as a novel thermal barrier coating candidate for high-temperature applications // *Journal of Alloys and Compounds*. 2018. Vol. 740. P. 519–528. DOI: [10.1016/j.jallcom.2018.01.021](https://doi.org/10.1016/j.jallcom.2018.01.021).
 12. Li Enbo, Ma Wen, Zhang Peng, Zhang Chennan, Bai Yu, Liu Hongxia, Yan Shufang, Dong Hongying, Meng Xiangfeng. The effect of Al³⁺ doping on the infrared radiation and thermophysical properties of SrZrO₃ perovskites as potential low thermal infrared material // *Acta Materialia*. 2021. Vol. 209. Article number 116795. DOI: [10.1016/j.actamat.2021.116795](https://doi.org/10.1016/j.actamat.2021.116795).
 13. Plaza A.V., Krause A.R. Mitigating CMAS Attack in Model YAlO₃ Environmental Barrier Coatings: Effect of YAlO₃ Crystal Orientation on Apatite Nucleation // *Coatings*. 2022. Vol. 12. № 10. Article number 1604. DOI: [10.3390/coatings12101604](https://doi.org/10.3390/coatings12101604).
 14. Turcer L.R., Krause A.R., Garces H.F., Lin Zhang, Padture N.P. Environmental-barrier coating ceramics for resistance against attack by molten calcia-magnesia-aluminosilicate (CMAS) glass: Part I, YAlO₃ and γ-Y₂Si₂O₇ // *Journal of the European Ceramic Society*. 2018. Vol. 38. № 11. P. 3905–3913. DOI: [10.1016/j.jeurceramsoc.2018.03.021](https://doi.org/10.1016/j.jeurceramsoc.2018.03.021).
 15. Gatzen C., Mack D.E., Guillon O., Vaben R. YAlO₃ – a novel environmental barrier coating for Al₂O₃/Al₂O₃–ceramic matrix composites // *Coatings*. 2019. Vol. 9. № 10. Article number 609. DOI: [10.3390/coatings9100609](https://doi.org/10.3390/coatings9100609).
 16. Haftani M., Heydari M.S., Baharvandi H.R., Ehsani N. Studying the oxidation of Ti₂AlC MAX phase in atmosphere: A review // *International Journal of Refractory Metals and Hard Materials*. 2016. Vol. 61. P. 51–60. DOI: [10.1016/j.jirmhm.2016.07.006](https://doi.org/10.1016/j.jirmhm.2016.07.006).
 17. Badie S., Sebold D., Vaben R., Guillon O., Gonzalez-Julian J. Mechanism for breakaway oxidation of the Ti₂AlC MAX phase // *Acta Materialia*. 2021. Vol. 215. Article number 117025. DOI: [10.1016/j.actamat.2021.117025](https://doi.org/10.1016/j.actamat.2021.117025).
 18. Eklund P., Rosen J., Persson P.O. Layered ternary M_{n+1}AX_n phases and their 2D derivative MXene: an overview from a thin-film perspective // *Journal of Physics D: Applied Physics*. 2017. Vol. 50. № 11. Article number 113001. DOI: [10.1088/1361-6463/aa57bc](https://doi.org/10.1088/1361-6463/aa57bc).
 19. Garkas W., Leyens C., Flores-Renteria A. Synthesis and characterization of Ti₂AlC and Ti₂AlN MAX phase coatings manufactured in an industrial-size coater // *Advanced Materials Research*. 2010. Vol. 89. P. 208–213. DOI: [10.4028/www.scientific.net/AMR.89-91.208](https://doi.org/10.4028/www.scientific.net/AMR.89-91.208).

20. Tang C., Klimenkov M., Jaentsch U., Leiste H., Rinke M., Ulrich S., Steinbruck M., Saifert H.J., Stueber M. Synthesis and characterization of Ti₂AlC coatings by magnetron sputtering from three elemental targets and ex-situ annealing // *Surface and Coatings Technology*. 2017. Vol. 309. P. 445–455. DOI: [10.1016/j.surfcoat.2016.11.090](https://doi.org/10.1016/j.surfcoat.2016.11.090).
21. Weyant C.M., Faber K.T. Processing–microstructure relationships for plasma-sprayed yttrium aluminum garnet // *Surface and Coatings Technology*. 2008. Vol. 202. № 24. P. 6081–6089. DOI: [10.1016/j.surfcoat.2008.07.008](https://doi.org/10.1016/j.surfcoat.2008.07.008).
22. Mechnich P., Braue W. Air plasma-sprayed Y₂O₃ coatings for Al₂O₃/Al₂O₃ ceramic matrix composites // *Journal of the European Ceramic Society*. 2013. Vol. 33. № 13-14. P. 2645–2653. DOI: [10.1016/j.jeurceramsoc.2013.03.034](https://doi.org/10.1016/j.jeurceramsoc.2013.03.034).

Исследование фазовых превращений в двухслойном жаростойком покрытии Ti–Al–C+Y–Al–O на жаропрочном никелевом сплаве

© 2023

Назаров Алмаз Юнирович^{*1,4}, кандидат технических наук,
доцент кафедры технологии машиностроения
Маслов Алексей Андреевич^{1,5}, лаборант кафедры технологии машиностроения
*Николаев Алексей Александрович*¹, ассистент кафедры технологии машиностроения
Шмаков Александр Николаевич^{2,3}, ведущий научный сотрудник
*Денисов Владимир Викторович*³, кандидат технических наук,
заведующий лабораторией пучково-плазменной инженерии поверхности
*Рамазанов Камиль Нуруллаевич*¹, доктор технических наук,
заведующий кафедрой технологии машиностроения

¹Уфимский университет науки и технологий, Уфа (Россия)²Федеральный исследовательский центр «Институт катализа им. Г.К. Борескова СО РАН», Новосибирск (Россия)³Институт сильноточной электроники СО РАН, Томск (Россия)*E-mail: nazarov_almaz15@mail.ru,
nazarov.ayu@ugatu.su⁴ORCID: <https://orcid.org/0000-0002-4711-4721>⁵ORCID: <https://orcid.org/0000-0002-2568-1784>

Поступила в редакцию 03.07.2023

Принята к публикации 17.11.2023

Аннотация: На сегодняшний день происходит активный рост требований к топливной эффективности и удельному весу авиационных турбореактивных двигателей. Существующие покрытия для защиты деталей двигателей на основе диоксида циркония во многом устарели и исчерпали потенциал развития, поэтому ведутся исследования новых керамических систем для производства защитных покрытий на их основе. В работе проведено исследование жаростойкого двухслойного покрытия на основе системы Y–Al–O (внешний слой) и MAX-фазы Ti₂AlC системы Ti–Al–C (подслой), полученного методом вакуумно-дугового осаждения на жаропрочном никелевом сплаве Inconel 738 и на молибдене поочередным осаждением слоев на основе Ti–Al–C и слоя Y–Al–O. При помощи синхротронного излучения исследованы фазовые превращения в покрытии при нагреве образцов до 1400 °C в вакууме и до 1100 °C в атмосфере с целью изучения процесса окисления и формирования покрытия в условиях присутствия кислорода. При помощи растровой электронной микроскопии изучены микроструктура и химический состав покрытия. Установлено, что нагрев покрытия в вакууме и в атмосфере вызывает в нем различные фазовые превращения, но в обоих случаях наблюдается формирование смеси оксидов группы Y–Al–O и дестабилизация подслоя на основе Ti–Al–C. После нагрева покрытия в атмосфере без предварительной термообработки при остывании покрытие разрушилось, чего не наблюдалось при нагреве покрытия в вакууме.

Ключевые слова: жаростойкое покрытие; керамическое покрытие; MAX-фаза; оксид иттрия; вакуумно-дуговое осаждение; синхротронное излучение.

Благодарности: Работа выполнена при финансовой поддержке Министерства науки и высшего образования Российской Федерации (проект № 075-15-2021-1348).

Статья подготовлена по материалам докладов участников XI Международной школы «Физическое материаловедение» (ШФМ-2023), Тольятти, 11–15 сентября 2023 года.

Для цитирования: Назаров А.Ю., Маслов А.А., Николаев А.А., Шмаков А.Н., Денисов В.В., Рамазанов К.Н. Исследование фазовых превращений в двухслойном жаростойком покрытии Ti–Al–C+Y–Al–O на жаропрочном никелевом сплаве // *Frontier Materials & Technologies*. 2023. № 4. С. 63–71. DOI: 10.18323/2782-4039-2023-4-66-6.

Simulation of electrical parameters of a galvanic cell in the process of microarc oxidation

© 2023

Ekaterina A. Pecherskaya¹, Doctor of Sciences (Engineering), Professor,
Head of Chair “Information and Measuring Equipment and Metrology”

Anatoly D. Semenov, Doctor of Sciences (Engineering),
professor of Chair “Information and Measuring Equipment and Metrology”

Pavel E. Golubkov^{*2}, PhD (Engineering),
assistant professor of Chair “Information and Measuring Equipment and Metrology”

Penza State University, Penza (Russia)

*E-mail: iit@pnzgu.ru,
golpavpnz@yandex.ru

¹ORCID: <https://orcid.org/0000-0001-5657-9128>

²ORCID: <https://orcid.org/0000-0002-4387-3181>

Received 26.06.2023

Accepted 11.12.2023

Abstract: Microarc oxidation is a promising technology for producing wear-resistant anticorrosive coatings for goods made of valve metals and alloys and is used in many industries. One of the main problems of this technology is low controllability caused by the complexity and interconnectedness of physical and chemical phenomena occurring during the coating process. To solve such problems, digital twins are currently actively used. The paper covers the development of mathematical models that are advisable to use as structural elements of the digital twin of the microarc oxidation process. An equivalent electrical circuit of a galvanic cell of microarc oxidation is given, which takes into account the electrolyte resistance, the part coating resistance in the form of a parallel connection of nonlinear active resistance and capacitive reactance. The authors propose a mathematical model describing the behaviour of the equivalent electrical circuit of a galvanic cell of microarc oxidation. A technique for determining the parameters of this model was developed, including the construction of a waveform of changes in the resistance of the cell and its approximation, estimation of the values of resistances and capacitance of the galvanic cell equivalent circuit. The authors proposed a calculation method and developed a Simulink model of the microarc oxidation process, which allows simulating the current and voltage waveforms of a galvanic cell. The analysis of the model showed that the model is stable, controllable and observable, but poorly conditioned, which leads to modelling errors, the maximum value of which is 7 % for voltage and 10 % for current. By the parametric identification method using experimental current and voltage waveforms, the dependences of the parameters of the galvanic cell equivalent circuit on the oxidation time are obtained. It is found that the change in the period average of the galvanic cell active resistance correlates with the coating thickness.

Keywords: microarc oxidation; equivalent electrical circuit; mathematical model; Simulink model; coating resistance and capacitance; model adequacy.

Acknowledgments: This work was supported by the Ministry of Science and Higher Education of the Russian Federation, project No. 1022041100284-5-2.3.1.

The paper was written on the reports of the participants of the XI International School of Physical Materials Science (SPM-2023), Togliatti, September 11–15, 2023.

For citation: Pecherskaya E.A., Semenov A.D., Golubkov P.E. Simulation of electrical parameters of a galvanic cell in the process of microarc oxidation. *Frontier Materials & Technologies*, 2023, no. 4, pp. 73–85. DOI: 10.18323/2782-4039-2023-4-66-7.

INTRODUCTION

Microarc oxidation (MAO) is used to improve the mechanical and physicochemical properties of the surfaces of parts made of aluminium alloys. The process is applicable both to aluminium and to other valve group metals, such as Ti, Zr, Mg, and Ta. The combination of high microhardness and wear resistance with corrosion resistance of coatings produced by the MAO method ensures the widespread application of products with such coatings in many industries [1; 2]. However, at present there are a number of unresolved issues hindering the MAO technology development, the main of which are high energy consumption [3; 4], and low controllability of the technological process, associated with the combined influence of many different factors on the properties of the formed coatings [5; 6].

Currently, one of the promising ways to manage complex production processes is the use of digital twins, which allows simulating and predicting the behaviour of a real object in the virtual world, using information received from sensors on the object throughout its entire life cycle. In this case, as a rule, models of real system components are known or easily created using CAD systems, such as, for example, 3D models in mechanical engineering production [7]. However, for complex multifactor technological processes, such as MAO, the process of creating a digital twin is significantly complicated due to the imperfection or absence of mathematical models of some physical phenomena, leading to the formation of oxide coatings. Many works are concerned with the study of the mechanism of coating formation during MAO [8; 9], however, only some of them provide its analytical description. Thus, in the review paper [10] dealing with the MAO of titanium alloys, there is

a sufficiently detailed mathematical interpretation of the mechanism of electrolysis at high voltage, but microplasma processes are not considered. The work [11] gives formulas for calculating the electron temperature of microdischarge plasma during MAO under the local thermodynamic equilibrium conditions, but no relationship with electrochemical processes is traced. Moreover, according to [10; 12], the fundamental theory of plasma electrolysis containing an analytical description of different phenomena (electrochemical, microplasma, etc.) occurring in the process of MAO as a single interconnected system, has not currently been developed.

Thus, an urgent scientific task is to build a mathematical model that could serve as the basis for a digital twin of the MAO process. At a first approximation, this model should estimate the thickness of the formed coatings based on the hidden information contained in the waveforms of current and voltage measured during the MAO process, by identifying the parameters of the galvanic cell equivalent circuit.

The purpose of the study is to identify the parameters of the equivalent electrical circuit of a galvanic cell, that correlate with the thickness of MAO coatings, and to develop a methodology for determining these parameters.

METHODS

During the study, 30 samples of MAO coatings were produced on blanks made of AD31 commercially pure aluminium, GOST 4784-97 (2000) (Table 1), with the dimensions of 20×15×2 mm. The MAO coatings were formed using an automated MAO installation developed by the authors containing a technological current source, measuring channels for current, voltage and electrolyte temperature, and a control module based on a microcontroller. The technological current source of this system is a series connection of a bank of capacitors with adjustable capacitance and a galvanic cell. The technological current source is powered by sinusoidal voltage from a 220 V 50 Hz mains. Before starting the MAO process, the amplitude value of the current through the galvanic cell was set by changing the capacitor bank capacitance (connecting the required number of capacitors), which remained constant until the MAO processing completion. MAO was carried out for 30 min at a current density of 5 A/dm² in the anodic-cathode mode with the ratio of the anodic, and cathodic current equal to 1, in an electrolyte of the NaOH (2 g/l), Na₂SiO₃ (9 g/l) composition, and the first sample was processed for 1 min, the second – for 2 min, etc. Every minute, waveforms of two periods of the forming voltage and current in the galvanic cell were measured using measuring channels built into the MAO installation, with a relative error of ±0.5 % and a sampling frequency of 128 points per period equal to the supply voltage period (20 ms). The electrolyte temperature, during the coating process did not exceed 30 °C. After processing, samples with MAO coatings were removed from the galvanic cell, washed with distilled water and dried. The thickness of the coatings was measured on transverse sections using a Mitaka PF-60 3D contour measuring station-profilometer. Software processing of the obtained experimental dependencies was carried out in the MATLAB+Simulink environment.

RESULTS

Mathematical model of the microarc oxidation process

Fig. 1 shows a characteristic view of experimentally measured waveforms of the galvanic cell voltage and current. The deviation of the forming voltage from the sinusoidal shape is caused by the supply voltage imperfection, as well as by the one-sided conductivity of the "anode – coating – electrolyte – cathode" system, as a result of which voltage rectification is observed (the so-called "valve effect"). Breaks in the voltage waveforms occurring in the anode half-cycle at a voltage of about 320 and 370 V are associated with the ignition and extinguishing of microdischarges. The difference between the current shape and the sinusoidal one (triangular current pulses in the anode and cathode half-cycles), is caused by the electrical breakdown of the oxide layer, which occurs only at the sinusoid peak, when the voltage on the sample exceeds the breakdown voltage. The nonlinearity of the current-voltage characteristics indicates the nonlinear nature of the coating formation process, and the presence of hysteresis with a characteristic loop indicates the capacitive nature of the load. To construct a mathematical model of the MAO process, we will use the nonlinear electrophysical model developed in [13] in the form of an electrical equivalent circuit of a galvanic cell (Fig. 2).

The electrolyte resistance is simulated by R_1 active resistance, the coating resistance is simulated by a parallel connection of R_2 nonlinear active resistance and C_2 capacitance reactance. C_1 capacitance connected in series with the galvanic cell does not belong to the sample under study, and is intended to simulate the output signal of the technological current source (current limiting in the circuit).

The mathematical model describing the behaviour of the MAO electrical equivalent circuit of the galvanic cell (Fig. 2) is as follows:

$$\begin{cases} \frac{1}{C_1} \int I_1 dt + R_1 I_1 + R_2(U_1) I_2 = U \\ \frac{1}{C_2} \int I_3 dt - R_2(U_1) I_2 = 0 \\ U_1 = U - \frac{1}{C_1} \int I_1 dt \\ I_1 = I_2 + I_3 \end{cases} \quad (1)$$

Let us change a model (1) to a state space model:

$$\begin{cases} \frac{dx}{dt} = \mathbf{Ax} + \mathbf{BU} \\ y = \mathbf{Cx} + \mathbf{DU} \end{cases} \quad (2)$$

where $\mathbf{x} = (I_1 \quad I_2)^T$;

$y = I_1 + \frac{U}{R_1}$;

$$\mathbf{A} = \begin{pmatrix} -\frac{C_1 + C_2}{C_1 C_2 R_1} & \frac{1}{C_2 R_1} \\ \frac{1}{C_2 R_2} & -\frac{1}{C_2 R_2} \end{pmatrix};$$

$$\mathbf{B} = \begin{pmatrix} \frac{1}{R_1} \\ 0 \end{pmatrix};$$

$$\mathbf{C} = (0 \ 1);$$

$$\mathbf{D} = 0; R_2 = f(U_1).$$

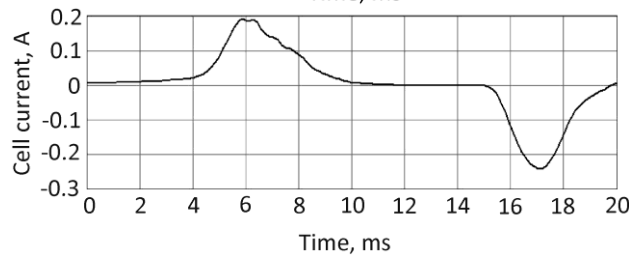
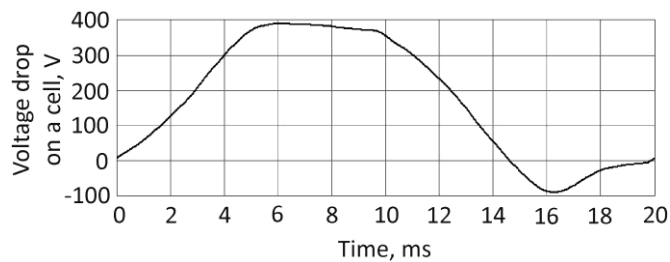
Let us estimate the parameters of the model of the MAO electrical equivalent circuit of the galvanic cell. Three equivalent circuit parameters are evaluated: the R_1 electrolyte active resistance, the R_2 nonlinear active resistance of the coating and its C_2 equivalent capacitance.

Since the model is nonlinear, the use of traditional identification methods is impractical and can lead to unacceptable errors in determining the model parameters. In this regard, the authors propose a sequential procedure for determining the model parameters.

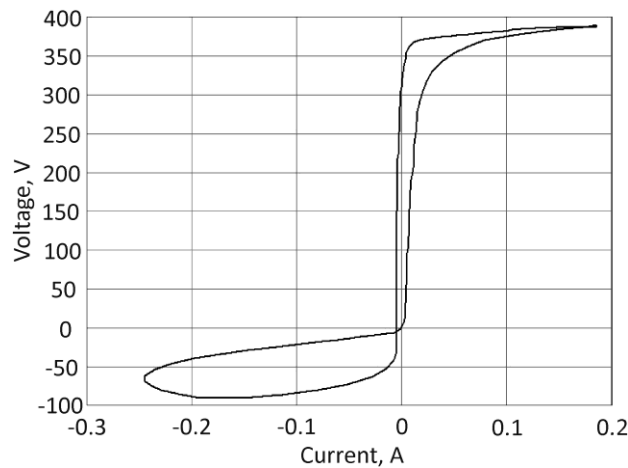
1. Construction of a waveform of changes in cell resistance and its approximation. To construct a waveform of changes in cell resistance, we find the derivative of the current-voltage characteristics:

Table 1. AD31 alloy composition
Таблица 1. Состав сплава АД31

Element	Si	Fe	Cu	Mn	Mg	Cr	Zn	Ti	Others	Al
Content, wt. %	0.2–0.6	0.5	0.1	0.1	0.45–0.9	0.1	0.2	0.15	0.15	The rest



a



b

Fig. 1. Waveforms of voltage and current of a galvanic cell (a) and its current-voltage characteristics (b)
Рис. 1. Осциллограммы напряжения и тока гальванической ячейки (a) и ее вольтамперная характеристика (b)

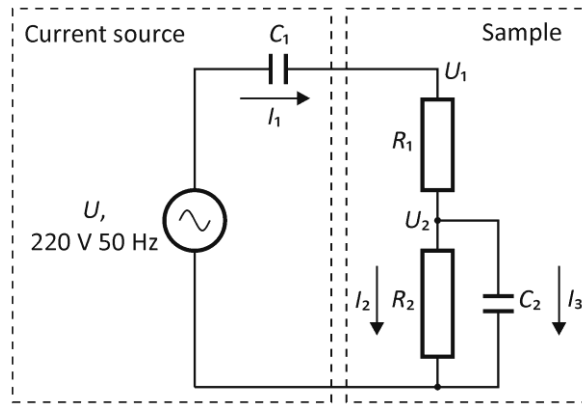


Fig. 2. An equivalent electrical circuit of the MAO process
 Рис. 2. Электрическая схема замещения процесса МДО

$$R_1 + R_2 \approx \frac{\Delta U_1}{\Delta I_1} \quad (3)$$

Fig. 3 shows waveforms of U_1 voltage, I_1 current and total resistance calculated by formula (3). It can be observed that the waveform of the total resistance of the galvanic cell contains four characteristic sections. In the first section ($\approx 2-7$ ms), coating breakdown occurs with a positive half-wave of the voltage applied to it, and the coating resistance sharply drops to a value of the order of 100Ω . In the second section ($\approx 7-13$ ms), the current in the cell changes polarity, and the coating resistance is restored to its original value of approximately $12 \text{ k}\Omega$. In the third section ($\approx 13-17$ ms), coating breakdown occurs with a negative voltage drop. In the fourth section ($\approx 17-22$ ms), the voltage on the cell changes sign and the coating resistance is restored.

It is known that the electrolyte specific conductivity lies in the range of $6.75 \dots 22.5 \text{ mS} \cdot \text{cm}^{-1}$ [14]. Assuming that the R_1 electrolyte resistance remains constant, one can consider that the coating resistance nonlinearly depends on the voltage applied to it and the current flowing through it.

The resulting waveforms allow finding the dependence $R_1 + R_2 = f(U_1)$, which is shown in Fig. 4. The values of the approximating curve of the dependence of the cell resistance on the voltage applied to it are summarised in Table 2.

Fig. 5 shows the approximation of the calculated cell resistance curve presented in Table 2 by a cosine equation

$$R_1 + R_2 = 70 \cdot \left(1 - \cos \left(\frac{U_1 - 150}{96} \right) \right)$$

2. Estimation of the value of R_1 and R_2 resistances. Taking into account that after the breakdown the R_2 coating resistance is close to zero, the estimate of R_1 will be

$$R_1 = \min(R_n), \quad (4)$$

where R_{im} is the set of galvanic cell impedances formed in the coating breakdown areas.

Fig. 6 shows areas of cell low resistance corresponding to time intervals from 2 to 7 ms and from 13 to 17 ms (see Fig. 3). The average resistance value in these sections is $R_{2f} = 163 \Omega$, which is an estimate of the R_2 low resistance value. An estimate of the high value of R_2 resistance can be the average value of the resistances taken from Table 2, which corresponds to the value of $R_{2h} = 5.9 \text{ k}\Omega$. In accordance with (4), the estimate of the R_1 electrolyte resistance will be equal to $R_1 = 22 \Omega$.

3. Estimation of the C_2 cell capacitance value. To estimate C_2 , write an expression for the conductivity transfer function. From (1), it follows that

$$W(p) = \frac{I_1(p)}{U_1(p)} = \frac{R_2 C_2 p + 1}{R_1 R_2 C_2 p + R_1 + R_2} \quad (5)$$

Using the MATLAB System Identification Toolbox application, let us find the parameters of the cell conductivity transfer function. As a result, the following time constants of the transfer function were obtained:

$$\begin{aligned} T_1 &= R_1 R_2 C_2 = 0,002417 \text{ s} \\ T_2 &= R_2 \hat{C}_2 = 0,0009829 \text{ s} \end{aligned} \quad (6)$$

Let us take the value of R_2 resistance equal to its average value over the period of supply voltage $R_{2av} = 4.4 \text{ k}\Omega$. Then, according to (6), the estimate of C_2 capacitance will be equal to $C_2 = 0.22 \mu\text{F}$.

Calculation of time and frequency characteristics of the model of the microarc oxidation process

From knowing the estimate of the model parameters (2), it is easy to calculate its time and frequency characteristics, using the MATLAB Control System Toolbox application. The main characteristics of the linearised model of the MAO process were calculated for the coating breakdown (short-circuit) and open-circuit modes, when the coating resistance is high (Fig. 7).

The transfer functions of conductivity with respect to I_2 current have the form:

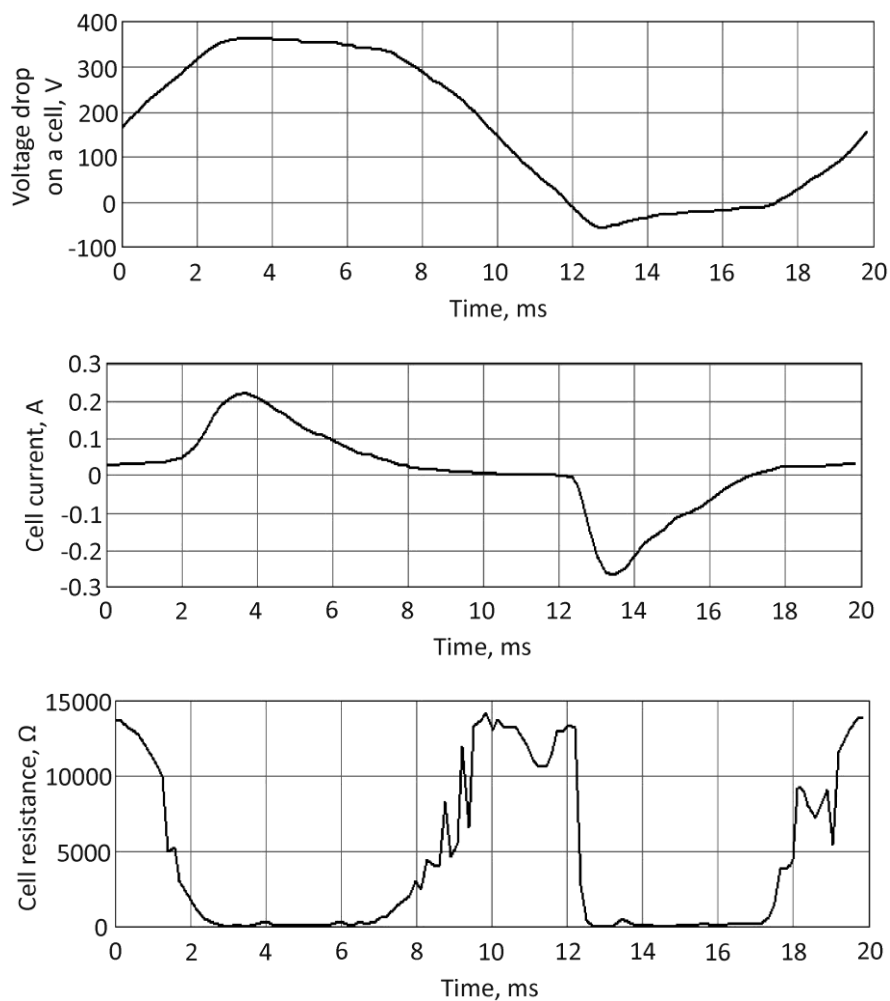


Fig. 3. Waveforms of voltage, current and resistance of a galvanic cell
Рис. 3. Осциллограммы напряжения, тока и сопротивления гальванической ячейки

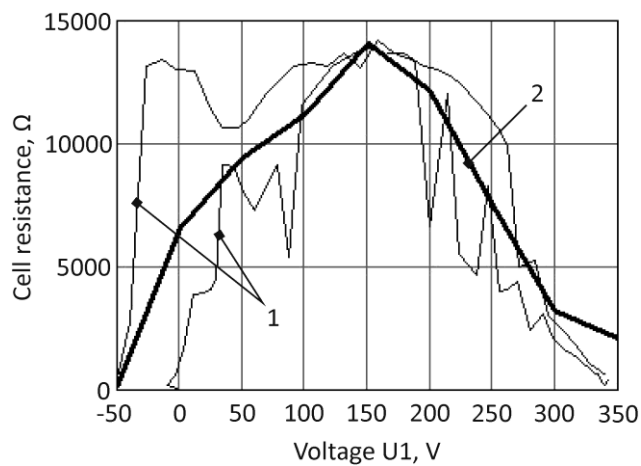


Fig. 4. Dependences of cell resistance on voltage applied to it
Рис. 4. Зависимости сопротивления ячейки от приложенного к ней напряжения

Table 2. Approximating curve values
Таблица 2. Значения аппроксимирующей кривой

Voltage, V	-100	-50	0	50	100	150	200	250	300	350	400
Resistance, kΩ	0.15	0.15	6.6	9.4	11.2	14.1	12.2	7.5	3.2	2.1	0.15

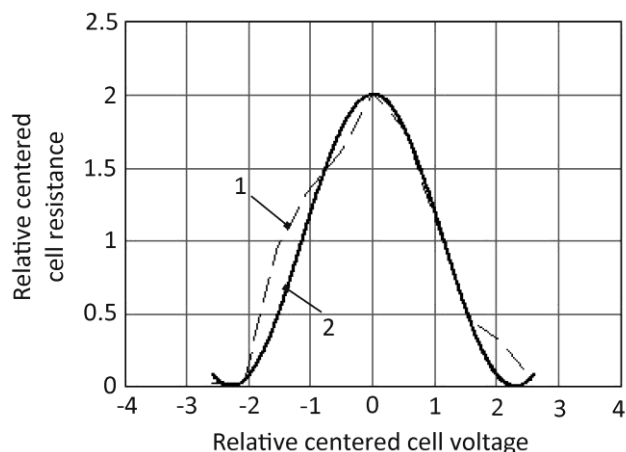


Fig. 5. Approximation of the calculated curve of cell resistance by the cosine equation
Рис. 5. Аппроксимация расчетной кривой сопротивления ячейки уравнением косинуса

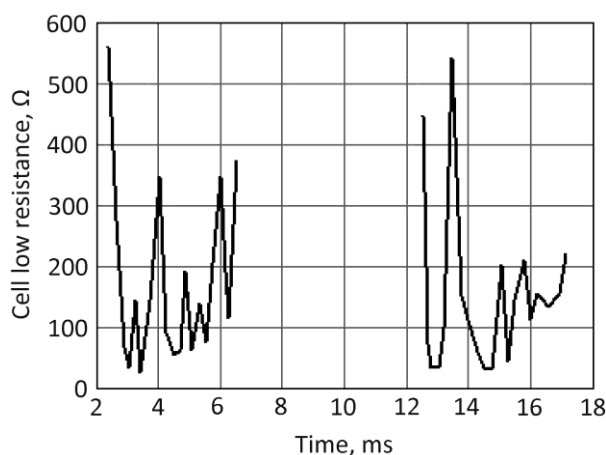


Fig. 6. Cell low resistance areas
Рис. 6. Участки низкого сопротивления ячейки

$$w_{i2} = \frac{46,957 \cdot s}{(s + 2,179 \cdot 10^5)(s + 48,97)} ;$$

$$w_{i2k} = \frac{46,957 \cdot (s - 5,639 \cdot 10^6)}{(s + 2,436 \cdot 10^5)(s + 11,82)} ,$$

where k index indicates the short-circuit model.

The accuracy of determining the parameters of the galvanic cell equivalent circuit using the parametric identification method was assessed in terms of stability, controllability, observability, and conditionality of the model using the time and frequency characteristics of the MAO process model. The authors revealed that the model is stable, since the performance equation roots are negative. The model is controllable and observable, since the ranks of the controllability and observability matrices are equal to the order of the system, but the model is poorly conditioned, which can

lead to significant errors in its parametric identification. The condition numbers for the open-circuit R_{oc} and short-circuit R_{sc} models are 8410 and 317, respectively. A large value of the model condition number indicates its poor conditioning, i. e., a small change in the input signal can lead to a fairly large change in the output signal, which introduces an error into the modeling results.

Simulation of current and voltage waveforms in the MAO process

The construction of a mathematical model (1) of the MAO process and the assessment of its parameters allow proceeding to modelling the process under consideration. The MAO process modelling was carried out in Simulink. Fig. 8 presents the simulation results. It is found that the maximum voltage modelling error in relation to the U_{max} amplitude value does not exceed 7 %, the maximum current modelling error in relation to the I_{max} amplitude value does not exceed 10 %.

Methodology for determining the significant parameters of the galvanic cell equivalent circuit of the MAO process

Based on the proposed mathematical models, a technique has been developed that allows establishing which parameters of the galvanic cell equivalent circuit change most significantly with increasing coating thickness during the MAO process. The technique is implemented as follows.

1. During the MAO-coating formation, 30 waveforms of the voltage drop and current drop of the galvanic cell are recorded sequentially every minute.
2. In each experiment, $R_{1i}+R_{2i}$ are calculated using formula (3) and the estimate of $R_1=\min(R_{1i}+R_{2i})$ is found.
3. The instantaneous value of R_2 resistance is calculated in each experiment:

$$R_1 + R_{2i} \approx \frac{\Delta U_{1i}}{\Delta I_{1i}}.$$

4. The time dependence of the period average R_2 resistance value is constructed (Fig. 9).

5. In each experiment, using the MATLAB System Identification Toolbox application, the parameters of the transfer function (5) are calculated.

6. Using formulas (6), taking $R_2=4400 \Omega$, the C_2 capacitance, the change graph of which is shown in Fig. 10 is calculated.

DISCUSSION

The developed MAO process models make it possible, using the parametric identification method, to estimate the numerical values of the parameters of the nonlinear electrical equivalent circuit of the galvanic cell, as well as to identify the most significant parameters correlating with the thickness of the coatings.

The nonlinear electrophysical model, used in the calculations in the form of a galvanic cell electrical equivalent circuit is simplified, and does not take into account some features of the process of formation of MAO-coatings. One of the sources of error of a model is the use of ideal C ca-

pacitance to simulate the oxide layer, while in electrochemical processes they usually use constant-phase elements CPE, with decomposition into a frequency-independent Q factor, and an n indicator of the degree of heterogeneity of the system [15; 16]. Nevertheless, the model gives satisfactory results (the maximum error in simulating the volt-ampere characteristic is no more than ± 7 % for voltage, no more than ± 10 % for current), and to a first approximation, can be used to formalise the coating deposition process.

The developed technique for sequential determination of the parameters of the galvanic cell equivalent circuit is physically justified, since the shape of the resulting waveform of changes in the total cell resistance confirms the existing ideas about the MAO process mechanism [17; 18]. For example, Fig. 3 clearly shows areas of the galvanic cell low resistance at maximum anodic and cathodic voltages corresponding to dielectric coating breakdown with subsequent ignition of microdischarges.

As can be observed in Fig. 4, the coating resistance value is 12–15 k Ω . On the other hand, it is known that the impedance modulus of oxide layers on aluminium alloys reaches values of 20–200 M $\Omega \cdot \text{cm}^2$, and the polarisation resistance reaches 130–150 M $\Omega \cdot \text{cm}^2$ and higher [15; 19]. The revealed discrepancy in the coating resistance values is explained by the fact that the known impedance modulus values were obtained at a low frequency (up to 10 Hz), and in this study the impedance was calculated using the current-voltage characteristics measured at a frequency of 50 Hz. According to available data [16], at this frequency, the coating impedance modulus is of the order of 10^4 – $10^5 \Omega/\text{cm}^2$, which is consistent with the experimental results.

In the graph of the dependence of the galvanic cell resistance on the forming voltage (Fig. 4), a maximum is observed, the presence of which is determined by the choice of a relatively simple approximating function (cosine equation) and is not associated with physical phenomena occurring in the galvanic cell. The choice of a simple approximating function improves the conditionality of the initially poorly conditioned equation for the MAO process dynamics. In fact, a sharp decrease in the R_2 resistance of the barrier layer is caused by its electrical breakdown by both positive and negative half-waves of the voltage applied to the galvanic cell. During the positive half-cycle, breakdown occurs at a voltage of about +320 V, during the negative half-cycle – about –40 V. Electrical breakdown of the barrier layer at the bottom of the pores when the electrolyte is depleted in ions leads to electrolyte boiling, the appearance of a vapour-gas bubble, and the ignition of a microarc discharge in it. The recovery of the barrier layer resistance is associated with the microarc discharge damping, which occurs because of an increase in the size and the vapour-gas bubble exit beyond the pore, and an accompanying drop in the field strength in it [16; 20]. Thus, the complex form of change in the R_2 barrier layer resistance is caused by a combination of various physical and chemical processes occurring in the pore channels of the barrier layer during the processes of its breakdown and recovery.

Fig. 8 presents the results of modelling the galvanic cell current and voltage waveforms in the Simulink environment. It can be observed that the calculated dependence, well approximates, the experimental curve in the anodic

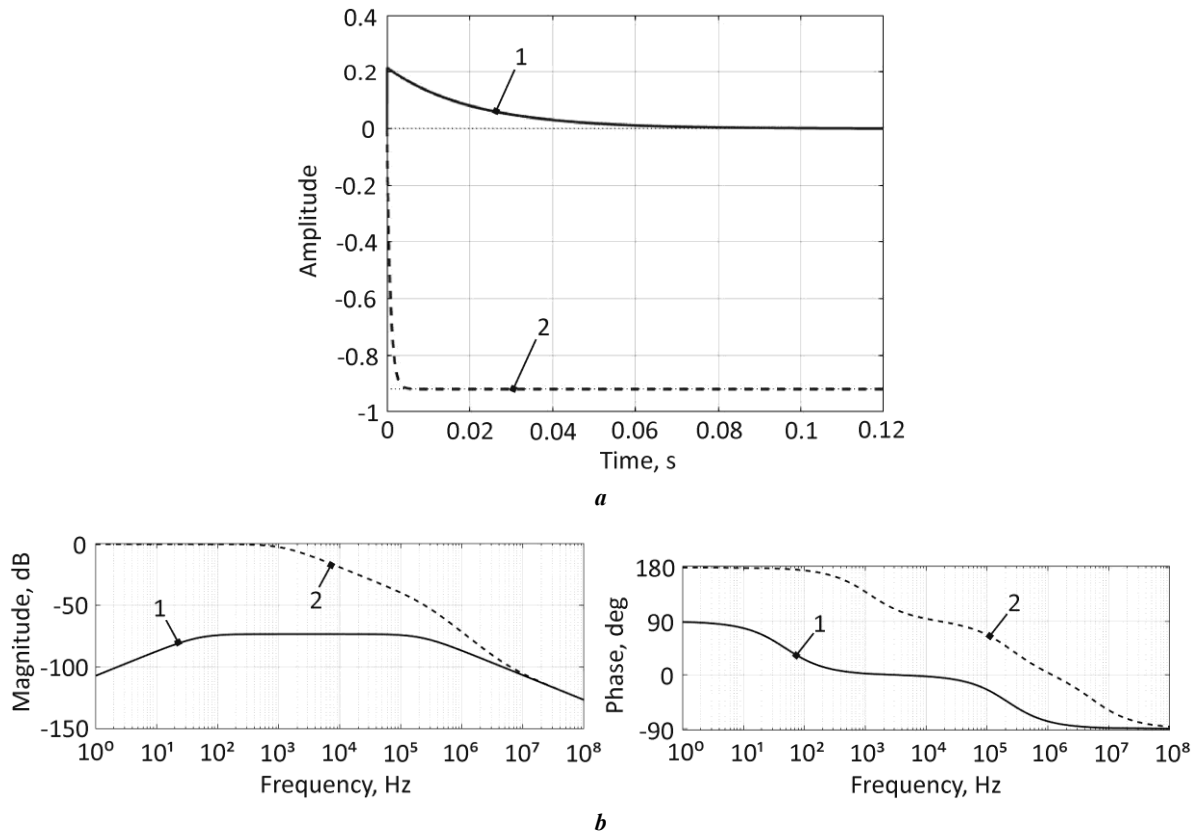


Fig. 7. Time (a) and frequency characteristics (b) of the MAO process model
Рис. 7. Временные (a) и частотные характеристики (b) модели процесса МДО

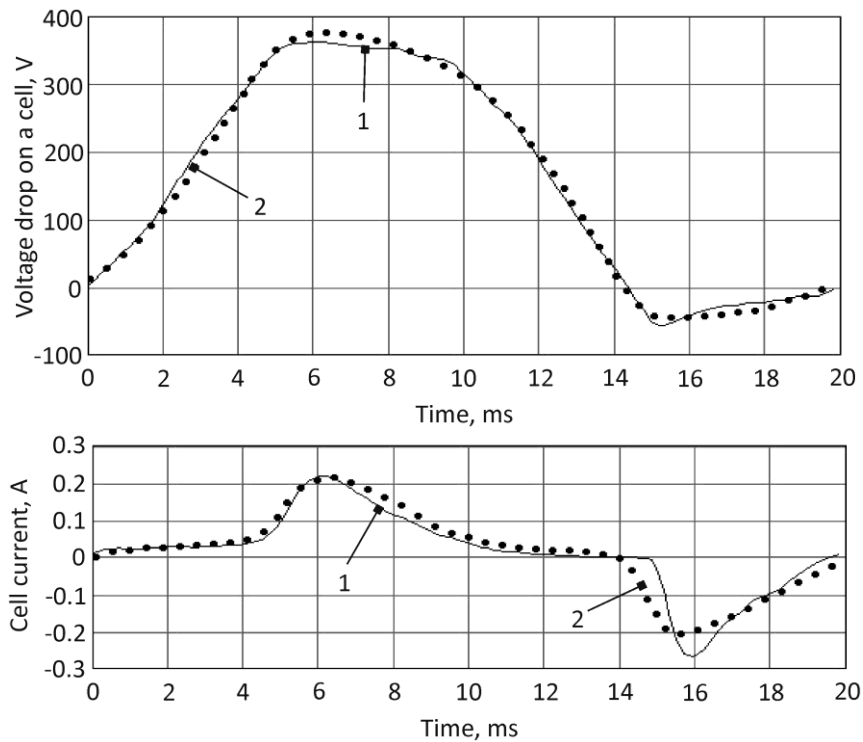


Fig. 8. Experimental and calculated waveforms of galvanic cell voltage and current
Рис. 8. Экспериментальные и расчетные осциллограммы напряжения и тока гальванической ячейки

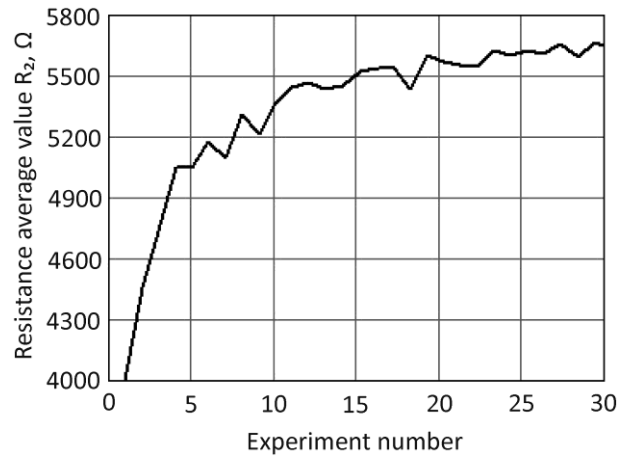


Fig. 9. Change in the period average value of R_2 resistance in each experiment
Рис. 9. Изменение за период среднего значения сопротивления R_2 в каждом опыте

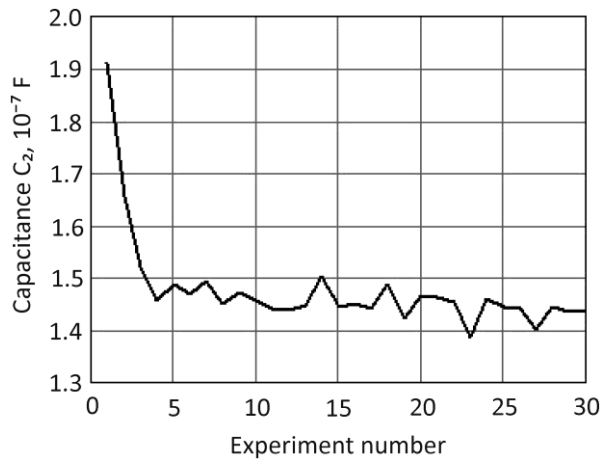


Fig. 10. Change in capacitance C_2
Рис. 10. Изменение емкости C_2

half-cycle, while in the cathodic half-cycle the discrepancy between these curves becomes significant. This is caused by the fact that the proposed electrical equivalent circuit of a galvanic cell, does not fully reflect the behaviour of a real electrochemical system, as well as by the error of the parametric identification method and the poor conditionality of the model.

Fig. 9 and 10 present the results of applying the developed technique for determining the significant parameters of the galvanic cell equivalent circuit of the MAO process. To identify the degree of relationship between resistance and capacitance and coating thickness, the authors performed a correlation analysis, during which point and interval estimates of the correlation factor were obtained using the Fisher criterion with a confidence probability of 95 %. The results of the correlation analysis are presented in Fig. 11 and Table 3. It can be observed that there is a strong direct correlation between resistance and coating thickness; in the case of capacitance, an inverse correlation occurs, but it is less pronounced (perhaps this is due to the peculiarities

of the galvanic cell equivalent circuit and the error of the model). Thus, as a significant parameter for determining the thickness of coatings in the MAO process, it is reasonable to use the coating resistance calculated according to the proposed technique using the current-voltage characteristics of the galvanic cell.

Taking into account the above, the authors can conclude the following. The proposed mathematical model fundamentally provides the ability of determining the thickness of coatings during the MAO process, despite the low accuracy. Moreover, the model allows reproducing waveforms of the galvanic cell current and voltage, which satisfactorily approximate the experimental data. Improving the model taking into account electrochemical impedances will allow improving the simulation accuracy, the result reproducibility and its convergence with experiment, and the use of experimental waveforms from the updated database in calculations, will provide the ability of predicting the thickness of coatings for various MAO processing modes.

Table 3. Correlation analysis results
Таблица 3. Результаты корреляционного анализа

Coating parameter	Correlation factor	Confidence interval
Resistance	0.968	[0.93; 0.98]
Capacitance	-0.611	[-0.80; -0.30]

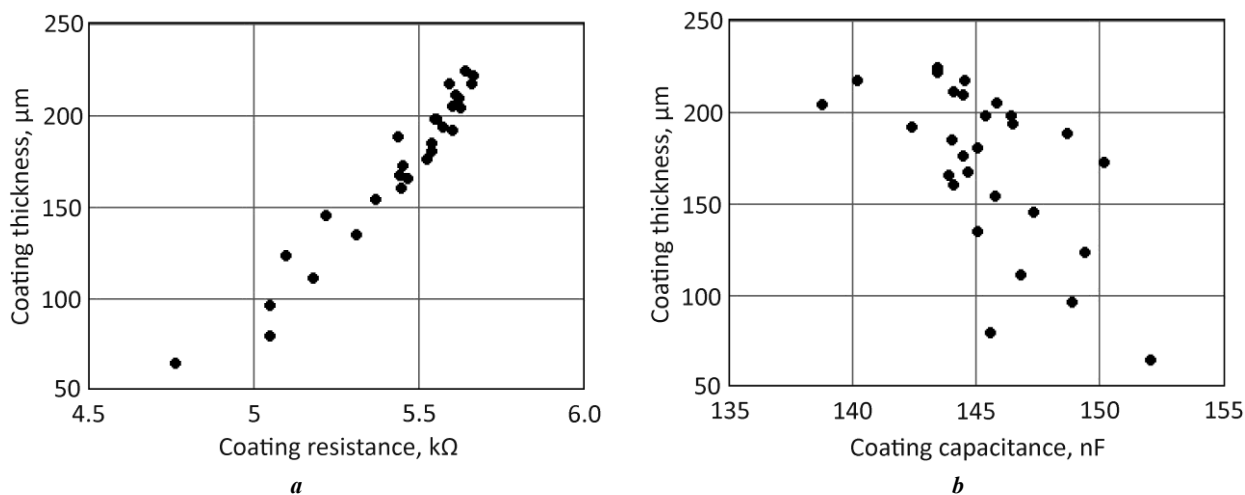


Fig. 11. Scattering graphs for coating resistance (a) and capacitance (b)
Рис. 11. Диаграммы рассеяния для сопротивления (a) и емкости (b) покрытия

The results of the study can be used both in scientific research when developing digital twins and automated control systems for the MAO process, and in production when developing the technology for applying microarc oxide coatings.

CONCLUSIONS

The proposed mathematical model based on the electrical equivalent circuit of a galvanic cell, reflects the relationship between current and voltage in a galvanic cell, and allows simulating current and voltage waveforms during the MAO process with an error of no more than $\pm 10\%$. The model is simplified; it does not take into account some physical and chemical laws of the oxide coating formation, which is its disadvantage. Nevertheless, the model has satisfactory accuracy, which allows using the calculation results as an initial approximation, when estimating the electrical parameters of coatings.

The developed technique for identifying the proposed model parameters allows determining the time dependences of the coating resistance, and capacitance during the MAO process using experimentally obtained waveforms of current and voltage in a galvanic cell. Using the correlation analysis method, the degree of relationship between these parameters, and the coating thickness was established. A strong correlation was found between resistance and coating thickness, which allows using the coating resistance

as a significant parameter for assessing the thickness of the coating during its formation.

Using the developed identification technique, the parameters of the electrical equivalent circuit of the galvanic cell correlating with the thickness of MAO-coatings were identified.

REFERENCES

1. Yu Ji-Min, Choe Han-Cheol. Morphology Changes and Bone Formation on PEO-treated Ti-6Al-4V Alloy in Electrolyte Containing Ca, P, Sr, and Si Ions. *Applied Surface Science*, 2019, vol. 477, pp. 121–130. DOI: [10.1016/j.apsusc.2017.11.223](https://doi.org/10.1016/j.apsusc.2017.11.223).
2. Simchen F., Sieber M., Kopp A., Lampke Th. Introduction to Plasma Electrolytic Oxidation – An Overview of the Process and Applications. *Coatings*, 2020, vol. 10, no. 7, article number 628. DOI: [10.3390/coatings10070628](https://doi.org/10.3390/coatings10070628).
3. Troughton S.C., Nomine A., Nomine A.V., Henrion G., Clyne T.W. Synchronised electrical monitoring and high speed video of bubble growth associated with individual discharges during plasma electrolytic oxidation. *Applied Surface Science*, 2015, vol. 359, pp. 405–411. DOI: [10.1016/j.apsusc.2015.10.124](https://doi.org/10.1016/j.apsusc.2015.10.124).
4. Yang Kai, Zeng Jiaquan, Huang Haisong, Chen Jiadui, Cao Biao. A Novel Self-Adaptive Control Method for Plasma Electrolytic Oxidation Processing of Aluminum

- Alloys. *Materials*, 2019, vol. 12, no. 17, article number 2744. DOI: [10.3390/ma12172744](https://doi.org/10.3390/ma12172744).
5. Pecherskaya E.A., Golubkov P.E., Karpanin O.V., Artamonov D.V., Safronov M.I., Pecherskiy A.V. Study on Effects of Technological Parameters of Micro-Arc Oxidation on Properties of Oxide Coatings. *Izvestiya vysshikh uchebnykh zavedeniy. Elektronika*, 2019, vol. 24, no. 4, pp. 363–369. DOI: [10.24151/1561-5405-2019-24-4-363-369](https://doi.org/10.24151/1561-5405-2019-24-4-363-369).
 6. Tu Wenbin, Zhu Zhunda, Zhuang Xiujuan, Cheng Yingliang, Skeldon P. Effect of frequency on black coating formation on AZ31 magnesium alloy by plasma electrolytic oxidation in aluminate-tungstate electrolyte. *Surface and Coatings Technology*, 2019, vol. 372, pp. 34–44. DOI: [10.1016/j.surfcoat.2019.05.012](https://doi.org/10.1016/j.surfcoat.2019.05.012).
 7. Botin-Sanabria D.M., Mihaita A.-S., Peimbert-Garcia R.E., Ramirez-Moreno M.A., Ramirez-Mendoza R.A., Lozoya-Santos J.J. Digital Twin Technology Challenges and Applications: A Comprehensive Review. *Remote Sensing*, 2022, vol. 14, no. 6, article number 1335. DOI: [10.3390/rs14061335](https://doi.org/10.3390/rs14061335).
 8. Zhu Lujun, Ke Xiaoxing, Li Jingwei, Zhang Yuefei, Zhang Zhenhua, Sui Manling. Growth mechanisms for initial stages of plasma electrolytic oxidation coating on Al. *Surfaces and Interfaces*, 2021, vol. 25, article number 101186. DOI: [10.1016/j.surfint.2021.101186](https://doi.org/10.1016/j.surfint.2021.101186).
 9. Rogov A.B., Huang Yingying, Shore D., Matthews A., Yerokhin A. Toward rational design of ceramic coatings generated on valve metals by plasma electrolytic oxidation: The role of cathodic polarization. *Ceramics International*, 2021, vol. 47, no. 24, pp. 34137–34158. DOI: [10.1016/j.ceramint.2021.08.324](https://doi.org/10.1016/j.ceramint.2021.08.324).
 10. Aliofkhaezrai M., Macdonald D.D., Matykina E., Parfenov E.V., Egorin V.S., Curran J.A., Troughton S.C., Sinebryukhov S.L., Gnedenkov S.V., Lampke T., Simchen F., Nabavi H.F. Review of plasma electrolytic oxidation of titanium substrates: Mechanism, properties, applications and limitations. *Applied Surface Science Advances*, 2021, vol. 5, article number 100121. DOI: [10.1016/j.apsadv.2021.100121](https://doi.org/10.1016/j.apsadv.2021.100121).
 11. Hussein R.O., Nie X., Northwood D.O., Yerokhin A., Matthews A. Spectroscopic study of electrolytic plasma and discharging behaviour during the plasma electrolytic oxidation (PEO) process. *Journal of Physics D: Applied Physics*, 2010, vol. 43, no. 10, article number 105203. DOI: [10.1088/0022-3727/43/10/105203](https://doi.org/10.1088/0022-3727/43/10/105203).
 12. Clyne T.W., Troughton S.C. A review of recent work on discharge characteristics during plasma electrolytic oxidation of various metals. *International Materials Reviews*, 2018, vol. 64, no. 3, pp. 1–36. DOI: [10.1080/09506608.2018.1466492](https://doi.org/10.1080/09506608.2018.1466492).
 13. Golubkov P.E., Pecherskaya E.A., Artamonov D.V., Zinchenko T.O., Gerasimova Yu.E., Rozenberg N.V. Electrophysical model of micro-arc oxidation process. *Russian Physics Journal*, 2020, vol. 62, no. 11, pp. 2137–2144. DOI: [10.1007/s11182-020-01958-z](https://doi.org/10.1007/s11182-020-01958-z).
 14. Mengesha G.A., Chu Jinn P., Lou Bih-Show, Lee Jyh-Wei. Corrosion performance of plasma electrolytic oxidation grown oxide coating on pure aluminum: effect of borax concentration. *Journal of Materials Research and Technology*, 2020, vol. 9, no. 4, pp. 8766–8779. DOI: [10.1016/j.jmrt.2020.06.020](https://doi.org/10.1016/j.jmrt.2020.06.020).
 15. Sowa M., Olesinski A., Szumski B., Maciej A., Bik M., Jelen P., Sitarz M., Simka W. Electrochemical characterization of anti-corrosion coatings formed on 6061 aluminum alloy by plasma electrolytic oxidation in the corrosion inhibitor-enriched aqueous solutions. *Electrochimica Acta*, 2022, vol. 424, article number 140652. DOI: [10.1016/j.electacta.2022.140652](https://doi.org/10.1016/j.electacta.2022.140652).
 16. Polunin A.V., Cheretaeva A.O., Borgardt E.D., Rastegaev I.A., Krishtal M.M., Katsman A.V., Yasnikov I.S. Improvement of oxide layers formed by plasma electrolytic oxidation on cast Al-Si alloy by incorporating TiC nanoparticles. *Surface and Coatings Technology*, 2021, vol. 423, article number 127603. DOI: [10.1016/j.surfcoat.2021.127603](https://doi.org/10.1016/j.surfcoat.2021.127603).
 17. Moga S.G., Negrea D.A., Ducu C.M., Malinovsky V., Schiopu A.G., Coaca E., Patrascu I. The Influence of Processing Time on Morphology, Structure and Functional Properties of PEO Coatings on AZ63 Magnesium Alloy. *Applied Sciences*, 2022, vol. 12, no. 24, article number 12848. DOI: [10.3390/app122412848](https://doi.org/10.3390/app122412848).
 18. Mortazavi G., Jiang Jiechao, Meletis E.I. Investigation of the plasma electrolytic oxidation mechanism of titanium. *Applied Surface Science*, 2019, vol. 488, pp. 370–382. DOI: [10.1016/j.apsusc.2019.05.250](https://doi.org/10.1016/j.apsusc.2019.05.250).
 19. Egorin V.S., Gnedenkov S.V., Sinebryukhov S.L., Vyalyi I.E., Gnedenkov A.S., Chizhikov R.G. Increasing thickness and protective properties of PEO-coatings on aluminum alloy. *Surface and Coatings Technology*, 2018, vol. 334, pp. 29–42. DOI: [10.1016/j.surfcoat.2017.11.025](https://doi.org/10.1016/j.surfcoat.2017.11.025).
 20. Kaseem M., Fatimah S., Nashrah N., Ko Young Gun. Recent progress in surface modification of metals coated by plasma electrolytic oxidation: Principle, structure, and performance. *Progress in Materials Science*, 2021, vol. 117, article number 100735. DOI: [10.1016/j.pmatsci.2020.100735](https://doi.org/10.1016/j.pmatsci.2020.100735).

СПИСОК ЛИТЕРАТУРЫ

1. Yu Ji-Min, Choe Han-Cheol. Morphology Changes and Bone Formation on PEO-treated Ti-6Al-4V Alloy in Electrolyte Containing Ca, P, Sr, and Si Ions // *Applied Surface Science*. 2019. Vol. 477. P. 121–130. DOI: [10.1016/j.apsusc.2017.11.223](https://doi.org/10.1016/j.apsusc.2017.11.223).
2. Simchen F., Sieber M., Kopp A., Lampke Th. Introduction to Plasma Electrolytic Oxidation – An Overview of the Process and Applications // *Coatings*. 2020. Vol. 10. № 7. Article number 628. DOI: [10.3390/coatings10070628](https://doi.org/10.3390/coatings10070628).
3. Troughton S.C., Nomine A., Nomine A.V., Henrion G., Clyne T.W. Synchronised electrical monitoring and high speed video of bubble growth associated with individual discharges during plasma electrolytic oxidation // *Applied Surface Science*. 2015. Vol. 359. P. 405–411. DOI: [10.1016/j.apsusc.2015.10.124](https://doi.org/10.1016/j.apsusc.2015.10.124).
4. Yang Kai, Zeng Jiaquan, Huang Haisong, Chen Jiadui, Cao Biao. A Novel Self-Adaptive Control Method for Plasma Electrolytic Oxidation Processing of Aluminum Alloys // *Materials*. 2019. Vol. 12. № 17. Article number 2744. DOI: [10.3390/ma12172744](https://doi.org/10.3390/ma12172744).
5. Печерская Е.А., Голубков П.Е., Карпанин О.В., Артамонов Д.В., Сафронов М.И., Печерский А.В. Исследование влияния технологических параметров процесса микродугового оксидирования на свойства

- оксидных покрытий // Известия высших учебных заведений. Электроника. 2019. Т. 24. № 4. С. 363–369. DOI: [10.24151/1561-5405-2019-24-4-363-369](https://doi.org/10.24151/1561-5405-2019-24-4-363-369).
6. Tu Wenbin, Zhu Zhunda, Zhuang Xiujuan, Cheng Yingliang, Skeldon P. Effect of frequency on black coating formation on AZ31 magnesium alloy by plasma electrolytic oxidation in aluminate-tungstate electrolyte // Surface and Coatings Technology. 2019. Vol. 372. P. 34–44. DOI: [10.1016/j.surfcoat.2019.05.012](https://doi.org/10.1016/j.surfcoat.2019.05.012).
 7. Botin-Sanabria D.M., Mihaita A.-S., Peimbert-Garcia R.E., Ramirez-Moreno M.A., Ramirez-Mendoza R.A., Lozoya-Santos J.J. Digital Twin Technology Challenges and Applications: A Comprehensive Review // Remote Sensing. 2022. Vol. 14. № 6. Article number 1335. DOI: [10.3390/rs14061335](https://doi.org/10.3390/rs14061335).
 8. Zhu Lujun, Ke Xiaoxing, Li Jingwei, Zhang Yuefei, Zhang Zhenhua, Sui Manling. Growth mechanisms for initial stages of plasma electrolytic oxidation coating on Al // Surfaces and Interfaces. 2021. Vol. 25. Article number 101186. DOI: [10.1016/j.surfin.2021.101186](https://doi.org/10.1016/j.surfin.2021.101186).
 9. Rogov A.B., Huang Yingying, Shore D., Matthews A., Yerokhin A. Toward rational design of ceramic coatings generated on valve metals by plasma electrolytic oxidation: The role of cathodic polarization // Ceramics International. 2021. Vol. 47. № 24. P. 34137–34158. DOI: [10.1016/j.ceramint.2021.08.324](https://doi.org/10.1016/j.ceramint.2021.08.324).
 10. Aliofkhaezai M., Macdonald D.D., Matykina E., Parfenov E.V., Egorkin V.S., Curran J.A., Troughton S.C., Sinebryukhov S.L., Gnedenkov S.V., Lampke T., Simchen F., Nabavi H.F. Review of plasma electrolytic oxidation of titanium substrates: Mechanism, properties, applications and limitations // Applied Surface Science Advances. 2021. Vol. 5. Article number 100121. DOI: [10.1016/j.apsadv.2021.100121](https://doi.org/10.1016/j.apsadv.2021.100121).
 11. Hussein R.O., Nie X., Northwood D.O., Yerokhin A., Matthews A. Spectroscopic study of electrolytic plasma and discharging behaviour during the plasma electrolytic oxidation (PEO) process // Journal of Physics D: Applied Physics. 2010. Vol. 43. № 10. Article number 105203. DOI: [10.1088/0022-3727/43/10/105203](https://doi.org/10.1088/0022-3727/43/10/105203).
 12. Clyne T.W., Troughton S.C. A review of recent work on discharge characteristics during plasma electrolytic oxidation of various metals // International Materials Reviews. 2018. Vol. 64. № 3. P. 1–36. DOI: [10.1080/09506608.2018.1466492](https://doi.org/10.1080/09506608.2018.1466492).
 13. Голубков П.Е., Печерская Е.А., Артамонов Д.В., Зинченко Т.О., Герасимова Ю.Е., Розенберг Н.В. Электрофизическая модель процесса микродугового оксидирования // Известия высших учебных заведений. Физика. 2019. Т. 62. № 11. С. 166–171. DOI: [10.17223/00213411/62/11/166](https://doi.org/10.17223/00213411/62/11/166).
 14. Mengesha G.A., Chu Jinn P., Lou Bih-Show, Lee Jyh-Wei. Corrosion performance of plasma electrolytic oxidation grown oxide coating on pure aluminum: effect of borax concentration // Journal of Materials Research and Technology. 2020. Vol. 9. № 4. P. 8766–8779. DOI: [10.1016/j.jmrt.2020.06.020](https://doi.org/10.1016/j.jmrt.2020.06.020).
 15. Sowa M., Olesinski A., Szumski B., Maciej A., Bik M., Jelen P., Sitarz M., Simka W. Electrochemical characterization of anti-corrosion coatings formed on 6061 aluminum alloy by plasma electrolytic oxidation in the corrosion inhibitor-enriched aqueous solutions // Electrochimica Acta. 2022. Vol. 424. Article number 140652. DOI: [10.1016/j.electacta.2022.140652](https://doi.org/10.1016/j.electacta.2022.140652).
 16. Polunin A.V., Cheretaeva A.O., Borgardt E.D., Rastegaev I.A., Krishtal M.M., Katsman A.V., Yasnikov I.S. Improvement of oxide layers formed by plasma electrolytic oxidation on cast Al-Si alloy by incorporating TiC nanoparticles // Surface and Coatings Technology. 2021. Vol. 423. Article number 127603. DOI: [10.1016/j.surfcoat.2021.127603](https://doi.org/10.1016/j.surfcoat.2021.127603).
 17. Moga S.G., Negrea D.A., Ducu C.M., Malinovschi V., Schiopu A.G., Coaca E., Patrascu I. The Influence of Processing Time on Morphology, Structure and Functional Properties of PEO Coatings on AZ63 Magnesium Alloy // Applied Sciences. 2022. Vol. 12. № 24. Article number 12848. DOI: [10.3390/app122412848](https://doi.org/10.3390/app122412848).
 18. Mortazavi G., Jiechao Jiang, Meletis E.I. Investigation of the plasma electrolytic oxidation mechanism of titanium // Applied Surface Science. 2019. Vol. 488. P. 370–382. DOI: [10.1016/j.apsusc.2019.05.250](https://doi.org/10.1016/j.apsusc.2019.05.250).
 19. Egorkin V.S., Gnedenkov S.V., Sinebryukhov S.L., Vyalii I.E., Gnedenkov A.S., Chizhikov R.G. Increasing thickness and protective properties of PEO-coatings on aluminum alloy // Surface and Coatings Technology. 2018. Vol. 334. P. 29–42. DOI: [10.1016/j.surfcoat.2017.11.025](https://doi.org/10.1016/j.surfcoat.2017.11.025).
 20. Kaseem M., Fatimah S., Nashrah N., Ko Young Gun. Recent progress in surface modification of metals coated by plasma electrolytic oxidation: Principle, structure, and performance // Progress in Materials Science. 2021. Vol. 117. Article number 100735. DOI: [10.1016/j.pmatsci.2020.100735](https://doi.org/10.1016/j.pmatsci.2020.100735).

Моделирование электрических параметров гальванической ячейки в процессе микродугового оксидирования

© 2023

*Печерская Екатерина Анатольевна*¹, доктор технических наук, профессор,
заведующий кафедрой «Информационно-измерительная техника и метрология»

Семёнов Анатолий Дмитриевич, доктор технических наук,
профессор кафедры «Информационно-измерительная техника и метрология»

Голубков Павел Евгеньевич^{*2}, кандидат технических наук,
доцент кафедры «Информационно-измерительная техника и метрология»

Пензенский государственный университет, Пенза (Россия)

*E-mail: iit@pnzgu.ru,
golpavpnz@yandex.ru

¹ORCID: <https://orcid.org/0000-0001-5657-9128>

²ORCID: <https://orcid.org/0000-0002-4387-3181>

Аннотация: Микродуговое оксидирование является перспективной технологией получения износостойких антикоррозионных покрытий изделий из вентильных металлов и сплавов и применяется во многих отраслях промышленности. Одной из основных проблем данной технологии является низкая управляемость, обусловленная сложностью и взаимосвязанностью физико-химических явлений, происходящих в процессе нанесения покрытий. Для решения подобных проблем в настоящее время активно используются цифровые двойники. Исследование посвящено разработке математических моделей, которые целесообразно использовать в качестве структурных элементов цифрового двойника процесса микродугового оксидирования. Представлена электрическая схема замещения гальванической ячейки микродугового оксидирования, учитывающая сопротивление электролита, сопротивление покрытия детали в виде параллельного соединения нелинейного активного сопротивления и реактивного емкостного сопротивления. Предложена математическая модель, описывающая поведение электрической схемы замещения гальванической ячейки микродугового оксидирования. Разработана методика определения параметров указанной модели, включающая построение осциллограммы изменения сопротивления ячейки и ее аппроксимацию, оценку значений сопротивлений и емкости схемы замещения гальванической ячейки. Предложен способ расчета и разработана Simulink-модель процесса микродугового оксидирования, позволяющая имитировать осциллограммы тока и напряжения гальванической ячейки. Анализ модели показал, что модель устойчива, управляема и наблюдаема, но плохо обусловлена, что приводит к возникновению ошибок моделирования, максимальное значение которых составляет 7 % для напряжения и 10 % для тока. Методом параметрической идентификации с использованием экспериментальных осциллограмм тока и напряжения получены зависимости параметров схемы замещения гальванической ячейки от времени оксидирования. Установлено, что изменение среднего за период активного сопротивления гальванической ячейки коррелирует с толщиной покрытия.

Ключевые слова: микродуговое оксидирование; электрическая схема замещения; математическая модель; Simulink-модель; сопротивление и емкость покрытия; адекватность модели.

Благодарности: Работа выполнена при поддержке Министерства науки и высшего образования РФ, проект № 1022041100284-5-2.3.1.

Статья подготовлена по материалам докладов участников XI Международной школы «Физическое материаловедение» (ШФМ-2023), Тольятти, 11–15 сентября 2023 года.

Для цитирования: Печерская Е.А., Семёнов А.Д., Голубков П.Е. Моделирование электрических параметров гальванической ячейки в процессе микродугового оксидирования // Frontier Materials & Technologies. 2023. № 4. С. 73–85. DOI: 10.18323/2782-4039-2023-4-66-7.

The influence of addition of ZrO₂ nanoparticles to the electrolyte on the structure and anticorrosion properties of oxide layers formed by plasma electrolytic oxidation on the Mg₉₇Y₂Zn₁ alloy

© 2023

Alisa O. Polunina^{*1}, researcher of the Research Institute of Advanced Technologies

*Anton V. Polunin*², PhD (Engineering), leading researcher of the Research Institute of Advanced Technologies

*Mikhail M. Krishtal*³, Doctor of Sciences (Physics and Mathematics), Professor,
chief researcher of the Research Institute of Advanced Technologies

Togliatti State University, Togliatti (Russia)

*E-mail: a.cheretaeva@tlttsu.ru,
alice_raduga@mail.ru

¹ORCID: <https://orcid.org/0000-0002-3952-9556>

²ORCID: <https://orcid.org/0000-0001-8484-2456>

³ORCID: <https://orcid.org/0000-0001-7189-0002>

Received 26.06.2023

Accepted 27.10.2023

Abstract: Magnesium alloys with a strengthening long-period stacking ordered structure (LPSO-phase) offer outstanding mechanical properties, but their low corrosion resistance necessitates additional surface protection. The work investigates the influence of adding ZrO₂ nanoparticles at a concentration of 1–4 g/l to the electrolyte on the thickness, structure, composition, wettability, and anticorrosion properties of oxide layers formed during plasma electrolytic oxidation (PEO) of the Mg₉₇Y₂Zn₁ alloy with the LPSO-phase. It was found that during PEO, under the influence of an electric field, ZrO₂ nanoparticles penetrate into the forming oxide layer and reduce its porosity. The study revealed a decrease in the quantity and size of pores near the barrier layer in places where the alloy LPSO-phase comes out to the interface with the oxide layer. Low concentrations of ZrO₂ nanoparticles (1–2 g/l) reduce the corrosion rate of the alloy up to two times compared to the base case. The minimum corrosion current density $i_{\text{corr}} \approx 14 \text{ nA/cm}^2$ and the highest polarization resistance $R_p \approx 2.6 \text{ M}\Omega \cdot \text{cm}^2$ are found in the sample formed in an electrolyte with the addition of 1 g/l of ZrO₂ nanoparticles. Calculation of the barrier zone parameters of oxide layers showed that an increase in the ZrO₂ concentration in the electrolyte leads to an increase in the barrier layer thickness and in its specific conductivity, which negatively affects the corrosion resistance of the formed oxide layers – the barrier zone resistance of the layer obtained by adding 4 g/l of ZrO₂, drops by ~20 % compared to the base case (up to ~1 M $\Omega \cdot \text{cm}^2$).

Keywords: magnesium alloy; Mg₉₇Y₂Zn₁; ZrO₂ nanoparticles; LPSO-phase; plasma electrolytic oxidation; nanoparticles; zirconium oxide; surface contact (wetting) angle; corrosion resistance; barrier zone conductivity.

Acknowledgments: The work was supported by the Russian Science Foundation (Project No. 21-19-00656, <https://rscf.ru/project/21-19-00656/>).

The paper was written on the reports of the participants of the XI International School of Physical Materials Science (SPM-2023), Togliatti, September 11–15, 2023.

For citation: Polunina A.O., Polunin A.V., Krishtal M.M. The influence of addition of ZrO₂ nanoparticles to the electrolyte on the structure and anticorrosion properties of oxide layers formed by plasma electrolytic oxidation on the Mg₉₇Y₂Zn₁ alloy. *Frontier Materials & Technologies*, 2023, no. 4, pp. 87–98. DOI: 10.18323/2782-4039-2023-4-66-8.

INTRODUCTION

Magnesium alloys (MA) belong to the most promising materials for technical and biomedical purposes due to their high specific strength, ability to absorb vibrations and block electromagnetic waves [1–3], as well as complete biocompatibility and biodegradability in the human body [4].

In the last decade, a significant progress has been achieved in the development of MA with an LPSO-structure (long-period stacking-ordered structure, LPSO-phase) [5; 6] with the ultimate strength and ductility comparable to the mechanical characteristics of aluminum alloys and structural steels [7]. However, the formation of an LPSO-structure in MA, as a rule, negatively affects their corrosion resistance due to the resulting potential difference between α -Mg and the strengthening LPSO-phase (up to 200–250 mV), which provokes alloy degradation contacting with a corrosive environment as a result of micro-galvanic

corrosion [8; 9]. Therefore, for such alloys it is necessary to provide additional technological solutions to increase their anticorrosion properties.

A promising method for MA surface hardening is micro-arc or plasma electrolytic oxidation (MAO or PEO), which allows forming the protective ceramic layers with high hardness, adhesive strength, wear resistance, and anticorrosion properties [10]. However, the presence of a strengthening LPSO-phase in the alloy complicates micro-arc breakdown and leads to disruption of the barrier layer continuity in places where this phase reaches the “alloy – oxide layer” interface, which reduces the quality and properties of oxide layers obtained in traditional PEO modes [9]. In [9], it was found that treatment of the Mg₉₇Y₂Zn₁ alloy in an aluminate electrolyte at an increased frequency of forming pulses (500 Hz) allows forming the most uniform and high-quality oxide layers with high short-term corrosion resistance (impedance modulus is $|Z|_{f=0.01 \text{ Hz}} \approx 2.2 \text{ M}\Omega \cdot \text{cm}^2$). However, after a day

of exposure to a corrosive environment, their resistance decreases by 1–2 orders of magnitude.

It is known that the introduction of micro- or nanosized particles (MPs or NPs) of simple SiO₂, ZrO₂, CeO₂, TiO₂, etc. oxides into the electrolyte, as a rule, leads to an increase in the PEO productivity and positively affects the quality and protective properties of oxide layers on magnesium alloys [11; 12]. In [13], a significant increase in the anticorrosion properties of oxide layers was revealed caused by the effect of sealing pores, and blocking access of the corrosive environment to the substrate. It was concluded in [14] that the introduction of ZrO₂ and SiO₂ NPs during PEO leads to an increase in the non-porous layer thickness, as evidenced by a decrease in the constant phase element (CPE₂). It was shown in [2] that a low concentration of NPs (2 g/l) positively affects the oxide layer microstructure, blocking pores and cracks, which gives significant anticorrosion resistance to the coating.

There are very few works on PEO of MAs with the LPSO-phase in Russian and foreign literature [15], and there is no experience in treatment these alloys after adding dispersed particles to the electrolyte. It was possible to find only one work [16], where the authors revealed a significant positive effect from the post-treatment of the oxide layer in a Ce-containing electrolyte on an LPSO alloy, however, this treatment was also carried out in solutions without a dispersed phase. The influence of nanoparticles on the PEO of LPSO alloys in highly-dispersive systems has been practically not studied and is of significant scientific and practical interest. To further improve the protective properties of oxide layers, and increase their long-term anticorrosion characteristics, there is a promising approach based on combining high-frequency PEO [17] and adding insoluble nanosized ZrO₂ particles to the electrolyte, since this substance has proven itself positively in PEO of magnesium alloys [14; 18].

The goal of this research is to study the influence of ZrO₂ nanoparticles, added to the electrolyte during plasma electrolytic oxidation of the Mg₉₇Y₂Zn₁ alloy, with the LPSO-phase on the structure, composition, and anticorrosion properties of the formed oxide layers.

METHODS

Samples of oxide layers were obtained on the Mg₉₇Y₂Zn₁ magnesium alloy (Solikamsk Experimental-Metallurgical Plant, Solikamsk, Russia), the chemical composition of which was determined on a Thermo Fisher Scientific ARL 4460 OES optical emission spectrometer (Table 1). The basis of the alloy is α-Mg, as well as the Mg₁₂YZn (LPSO-phase) and Mg₃Zn₃Y₂ (eutectic phase) phases.

The alloy ingots were preliminary subjected to heat treatment according to the T61 mode: homogenising annealing (525±5 °C, 24 h), quenching in water, and subsequent ageing (200±5 °C, 100 h). Then blanks for PEO were produced in the form of flat parallelepipeds, with a size of 60×20×6 mm³ and a roughness of $R_a \approx 1 \mu\text{m}$.

Plasma electrolytic oxidation was carried out using alternating current from a power source of own design in a step mode for 10 min. PEO included 3 stages: stage I – “pre-anodising”, with anodic forming pulses at a current density of 3 A/dm² for 60 s; stage II – increasing (in 10 s), the current density j (RMS) up to 6 A/dm² with simultaneous activation of the supply of cathode pulses, at the ratio of currents in the cathode and anode half-periods $j_K/j_A=0.5\pm0.02$, and maintaining the mode for 110 s; stage III – increasing j (RMS) up to 7.5 A/dm² at $j_K/j_A=0.5$ and oxidation for 420 s.

At all PEO stages, the pulse frequency f was 1000 Hz, the duty cycle was 50 %, the ratio of the duration of the anodic and cathodic pulse half-periods was 50/50 %, and the ratio of the duration of pauses between half-periods was 50/50 %.

An aqueous solution of potassium hydroxide KOH (1 g/l), sodium phosphate dibasic dodecahydrate Na₂HPO₄×12H₂O (10 g/l), sodium fluoride NaF (10 g/l), and sodium aluminate NaAlO₂ (15 g/l) were used as the base electrolyte. During the treatment, continuous circulation and stirring of the electrolyte was ensured at a constant temperature of (14±1) °C. Nanoparticles of crystalline (monoclinic system with a space group of symmetry P21/a) zirconium dioxide ZrO₂ (Plasmotherm Nanopowders, Moscow, Russia), with a dispersion of 40–75 nm at a concentration of 1, 2, 3 or 4 g/l were added to the base electrolyte. The samples of oxide layers obtained in the base electrolyte, as well as in the electrolyte with additions of ZrO₂ nanoparticles, are further marked as B, Z1, Z2, Z3, and Z4, respectively.

Structural studies of oxide layers were carried out on transverse metallographic sections, using a Carl Zeiss field-emission scanning electron microscope (SEM) in the backscattered electron mode. The elemental (chemical) composition of the oxide layers was determined by energy dispersive X-ray microanalysis (EDX, EDAX TEAM EDS analyzer based on SDD Apollo X Sigma SEM). To eliminate polarisation effects during SEM studies, a conductive Pt layer was preliminarily applied to the sections using cold magnetron sputtering. The thickness (T , μm) and porosity (P , %) of the oxide layers were estimated from three panoramic cross-sectional images (≥500 μm in length) using ImageJ software.

Table 1. Chemical composition of the Mg₉₇Y₂Zn₁ alloy
Таблица 1. Химический состав сплава Mg₉₇Y₂Zn₁

Element	Mg	Y	Zn	Zr	Nd	Mn
Content, wt. %	89.90±0.15	6.67±0.17	2.27±0.10	1.07±0.26	0.056±0.001	<0.005

Note. ±3σ is given as an error. Al and Fe content is <0.002 wt. %.

Примечание. В качестве погрешности приведено ±3σ. Содержание Al и Fe <0,002 мас. %.

The wettability (degree of hydrophobicity/hydrophilicity) of the surface of the oxide layers, was assessed by the sessile drop method using a KRUSS DSA-25E contact angle analyser (Germany) with an automatic precision dosing system. Drop volume – 3 μ l, application speed – 1 μ l/s. Wetting (contact) liquid – 3.5 wt. % NaCl solution.

Electrochemical tests were carried out by potentiodynamic polarisation and impedance spectroscopy using a SmartStat PS-50 potentiostat-galvanostat (Electrochemical Instruments, Russia) with a built-in module for measuring electrochemical impedance of 3.5 wt. % NaCl (295 \pm 2 K), in a three-electrode electrochemical cell CS936 (CorrTest, China) with a fixed contact area of 1 cm². A platinum grid (20 \times 20 mm²) served as an auxiliary electrode; a silver chloride electrode filled with a saturated potassium chloride solution (Ag/AgCl/KCl_{sat}) was used as a reference electrode. Stabilisation of the electrode potential of the samples (E_{oc} – open circuit potential, V) was carried out for 60 min. Potentiodynamic polarisation of the samples was carried out in the range from –150 mV to +1000 mV relative to E_{oc} with a potential scanning rate of 1 mV/s. The polarisation resistance R_p was determined according to the recommendations of ASTM G102-89(2015)e1 using the Stern–Geary constant. The effective interconnected porosity (P_{eff} , %) of the oxide layers was assessed using the electrochemical method in a similar way [19].

Measurements using the electrochemical impedance spectroscopy (EIS) method were carried out with a sinusoidal disturbing signal, with an amplitude of 10 mV at a stabilised E_{oc} value, in the frequency range from 500 kHz to 10 mHz. Analysis of experimental data and calculation of parameters of equivalent circuits, were carried out using ZView software (Scribner Associates, USA). The barrier zone parameters (thickness and conductivity) were determined from data on processing impedance spectra in a similar way [20].

RESULTS

Structure and chemical (elemental) composition of oxide layers

The base oxide layer *B* formed in the electrolyte without NP additives contains multiple transverse pores and cracks, which can reach almost the barrier layer or magnesium substrate (Fig. 1 a). A large number of closed pores formed as a result of a sharp discharge of hot gases, from the layer formation zone are observed, and the internal (barrier) layer at the “oxide layer – magnesium alloy” interface has a pronounced mesoporous structure and discontinuities, and has discontinuities in the areas of LPSO-phase release to the surface (Fig. 1 b).

The introduction of ZrO₂ NPs into the electrolyte, leads to the formation of oxide layers with a more uniform structure, their porosity in the cross section decreases from ~9 % to ~5.5–7 %, the length and number of voids and pores near the barrier layer, and at the points of LPSO-phase, exit to the interface with the magnesium substrate are reduced (Fig. 1 c–f). In this case, a semblance of a bordering with a changed phase contrast appears above the LPSO-phase, which indicates the oxidation of this phase along the perimeter, and the barrier layer formation in places where it reaches the “oxide layer – magnesium alloy” interface.

In the images of the structure of the Z1–Z4 oxide layers, multiple bright points and globules, with sizes ranging from a fraction of a micron to 5–10 μ m, with a sharp phase contrast are observed (Fig. 1 c–f), which indicates the presence of heavy elements in them, and taking into account the experimental factor, allows stating that these are embedded ZrO₂ NPs or products of their reactions, with other components of the system. An increase in the proportion of Zr from ~6.9 % for the base sample to ~9.3 wt. % for the sample produced by adding 4 g/l ZrO₂ to the electrolyte, indicates the successful inclusion of nanoparticle substance into the layer (EDX analysis data, Table 2). Zirconium replaces predominantly F and Na in the layer, and the content of other elements remains virtually unchanged (Table 2).

The addition of ZrO₂ NPs had virtually no effect on the PEO efficiency – an increase in the average oxide layer thickness from ~22 to ~26 μ m is observed only in the case of a low concentration of the dispersed phase in the electrolyte (sample Z1), while the average thickness of the Z2–Z4 oxide layers is at the base layer level and is ~20–22 μ m (Fig. 1).

Wettability and anticorrosion properties of oxide layers

The addition of ZrO₂ nanoparticles to the electrolyte changes the surface contact properties of the formed oxide layers – the surface contact (wetting) angle Θ of Z1–Z4 samples is 95–115° versus ~91° for the base oxide layer, i. e., it is increased by 5–20 %, which indicates an increase in the hydrophobicity of the Z1–Z4 oxide layers (Fig. 2). Moreover, over time (10 min), the change in the contact (wetting) angle for samples Z1–Z4 is significantly less (less than 20°) than for the base oxide layer, which indirectly indicates a lower open porosity of the oxide layers, as well as a more developed surface microrelief.

Fig. 3 shows the polarisation curves of the samples under study in the logarithmic scale of current density. The original Mg₉₇Y₂Zn₁ alloy (without an oxide layer) has a relatively low corrosion resistance (i_{corr} ~5 μ A/cm², R_p ~8 k Ω ·cm²) and is prone to pitting corrosion in chloride-containing environments (Fig. 3, Table 3). MA PEO in the base electrolyte reduces the corrosion rate of the alloy by more than 2 orders of magnitude – to i_{corr} ~26 nA/cm² and R_p ~1.6 M Ω ·cm².

The addition of ZrO₂ nanoparticles at a concentration of 1–2 g/l leads to a decrease in the average values of i_{corr} by ~1.5–2 times (up to 14–17 nA/cm²), and an increase in R_p from ~1.6 M Ω ·cm² for the base layer to ~2.6 and 2.3 M Ω ·cm² for samples Z1 and Z2, respectively, as well as to a decrease in the effective interconnected porosity P_{eff} up to 0.009 % and 0.013 % for these samples versus 0.019 % for the base oxide layer (Table 3). However, at a higher polarising voltage (+1 V), this effect is leveled out, and the anodic current densities of both the base sample and samples Z1–Z4 almost reach the current density of the alloy without an oxide layer (Fig. 3, Table 3). An increase in the concentration of ZrO₂ NPs in the electrolyte to 3–4 g/l worsens the anticorrosion properties of the layers to the level of the base layer *B* with a slight decrease in P_{eff} from ~0.19 % to 0.14–0.17 % (Table 3).

The Nyquist (Fig. 4 a) and Bode plots (Fig. 4 b), which make it possible to determine the electrical parameters of the “alloy – electrolyte” interface, show that a protective

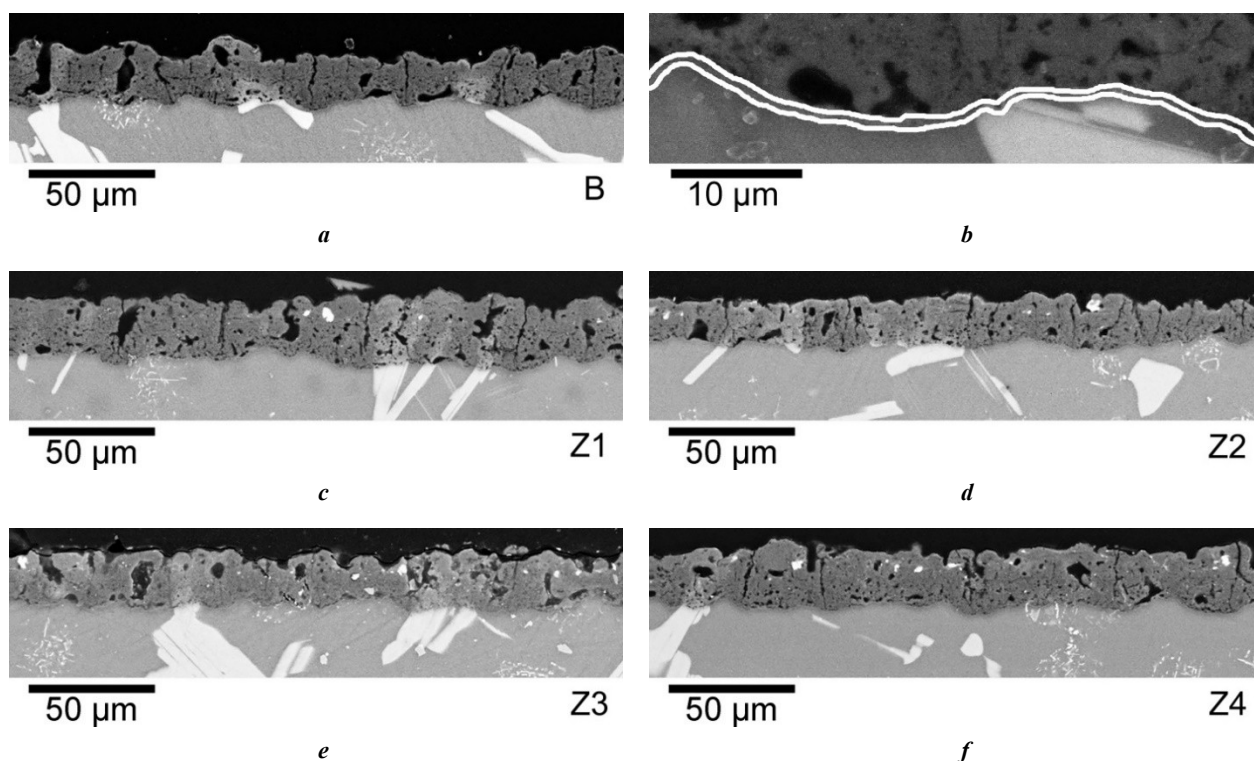


Fig. 1. Microstructures (cross sections, SEM) of the base (B) oxide layer (panoramic view (a) and detailing of the barrier zone (b)) and the oxide layers produced when adding ZrO₂ nanoparticles to the electrolyte (Z1–Z4): 1 g/l (c), 2 g/l (d), 3 g/l (e), 4 g/l (f)
Рис. 1. Микроструктура (поперечные сечения, СЭМ) базового (B) оксидного слоя (панорамный снимок (a) и детализация барьерной зоны (b)) и оксидных слоев, полученных при добавлении в электролит наночастиц ZrO₂ (Z1–Z4): 1 г/л (c), 2 г/л (d), 3 г/л (e), 4 г/л (f)

Table 2. Chemical (elemental) composition of oxide layers (EDX, wt. %)
Таблица 2. Химический (элементный) состав оксидных слоев (EDX, мас. %)

Sample	Mg	O	Al	F	Na	P	Y	Zr
B	31.9±2.2	29.9±0.4	15.2±1.3	7.3±0.7	2.3±1.1	2.1±0.4	3.6±1.4	6.9±0.8
Z1	32.6±1.0	29.7±0.6	16.3±1.0	6.5±1.2	1.3±0.7	2.4±0.5	3.3±1.0	7.4±0.6
Z2	31.8±1.9	29.7±0.9	15.6±0.9	6.6±0.8	1.9±0.7	2.1±0.4	3.6±1.9	8.0±0.5
Z3	30.1±1.6	30.8±0.3	15.7±1.0	5.5±0.8	1.4±0.8	2.4±0.3	4.5±1.6	9.1±0.8
Z4	32.1±1.5	29.7±0.5	15.7±1.0	6.4±0.7	2.0±0.3	2.1±0.3	2.7±0.3	9.3±0.6

Note. $\pm 3\sigma$ is given as an error.

Примечание. В качестве погрешности приведено $\pm 3\sigma$.

passivating film is formed on the non-oxidised Mg₉₇Y₂Zn₁ alloy after 60 min of exposure to a corrosive environment, the best description of which is achieved in the case of using a simple equivalent circuit, with one R–C chain (Fig. 4 c) simulating the double-layer capacitance, and the resistance of charge transfer across the interface.

The spectra of samples with oxide layers have two extrema in the phase angle graph (Fig. 4 b), therefore, to process them, a double-loop circuit was used, which corresponds to two time constants (Fig. 4 d). The first inflection in the high-frequency range is determined by

the presence of an outer porous layer R_{out} , and the second one (in the range of medium and low frequencies) characterises the inner barrier zone R_b .

PEO allowed increasing significantly the corrosion resistance of the Mg₉₇Y₂Zn₁ alloy – the charge transfer resistance of the barrier zone R_b of the base oxide layer was $\approx 1.3 \text{ M}\Omega \text{ cm}^2$ versus $\approx 0.9 \text{ k}\Omega \text{ cm}^2$ for the natural passive film on the alloy, i. e., by more than 3 orders of magnitude (Fig. 4, Table 4). The addition of ZrO₂ NPs introduced into the electrolyte in concentrations of 1–2 g/l increased R_b of the oxide layers up to ≈ 1.8 and $1.6 \text{ M}\Omega \text{ cm}^2$, respectively,

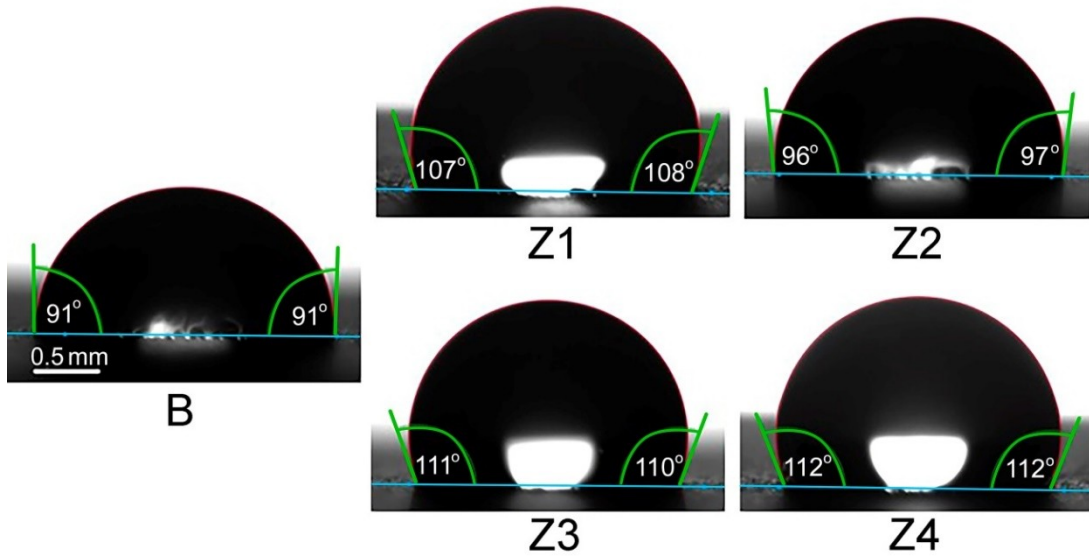


Fig. 2. Wettability of the surface of oxide layers formed in the base electrolyte (B) and with additions of ZrO₂ NPs from 1 to 4 g/l (Z1, Z2, Z3, Z4). Contact medium is 3.5 wt. % NaCl
Рис. 2. Смачиваемость оксидных слоев, сформированных в базовом электролите (B) и с добавками НЧ ZrO₂ от 1 до 4 г/л (Z1, Z2, Z3, Z4). Контактная среда – 3,5 мас. % NaCl

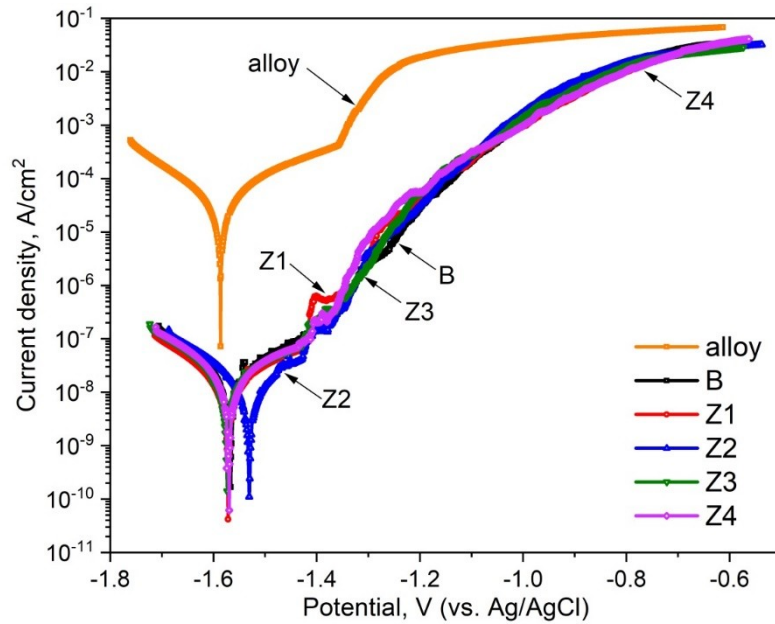


Fig. 3. Polarization curves of samples from the Mg₉₇Y₂Zn₁ alloy in the initial state and with oxide layers formed in the base electrolyte (B) and with additions of ZrO₂ NPs from 1 to 4 g/l (Z1, Z2, Z3, Z4)
Рис. 3. Поляризационные кривые образцов из сплава Mg₉₇Y₂Zn₁ в исходном состоянии и с оксидными слоями, сформированными в базовом электролите (B) и с добавками НЧ ZrO₂ от 1 до 4 г/л (Z1, Z2, Z3, Z4)

i. e. by ~30 and ~15 % compared to the base oxide layer. However, a further increase in the ZrO₂ concentration in the electrolyte (especially 4 g/l) led to a decrease in the protective properties of the oxide layers to the level of the base oxide layer (Fig. 4, Table 4).

The main studied characteristics of the oxide layers, determining their properties were divided into two groups

(Table 5). The first group (thickness T , structural (visual) porosity P , and surface wettability Θ) refers to the characteristics of the outer (porous) zone of the layer. The second group (the barrier zone thickness T_b , effective interconnected porosity P_{eff} , and specific conductivity σ_b) characterises mainly the parameters of the inner barrier zone, of the oxide layer at the interface with the alloy.

Table 3. The results of polarization tests of the Mg₉₇Y₂Zn₁ alloy before and after PEO in the base electrolyte and with additions of ZrO₂ NPs (3.5 wt. % NaCl)
Таблица 3. Результаты поляризационных испытаний сплава Mg₉₇Y₂Zn₁ до и после ПЭО в базовом электролите и с добавками НЧ ZrO₂ (3,5 мас. % NaCl)

Sample	E_{oc} , V	i_{corr} , nA/cm ²	E_{corr} , V	R_p , MΩ·cm ²	P_{eff} , %
Alloy	-1.584±0.028	4600±3641	-1.470±0.028	0.008±0.004	–
B	-1.528±0.020	25.7±11.5	-1.540±0.019	1.56±0.80	0.19±0.04
Z1	-1.537±0.027	13.7±1.7	-1.558±0.018	2.58±0.50	0.09±0.01
Z2	-1.527±0.027	17.3±2.1	-1.541±0.036	2.28±0.73	0.13±0.02
Z3	-1.557±0.012	22.0±0.6	-1.556±0.034	1.68±0.61	0.14±0.02
Z4	-1.566±0.022	25.8±9.9	-1.580±0.014	1.67±0.50	0.17±0.03

Note. E_{oc} is open circuit potential; i_{corr} is corrosion current density; E_{corr} is corrosion potential; R_p is polarisation resistance; P_{eff} is effective interconnected porosity.
 Примечание. E_{oc} – потенциал разомкнутой цепи; i_{corr} – плотность тока коррозии; E_{corr} – потенциал коррозии; R_p – поляризационное сопротивление; P_{eff} – эффективная сквозная пористость.

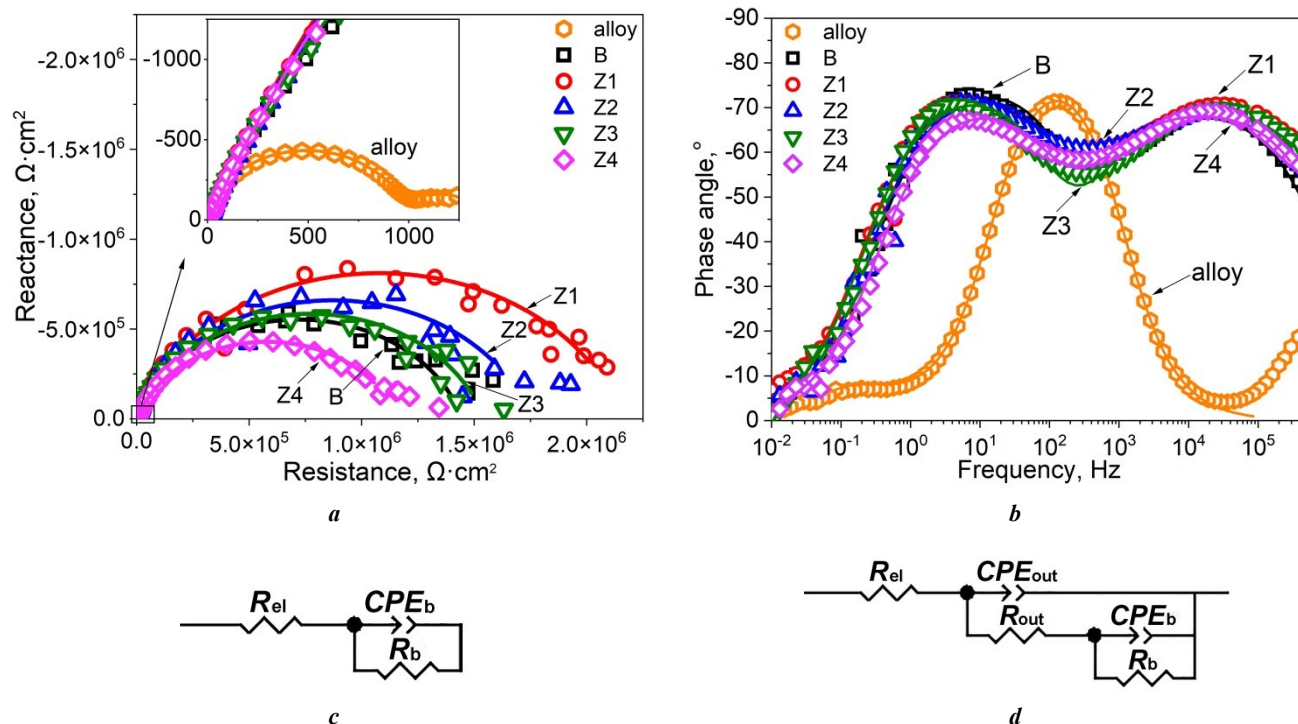


Fig. 4. Nyquist (a) and Bode (b) plots of Mg₉₇Y₂Zn₁ alloy samples without coating (insert) and with oxide layers formed in the base electrolyte (B) and with additions of ZrO₂ NPs from 1 to 4 g/l (Z1, Z2, Z3, Z4). Equivalent electrical circuits used to describe the impedance spectra of uncoated alloy (c) and samples of alloy with oxide layers (d)

Рис. 4. Кривые Найквиста (a) и Бодэ (b) образцов из сплава Mg₉₇Y₂Zn₁ без покрытия (вставка) и с оксидными слоями, сформированными в базовом электролите (B) и с добавками НЧ ZrO₂ от 1 до 4 г/л (Z1, Z2, Z3, Z4). Эквивалентные электрические схемы, используемые для описания спектров импеданса образцов из сплава без покрытия (c) и с оксидными слоями (d)

Table 4. The results of processing EIS data of the Mg₉₇Y₂Zn₁ alloy before and after PEO in the base electrolyte and with additions of ZrO₂ nanoparticles (3.5 wt. % NaCl)
Таблица 4. Результаты обработки данных ЭИС сплава Mg₉₇Y₂Zn₁ до и после ПЭО в базовом электролите и с добавками наночастиц ZrO₂ (3,5 мас. % NaCl)

Sample	R_{out} , kΩ·cm ²	CPE _{out}		R_b , MΩ·cm ²	CPE _b	
		Q_{out} , Ω ⁻¹ ·cm ⁻² ·s ⁿ	n_{out}		Q_b , Ω ⁻¹ ·cm ⁻² ·s ⁿ	n_b
Alloy	–	–	–	(1±0.3)·10 ⁻³	(1.6±0.1)·10 ⁻⁵	0.94±0.01
B	10.5±0.6	(3.0±0.3)·10 ⁻⁷	0.79±0.01	1.27±0.30	(1.5±0.2)·10 ⁻⁷	0.91±0.03
Z1	13.7±2.3	(2.8±0.3)·10 ⁻⁷	0.79±0.01	2.14±1.04	(1.6±0.2)·10 ⁻⁷	0.88±0.01
Z2	11.6±4.9	(3.0±0.2)·10 ⁻⁷	0.79±0.01	1.74±0.96	(1.7±0.5)·10 ⁻⁷	0.88±0.03
Z3	11.0±2.7	(3.1±0.3)·10 ⁻⁷	0.78±0.01	1.53±0.50	(2.8±0.7)·10 ⁻⁷	0.86±0.04
Z4	13.5±2.7	(2.9±0.1)·10 ⁻⁷	0.79±0.01	1.01±0.24	(2.2±0.5)·10 ⁻⁷	0.84±0.03

Note. R_{out} and R_b are the resistances of the outer and barrier zones of the oxide layer; CPE_{out} and CPE_b are the constant phase elements characterizing the capacitance of the outer (porous) and inner (barrier) zones, taking into account the degree of their heterogeneity; Q is a frequency-independent parameter; n is an exponential factor ($n \leq 1$).
 Примечание. R_{out} и R_b – сопротивление внешней и барьерной зон оксидного слоя; CPE_{out} и CPE_b – элементы постоянной фазы, характеризующие емкость внешней (пористой) и внутренней (барьерной) зон с учетом степени их гетерогенности; Q – частотно-независимый параметр; n – экспоненциальный фактор ($n \leq 1$).

Table 5. Characteristics of zones of oxide layers
Таблица 5. Характеристики зон оксидных слоев

Sample	Outer layer			Barrier layer		
	T , μm	P , %	Θ , °	T_b , nm	P_{eff} , %	σ_b , pS/cm
B	21.9±2.5	8.8±0.5	91.2±1.3	215±78	0.19±0.04	12.3±1.6
Z1	25.8±3.1	7.7±0.1	107.5±2.6	307±97	0.09±0.01	18.7±2.6
Z2	19.1±4.2	5.4±0.2	96.6±1.9	274±62	0.13±0.02	20.3±7.2
Z3	21.7±3.3	6.7±0.1	110.4±2.1	250±111	0.14±0.02	23.2±5.2
Z4	22.1±4.3	5.6±0.9	111.9±2.8	382±96	0.17±0.03	33.8±8.4

Note. T is oxide layer thickness; P is structural porosity; Θ is contact angle of surface wettability; T_b is barrier zone thickness; P_{eff} is effective interconnected porosity; σ_b is barrier layer conductivity.

Примечание. T – толщина оксидного слоя; P – структурная пористость; Θ – краевой угол смачиваемости поверхности; T_b – толщина барьерной зоны; P_{eff} – эффективная сквозная пористость; σ_b – удельная проводимость барьерного слоя.

DISCUSSION

The results of the study of the chemical (elemental) composition showed the inclusion of ZrO₂ NPs in the formed oxide layer, and with an increase in the dispersed additive concentration in the electrolyte by 1 g/l, the Zr proportion in the layer increases by ≈0.5–1 wt. %. One can assume that the introduction of ZrO₂ particles occurs both in the original (nanosized) and agglomerated form. The particles were detected mainly in the upper zones of the layers (30–50 % of the coating thickness), and have a clearly de-

defined contrast boundary with the oxide layer material, which indicates their inclusion as a result of being captured by a molten metal splash with subsequent fixation in the layer. The absence of transition colour zones in the phase contrast, as well as the phase contrast heterogeneity in the zones of inclusion of ZrO₂ particles in the layer, and the light areas themselves, indirectly indicates the inclusion of ZrO₂ NPs exactly in the form of particles without participation in chemical reactions, and the formation of Zr-containing phases. The presence of zirconium in the base layer (Table 2), as well as characteristic contrasting (light

zones in the images of the transverse structure (Fig. 1 a), indicates the effect of the oxide layer inheriting the structure, and chemical heterogeneity of the processed alloy, which was previously revealed during PEO of aluminum-silicon alloys [21].

The inclusion of ZrO₂ NPs in agglomerated micro- and nanosized form into the oxide layer, and in particular, into its surface is also evidenced by data on the wettability of oxide layers (Fig. 2). It is known that with a decrease in the radius of the surface morphological element that comes into contact with the liquid, the necessary external pressure to ensure surface wettability (Laplace formula), sharply increases [22]. And at constant external pressure, the contact liquid cannot go around and wet objects with a certain critical R due to the surface tension in the liquid. A change in the contact wetting angle (Fig. 2, Table 5), suggests that, along with a change in the effective interconnected porosity of the oxide layers, there is an increase in the surface microrelief development, due to the introduction of ZrO₂ particles into it, which creates numerous micro- and nano-objects that cannot be wetted with contact fluid at atmospheric external pressure. As a consequence, as a result of microscopic effects, macroscopic changes in contact wetting angles are observed in terms of increasing the hydrophobicity of the oxide layers. Due to the effects of charge accumulation on the oxide layer surface, and as a consequence, the appearance of polarisation artifacts in microscopic areas of the sample, we were unable to resolve and visualise individual ZrO₂ nanoparticles embedded in the layer using the SEM method, therefore, this will be the subject of further research using the method of atomic force microscopy, and optical profilometry based on white light interferometry.

The influence of ZrO₂ NPs on the oxide layer structure, and most importantly, the structure and quality of its barrier zone, is evidenced as well by the EIS measurement data. It is known that oxide layers, formed by PEO have a two- and/or three-zone structure [17; 23]. The outer (porous) zone of the layer is the primary barrier limiting the contact

of the corrosive environment with the alloy surface. The main indicators of high anticorrosion properties of the outer zone, as a rule, are low porosity, as well as surface hydrophobicity, which prevents the penetration of an aggressive environment into the pores and channels of micro-arc discharges. It is considered that the internal (barrier) zone at the interface with the alloy, makes the main contribution to the anticorrosion properties of oxide layers [24]. It is known that the thickness of the oxide layer barrier zone according to microstructure photographs (SEM) ranges from several tens of nm to several microns. Depending on the anodising or PEO mode [10], however, it is quite difficult to measure this value clearly due to the microscope resolution and polarisation effects (non-conducting layer) [23].

The study showed, that no correlation between the parameters of the outer zone of oxide layers B , and Z1–Z4 with their anticorrosion properties is observed: the inclusion of ZrO₂ NPs in the oxide layers reduces their structural porosity, but does not affect the increase in their protective properties (Fig. 5 a). The corrosion current density of sample Z4, which has the lowest porosity ($P \approx 5.6\%$), is higher than that of the base layer, i. e., even the opposite trend is observed. The influence of the hydrophobicity degree, on the anticorrosion properties of oxide layers, was identified only for cases of low concentration of ZrO₂ NPs added to the electrolyte (1–2 g/l). A further increase in the concentration of nanoparticles, despite an increase in the contact (wetting) angle, leads to an increase in the corrosion rate of the alloy (Fig. 5 b).

Despite the increase in the thickness of the inner zone T_b (Table 5) under the influence of the addition of ZrO₂ NPs to the electrolyte, an increase in the Zr concentration in the layer leads to an increase in effective interconnected porosity and an increase in specific conductivity (Table 5). Probably, solid hard ZrO₂ nanoparticles are accelerated in the vapour-gas phase, preceding the microarc discharge breakdown, under the influence of an electric field they break through the oxide layer to the barrier zone and penetrate into it, thereby changing its conductivity

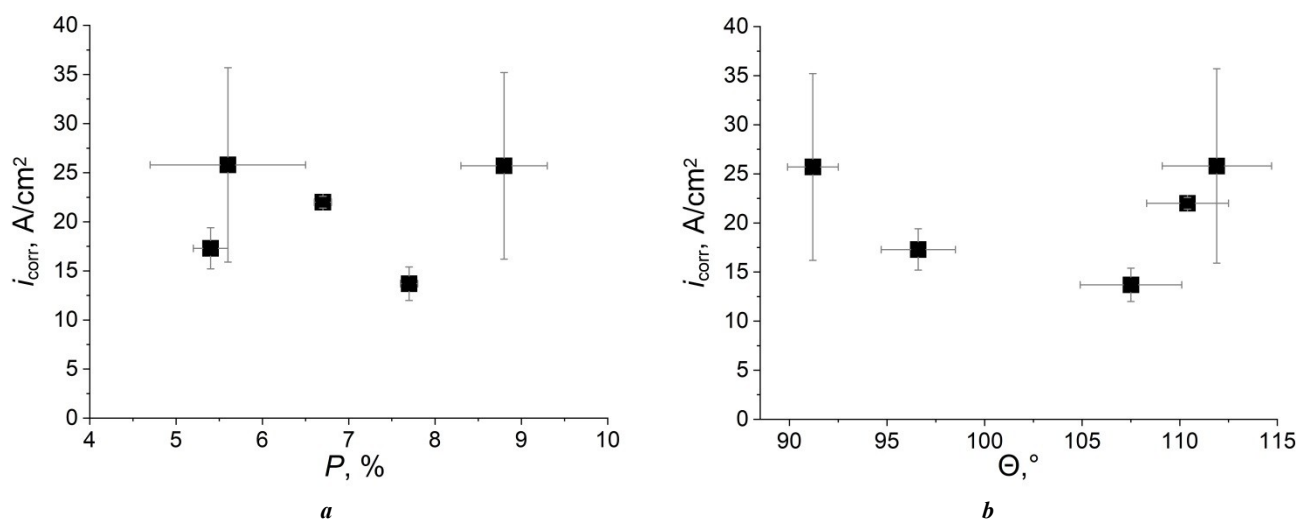


Fig. 5. Relationship between the corrosion current density of oxide layers and their structural porosity (a) and the contact angle of surface wettability (b)

Рис. 5. Связь плотности тока коррозии оксидных слоев с их структурной пористостью (a) и краевым углом смачивания поверхности (b)

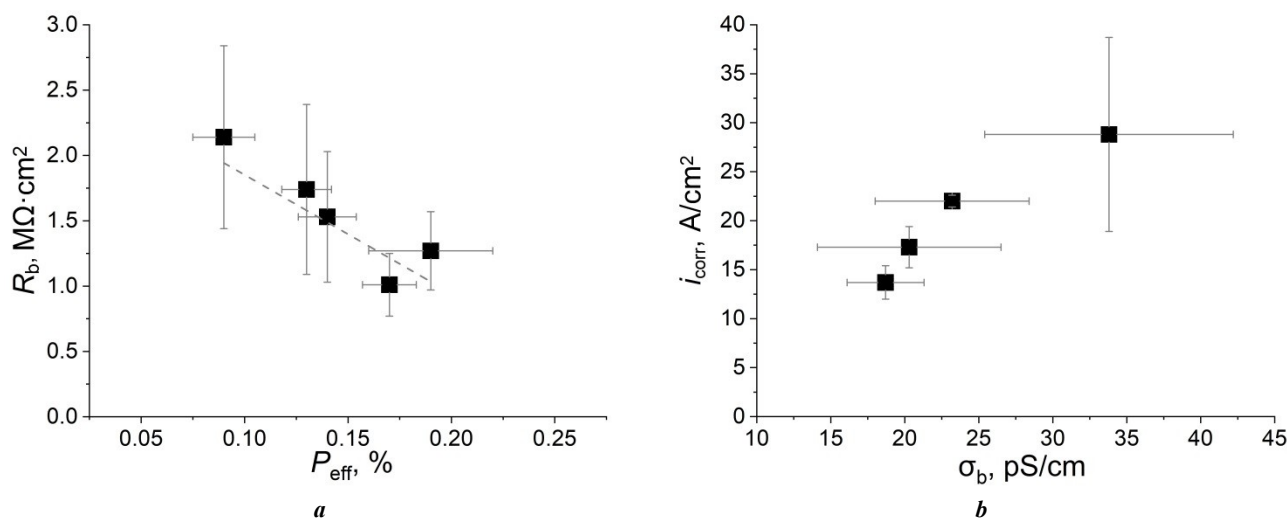


Fig. 6. Resistance of the barrier zone of oxide layers depending on their effective interconnected porosity (a) and the relationship between the corrosion current density of layers Z1–Z4 and the barrier zone specific conductivity (b)
Рис. 6. Сопротивление барьерной зоны оксидных слоев в зависимости от их эффективной сквозной пористости (a) и связь плотности тока коррозии слоев Z1–Z4 с удельной проводимостью барьерной зоны (b)

(Table 5). Apparently, as a result of the inelastic collision of nanoparticles with a layer, nanosized channels and nanocracks are formed in the barrier layer [25], which reduce the effective thickness of the barrier layer, and in the case of contact with a corrosive environment, reduce its electrical resistance.

With increasing barrier zone conductivity, a sharp decrease in anticorrosion properties is observed: an almost linear decrease in the barrier layer resistance with increasing P_{eff} (Fig. 6 a), as well as a sharp increase in the corrosion rate of the alloy (i_{corr}) (Fig. 6 b) is revealed. Thus, the barrier layer dielectric properties and continuity have a decisive influence on the anticorrosion properties of the oxide layers.

CONCLUSIONS

1. The addition of ZrO₂ nanoparticles to the electrolyte during PEO of the Mg LPSO alloy Mg₉₇Y₂Zn₁ at a concentration of 1–2 g/l reduces the porosity of the formed oxide layers, and promotes the oxidation of the LPSO-phase emerging at the “magnesium alloy – oxide layer” interface, as well as the formation of a continuous and dense barrier layer.

2. The addition of ZrO₂ nanoparticles to the electrolyte at a concentration of 1 g/l increases the thickness of the oxide layer by ≈20 %, and increases the oxide layer anticorrosion properties by ~2 times compared to the base version. When the concentration of ZrO₂ NPs in the electrolyte increases to 3–4 g/l, the thickness and protective properties of the oxide layers return to the base level.

3. It was identified that the main parameters influencing the anticorrosion properties of the formed oxide layers, are their effective interconnected porosity P_{eff} and the barrier zone specific conductivity σ_b that increase with increasing ZrO₂ concentration in the electrolyte from 1 to 4 g/l, which negatively affects anticorrosion properties of oxide layers, reducing their complex resistance.

4. It is shown that under the influence of an electric field, solid ZrO₂ nanoparticles, as a result of inelastic collision, break through the oxide layer to the barrier zone and

penetrate into it, which changes its thickness and conductivity due to the formation of breakdown channels, and nano- and microcracks, and as a consequence, leads to reducing the oxide layer anticorrosion properties.

REFERENCES

- Landkof B. Magnesium Applications in Aerospace and Electronic Industries. *Magnesium Alloys and their Applications*, 2006, pp. 168–172. DOI: [10.1002/3527607552.CH28](https://doi.org/10.1002/3527607552.CH28).
- Ur Rehman Z., Choi Dongjin. Investigation of ZrO₂ nanoparticles concentration and processing time effect on the localized PEO coatings formed on AZ91 alloy. *Journal of Magnesium and Alloys*, 2019, vol. 7, no. 4, pp. 555–565. DOI: [10.1016/J.JMA.2019.10.001](https://doi.org/10.1016/J.JMA.2019.10.001).
- Fattah-alhosseini A., Chaharmahali R., Babaei K., Nouri M., Keshavarz M.K., Kaseem M. A review of effective strides in amelioration of the biocompatibility of PEO coatings on Mg alloys. *Journal of Magnesium and Alloys*, 2022, vol. 10, no. 9, pp. 2354–2383. DOI: [10.1016/J.JMA.2022.09.002](https://doi.org/10.1016/J.JMA.2022.09.002).
- Sedelnikova M.B., Kashin A.D., Uvarkin P.V., Tolmachev A.I., Sharkeev Y.P., Ugodchikova A.V., Luginin N.A., Bakina O.V. Porous biocoatings based on diatomite with incorporated ZrO₂ particles for biodegradable magnesium implants. *Journal of Functional Biomaterials*, 2023, vol. 14, no. 5, article number 241. DOI: [10.3390/JFB14050241](https://doi.org/10.3390/JFB14050241).
- Xu Daokui, Han En-hau, Xu Yongbo. Effect of long-period stacking ordered phase on microstructure, mechanical property and corrosion resistance of Mg alloys: A review. *Progress in Natural Science: Materials International*, 2016, vol. 26, no. 2, pp. 117–128. DOI: [10.1016/J.PNSC.2016.03.006](https://doi.org/10.1016/J.PNSC.2016.03.006).
- Wang Guoxin, Mao Pingli, Wang Zhi, Zhou Le, Wang Feng, Liu Zheng. High strain rates deformation

- behavior of an as-extruded Mg-2.5Zn-4Y magnesium alloy containing LPSO phase at high temperatures. *Journal of Materials Research and Technology*, 2022, vol. 21, pp. 40–53. DOI: [10.1016/J.JMRT.2022.08.131](https://doi.org/10.1016/J.JMRT.2022.08.131).
7. Qian Yafeng, Zhao Yanhui, Dong Xiaorui, Yu Wei, Feng Jianhang, Yu Hui. Microstructure, mechanical properties and fire resistance of high strength Mg-Gd-Y-Zr alloys. *Metals*, 2022, vol. 12, no. 9, article number 1456. DOI: [10.3390/MET12091456](https://doi.org/10.3390/MET12091456).
 8. Li C.Q., Xu D.K., Zeng Z.R., Wang B.J., Sheng L.Y., Chen X.B., Han E.H. Effect of volume fraction of LPSO phases on corrosion and mechanical properties of Mg-Zn-Y alloys. *Materials & Design*, 2017, vol. 121, pp. 430–441. DOI: [10.1016/j.matdes.2017.02.078](https://doi.org/10.1016/j.matdes.2017.02.078).
 9. Cheretaeva A.O., Glukhov P.A., Shafeev M.R., Denisova A.G., Borgardt E.D., Polunin A.V., Katsman A.V., Krishtal M.M. Improvement of protective oxide layers formed by high-frequency plasma electrolytic oxidation on Mg-RE alloy with LPSO-phase. *Chimica Techno Acta*, 2023, vol. 10, no. 2, article number 202310212. DOI: [10.15826/chimtech.2023.10.2.12](https://doi.org/10.15826/chimtech.2023.10.2.12).
 10. Simchen F., Sieber M., Kopp A., Lampke T. Introduction to plasma electrolytic oxidation – an overview of the process and applications. *Coatings*, 2020, vol. 10, no. 7, article number 628. DOI: [10.3390/COATINGS10070628](https://doi.org/10.3390/COATINGS10070628).
 11. Lu Xiaopeng, Blawert C., Huang Yuanding, Ovi H., Zheludkevich M.L., Kainer K.U. Plasma electrolytic oxidation coatings on Mg alloy with addition of SiO₂ particles. *Electrochimica Acta*, 2016, vol. 187, pp. 20–33. DOI: [10.1016/J.ELECTACTA.2015.11.033](https://doi.org/10.1016/J.ELECTACTA.2015.11.033).
 12. Mashtalyar D.V., Imshinetskiy I.M., Nadaraia K.V. et al. Effect of TiO₂ nanoparticles on the photocatalytic properties of PEO coatings on Mg alloy. *Journal of Magnesium and Alloys*, 2023, vol. 11, no. 2, pp. 735–752. DOI: [10.1016/J.JMA.2022.10.021](https://doi.org/10.1016/J.JMA.2022.10.021).
 13. Bordbar-Khiabani A., Yarmand B., Mozafari M. Enhanced corrosion resistance and in-vitro biodegradation of plasma electrolytic oxidation coatings prepared on AZ91 Mg alloy using ZnO nanoparticles-incorporated electrolyte. *Surface and Coatings Technology*, 2019, vol. 360, pp. 153–171. DOI: [10.1016/J.SURFCOAT.2019.01.002](https://doi.org/10.1016/J.SURFCOAT.2019.01.002).
 14. Gnednikov S.V., Sinebryukhov S.L., Mashtalyar D.V., Imshinetskiy I.M., Samokhin A.V., Tsvetkov Y.V. Fabrication of coatings on the surface of magnesium alloy by plasma electrolytic oxidation using ZrO₂ and SiO₂ Nanoparticles. *Journal of Nanomaterials*, 2015, vol. 2015, article number 154298. DOI: [10.1155/2015/154298](https://doi.org/10.1155/2015/154298).
 15. Wu Jiahao, Wu Liang, Yao Wenhui, Chen Yanning, Chen Yonghua, Yuan Yuan, Wang Jingfeng, Atrens A., Pan Fusheng. Effect of electrolyte systems on plasma electrolytic oxidation coatings characteristics on LPSO Mg-Gd-Y-Zn alloy. *Surface and Coatings Technology*, 2023, vol. 454, article number 129192. DOI: [10.1016/J.SURFCOAT.2022.129192](https://doi.org/10.1016/J.SURFCOAT.2022.129192).
 16. Mohedano M., Pérez P., Matykina E., Pillado B., Garcés G., Arrabal R. PEO coating with Ce-sealing for corrosion protection of LPSO Mg-Y-Zn alloy. *Surface and Coatings Technology*, 2020, vol. 383, article number 125253. DOI: [10.1016/J.SURFCOAT.2019.125253](https://doi.org/10.1016/J.SURFCOAT.2019.125253).
 17. Liu Xiaohe, Liu Lei, Dong Shuai, Chen Xiao-Bo, Dong Jie. Towards dense corrosion-resistant plasma electrolytic oxidation coating on Mg-Gd-Y-Zr alloy by using ultra-high frequency pulse current. *Surface and Coatings Technology*, 2022, vol. 447, article number 128881. DOI: [10.1016/J.SURFCOAT.2022.128881](https://doi.org/10.1016/J.SURFCOAT.2022.128881).
 18. Kang Min Lee, Ki Ryong Shin, Seung Namgung, Bongyoung Yoo, Dong Hyuk Shin. Electrochemical response of ZrO₂-incorporated oxide layer on AZ91 Mg alloy processed by plasma electrolytic oxidation. *Surface and Coatings Technology*, 2011, vol. 205, no. 13–14, pp. 3779–3784. DOI: [10.1016/J.SURFCOAT.2011.01.033](https://doi.org/10.1016/J.SURFCOAT.2011.01.033).
 19. Kaseem M., Fatimah S., Nashrah N., Ko Y.G. Recent progress in surface modification of metals coated by plasma electrolytic oxidation: Principle, structure, and performance. *Progress in Materials Science*, 2021, vol. 117, article number 100735. DOI: [10.1016/J.PMATSCI.2020.100735](https://doi.org/10.1016/J.PMATSCI.2020.100735).
 20. Benfedda B., Hamadou L., Benbrahim N., Kadri A., Chaintet E., Charlot F. Electrochemical Impedance Investigation of Anodic Alumina Barrier Layer. *Journal of The Electrochemical Society*, 2012, vol. 159, no. 8, pp. C372–C381. DOI: [10.1149/2.068208JES](https://doi.org/10.1149/2.068208JES).
 21. Krishtal M.M., Ryumkin M.Y. Inherited chemical inhomogeneity in oxide layers deposited by the method of microarc oxidizing on hypereutectic silumins. *Metal Science and Heat Treatment*, 2007, vol. 49, no. 3–4, pp. 111–117. DOI: [10.1007/s11041-007-0021-x](https://doi.org/10.1007/s11041-007-0021-x).
 22. Siqveland L.M., Skjæveland S.M. Derivations of the Young-Laplace equation. *Capillarity*, 2021, vol. 4, no. 2, pp. 23–30. DOI: [10.46690/CAPI.2021.02.01](https://doi.org/10.46690/CAPI.2021.02.01).
 23. Dilimon V.S., Shibli S.M.A. A Review on the application-focused assessment of plasma electrolytic oxidation (PEO) coatings using electrochemical impedance spectroscopy. *Advanced Engineering Materials*, 2023, vol. 25, no. 12, article number 2201796. DOI: [10.1002/ADEM.202201796](https://doi.org/10.1002/ADEM.202201796).
 24. Lu Xiaopeng, Chen Yan, Blawert C., Li Yan, Zhang Tao, Wang Fuhui, Kainer K.U., Zheludkevich M. Influence of SiO₂ particles on the corrosion and wear resistance of plasma electrolytic oxidation-coated AM50 Mg alloy. *Coatings*, 2018, vol. 8, no. 9, article number 306. DOI: [10.3390/COATINGS8090306](https://doi.org/10.3390/COATINGS8090306).
 25. Polunin A.V., Cheretaeva A.O., Borgardt E.D., Rastegaev I.A., Krishtal M.M., Katsman A.V., Yasnikov I.S. Improvement of oxide layers formed by plasma electrolytic oxidation on cast AlSi alloy by incorporating TiC nanoparticles. *Surface and Coatings Technology*, 2021, vol. 423, article number 127603. DOI: [10.1016/J.SURFCOAT.2021.127603](https://doi.org/10.1016/J.SURFCOAT.2021.127603).

СПИСОК ЛИТЕРАТУРЫ

1. Landkof B. Magnesium Applications in Aerospace and Electronic Industries // Magnesium Alloys and their Applications. 2006. P. 168–172. DOI: [10.1002/3527607552.CH28](https://doi.org/10.1002/3527607552.CH28).
2. Ur Rehman Z., Choi Dongjin. Investigation of ZrO₂ nanoparticles concentration and processing time effect on the localized PEO coatings formed on AZ91 alloy // Journal of Magnesium and Alloys. 2019. Vol. 7. № 4. P. 555–565. DOI: [10.1016/J.JMA.2019.10.001](https://doi.org/10.1016/J.JMA.2019.10.001).

- Fattah-alhosseini A., Chaharmahali R., Babaei K., Nouri M., Keshavarz M.K., Kaseem M. A review of effective strides in amelioration of the biocompatibility of PEO coatings on Mg alloys // *Journal of Magnesium and Alloys*. 2022. Vol. 10. № 9. P. 2354–2383. DOI: [10.1016/J.JMA.2022.09.002](https://doi.org/10.1016/J.JMA.2022.09.002).
- Sedelnikova M.B., Kashin A.D., Uvarin P.V., Tolmachev A.I., Sharkeev Y.P., Ugodchikova A.V., Luginin N.A., Bakina O.V. Porous biocoatings based on diatomite with incorporated ZrO₂ particles for biodegradable magnesium implants // *Journal of Functional Biomaterials*. 2023. Vol. 14. № 5. Article number 241. DOI: [10.3390/JFB14050241](https://doi.org/10.3390/JFB14050241).
- Xu Daokui, Han En-hau, Xu Yongbo. Effect of long-period stacking ordered phase on microstructure, mechanical property and corrosion resistance of Mg alloys: A review // *Progress in Natural Science: Materials International*. 2016. Vol. 26. № 2. P. 117–128. DOI: [10.1016/J.PNSC.2016.03.006](https://doi.org/10.1016/J.PNSC.2016.03.006).
- Wang Guoxin, Mao Pingli, Wang Zhi, Zhou Le, Wang Feng, Liu Zheng. High strain rates deformation behavior of an as-extruded Mg-2.5Zn-4Y magnesium alloy containing LPSO phase at high temperatures // *Journal of Materials Research and Technology*. 2022. Vol. 21. P. 40–53. DOI: [10.1016/J.JMRT.2022.08.131](https://doi.org/10.1016/J.JMRT.2022.08.131).
- Qian Yafeng, Zhao Yanhui, Dong Xiaorui, Yu Wei, Feng Jianhang, Yu Hui. Microstructure, mechanical properties and fire resistance of high strength Mg-Gd-Y-Zr alloys // *Metals*. 2022. Vol. 12. № 9. Article number 1456. DOI: [10.3390/MET12091456](https://doi.org/10.3390/MET12091456).
- Li C.Q., Xu D.K., Zeng Z.R., Wang B.J., Sheng L.Y., Chen X.B., Han E.H. Effect of volume fraction of LPSO phases on corrosion and mechanical properties of Mg-Zn-Y alloys // *Materials & Design*. 2017. Vol. 121. P. 430–441. DOI: [10.1016/j.matdes.2017.02.078](https://doi.org/10.1016/j.matdes.2017.02.078).
- Cheretaeva A.O., Glukhov P.A., Shafeev M.R., Denisova A.G., Borgardt E.D., Polunin A.V., Katsman A.V., Krishtal M.M. Improvement of protective oxide layers formed by high-frequency plasma electrolytic oxidation on Mg-RE alloy with LPSO-phase // *Chimica Techno Acta*. 2023. Vol. 10. № 2. Article number 202310212. DOI: [10.15826/chimtech.2023.10.2.12](https://doi.org/10.15826/chimtech.2023.10.2.12).
- Simchen F., Sieber M., Kopp A., Lampke T. Introduction to plasma electrolytic oxidation – an overview of the process and applications // *Coatings*. 2020. Vol. 10. № 7. Article number 628. DOI: [10.3390/COATINGS10070628](https://doi.org/10.3390/COATINGS10070628).
- Lu Xiaopeng, Blawert C., Huang Yuanding, Ovri H., Zheludkevich M.L., Kainer K.U. Plasma electrolytic oxidation coatings on Mg alloy with addition of SiO₂ particles // *Electrochimica Acta*. 2016. Vol. 187. P. 20–33. DOI: [10.1016/J.ELECTACTA.2015.11.033](https://doi.org/10.1016/J.ELECTACTA.2015.11.033).
- Mashtalyar D.V., Imshinetskiy I.M., Nadaraia K.V. et al. Effect of TiO₂ nanoparticles on the photocatalytic properties of PEO coatings on Mg alloy // *Journal of Magnesium and Alloys*. 2023. Vol. 11. № 2. P. 735–752. DOI: [10.1016/J.JMA.2022.10.021](https://doi.org/10.1016/J.JMA.2022.10.021).
- Bordbar-Khiabani A., Yarmand B., Mozafari M. Enhanced corrosion resistance and in-vitro biodegradation of plasma electrolytic oxidation coatings prepared on AZ91 Mg alloy using ZnO nanoparticles-incorporated electrolyte // *Surface and Coatings Technology*. 2019. Vol. 360. P. 153–171. DOI: [10.1016/J.SURFCOAT.2019.01.002](https://doi.org/10.1016/J.SURFCOAT.2019.01.002).
- Gnedenkov S.V., Sinebryukhov S.L., Mashtalyar D.V., Imshinetskiy I.M., Samokhin A.V., Tsvetkov Y.V. Fabrication of coatings on the surface of magnesium alloy by plasma electrolytic oxidation using ZrO₂ and SiO₂ Nanoparticles // *Journal of Nanomaterials*. 2015. Vol. 2015. Article number 154298. DOI: [10.1155/2015/154298](https://doi.org/10.1155/2015/154298).
- Wu Jiahao, Wu Liang, Yao Wenhui, Chen Yanning, Chen Yonghua, Yuan Yuan, Wang Jingfeng, Atrens A., Pan Fusheng. Effect of electrolyte systems on plasma electrolytic oxidation coatings characteristics on LPSO Mg-Gd-Y-Zn alloy // *Surface and Coatings Technology*. 2023. Vol. 454. Article number 129192. DOI: [10.1016/J.SURFCOAT.2022.129192](https://doi.org/10.1016/J.SURFCOAT.2022.129192).
- Mohedano M., Pérez P., Matykina E., Pillado B., Garcés G., Arrabal R. PEO coating with Ce-sealing for corrosion protection of LPSO Mg–Y–Zn alloy // *Surface and Coatings Technology*. 2020. Vol. 383. Article number 125253. DOI: [10.1016/J.SURFCOAT.2019.125253](https://doi.org/10.1016/J.SURFCOAT.2019.125253).
- Liu Xiaohu, Liu Lei, Dong Shuai, Chen Xiao-Bo, Dong Jie. Towards dense corrosion-resistant plasma electrolytic oxidation coating on Mg-Gd-Y-Zr alloy by using ultra-high frequency pulse current // *Surface and Coatings Technology*. 2022. Vol. 447. Article number 128881. DOI: [10.1016/J.SURFCOAT.2022.128881](https://doi.org/10.1016/J.SURFCOAT.2022.128881).
- Kang Min Lee, Ki Ryong Shin, Seung Namgung, Bongyoung Yoo, Dong Hyuk Shin. Electrochemical response of ZrO₂-incorporated oxide layer on AZ91 Mg alloy processed by plasma electrolytic oxidation // *Surface and Coatings Technology*. 2011. Vol. 205. № 13–14. P. 3779–3784. DOI: [10.1016/J.SURFCOAT.2011.01.033](https://doi.org/10.1016/J.SURFCOAT.2011.01.033).
- Kaseem M., Fatimah S., Nashrah N., Ko Y.G. Recent progress in surface modification of metals coated by plasma electrolytic oxidation: Principle, structure, and performance // *Progress in Materials Science*. 2021. Vol. 117. Article number 100735. DOI: [10.1016/J.PMATSCI.2020.100735](https://doi.org/10.1016/J.PMATSCI.2020.100735).
- Benfedda B., Hamadou L., Benbrahim N., Kadri A., Chainet E., Charlot F. Electrochemical Impedance Investigation of Anodic Alumina Barrier Layer // *Journal of The Electrochemical Society*. 2012. Vol. 159. № 8. P. C372–C381. DOI: [10.1149/2.068208JES](https://doi.org/10.1149/2.068208JES).
- Krishtal M.M., Ryumkin M.Y. Inherited chemical inhomogeneity in oxide layers deposited by the method of microarc oxidizing on hypereutectic silumins // *Metal Science and Heat Treatment*. 2007. Vol. 49. № 3–4. P. 111–117. DOI: [10.1007/s11041-007-0021-x](https://doi.org/10.1007/s11041-007-0021-x).
- Siqveland L.M., Skjaeveland S.M. Derivations of the Young-Laplace equation // *Capillarity*. 2021. Vol. 4. № 2. P. 23–30. DOI: [10.46690/CAP1.2021.02.01](https://doi.org/10.46690/CAP1.2021.02.01).
- Dilimon V.S., Shibli S.M.A. A Review on the application-focused assessment of plasma electrolytic oxidation (PEO) coatings using electrochemical impedance spectroscopy // *Advanced Engineering Materials*. 2023. Vol. 25. № 12. Article number 2201796. DOI: [10.1002/ADEM.202201796](https://doi.org/10.1002/ADEM.202201796).
- Lu Xiaopeng, Chen Yan, Blawert C., Li Yan, Zhang Tao, Wang Fuhui, Kainer K.U., Zheludkevich M. Influence of SiO₂ particles on the corrosion and wear resistance of plasma electrolytic oxidation-coated

AM50 Mg alloy // Coatings. 2018. Vol. 8. № 9. Article number 306. DOI: [10.3390/COATINGS8090306](https://doi.org/10.3390/COATINGS8090306).
 25. Polunin A.V., Cheretaeva A.O., Borgardt E.D., Rastegaev I.A., Krishtal M.M., Katsman A.V., Yasnikov I.S. Improvement of oxide layers formed by plasma electro-

lytic oxidation on cast AlSi alloy by incorporating TiO₂ nanoparticles // Surface and Coatings Technology. 2021. Vol. 423. Article number 127603. DOI: [10.1016/J.SURFCOAT.2021.127603](https://doi.org/10.1016/J.SURFCOAT.2021.127603).

Влияние добавки наночастиц ZrO₂ в электролит на структуру и антикоррозионные свойства оксидных слоев, формируемых плазменно-электролитическим оксидированием на сплаве Mg₉₇Y₂Zn₁

© 2023

Полунина Алиса Олеговна^{*1}, научный сотрудник НИИ прогрессивных технологий
*Полунин Антон Викторович*², кандидат технических наук, ведущий научный сотрудник НИИ прогрессивных технологий
*Криштал Михаил Михайлович*³, доктор физико-математических наук, профессор, главный научный сотрудник НИИ прогрессивных технологий
 Тольяттинский государственный университет, Тольятти (Россия)

*E-mail: a.cheretaeva@tlttsu.ru,
alice_raduga@mail.ru

¹ORCID: <https://orcid.org/0000-0002-3952-9556>

²ORCID: <https://orcid.org/0000-0001-8484-2456>

³ORCID: <https://orcid.org/0000-0001-7189-0002>

Поступила в редакцию 26.06.2023

Принята к публикации 27.10.2023

Аннотация: Магниево-цинковые сплавы с упрочняющей длиннопериодической упорядоченной структурой (long-period stacking ordered structure, LPSO-фаза) обладают выдающимися механическими свойствами, однако их низкая коррозионная стойкость обуславливает необходимость в дополнительной поверхностной защите. В работе исследовано влияние добавок в электролит наночастиц ZrO₂ в концентрации 1–4 г/л на толщину, структуру, состав, смачиваемость и антикоррозионные свойства оксидных слоев, формируемых при плазменно-электролитическом оксидировании (ПЭО) сплава Mg₉₇Y₂Zn₁ с LPSO-фазой. Установлено, что при ПЭО наночастицы ZrO₂ под действием электрического поля внедряются в формирующийся оксидный слой, а также снижают его пористость. Выявлено снижение количества и размеров пор вблизи барьерного слоя в местах выхода LPSO-фазы сплава к границе раздела с оксидным слоем. Малые концентрации наночастиц ZrO₂ (1–2 г/л) снижают скорость коррозии сплава по сравнению с базовым вариантом до двух раз. Минимальной плотностью тока коррозии $i_{корр} \approx 14$ нА/см² и наибольшим поляризационным сопротивлением $R_p \approx 2,6$ МОм·см² обладает образец, сформированный в электролите с добавкой 1 г/л наночастиц ZrO₂. Расчет параметров барьерной зоны оксидных слоев показал, что повышение концентрации ZrO₂ в электролите приводит к увеличению толщины барьерного слоя и росту его удельной проводимости, что отрицательно сказывается на коррозионной стойкости формируемых оксидных слоев: сопротивление барьерной зоны слоя, полученного при добавке 4 г/л ZrO₂, падает на ~20 % по сравнению с базовым вариантом (до ~1 МОм·см²).

Ключевые слова: магниевый сплав; Mg₉₇Y₂Zn₁; наночастицы ZrO₂; LPSO-фаза; плазменно-электролитическое оксидирование; наночастицы; оксид циркония; краевой угол смачивания поверхности; коррозионная стойкость; проводимость барьерной зоны.

Благодарности: Работа выполнена при поддержке Российского научного фонда (проект № 21-19-00656, <https://rscf.ru/project/21-19-00656/>).

Статья подготовлена по материалам докладов участников XI Международной школы «Физическое материаловедение» (ШФМ-2023), Тольятти, 11–15 сентября 2023 года.

Для цитирования: Полунина А.О., Полунин А.В., Криштал М.М. Влияние добавки наночастиц ZrO₂ в электролит на структуру и антикоррозионные свойства оксидных слоев, формируемых плазменно-электролитическим оксидированием на сплаве Mg₉₇Y₂Zn₁ // Frontier Materials & Technologies. 2023. № 4. С. 87–98. DOI: 10.18323/2782-4039-2023-4-66-8.

Structure and micromechanical properties of SHS composites with a copper matrix: peculiarities of formation

© 2023

*Nataliya B. Pugacheva*¹, Doctor of Sciences (Engineering),
Associate Professor, chief researcher

Tatyana M. Bykova^{*2}, PhD (Engineering), senior researcher

*Ekaterina I. Senaeva*³, junior researcher

Institute of Engineering Science of the Ural Branch of RAS, Yekaterinburg (Russia)

*E-mail: nat@imach.uran.ru,
tatiana_8801@mail.ru

¹ORCID: <https://orcid.org/0000-0001-8015-8120>

²ORCID: <https://orcid.org/0000-0002-8888-6410>

³ORCID: <https://orcid.org/0000-0001-8625-2310>

Received 22.06.2023

Accepted 19.10.2023

Abstract: Self-propagating high-temperature synthesis (SHS) is one of the promising methods for producing strong and wear-resistant composites. The use of copper as a matrix due to the unique combination of electrical and thermal conductivity is of particular interest. Monolithic SHS composites of the Cu–Ti–C–B and Cu–Ti–C systems are currently little studied. The information on the phase composition of such composites is contradictory, and data on micromechanical properties is practically absent. The paper presents the results of a comparative analysis of the structure and micromechanical properties of composites of the Cu–Ti–C and Cu–Ti–C–B systems. It is found that the matrix of both composites is a copper-based solid solution supersaturated with titanium, in which nanosized Cu₄Ti intermetallic compound particles precipitate upon cooling. TiC particles (Cu–Ti–C composite) and TiC and TiB₂ particles (Cu–Ti–C–B composite) are the strengthening phases resulting from SHS. In the Cu–Ti–C–B composite, the original particles of unreacted B₄C boron carbide were preserved, the microhardness of which was 3680 HV 0.1. The most ductile structural constituent in the Cu–Ti–B system composite is the Cu+Cu₄Ti mechanical mixture, due to which further plastic deformation is possible to obtain parts of a given shape. During the study of micromechanical properties, the maximum strength indicators of H_{IT} , HV, W_e , R_e , H_{IT}/E^* were recorded in the Cu–Ti–C–B system composite, which allows expecting high wear resistance of products made of it.

Keywords: self-propagating high-temperature synthesis; monolithic SHS composites; copper matrix; structural constituents; strengthening phases; intermetallics; titanium carbide; titanium diboride; micromechanical properties; hardness.

Acknowledgments: The research was supported by the Russian Science Foundation grant No. 22-29-00188 “The Development of Scientific and Technological Foundations for the Formation of Monolithic SHS Composites of the Cu–Ti–C–B System with Specified Functional Properties”, <https://rscf.ru/project/22-29-00188/>.

The work was performed on the equipment of the “Plastometria” Core Facility Center of the Federal State Budgetary Institution of Science Institute of Engineering Science, Ural Branch of the Russian Academy of Sciences.

The paper was prepared on the reports of the participants of the XI International School of Physical Materials Science (SPM-2023), Togliatti, September 11–15, 2023.

For citation: Pugacheva N.B., Bykova T.M., Senaeva E.I. Structure and micromechanical properties of SHS composites with a copper matrix: peculiarities of formation. *Frontier Materials & Technologies*, 2023, no. 4, pp. 99–108. DOI: 10.18323/2782-4039-2023-4-66-9.

INTRODUCTION

The method of self-propagating high-temperature synthesis (SHS) is widely recognised in the field of creating new powder materials [1–3]. Currently, this process is being studied in 47 countries around the world. The SHS process is based on carrying out exothermic chemical reactions of interaction of initial reagents in the form of combustion, where the target combustion product is solid chemical compounds (carbides, nitrides, borides, oxides, etc.) and materials based on them [4]. The main reagents in SHS processes are powders of metals and non-metals, and the final product is powders, sintered bulk materials or coatings [5–7].

The advantages of SHS technology include a significant reduction in energy costs for heating to high temperatures, as the heat generated by the combustion reaction works, as well as the use of simple, small-scale equipment, and the implementation of high process speeds [8–10]. Currently,

about 100 varieties of SHS technology have been created, which allow synthesising over 1000 substances and materials, applying coatings, and welding parts. In Russia, six types of SHS technologies are common: reactor powder, sintering, power compaction, casting and weld facing, welding, and vapour transport coatings [3; 8]. SHS technologies are widely used in mechanical engineering (abrasive, blade and stamp tools, high-temperature and wear-resistant parts), metallurgy (refractory products, weld facing, electrodes, ferroalloys, metal-supplying pipes), electrical engineering and electronics (ferrites, ferroelectric materials, insulators, heating elements, high-temperature superconductors), chemical industry (catalysts), medicine (implants made of shape memory alloys) [9]. The SHS process is also very promising for the production of nanomaterials: nanosized powders, fibres and films, as well as nanostructured compact materials [10].

SHS is a rather complex physical and chemical process; its behaviour depends on many factors: the reaction heat,

the composition and structure of the initial mixture of powders, the size of their particles, density, size and temperature of samples, the composition and pressure of the surrounding gas, etc. SHS is based on the exothermic reactions leading to heating of the initial mixture up to the melting point of the metal powders that form the composite matrix [3; 4]. After the SHS completion, the produced composite is cooled, and, as a result, phase transformations are possible in the metal matrix that largely determine the composite properties. Until now, research has been focused mainly on studying the theory of combustion and synthesis processes, understanding their mechanisms, identifying the influence of various technological parameters on the composition, structure and properties of the resulting product, as well as developing the equipment for the SHS process implementation [3; 4]. The study of the structure and properties of the matrix is rather neglected. However, it is in it that significant changes occur both during the synthesis process and during subsequent thermal treatments [11–13]: during the combustion process, supersaturated solid solutions, non-equilibrium phases and intermediate products are formed, which upon subsequent heating, can decay and interact with each other, forming new phases.

Copper has a unique combination of electromagnetic and thermophysical properties [14]. Therefore, composites with a copper matrix are a very promising new material for structures requiring high electrical and thermal conductivity [15; 16]. The authors of works [14; 17] showed that severe plastic deformation of Cu/Mg composites, in combination with heat treatment allows obtaining unique properties due to a combination of high electrical conductivity and strength. Previous studies have demonstrated that composites of the Cu–Ti–C and Cu–Ti–C–B systems are characterised by high wear resistance [18; 19]. It has been found that abrasive wear of these composites occurs through plastic displacement of the cut material, which allows forming a surface with a high degree of roughness [19]. Moreover, copper and alloys based on it are quite easily deformed, which allows implementing deformation-thermal treatment of the composite to change its properties and give it a defined shape. Thus, in the work [20], temperatures and pressures were found at which it is possible to realise plastic deformation of the Cu–Ti–C–B SHS composite without destruction. In this regard, the study of composites of the Cu–Ti–C and Cu–Ti–C–B systems is of great practical interest.

The available information on the phase composition of SHS composites of the Cu–Ti–C and Cu–Ti–C–B systems is quite contradictory. Thus, the authors of [18] discovered, except for the particles of strengthening TiC phases formed as a result of the Cu–Ti–C composite SHS, a whole series of titanium cuprides of various compositions. The works [19; 20] show that in the copper matrix of Cu–Ti–C–B composites, nano-sized particles of only one intermetallic compound, Cu_4Ti , homogeneously precipitate. Moreover, previous studies [21] showed that when forming Cu–Ti–C–B system composites, it is possible to retain a small amount of B_4C particles, that do not have time to react with titanium [21]. In this regard, it is of interest to conduct a comparative analysis of the structure of Cu–Ti–C and Cu–Ti–C–B composites produced under the same conditions using the same Cu, Ti, and C

powders, differing only in the addition of B_4C powder to the composition of the original mixtures.

The purpose of the work is to carry out a comparative analysis of the structure and micromechanical properties of SHS composites of the Cu–Ti–C and Cu–Ti–C–B systems.

METHODS

Monolithic composites of the Cu–Ti–C and Cu–Ti–C–B systems were produced using a technology described in detail previously in [22].

The initial powder mixture consists of thermoreactive and matrix components. Thermoreactive components (TRC) are powders of PTM-1 titanium, P-804T carbon black and B_4C boron carbide of M20 grade, which ensure the occurrence of exothermic synthesis reactions. Cu powder of PMS-1 grade is the matrix component. The TRC fraction in the initial powder mixture was 23 wt. %. The mixture of powders was thoroughly stirred and poured into a pipe container made of St3 low-carbon structural steel. Primary compaction of the powder mixture was carried out using special equipment. Then the blank was placed in an electric furnace, and heated to the temperature when exothermic reactions began (about 1000 °C). After SHS completion, the hot blank was transferred to a hydraulic press and deformed with a load of at least 250 MPa to eliminate internal porosity. As a result, sandwich plates were obtained, the appearance of which is shown in Fig. 1.

The structure of the composites was studied using a TESCAN VEGAII XMU scanning electron microscope. Rockwell hardness was measured using a hardness tester. The local chemical composition of the composite phases was determined using an OXFORD energy dispersive attachment to a scanning microscope. The average chemical composition of the composites was determined by averaging the scanning results of 10 fragments of the polished section surface with an area of 2×2 mm. Phase X-ray diffraction analysis was performed on a SHIMADZU X-ray diffractometer in chromium k_α -radiation.

Instrumental indentation was carried out on a Fischer-scope HM2000 XYm measuring system, using a Vickers indenter and WIN-HCU software at a maximum load of 0.980 N, loading time of 30 s, holding at the load during 50 s and unloading time of 30 s according to ISO 14577 standard. Accuracy of microhardness and microindentation characteristics based on 10 measurements was calculated with a confidence factor of $p=0.95$.

Based on the indentation results, the following indicators of micromechanical properties were determined: Vickers microhardness (HV), contact elasticity modulus (E^*), elastic recovery index (R_e), component of elastic strain work during indentation (φ), creeping during indentation (C_{IT}), index of elastic deformation fraction in the total deformation during indentation H_{IT}/E (H_{IT} is indentation hardness values at maximum load). The values of the R_e , φ and C_{IT} indicators were calculated using the formulas:

$$R_e = \frac{h_{\max} - h_p}{h_{\max}} \cdot 100 \% ;$$

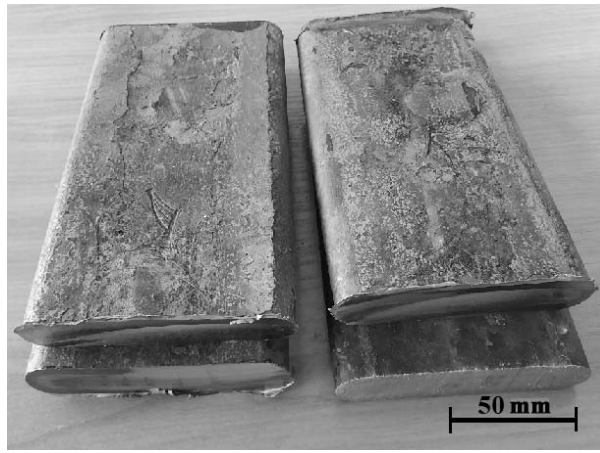


Fig. 1. Appearance of sandwich plates made of Cu-Ti-C and Cu-Ti-C-B composites
Рис. 1. Внешний вид сэндвич-пластин из композитов Cu-Ti-C и Cu-Ti-C-B

$$\varphi = \left(1 - \frac{W_e}{W_t}\right) \cdot 100\% ;$$

$$C_{IT} = \frac{h_{\max} - h_1}{h_1} \cdot 100\% ,$$

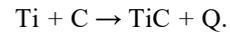
where W_e is the elastic strain work during indentation released when the applied load is removed;
 W_t is the total mechanical work during indentation determined by the area under the loading curve;
 h_1 is the indenter penetration depth corresponding to the initial point of the horizontal section on the loading curve;
 h_{\max} is the maximum penetration depth of the indenter.

Fig. 2 shows the general view of the loading curves and the measured experimental parameters.

RESULTS

Hot pressing of blanks immediately after synthesis completion makes it possible to obtain solid pore-free composites. The average chemical composition of the produced SHS composites is given in Table 1.

According to the results of phase X-ray diffraction analysis, three phases were registered in the Cu-Ti-C composite: a solid solution based on Cu, Cu_4Ti and TiC. TiC particles were formed as a result of an exothermic reaction:



Since the SHS process is implemented in air, a carbon combustion reaction occurs in the powder mixture:

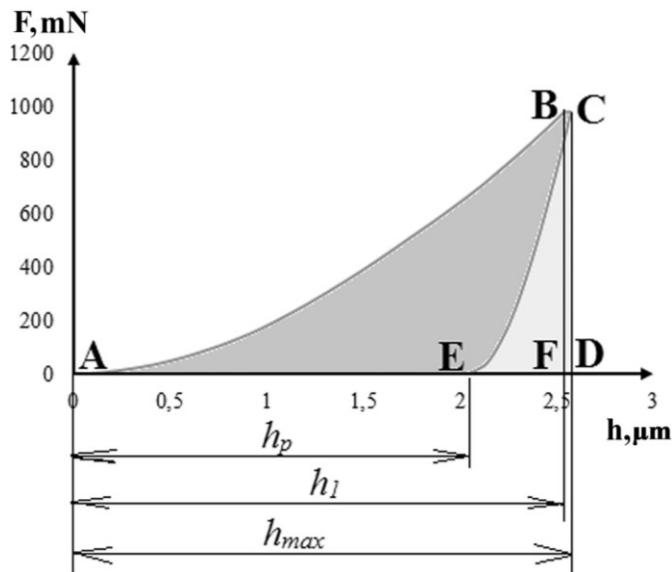
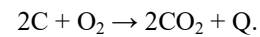


Fig. 2. Loading diagrams and measured parameters
Рис. 2. Диаграммы нагружения и измеряемые параметры

Phases and chemical elements are distributed nonuniformly over the cross section of the Cu–Ti–C system composite (Fig. 3). Some regions contain a minimal amount of TiC particles (region 1 in Fig. 3 a), while others contain their aggregate (region 2 in Fig. 3 a). Cu₄Ti particles are not visible when examined with a scanning electron microscope due to their small size. When performing a composite EDS analysis, it is impossible to separate phases from each other, so the chemical composition of conventionally identified two structural constituents of the composite was determined: 1 – mechanical mixture of a solid solution based on copper and Cu₄Ti particles with a minimum amount of TiC particles; 2 – Cu+TiC+Cu₄Ti mechanical mixture (Table 2).

The heterogeneity of the distribution of TiC particles throughout the volume of the composite caused the heterogeneity of the distribution of micromechanical properties. In the loading diagrams (Fig. 4 a), the far right curve corresponds to section 1 in Fig. 3 a, and the far left – to section 2 in Fig. 3 a. Consequently, the values of micromechanical properties in Table 3 correspond to the sections indicated in Fig. 3 a. The total hardness of the Cu–Ti–C system composite was 33 HRC.

In the Cu–Ti–C–B system composite, X-ray diffraction analysis, except for the phases found in the Cu–Ti–C composite, additionally detected TiB₂ particles resulting from an exothermic reaction



If TiC particles are uniformly distributed throughout the composite volume, then TiB₂ particles are nonuniformly distributed; there are areas where they are absent. EDS analysis found that TiC particles contain a certain amount of boron (Table 4). It is known that the TiC and TiB compounds are isomorphic, therefore this phase should be designated as Ti(C,B). In the Cu–Ti–C–B composite, two structural components were conventionally identified. Since they differ in chemical composition from the structural constituents of the Cu–Ti–C system composite, letter designations were accepted for them: A – Cu+Cu₄Ti+Ti(C,B) mechanical mixture; B – Cu+Cu₄Ti+Ti(C,B)+TiB₂ mechanical mixture (Fig. 5 a). Moreover, particles of unreacted B₄C boron carbide were found in the Cu–Ti–C–B composite (Fig. 5). Thin pure titanium interlayers (marked by arrows in Fig. 5 b) were observed around the B₄C particles.

Since the Cu–Ti–C–B composite additionally contains particles of the strengthening TiB₂ and B₄C phases, its hardness turned out to be slightly higher in comparison to the Cu–Ti–C system composite and amounted to 36 HRC. Micromechanical properties vary throughout the volume of the Cu–Ti–C–B system composite. Compared to the Cu–Ti–C composite, the indicators characterising the strength of the structural components, namely *HV*, *E**, *R_e*, *H_{1T}/E**, are higher, and the indicators conditionally characterizing plasticity (*h_{max}*, *φ*, *C_T*) are lower (Table 5).

DISCUSSION

The composites studied in this work differ from those considered previously [19–21] by the lower TRC content in the initial powder mixture. Previously, it was found that the Cu–Ti–C–B system composites retain a certain amount of unreacted B₄C boron carbide. Boron carbide has excessively high hardness and brittleness, and therefore is a source of microcrack initiation under external mechanical loading of parts and structural elements made of this composite during their operation. It turned out that the absence of B₄C particles in the initial powder mixture did not lead to a noticeable decrease in the hardness of the resulting composite. Titanium, which does not participate in exothermic reactions, dissolves in the copper crystal lattice forming a supersaturated solid solution. When cooling the composite in a copper-based solid solution supersaturated with titanium, nano-sized particles of the Cu₄Ti intermetallic compound homogeneously precipitate. These particles significantly strengthen the composite even with a small amount of TiC particles formed and in the absence of TiB₂ particles. The work [18] shows that the Cu–Ti–C system composite has increased resistance to abrasive wear compared to the quench-hardened H12MFL tool die steel, which gives reason to expect high wear resistance of the studied composite.

As shown in [19–21], reducing the TRC proportion in the initial powder mixture for the composite synthesis from 30 wt. % up to 23 wt. % did not affect the retention of unreacted initial B₄C particles in the Cu–Ti–C–B system composite. Obviously, boron carbide particles do not have time to react completely with titanium during the SHS process due to the rapid melting of copper (its melting point is 1083 °C) and the filling of the container mold

Table 1. Chemical composition of SHS composites
Таблица 1. Химический состав СВС-композиатов

System	Units	Ti	C	B	Cu
Cu–Ti–C	Wt. %	23.7±2.3	2.6±0.4	0	The rest
	At. %	26.3±2.1	11.7±1.7	0	
Cu–Ti–C–B	Wt. %	20.4±1.3	3.0±0.4	8.2±1.1	
	At. %	17.0±1.0	9.9±0.9	30.1±3.0	

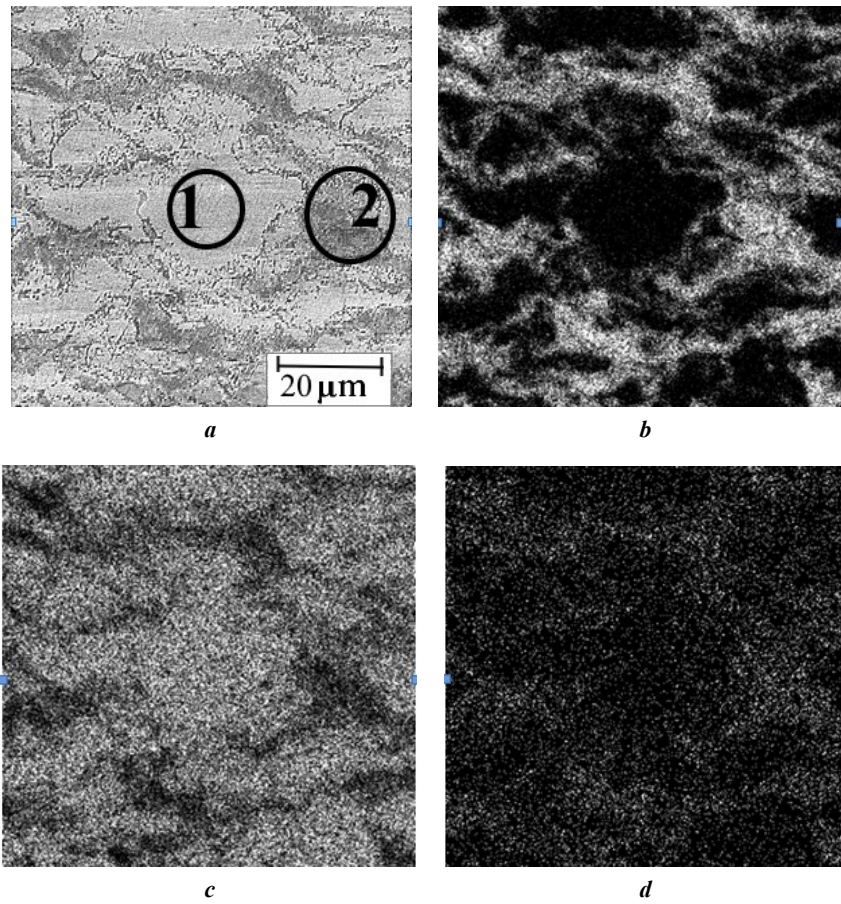


Fig. 3. Microstructure and pattern of distribution of chemical elements in the Cu-Ti-C system composite:
a – secondary electron image; *b* – characteristic X-rays Ti; *c* – Cu; *d* – C

Рис. 3. Микроструктура и характер распределения химических элементов в композите системы Cu-Ti-C:
a – изображение во вторичных электронах; *b* – в характеристическом рентгеновском излучении Ti; *c* – Cu; *d* – C

Table 2. Chemical composition of structural constituents of the Cu-Ti-C system composite, at. % shown in Fig. 3
Таблица 2. Химический состав структурных составляющих композита системы Cu-Ti-C, ат. %, представленного на рис. 3

Structural constituents	C	Ti	Cu	Phases
1	2	22	76	Cu+Cu ₄ Ti
2	16	52	32	Cu+TiC

Table 3. Average values of micromechanical properties of structural constituents of the Cu-Ti-C composite
Таблица 3. Средние значения микромеханических свойств структурных составляющих композита Cu-Ti-C

No. in Fig. 3 a	H_{IT} , GPa (± 1.5)	$HV_{0,1}$ (± 1.4)	E^* , GPa (± 15)	W_t , nJ (± 6.3)	W_e , nJ (± 1.2)	h_{max} , μm (± 0.2)	h_1 , μm (± 0.2)	h_p , μm (± 0.2)	R_{es} , %	H_{IT}/E^*	ϕ , %	C_{IT} , %
1	1.2	116	93	204	20	5.9	5.8	5.0	15	0.013	91	3.4
2	4.9	458	204	105	20	3.1	3.1	2.6	16	0.024	81	1.3

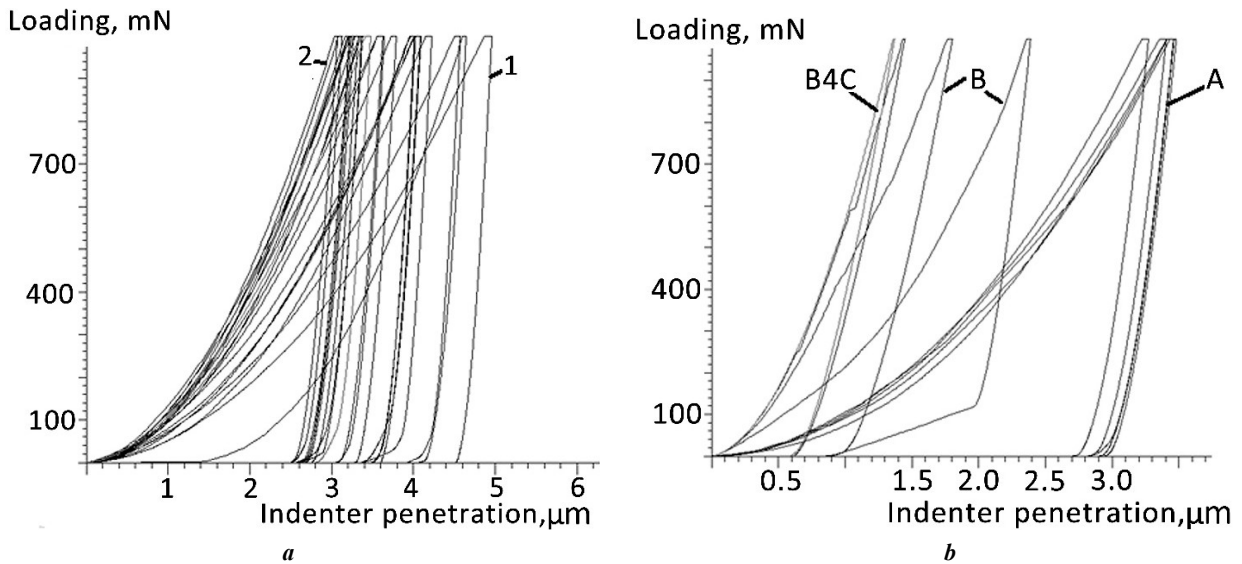


Fig. 4. Loading diagrams of composites:
a – Cu–Ti–C (1 – Cu+Cu₄Ti; 2 – Cu+TiC+Cu₄Ti); *b* – Cu–Ti–C–B (A – Cu+Cu₄Ti+TiC; B – Cu+TiC+TiB₂)
Рис. 4. Диаграммы нагружения композитов:
a – Cu–Ti–C (1 – Cu+Cu₄Ti; 2 – Cu+TiC+Cu₄Ti); *b* – Cu–Ti–C–B (A – Cu+Cu₄Ti+TiC; B – Cu+TiC+TiB₂)

Table 4. Chemical composition of structural constituents of the Cu–Ti–C–B composite, at. % (Fig. 5 a)
Таблица 4. Химический состав структурных составляющих композита Cu–Ti–C–B, ат. % (рис. 5 а)

Structural constituents	B	C	Ti	Cu	Phases
A	8	10	25	58	Cu+Cu ₄ Ti+Ti(C,B)
B	20	11	37	32	Cu+Cu ₄ Ti+Ti(C,B)+TiB ₂
B ₄ C	70	30	0	0	B ₄ C

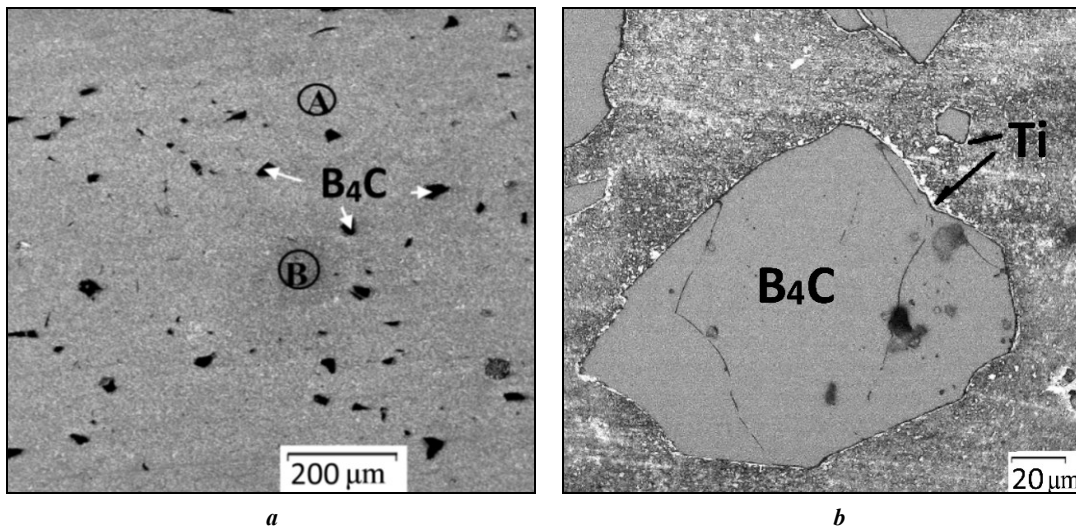


Fig. 5. Microstructure of the Cu–Ti–C–B system composite: *a* – magnification ×200; *b* – magnification ×1000, arrows show titanium interlayers.
A – Cu+Cu₄Ti+Ti(C,B) mechanical mixture; *B* – Cu+Cu₄Ti+Ti(C,B)+TiB₂ mechanical mixture
Рис. 5. Микроструктура композита системы Cu–Ti–C–B: *a* – увеличение ×200; *b* – увеличение ×1000, стрелками указаны прослойки титана.
A – механическая смесь Cu+Cu₄Ti+Ti(C,B); *B* – механическая смесь Cu+Cu₄Ti+Ti(C,B)+TiB₂

Table 5. Average values of micromechanical properties of structural constituents of the Cu–Ti–C–B composite (Fig. 5 a)
Таблица 5. Средние значения микромеханических свойств структурных составляющих композита Cu–Ti–C–B (рис. 5 а)

Structural constituents	H_{IT} , GPa (± 1.5)	$HV\ 0,1$ (± 1.4)	E^* , GPa (± 15)	W_p , nJ (± 6.3)	W_e , nJ (± 1.2)	h_{max} , μm (± 0.2)	h_1 , μm (± 0.2)	h_p , μm (± 0.2)	R_e , %	H_{IT}/E^*	ϕ , %	C_{IT} , %
A	3.7	354	180	110	20.0	3.50	3.30	2.90	16	0.021	82	6.0
B	8.3	786	280	80	30.0	2.40	2.30	0.90	64	0.029	63	4.0
B ₄ C	38.9	3680	283	82	26.2	1.37	1.36	0.58	57	0.093	40	0.7

with the melt. All B₄C particles retained in the composite are surrounded by layers of titanium, which, upon subsequent annealing, is capable of reacting with B₄C particles to form TiB₂ particles, as was shown previously in [21].

The ability to undergo plastic deformation to obtain products of a specified shape is very important for composites. Previously, it was found [20] that plastic deformation of the Cu–Ti–C–B system composites occurs due to the most plastic phases and structural components. From this point of view, the Cu–Ti–C system composite has advantages over the Cu–Ti–C–B system composite, since it contains the Cu+Cu₄Ti structural component with maximum values of the h_{max} , ϕ and C_{IT} indicators, which characterise the ability to change shape, i. e. to plastic deformation. Since nano-sized particles of the Cu₄Ti intermetallic compound dissolve when heated to temperatures above 700 °C, significant deformation of the Cu–Ti–C system composite should be expected at temperatures of 700–800 °C.

The presence of hard and brittle B₄C particles in the Cu–Ti–C–B system composite reduces its structural strength. Cu+Cu₄Ti+TiC is the most plastic structural constituent in it, which is characterised by higher values of H_{IT} , HV , W_e , R_e , H_{IT}/E^* compared to the Cu+Cu₄Ti constituent in the Cu–Ti–C composite. Nevertheless, plastic deformation of the Cu–Ti–C–B system composite is possible as well under the conditions considered in [20].

The structural constituents of the Cu–Ti–C–B composite are characterised by higher strengthening, which shows a shift of all loading diagrams in the region of smaller indenter penetration depths (Fig. 4), as well as higher values of the H_{IT} , HV , W_e , R_e , H_{IT}/E^* indicators (Table 5). The H_{IT}/E^* ratio determines the proportion of elastic deformation in the total deformation during indentation, and indirectly characterises the wear resistance of the structural components of the composite. For that reason, the Cu–Ti–C–B composite should be expected to demonstrate higher wear resistance compared to the Cu–Ti–C composite, although they practically do not differ in hardness.

CONCLUSIONS

The Cu–Ti–C system composite produced by the SHS method consists of a supersaturated solid titanium solution in a copper crystal lattice, in which nano-sized particles of the Cu₄Ti intermetallic compound homogeneously, precipitated during cooling of the composite are uniformly distributed, and TiC particles formed as a result of the synthesis.

Reducing the TRC proportion in the initial powder mixture from the previously used 30 wt. % up to 23 wt. % did not lead to a decrease in the probability of retaining particles of the original B₄C boron carbide that did not react with the titanium powder through an exothermic reaction.

The most plastic Cu+Cu₄Ti structural component in the Cu–Ti–C composite provides the possibility of subsequent plastic deformation of the composite to obtain a product of a specified shape.

Higher strength indicators of the structural components of the Cu–Ti–C–B system composite determine the expected high wear resistance of products.

REFERENCES

- Levashov E.A., Rogachev A.S., Kurbatkina V.V., Maksimov Yu.M., Yuhvid V.I. *Perspektivnye materialy i tekhnologii samorasprostranyayushchegosya vysokotemperaturnogo sinteza* [Promissory Materials and Processes of Self-Propagating High-Temperature Synthesis]. Moscow, MISiS Publ., 2011. 378 p.
- Rogachev A.S., Mukasyan A.S. *Goreniya dlya sinteza materialov* [Combustions for synthesizing materials]. Moscow, FIZMATLIT Publ., 2012. 400 p.
- Amosov A.P., Borovinskaya I.P., Merzhanov A.G. *Poroshkovaya tekhnologiya samorasprostranyayushchegosya vysokotemperaturnogo sinteza materialov* [Powder technology of self-propagating high-temperature synthesis of materials]. Moscow, Mashinostroenie-1 Publ., 2007. 567 p.
- Merzhanov A.G. Self-propagating high-temperature synthesis. *Fizicheskaya khimiya. Sovremennye problemy*. Moscow, Khimiya Publ., 1983, pp. 6–44.
- Latukhin E.I., Umerov E.R., Luts A.R. Self-propagating high-temperature synthesis of porous titanium carbide blanks for subsequent infiltration by melts. *Zagotovitelnye proizvodstva v mashinostroenii*, 2021, vol. 19, no. 7, pp. 322–330. DOI: [10.36652/1684-1107-2021-19-7-322-330](https://doi.org/10.36652/1684-1107-2021-19-7-322-330).
- Korosteleva E.N., Korzhova V.V. Structure and phase composition of (TiB)-Ti metal matrix composites obtained by SHS and vacuum sintering. *Russian Physics Journal*, 2020, vol. 63, no. 7, pp. 1195–1201. DOI: [10.1007/s11182-020-02159-4](https://doi.org/10.1007/s11182-020-02159-4).
- Sitnikov A.A., Sobachkin A.V., Markov A.M. Peculiarities in formation of different functional coatings of SHS-mechano-composites using technologies of gas-

- detonation sputtering. *Naukoemkie tekhnologii v mashinostroyeni*, 2020, no. 2, pp. 22–28. DOI: [10.30987/2223-4608-2020-2-22-28](https://doi.org/10.30987/2223-4608-2020-2-22-28).
8. Fedotov A.F., Amosov A.P., Radchenko V.P. *Modelirovanie protsessa pressovaniya poroshkovykh materialov v usloviyakh samorasprostranyayushchegosya vysokotemperaturnogo sinteza* [Modeling the Powder Material Compaction in Conditions of the Self-Propagating High-Temperature Synthesis]. Moscow, Mashinostroyeniye-1 Publ., 2005. 281 p.
 9. Kovalev D.Yu., Bolotskaya A.V., Mikheev M.V. Self-propagating high-temperature synthesis in the Ti–B–Fe system with AlN additions. *Inorganic Materials*, 2022, vol. 58, no. 9, pp. 922–930. EDN: [UTUZNA](https://www.edn.net/UTUZNA).
 10. Krivolutskiy K.S., Amosov A.P., Samboruk A.R. Self-propagating high-temperature synthesis ultradispersed and nanosized the powder composition TiC–SiC and TiC–NbC. *Vestnik Samarskogo gosudarstvennogo tekhnicheskogo universiteta. Seriya: Tekhnicheskie nauki*, 2016, no. 3, pp. 136–143. EDN: [XVSVKB](https://www.edn.net/XVSVKB).
 11. Shehukin A.S., Sytshev A.E. Peculiarities of a NiAl/Mo transition zone formed during self-propagating high-temperature synthesis. *The Physics of Metals and Metallography*, 2019, vol. 120, no. 9, pp. 848–852. DOI: [10.1134/S0031918X19090138](https://doi.org/10.1134/S0031918X19090138).
 12. Lazarev P.A., Busurina M.L., Gryadunov A.N., Sytshev A.E., Boyarchenko O.D., Karpov A.V. structure and phase formation of a Ti–Al–Si based alloy prepared by self-propagating high-temperature synthesis compaction. *Inorganic Materials*, 2022, vol. 58, no. 9, pp. 1005–1010. EDN: [QPVISC](https://www.edn.net/QPVISC).
 13. Lazarev P.A., Busurina M.L., Sychev A.E. Self-propagating high-temperature synthesis in Ti–Al–Mn. *Fizika goreniya i vzryva*, 2023, vol. 59, no. 1, pp. 85–91. DOI: [10.15372/FGV20230109](https://doi.org/10.15372/FGV20230109).
 14. Volkov A.Y., Patrakov E.I., Volkova E.G., Komkova D.A., Kalonov A.A., Glukhov A.V., Antonov B.D. Abnormally high strength and low electrical resistivity of the deformed Cu/Mg-composite with a big number of Mg-filaments. *Materials & Design*, 2020, vol. 185, article number 108276. DOI: [10.1016/j.matdes.2019.108276](https://doi.org/10.1016/j.matdes.2019.108276).
 15. Kim Ji Soon, Dudina D.V., Kim Jin Chun, Kwon Soon Young, Park Jin Ju, Rhee Chang Kyu. Properties of Cu-based nanocomposites produced by mechanically – activated self – propagating high – temperature synthesis and spark – plasma sintering. *Journal of Nanoscience and Nanotechnology*, 2010, vol. 10, no. 1, pp. 252–257. DOI: [10.1166/jnn.2010.1523](https://doi.org/10.1166/jnn.2010.1523).
 16. Oanh Nguyen Thi Hoang, Viet Nguyen-Hoang, Kim Ji Soon, Dudina D.V. Structural Investigation of Ti–Cu Nanocomposites Prepared by Ball Milling and Spark Plasma Sintering. *Metals*, 2017, vol. 7, no. 4, article number 123. DOI: [10.3390/met7040123](https://doi.org/10.3390/met7040123).
 17. Volkov A.Yu., Kalonov A.A., Komkova D.A. Effect of annealing on the structure, mechanical and electrical properties of Cu/Mg-composite wires. *Materials Characterization*, 2022, vol. 183, article number 111606. DOI: [10.1016/j.matchar.2021.111606](https://doi.org/10.1016/j.matchar.2021.111606).
 18. Tsikarev V.G., Filippenkov A.A., Filippov M.A., Alabushev A.V., Sharapova V.A. Obtaining Ti–Cu–C system composite materials by SHS process. *Izvestiya vysshikh uchebnykh zavedeniy. Poroshkovaya metallurgiya i funktsionalnye pokrytiya*, 2021, vol. 15, no. 4, pp. 4–11. DOI: [10.17073/1997-308X-2021-4-11](https://doi.org/10.17073/1997-308X-2021-4-11).
 19. Pugacheva N.B., Bykova T.M., Senaeva E.I., Nikolin Y.V. Structure and properties of a SHS Cu–Ti–C–B composite. *The Physics of Metals and Metallography*, 2022, vol. 123, no. 1, pp. 43–49. DOI: [10.1134/S0031918X22010100](https://doi.org/10.1134/S0031918X22010100).
 20. Pugacheva N., Kryuchkov D., Bykova T., Vichuzhanin D. Studying the Plastic Deformation of Cu–Ti–C–B Composites in a Favorable Stress State. *Materials*, 2023, vol. 16, no. 8, article number 320. DOI: [10.3390/ma16083204](https://doi.org/10.3390/ma16083204).
 21. Pugacheva N.B., Bykova T.M., Senaeva E.I., Goruleva L.S. Thermophysical properties of a Cu–Ti–C–B SHS composite. *Diagnostics, Resource and Mechanics of Materials and Structures*, 2023, no. 3, pp. 50–65. DOI: [10.17804/2410-9908.2023.3.050-065](https://doi.org/10.17804/2410-9908.2023.3.050-065).
 22. Nikolin B.V., Matevosyan M.B., Kochugov S.P., Pugacheva N.B. *Sposob izgotovleniya mnogosloynnoy iznosostoykoj plastiny* [Method of manufacturing a multilayer wear-resistant plate], patent RF na izobretenie no. 2680489, 2019. 11 p.

СПИСОК ЛИТЕРАТУРЫ

1. Левашов Е.А., Рогачев А.С., Курбаткина В.В., Максимов Ю.М., Юхвид В.И. Перспективные материалы и технологии самораспространяющегося высокотемпературного синтеза. М.: МИСиС, 2011. 378 с.
2. Рогачев А.С., Мукасян А.С. Горения для синтеза материалов. М.: ФИЗМАТЛИТ, 2012. 400 с.
3. Амосов А.П., Боровинская И.П., Мержанов А.Г. Порошковая технология самораспространяющегося высокотемпературного синтеза материалов. М.: Машиностроение-1, 2007. 567 с.
4. Мержанов А.Г. Самораспространяющийся высокотемпературный синтез // Физическая химия. Современные проблемы. М.: Химия, 1983. С. 6–44.
5. Латухин Е.И., Умеров Э.Р., Луц А.Р. Самораспространяющийся высокотемпературный синтез заготовок пористого карбида титана для последующей инфльтрации расплавами // Заготовительные производства в машиностроении. 2021. Т. 19. № 7. С. 322–330. DOI: [10.36652/1684-1107-2021-19-7-322-330](https://doi.org/10.36652/1684-1107-2021-19-7-322-330).
6. Коростелева Е.Н., Коржова В.В. Структура и фазовый состав металломатричных композитов (TiB) – Ti, полученных в процессе СВС и вакуумного спекания // Известия вузов. Физика. 2020. Т. 63. № 7. С. 81–87. DOI: [10.17223/00213411/63/7/81](https://doi.org/10.17223/00213411/63/7/81).
7. Ситников А.А., Собачкин А.В., Марков А.М. Особенности формирования различных функциональных покрытий из СВС-механокомпозитов с помощью технологии газодетонационного напыления // Наукоемкие технологии в машиностроении. 2020. № 2. С. 22–28. DOI: [10.30987/2223-4608-2020-2-22-28](https://doi.org/10.30987/2223-4608-2020-2-22-28).
8. Федотов А.Ф., Амосов А.П., Радченко В.П. Моделирование процесса прессования порошковых материалов в условиях самораспространяющегося высокотемпературного синтеза. М.: Машиностроение-1, 2005. 281 с.
9. Ковалев Д.Ю., Болоцкая А.В., Михеев М.В. Самораспространяющийся высокотемпературный синтез

- в системе Ti–B–Fe с добавкой AlN // Неорганические материалы. 2022. Т. 58. № 9. С. 956–964. EDN: [TJQGMZ](#).
10. Криволицкий К.С., Амосов А.П., Самборук А.Р. Самораспространяющийся высокотемпературный синтез ультрадисперсных и наноразмерных порошков композиций TiC–SiC и TiC–NbC // Вестник Самарского государственного технического университета. Серия: Технические науки. 2016. № 3. С. 136–143. EDN: [XVSVKB](#).
 11. Щукин А.С., Сычёв А.Е. Особенности строения переходной зоны NiAl/Mo, сформированной в процессе самораспространяющегося высокотемпературного синтеза // Физика металлов и металловедения. 2019. Т. 120. № 9. С. 925–930. DOI: [10.1134/S0015323019090134](#).
 12. Лазарев П.А., Бусурина М.Л., Грядун А.Н., Сычев А.Е., Боярченко О.Д., Карпов А.В. Особенности структуры и фазообразования сплава на основе Ti–Al–Si, полученного методом СВС-компактирования // Неорганические материалы. 2022. Т. 58. № 9. С. 1039–1044. EDN: [XTLFSK](#).
 13. Лазарев П.А., Бусурина М.Л., Сычёв А.Е. Самораспространяющийся высокотемпературный синтез в системе Ti–Al–Mn // Физика горения и взрыва. 2023. Т. 59. № 1. С. 85–91. DOI: [10.15372/FGV20230109](#).
 14. Volkov A.Y., Patrakov E.I., Volkova E.G., Komkova D.A., Kalonov A.A., Glukhov A.V., Antonov B.D. Abnormally high strength and low electrical resistivity of the deformed Cu/Mg-composite with a big number of Mg-filaments // Materials & Design. 2020. Vol. 185. Article number 108276. DOI: [10.1016/j.matdes.2019.108276](#).
 15. Kim Ji Soon, Dudina D.V., Kim Jin Chun, Kwon Soon Young, Park Jin Ju, Rhee Chang Kyu. Properties of Cu-based nanocomposites produced by mechanically – activated self – propagating high – temperature synthesis and spark – plasma sintering // Journal of Nanoscience and Nanotechnology. 2010. Vol. 10. № 1. P. 252–257. DOI: [10.1166/jnn.2010.1523](#).
 16. Oanh Nguyen Thi Hoang, Viet Nguyen-Hoang, Kim Ji Soon, Dudina D.V. Structural Investigation of TiC–Cu Nanocomposites Prepared by Ball Milling and Spark Plasma Sintering // Metals. 2017. Vol. 7. № 4. Article number 123. DOI: [10.3390/met7040123](#).
 17. Volkov A.Yu., Kalonov A.A., Komkova D.A. Effect of annealing on the structure, mechanical and electrical properties of Cu/Mg-composite wires // Materials Characterization. 2022. Vol. 183. Article number 111606. DOI: [10.1016/j.matchar.2021.111606](#).
 18. Цикарев В.Г., Филиппенков А.А., Филиппов М.А., Алабушев А.В., Шарапова В.А. Опыт получения композиционных материалов системы Ti–Cu–C СВС-процессом // Известия высших учебных заведений. Порошковая металлургия и функциональные покрытия. 2021. Т. 15. № 4. С. 4–11. DOI: [10.17073/1997-308X-2021-4-11](#).
 19. Пугачева Н.Б., Николин Ю.В., Быкова Т.М., Сенаева Е.И. Структура и свойства СВС-композиата системы Cu–Ti–C–B // Физика металлов и металловедение. 2022. Т. 123. № 1. С. 47–54. DOI: [10.31857/S0015323022010107](#).
 20. Pugacheva N., Kryuchkov D., Bykova T., Vichuzhanin D. Studying the Plastic Deformation of Cu–Ti–C–B Composites in a Favorable Stress State // Materials. 2023. Vol. 16. № 8. Article number 320. DOI: [10.3390/ma16083204](#).
 21. Пугачева Н.Б., Быкова Т.М., Сенаева Е.И., Горулёва Л.С. Теплофизические свойства СВС композитов Cu–Ti–C–B // Diagnostics, Resource and Mechanics of Materials and Structures. 2023. № 3. С. 50–65. DOI: [10.17804/2410-9908.2023.3.050-065](#).
 22. Николин Б.В., Матевосян М.Б., Кочугов С.П., Пугачева Н.Б. Способ изготовления многослойной износостойкой пластины: патент РФ на изобретение № 2680489, 2019. 11 с.

Структура и микромеханические свойства СВС-композиатов с медной матрицей: особенности формирования

© 2023

Пугачева Наталия Борисовна¹, доктор технических наук, доцент, главный научный сотрудник
Быкова Татьяна Михайловна^{*2}, кандидат технических наук, старший научный сотрудник
Сенаева Екатерина Игоревна³, младший научный сотрудник

Институт машиноведения имени Э.С. Горкунова Уральского отделения РАН, Екатеринбург (Россия)

*E-mail: nat@imach.uran.ru,
tatiana_8801@mail.ru

¹ORCID: <https://orcid.org/0000-0001-8015-8120>

²ORCID: <https://orcid.org/0000-0002-8888-6410>

³ORCID: <https://orcid.org/0000-0001-8625-2310>

Поступила в редакцию 22.06.2023

Принята к публикации 19.10.2023

Аннотация: Самораспространяющийся высокотемпературный синтез (СВС) является одним из перспективных способов получения прочных и износостойких композиатов. Особый интерес представляет использование меди в качестве матрицы из-за уникального сочетания электро- и теплопроводности. Монолитные СВС-композиаты системы Cu–Ti–C–B и Cu–Ti–C в настоящее время мало изучены. Сведения о фазовом составе таких композиатов весьма противоречивы, а данные по микромеханическим свойствам практически отсутствуют. В работе представлены результаты сравнительного анализа структуры и микромеханических свойств композиатов систем Cu–Ti–C

и Cu–Ti–C–B. Установлено, что матрицей обоих композитов является пересыщенный титаном твердый раствор на основе меди, в котором при охлаждении выделяются наноразмерные частицы интерметаллида Cu_4Ti . Упрочняющими фазами, образующимися в результате СВС, являются частицы TiC (композит Cu–Ti–C) и частицы TiC и TiB_2 (композит Cu–Ti–C–B). В композите Cu–Ti–C–B сохранились исходные частицы непрореагировавшего карбида бора B_4C , микротвердость которых составила $3680\text{ HV }0,1$. Наиболее пластичной структурной составляющей является механическая смесь Cu+ Cu_4Ti в композите системы Cu–Ti–B, за счет которой возможна последующая пластическая деформация с целью получения деталей заданной формы. При исследовании микромеханических свойств максимальные показатели прочности H_{IT} , HV , W_e , R_e , H_{IT}/E^* были зафиксированы в композите системы Cu–Ti–C–B, что позволяет ожидать высокую износостойкость изделий из него.

Ключевые слова: самораспространяющийся высокотемпературный синтез; монолитные СВС-композиты; медная матрица; структурные составляющие; упрочняющие фазы; интерметаллиды; карбид титана; диборид титана; микромеханические свойства; твердость.

Благодарности: Исследования выполнены за счет гранта РНФ № 22-29-00188 «Разработка научных и технологических основ формирования монолитных СВС-композитов системы Cu–Ti–C–B с заданными функциональными свойствами», <https://rscf.ru/project/22-29-00188/>.

Работа выполнена на оборудовании Центра коллективного пользования «Пластометрия» федерального государственного бюджетного учреждения науки Института машиноведения имени Э.С. Горкунова Уральского отделения Российской академии наук.

Статья подготовлена по материалам докладов участников XI Международной школы «Физическое материаловедение» (ШФМ-2023), Тольятти, 11–15 сентября 2023 года.

Для цитирования: Пугачева Н.Б., Быкова Т.М., Сенаева Е.И. Структура и микромеханические свойства СВС-композитов с медной матрицей: особенности формирования // Frontier Materials & Technologies. 2023. № 4. С. 99–108. DOI: 10.18323/2782-4039-2023-4-66-9.

The influence of frictional treatment and liquid carburizing on general corrosion resistance of chromium-nickel austenitic steels

© 2023

Polina A. Skorynina^{*1,3}, junior researcher
Aleksey V. Makarov^{1,2,4}, Doctor of Science (Engineering),
Corresponding Member of RAS,

Head of Department of Materials Science, Head of Laboratory of Mechanical Properties

Roman A. Savrai^{1,5}, PhD (Engineering),
Head of Laboratory of Constructional Material Science

¹*Institute of Engineering Science of the Ural Branch of RAS, Yekaterinburg (Russia)*

²*M.N. Mikheev Institute of Metal Physics of the Ural Branch of RAS, Yekaterinburg (Russia)*

*E-mail: skorynina@imach.uran.ru,
polina.skorynina@mail.ru

³ORCID: <https://orcid.org/0000-0002-8904-7600>

⁴ORCID: <https://orcid.org/0000-0002-2228-0643>

⁵ORCID: <https://orcid.org/0000-0001-9873-3621>

Received 27.06.2023

Accepted 17.11.2023

Abstract: Currently, to increase the hardness, strength and wear resistance of thermally non-hardenable austenitic chromium-nickel steels, such methods as frictional treatment with a sliding indenter and liquid carburizing have been used. However, along with an effective increase in mechanical characteristics, the application of these types of treatment may be accompanied by a decrease in the corrosion resistance of austenitic steels. Therefore, it is reasonable to study the influence of frictional treatment and liquid carburizing on the general corrosion resistance of Cr–Ni austenitic steels. In this work, the surface microhardness of the 12Cr18Ni10Ti and AISI 321 steels was determined using the recovered indentation method after electropolishing, mechanical grinding, frictional treatment, and liquid carburizing at a temperature of 780 °C. Using scanning electron microscopy and optical profilometry, the authors studied steel surfaces subjected to the specified types of treatment and determined their roughness. The corrosion resistance of steel was studied by testing for general corrosion using the gravimetric method. When testing for general corrosion, it was found that hardening (up to 710 HV 0.025) frictional treatment leads to an increase in the corrosion rate of the 12Cr18Ni10Ti austenitic steel compared to the electropolished state (from $k_m=0.35$ g/(m²·h) to $k_m=0.53–0.54$ g/(m²·h)). The corrosion rate of the ground steel is $k_m=0.58$ g/(m²·h), while mechanical grinding does not provide a significant increase in the microhardness of the steel under study (from 220 to 240 HV 0.025). It is shown that the corrosion behavior of 12Cr18Ni10Ti steel subjected to various types of treatment is determined by the following factors: the presence/absence of strain-induced α' -martensite in the structure, the quality of the formed surface and, apparently, the dispersion of the formed structure. Liquid carburizing of the AISI 321 austenitic steel leads simultaneously to an increase in its microhardness to 890 HV 0.025 and a certain increase in corrosion resistance compared to fine mechanical grinding. This is related to the fact that carbon embedding atoms stabilize the electronic structure of iron (austenite and martensite), thereby increasing its corrosion resistance.

Keywords: austenitic chromium-nickel steel; frictional treatment; liquid carburizing; microhardness; phase composition; roughness; corrosion resistance.

Acknowledgments: The authors express gratitude to V.V. Berezovskaya, Doctor of Science (Engineering), for participation in work.

The work was carried out within the government assignment to the Institute of Engineering Science, UB RAS on the topic No. AAAA-A18-118020790148-1 and the Institute of Metal Physics, UB RAS on the topic No. 122021000033-2. Experimental studies were carried out using the equipment of the “Plastometry” Core Facility Center of the IES UB RAS.

The paper was written on the reports of the participants of the XI International School of Physical Materials Science (SPM-2023), Togliatti, September 11–15, 2023.

For citation: Skorynina P.A., Makarov A.V., Savrai R.A. The influence of frictional treatment and liquid carburizing on general corrosion resistance of chromium-nickel austenitic steels. *Frontier Materials & Technologies*, 2023, no. 4, pp. 109–119. DOI: 10.18323/2782-4039-2023-4-66-10.

INTRODUCTION

Chromium-nickel austenitic steels of the 18Cr–10Ni type are widely used among corrosion-resistant materials. In particular, metastable austenitic 12Cr18Ni10Ti steel and its foreign analogues – AISI steels of the 300 series (AISI 304, AISI 321) are used in the food, medical, chemical, and oil refining industries. This is conditioned by

a combination of their advantages, such as high workability, plasticity, heat resistance [1] and resistance to corrosion in various liquid and gas environments, as well as in solutions of salts and acids [2–4]. However, with all the listed advantages, austenitic steels are characterized by low levels of strength characteristics and wear resistance [5; 6].

Currently, to eliminate the above-mentioned disadvantages of austenitic Cr–Ni steels, various methods based

on plastic deformation [7–9] and chemical-thermal (nitriding [10, 11], carburizing [12, 13]) surface modification are used. Among the known methods of strain hardening, frictional treatment with a sliding indenter can be distinguished [10; 14; 15]. When applied to austenitic steels that are prone to adhesion during contact interaction, such treatment, along with effective strengthening of the surface layer up to 500 μm deep, allows obtaining a surface with low roughness in the absence of material continuity defects. Among the processes of chemical-thermal treatment of austenitic Cr–Ni steel, carburizing is of particular interest, which, compared to nitriding, allows forming deeper hardened layers that remain weakly magnetic [16].

It should be taken into account that the application of these types of strengthening treatment, can lead to a decrease in the corrosion resistance of metastable austenitic Cr–Ni steels due to the formation of strain-induced martensite, and carbide phases during intense deformation, and when the surface layer is saturated with carbon [1; 7]. However, the appearance of a new phase component is not always accompanied by a decrease in the corrosion properties of austenitic steels [12; 17]. Thus, in the work [17] it is shown that the pitting corrosion rate of the 12Cr18Ni10Ti steel decreases with an increase in the degree of tensile strain, and accordingly, with an increase in the α' -phase amount, which is formed in the material, and leads to an increase in its ability to passivate. Moreover, it is worth considering that the factors determining the corrosion behaviour of austenitic stainless steels may also include the topography of the surface formed during hardening treatment [7; 17; 18]. It was noted in [18] that mechanical grinding, compared to frictional treatment, leads to a two-fold increase in the corrosion rate of the 03Cr16Ni14M3Ti steel due to the occurrence of microcracks and metal pits on the surface.

Thus, in the literature there is ambiguous information about the influence of the phase composition, and surface topography on the corrosion behaviour of steels of the 18Cr–10Ni type, subjected to various types of deformation and chemical-thermal surface modification. It should be noted, as well, that there are no works covering the influence of frictional treatment on the corrosion properties of metastable austenitic steels. Therefore, it is reasonable to conduct a comprehensive study that would take into account the influence of the phase composition, and topography of the surface of austenitic Cr–Ni steels formed during frictional treatment and liquid carburizing on the general corrosion resistance.

The purpose of this work is to study the influence of frictional treatment, and liquid carburizing on the corrosion properties of metastable austenitic 12Cr18Ni10Ti and AISI 321 steels.

METHODS

The authors studied the industrial austenitic metastable steels of two grades: 12Cr18Ni10Ti (GOST 5632-2014) and AISI 321. The chemical composition of the steels, which was determined using a SPECTROMAXx optical emission spectrometer, is given in Table 1. The samples for research were cut from rolled sheets. Before subsequent treatment, the samples were subjected to hardening from 1100 $^{\circ}\text{C}$ in water, mechanical grinding using M63, M50, M20 (GOST 3647-80) abrasive cloths and ASM 14/10 NOMG, ASM 7/5 NOMG (GOST 25593-83) diamond pastes with a successive abrasive grid reduction, and then electrolytic polishing in a solution of 100 g H_2SO_4 + 400 g H_3PO_4 + 50 g CrO_3 at a temperature of 60–70 $^{\circ}\text{C}$.

12Cr18Ni10Ti steel samples with dimensions of 98×38×8.6 mm were subjected to frictional treatment with a sliding indenter made of hemispherical synthetic diamond with a hemisphere radius of $R=3$ mm. The treatment was carried out in a non-oxidizing argon environment with a load on the indenter of $P=392$ N, with an indenter displacement of $d=0.1$ mm for each double stroke and with a number of indenter scans over the sample surface of $n=1$ and $n=11$.

Liquid carburizing of AISI 321 steel samples with dimensions of 40×52×10 mm was carried out in molten salts with the addition of silicon carbide of the 80 % Na_2CO_3 + 10 % NaCl + 10 % SiC composition (in wt. %) at a temperature of 780 $^{\circ}\text{C}$ for 15 h with subsequent cooling in water. For carburizing, a laboratory furnace and a crucible with a diameter of $d=100$ mm and a height of $h=300$ mm were used. To remove the oxide film, the samples after carburizing were subjected to electrolytic etching in a solution of 90 wt. % CH_3COOH + 10 wt. % H_2ClO_4 for 30 s.

All samples were cut using electrical discharge cutting on a FANUC Robocut α -0iE machine. Microhardness was determined on a SHIMADZU HMV-G21DT device using the recovered indentation method at the load on a Vickers indenter of 0.245 N. The phase composition was determined on a SHIMADZU XRD-7000 X-ray diffractometer in CrK_α radiation (with a tube voltage of 30 kV and a tube current of 30 mA). Continuous shooting was carried out,

Table 1. Chemical composition of steels under study, wt. %
Таблица 1. Химический состав исследуемых сталей, мас. %

Steel	C	Cr	Ni	Ti	Mn	Si	Mo	Co	Nb	Cu
12Cr18Ni10Ti	0.10	17.72	10.04	0.63	1.33	0.57	0.23	0.064	0.014	0.057
AISI 321	0.05	16.80	8.44	0.33	1.15	0.67	0.26	0.13	0.03	0.31

Note. S and P content does not exceed 0.036 %, the rest is Fe.

Примечание. Содержание S и P не превышает 0,036 %, остальное Fe.

with a scanning rate of 1 °/min, a step of 0.05° and an exposure time of 3 s. The phase composition was determined by the method of homologous pairs. The amount of α -phase $V\alpha$ was calculated using the formula

$$V\alpha = \frac{100}{1 + 1,45 \frac{I(111)\gamma}{I(110)\alpha}}, \text{ vol. \%},$$

where $I(111)\gamma$ and $I(110)\alpha$ are the integral intensities of γ -lines and α -phases [19].

The depth of the analyzed layer when determining the phase composition was $\sim 7 \mu\text{m}$. The surface of the samples was studied by scanning electron microscopy using a Tescan VEGA II XMU microscope. To determine the surface roughness parameters of the samples, a Wyko NT-1100 optical profilometer was used. Measurements were carried out on the $211 \times 278 \mu\text{m}$ sections, and the arithmetic average deviation of the Ra profile was determined. The phase composition, and surface roughness were determined directly on samples prepared for corrosion tests.

Tests for general corrosion were carried out by the gravimetric method according to GOST R 9.905-2007 in a solution of 20 wt. % NaCl + 30 wt. % HCl (1:1) at room temperature. Due to its ability to destroy a passivation layer, this environment has a strong corrosive effect on the materials under study, thus ensuring the continuous occurrence of the corrosion process.

Samples for testing were prepared from 12Cr18Ni10Ti steel with dimensions of $10 \times 10 \times 2 \text{ mm}$ in the following conditions: after electropolishing, grinding on M20 abrasive cloth (GOST 3647-80) with a grain size of 20/14 μm , and after frictional treatment at $n=1$ and $n=11$. Samples of AISI 321 steel with dimensions of $7 \times 7 \times 2 \text{ mm}$ were tested in the following conditions: after grinding with ASM 14/10 NOMG diamond paste with a grain size of 14/10 μm (GOST 25593-83) and after liquid carburizing. For each condition, two samples were subjected to corrosion tests.

The prepared samples were immersed in a corrosive environment for 18 h until the corrosion rate stabilised, while the environment pH was not controlled. During testing, samples were weighed periodically. Before weighing, to remove corrosion products, the samples were washed in water, dried with filter paper, and degreased with acetone. This allowed determining accurately the weight loss of

the sample after soaking in a corrosive environment. Weight loss was determined on a Demcom DA-65C laboratory scale with an accuracy of up to 0.01 mg. The corrosion rate k_m was calculated using the formula

$$k_m = \frac{\Delta m}{S \cdot \tau}, \text{ g}/(\text{m}^2 \cdot \text{h}),$$

where Δm is weight loss, g;
 S is surface area of test samples, m^2 ;
 τ is testing time, h.

For a comparative assessment of the corrosion behaviour of test samples, the average corrosion rate in steady state was calculated.

RESULTS

According to the data in Table 2 and Fig. 1 a, the structure of quenched (after electrolytic polishing) 12Cr18Ni10Ti steel contains 100 vol. % γ -phase (austenite), and α' -phase (strain-induced martensite) is absent.

After mechanical grinding, except for the γ -phase, the structure of steel under study also contains the α' -phase, the volume fraction of which is 7 vol. % (Table 2, Fig. 1 b). During frictional treatment in the surface layer of the steel under study, the deformation $\gamma \rightarrow \alpha'$ -transformation develops more intensively (Fig. 1 c, 1 d). The amount of α' -martensite formed in the surface layer of steel reaches 55–70 vol. % (Table 2).

The microhardness of steel in the initial electropolished state is 220 HV 0.025 (Table 2). Mechanical grinding practically, does not lead to an increase in the microhardness of the surface of the steel under study (only up to 240 HV 0.025). Frictional treatment ensures an increase in the microhardness of the steel under study by 2.5 times (up to 560 HV 0.025) already with one-fold ($n=1$) scanning of the indenter over the sample surface. Increasing the frictional loading multiplicity to $n=11$ leads to an additional increase in the microhardness of steel to 710 HV 0.025 (Table 2). This is consistent with an increase in the α' -phase amount from 55 to 70 vol. % as the number of indenter scans along the sample surface increases from $n=1$ to $n=11$.

According to the data in Table 2, the surfaces of 12Cr18Ni10Ti steel after electropolishing and mechanical grinding using fine-grained (20/14 μm) cloth are characterized by similar levels of the arithmetic average deviation

Table 2. Microhardness HV 0.025, phase composition (amount of α' -martensite) and roughness parameter Ra of the surface of 12Cr18Ni10Ti steel samples after different types of treatment
Таблица 2. Микротвердость HV 0,025, фазовый состав (количество α' -мартенсита) и параметр шероховатости Ra поверхности образцов из стали 12Х18Н10Т после различных обработок

Types of treatment	HV 0.025	α' , vol. %	Ra, μm
Electropolishing	220±20	0	0.06±0.01
Grinding (abrasive 20/14 μm)	240±5	7±2	0.11±0.01
Frictional treatment at $n=1$	560±27	55±3	0.17±0.01
Frictional treatment at $n=11$	710±43	70±3	0.33±0.03

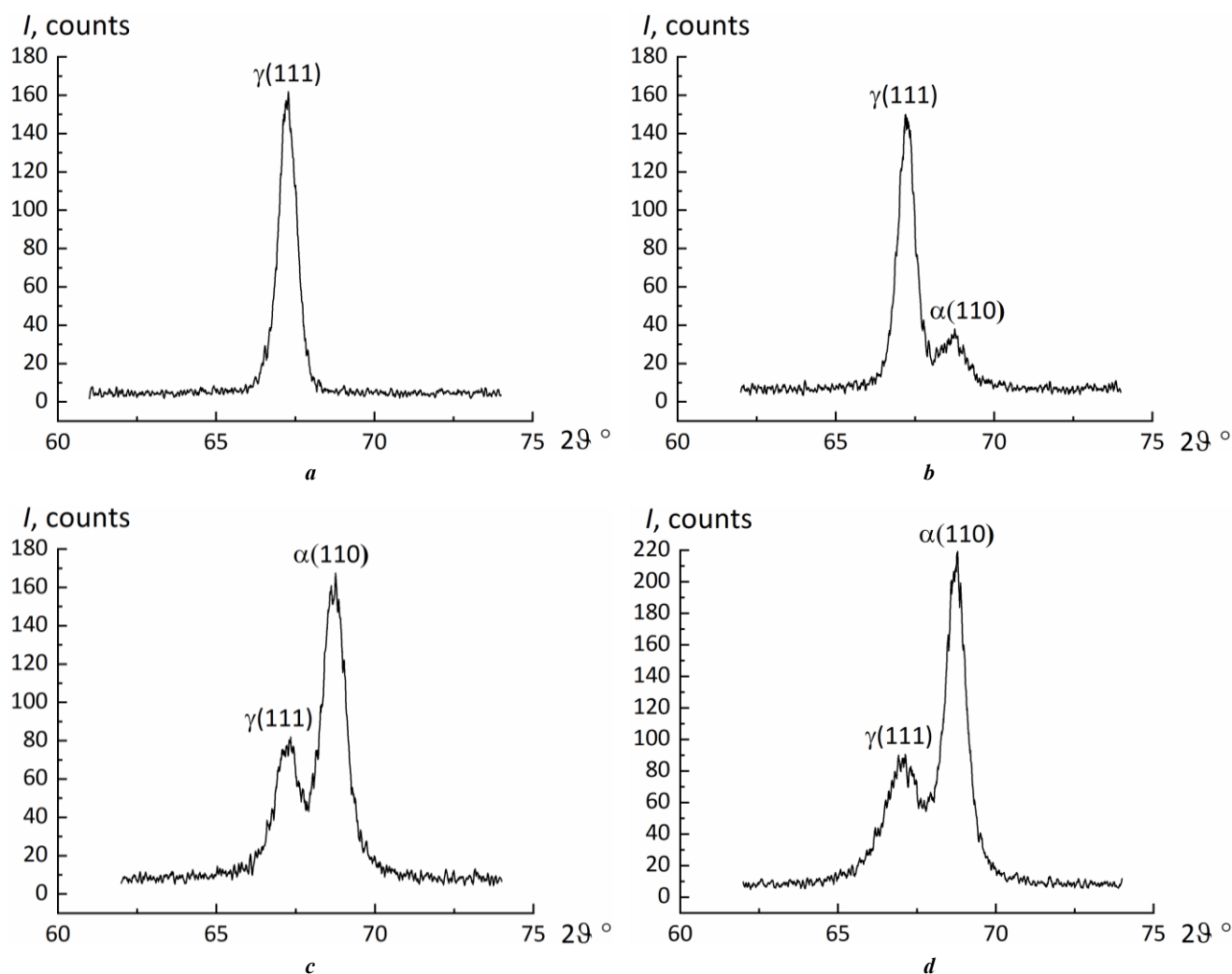


Fig. 1. X-ray diffraction patterns of the surface of 12Cr18Ni10Ti steel in quenched condition (a), after grinding with an abrasive grit of 20/14 μm (b), and frictional treatment at $n=1$ (c) and $n=11$ (d)
Рис. 1. Рентгеновские дифрактограммы поверхности стали 12Х18Н10Т в закаленном состоянии (а), после шлифования абразивом зернистостью 20/14 мкм (b) и фрикционной обработки при $n=1$ (c) и $n=11$ (d)

of the profile Ra (0.06 and 0.11 μm). The steel surface after frictional treatment demonstrates higher values of this parameter: $Ra=0.17\text{--}0.33 \mu\text{m}$.

Electrolytic polishing leads to the formation of a smooth 12Cr18Ni10Ti steel surface characterized by the presence of a small amount of shallow etching pitting (Fig. 2 a). This determines the recorded minimum values of the parameter $Ra=0.06 \mu\text{m}$. The steel surface after grinding is characterized by the presence of micro damages, and shallow grooves (dimples) oriented in the grinding direction (Fig. 2 b). This causes slightly higher values of the parameter $Ra=0.11 \mu\text{m}$ than for the electropolished surface.

The recorded slightly larger values of the arithmetic average profile deviation Ra after frictional treatment are associated with the fact that the steel surface is characterized by the presence of plastic displacement stripes, alternating longitudinal protrusions and dimples (Fig. 2 c, 2 d). At the same time, on the surfaces under consideration after exposure to a synthetic diamond indenter, there are no continuity defects in the form of pits and cracks characteristic of a polished surface (Fig. 2 b).

From the data shown in Fig. 3, it follows that austenitic 12Cr18Ni10Ti steel with an electropolished surface is characterized by the lowest corrosion rate: $k_m=0.35\pm 0.05 \text{ g}/(\text{m}^2\cdot\text{h})$. The corrosion rate of steel in the polished state is 1.6 times higher: $k_m=0.58\pm 0.12 \text{ g}/(\text{m}^2\cdot\text{h})$. Steel after frictional treatment has a slightly lower corrosion rate. At the same time, for steel processed in two modes with different numbers of indenter scans ($n=1$ and $n=11$), similar levels of corrosion rate are recorded: $k_m=0.53\pm 0.09 \text{ g}/(\text{m}^2\cdot\text{h})$ and $k_m=0.54\pm 0.07 \text{ g}/(\text{m}^2\cdot\text{h})$.

X-ray phase analysis showed (Table 3, Fig. 4 a) that AISI 321 steel in the quenched state (after electropolishing) contains 100 vol. % γ -phase (α' -phase is absent). As a result of mechanical grinding, 9 vol. % α' -martensite is formed in the surface layer of the steel under study (Table 3, Fig. 4 b). After liquid carburizing at a temperature of 780 $^\circ\text{C}$, the structure of the steel surface layer consists of carbon-rich austenite γ_C , α' -martensite, Cr_{23}C_6 chromium carbides and Fe_3C cementite (Fig. 4 c). In this case, the amount of α' -phase is 20 vol. % (Table 3).

The microhardness of AISI 321 steel in the initial state is 200 HV 0.025. Mechanical grinding leads to a slight

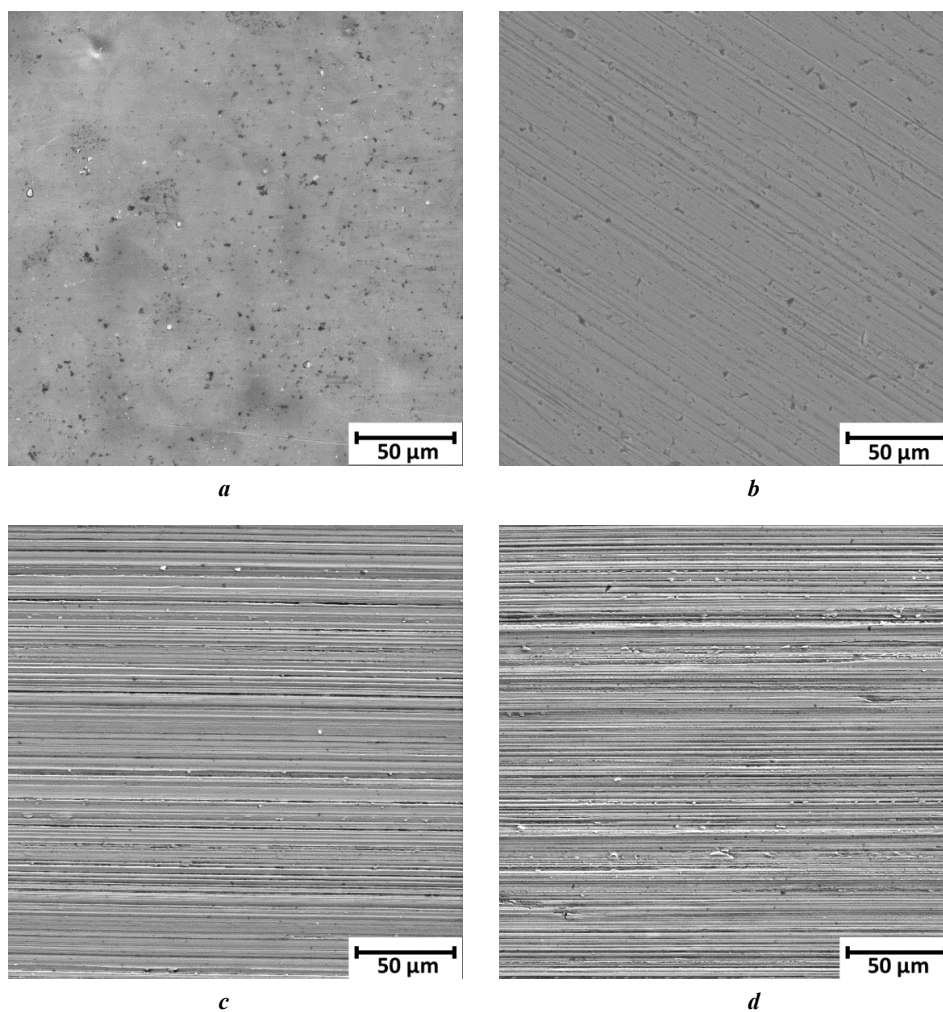


Fig. 2. Images of the surface of 12Cr18Ni10Ti steel samples after electropolishing (a), grinding with an abrasive grit of 20/14 μm (b), frictional treatment at $n=1$ (c) and $n=11$ (d)
Рис. 2. Изображения поверхности образцов из стали 12Х18Н10Т после электролитического полирования (а), шлифования абразивом зернистостью 20/14 мкм (b), фрикционной обработки при $n=1$ (c) и $n=11$ (d)

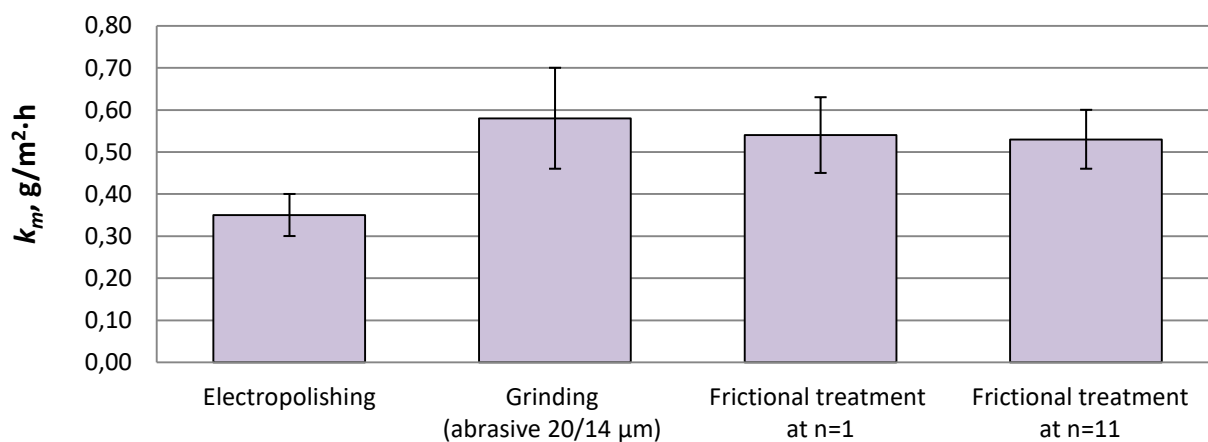


Fig. 3. The dependence of corrosion rate k_m of 12Cr18Ni10Ti steel samples on the type of surface treatment
Рис. 3. Зависимость скорости коррозии k_m образцов из стали 12Х18Н10Т от вида обработки поверхности

Table 3. Microhardness HV 0.025, phase composition (quantity of α' -martensite) and roughness parameter Ra of the surface of AISI 321 steel samples after different types of treatment
Таблица 3. Микротвердость HV 0,025, фазовый состав (количество α' -мартенсита деформации) и параметр шероховатости Ra поверхности образцов из стали AISI 321 после различных обработок

Types of treatment	HV 0.025	α' , vol. %	Ra, μm
Electropolishing	200 \pm 7	0	–
Grinding (abrasive 14/10 μm)	260 \pm 8	9 \pm 2	0.08 \pm 0.02
Liquid carburizing	890 \pm 110	20 \pm 2	0.52 \pm 0.13

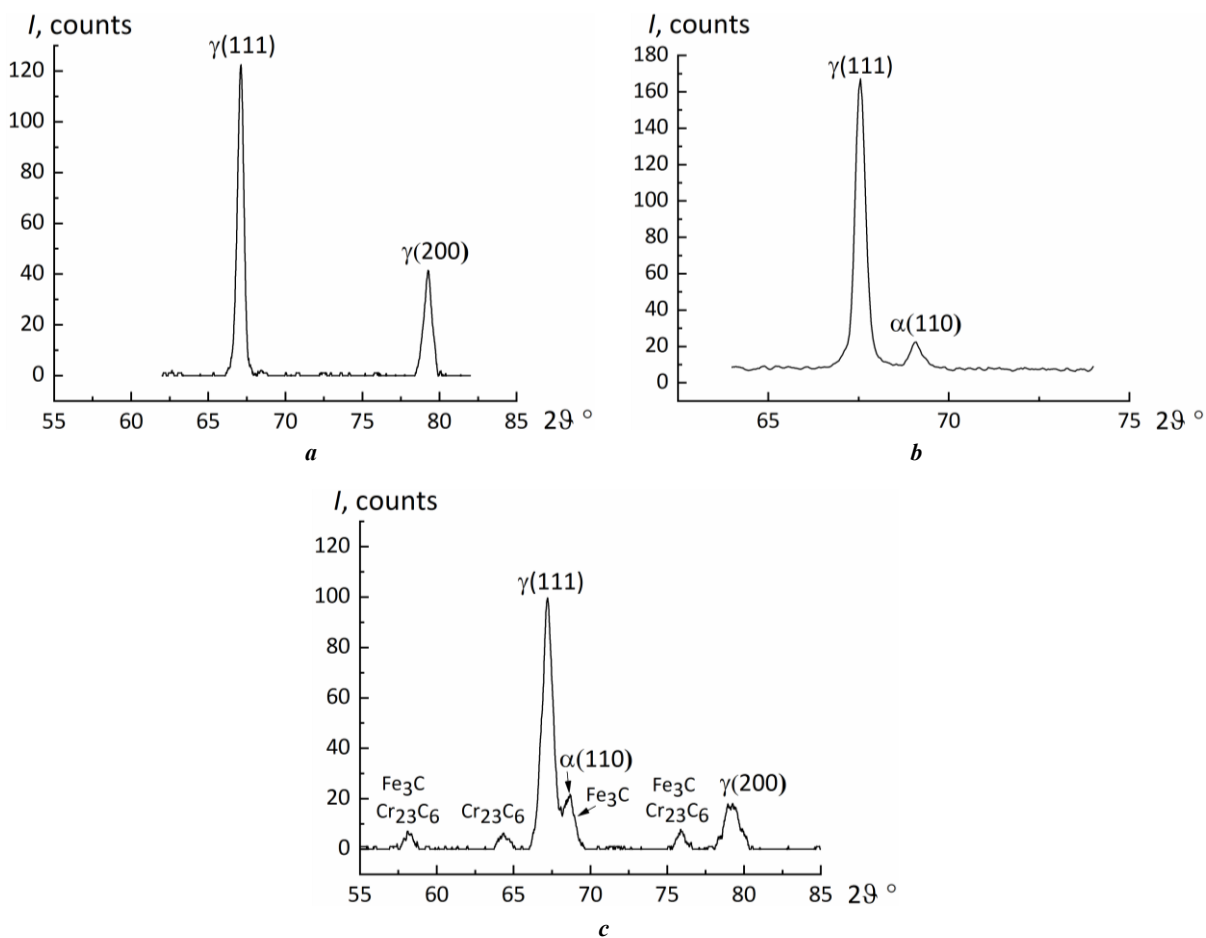


Fig. 4. X-ray diffraction patterns of the surface of AISI 321 steel in quenched condition (a), after grinding with an abrasive grit of 14/10 μm (b), and liquid carburizing (c)
Рис. 4. Рентгеновские дифрактограммы поверхности стали AISI 321 в закаленном состоянии (a), после шлифования абразивом зернистостью 14/10 мкм (b) и жидкостной цементации (c)

increase in the microhardness of the surface of the steel under study (up to 260 HV 0.025). After liquid carburizing, the microhardness of austenitic steel increases by 4.5 times – up to 890 HV 0.025.

After mechanical grinding with diamond paste, the AISI 321 steel surface is characterized by the presence of shallow grooves oriented in the grinding direction and low values of the arithmetic average profile deviation $Ra=0.08 \mu\text{m}$ (Fig. 5 a, Table 3). The steel surface after carburizing has a higher roughness ($Ra=0.52 \mu\text{m}$). This

may be caused by the fact that a clear relief is visible on the surface of the carburized steel along the grain boundaries, which is associated with their etching during electrolytic removal after oxide film carburizing (Table 3, Fig. 5 b).

Histograms shown in Fig. 6 indicate that austenitic AISI 321 steel after grinding and after carburizing is characterized by similar corrosion rates: $k_m=0.40\pm0.04 \text{ g}/(\text{m}^2\cdot\text{h})$ and $k_m=0.32\pm0.02 \text{ g}/(\text{m}^2\cdot\text{h})$ respectively. At the same time, the corrosion rate of carburized steel is even lower.

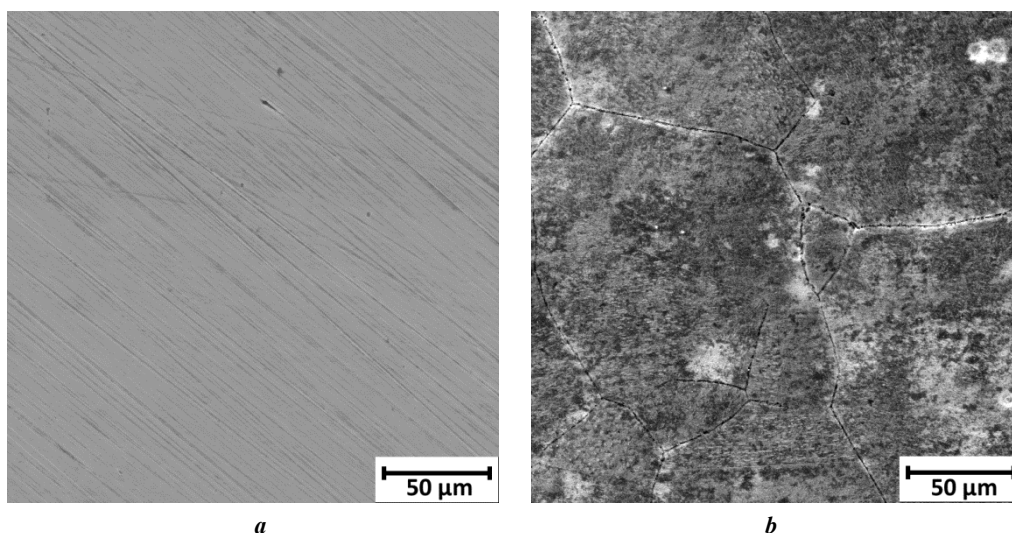


Fig. 5. Images of the surface of AISI 321 steel samples after grinding with an abrasive grit of 14/10 μm (a) and liquid carburizing (b)

Рис. 5. Изображения поверхности образцов из стали AISI 321 после шлифования абразивом зернистостью 14/10 мкм (a) и жидкостной цементации (b)

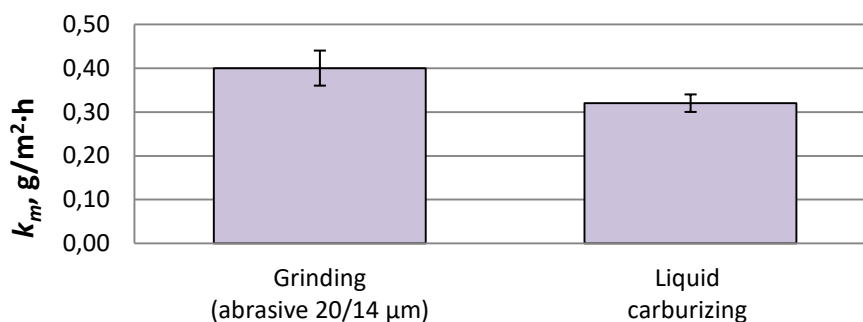


Fig. 6. The dependence of corrosion rate k_m of AISI 321 steel samples on the type of surface treatment

Рис. 6. Зависимость скорости коррозии k_m образцов из стали AISI 321 от вида обработки поверхности

DISCUSSION

The registered more than three-fold strengthening (up to 710 HV 0.025) of 12Cr18Ni10Ti steel during frictional treatment, is caused by the formation of a highly dispersed (up to nano- and submicrocrystalline state) martensitic-austenitic structure [5], and the formation of 70 vol. % strain-induced α' -martensite as a result of the implementation of the deformation phase transformation. In [15], in the surface layer of austenitic AISI 321 steel during frictional treatment, a complete deformation $\gamma \rightarrow \alpha'$ -transformation was observed, which was facilitated by a lower content of the strong nickel austenite stabilizer in the steel (8.44 wt. % Ni) than in 12Cr18Ni10Ti steel (10.04 wt. % Ni, Table 1). However, the revealed relatively low level of microhardness on the AISI 321 steel surface (480 HV 0.025), indicates lower degrees of plastic deformation and structure dispersion achieved in the work [15]. Consequently, it is not the strain-induced martensitic transformation of low-carbon austenite, but the activation of the grain-boundary strengthening mechanism during grain refinement during frictional treat-

ment, that contributes decisively to the strengthening of the 12Cr18Ni10Ti steel studied in this work.

The austenitic 12Cr18Ni10Ti steel surface, which is prone to setting during friction, formed during frictional treatment, is characterized by rather low values of the roughness parameter $Ra=0.17-0.33 \mu\text{m}$ during profilemetry of areas with dimensions of $211 \times 278 \mu\text{m}$. In the work [20], during frictional treatment of high-nitrogen austenitic steel, a surface with a roughness parameter $Ra=0.39 \mu\text{m}$ was formed. At the same time, during shot peening, the surface of AISI 304 steel was characterized by significantly higher roughness: $Ra=2.8-3.8 \mu\text{m}$ [21]. Thus, frictional treatment provides both effective strengthening of 12Cr18Ni10Ti steel, and high quality of its surface.

The registered increased corrosion rate of 12Cr18Ni10Ti steel in a deformed state (after mechanical grinding and frictional treatment) (Fig. 3), may be caused by the presence of strain-induced martensite in the surface layers. In the work [22], the occurrence of pitting corrosion on the surface of 304 L steel was associated with the presence of electro-

chemical heterogeneity, which is caused by the appearance of α' -martensite. However, the volume fraction of the α' -phase formed during grinding of 12Cr18Ni10Ti steel is significantly less (7 vol. %), than during frictional treatment (55–70 vol. %), and the corrosion rate of steel in the ground state is slightly higher (Table 2, Fig. 3). The registered positive effect of frictional treatment on corrosion resistance, despite the intensive development of martensitic transformation during loading with an indenter, can be explained by the strong structure fragmentation during frictional treatment [5], which contributes to the accelerated formation of passive films on the stainless steel surface [23]. Thus, in terms of the corrosion resistance of 12Cr18Ni10Ti steel, frictional treatment has a certain advantage over mechanical grinding.

Previously, it was noted, as well, that grinding, and frictional treatment cause an increase in the surface roughness of 12Cr18Ni10Ti steel compared to electropolishing: $Ra=0.11\text{--}0.33\ \mu\text{m}$ and $Ra=0.06\ \mu\text{m}$, respectively. In this case, the presence of defects in the material continuity (small pits and cracks, Fig. 2 b) are registered on the polished surface, and as a result of frictional treatment, pronounced traces of deformation appear on the surface in the form of longitudinal ridges, dimples and smoothed stripes (Fig. 2 c, 2 d). It has been shown that an increase in the steel surface roughness, is accompanied by a growth in the corrosion rate [18; 24], and defects can act as additional sources of corrosion destruction, and prevent material passivation [25]. Thus, apparently, the corrosion behaviour of austenitic steel is influenced significantly by the quality of its surface (roughness, presence or absence of defects).

The effective increase in the microhardness of austenitic AISI 321 steel (from 200 to 890 HV 0.025) achieved during liquid carburizing, is associated with solid solution strengthening due to austenite saturation with carbon, dispersion strengthening during the precipitation of carbide phases, the formation of α' -martensite and an increase in the density of structure defects during plastic deformation [13].

Despite the formation of 20 vol. % strain-induced α' -martensite, carbides, and a small amount of ϵ -martensite [13], as well as a higher surface roughness, there is a slightly lower level of corrosion rate of AISI 321 steel after liquid carburizing than after grinding (Fig. 6). This is associated with the fact that interstitial atoms, in particular carbon, stabilize the electronic state of iron, thereby increasing its corrosion resistance [26]. This is true for both austenite and martensite [27]. Along with this, oxyanions such as HCO_3^- and CO_3^{2-} are effective inhibitors for suppressing anodic corrosion [26].

CONCLUSIONS

General corrosion tests in a solution of 20 wt. % NaCl + 30 wt. % HCl (1:1) showed that, compared to electropolishing, effective hardening of the surface of austenitic metastable 12Cr18Ni10Ti steel by frictional treatment (from 220 to 710 HV 0.025), is accompanied by an increase in the corrosion rate from $k_m=0.35\ \text{g}/(\text{m}^2\cdot\text{h})$ to $k_m=0.53\text{--}0.54\ \text{g}/(\text{m}^2\cdot\text{h})$. However, even despite the formation on the surface of steel of 55–70 vol. % strain-induced martensite, under the influence of a sliding indenter, frictional treatment does not lead to a corrosion resistance deterioration, compared to another mechanical post-processing of

austenitic steel – grinding with fine-grained (20/14 μm) cloth, which does not provide a significant increase in surface microhardness (only up to 240 HV 0.025), and the development of strain-induced martensitic austenite transformation. In this case, the corrosion rate of polished steel reaches $k_m=0.58\ \text{g}/(\text{m}^2\cdot\text{h})$.

The corrosion behaviour of 12Cr18Ni10Ti steel subjected to electrolytic polishing, grinding, and frictional treatment is determined by the following factors: the presence/absence of strain-induced α' -martensite in the structure, the formed surface quality (roughness, presence or absence of continuity defects), and apparently, the formed structure dispersion.

It has been found that liquid carburizing at a temperature of 780 °C simultaneously leads to effective hardening (from 200 to 890 HV 0.025) of electropolished austenitic AISI 321 steel, and a slight increase in corrosion resistance compared to fine mechanical grinding with diamond paste. The corrosion rate of ground steel is $k_m=0.40\ \text{g}/(\text{m}^2\cdot\text{h})$, and of carburized one is $k_m=0.32\ \text{g}/(\text{m}^2\cdot\text{h})$. This is related to the fact that interstitial carbon atoms stabilize the electronic state of iron (both of austenite and martensite), thereby increasing its corrosion resistance.

REFERENCES

- Borgioli F. From austenitic stainless steel to expanded austenite-S phase: formation, characteristics and properties of an elusive metastable phase. *Metals*, 2020, vol. 10, no. 2, article number 187. DOI: [10.3390/met10020187](https://doi.org/10.3390/met10020187).
- Pradhan K.K., Matawale C.R., Murarka S. Analysis of erosion-corrosion resistance and various application in domestic and industrial field of stainless steel grade 304. *International Journal of Research (IJR)*, 2015, vol. 2, no. 4, pp. 807–811.
- Wei Xinlong, Ling Xiang, Zhang Meng. Influence of surface modifications by laser shock processing on the acid chloride stress corrosion cracking susceptibility of AISI 304 stainless steel. *Engineering Failure Analysis*, 2018, vol. 91, pp. 165–171. DOI: [10.1016/j.engfailanal.2018.04.045](https://doi.org/10.1016/j.engfailanal.2018.04.045).
- Kostina M.V., Kostina V.S., Kudryashov A.E., Muradyan S.O., Krivorotov V.I. The features of the chemical composition and structural-phase state determining a decrease in the corrosion resistance of 18Cr–10Ni steel parts. *Steel in Translation*, 2021, vol. 51, no. 3, pp. 168–179. DOI: [10.3103/S0967091221030050](https://doi.org/10.3103/S0967091221030050).
- Makarov A.V., Skorynina P.A., Osintseva A.L., Yurovskikh A.S., Savrai R.A. Improving the tribological properties of austenitic 12Kh18N10T steel by nanostructuring frictional treatment. *Obrabotka Metallov (Metal Working and Material Science)*, 2015, no. 4, pp. 80–92. DOI: [10.17212/1994-6309-2015-4-80-92](https://doi.org/10.17212/1994-6309-2015-4-80-92).
- Zagibalova E.A., Moskvina V.A., Mayer G.G. The influence of method and temperature of ion-plasma treatment on physical and mechanical properties of surface layers in austenitic stainless steel. *Frontier Materials & Technologies*, 2021, no. 4, pp. 17–26. DOI: [10.18323/2782-4039-2021-4-17-26](https://doi.org/10.18323/2782-4039-2021-4-17-26).
- Balusamy T., Sankara Narayanan T.S.N., Ravichandran K., Park Il Song, Lee Min Ho. Influence of surface mechanical attrition treatment (SMAT) on the corrosion

- behaviour of AISI 304 stainless steel. *Corrosion Science*, 2013, vol. 74, pp. 332–344. DOI: [10.1016/j.corsci.2013.04.056](https://doi.org/10.1016/j.corsci.2013.04.056).
8. Wang Cong, Han Jing, Zhao Jiyun, Song Yuanming, Man Jiexiang, Zhu Hua, Sun Jiapeng, Fang Liang. Enhanced wear resistance of 316 L stainless steel with a nanostructured surface layer prepared by ultrasonic surface rolling. *Coatings*, 2019, vol. 9, no. 4, article number 276. DOI: [10.3390/coatings9040276](https://doi.org/10.3390/coatings9040276).
 9. Li Yang, Lian Yang, Jing Fengyu, He Tiantian, Zou Yun. Improvement in the tribological behaviour of surface-nanocrystallised 304 stainless steel through supersonic fine particle bombardment. *Applied Surface Science*, 2023, vol. 627, article number 157334. DOI: [10.1016/j.apsusc.2023.157334](https://doi.org/10.1016/j.apsusc.2023.157334).
 10. Makarov A.V., Savrai R.A., Skorynina P.A., Volkova E.G. Development of methods for steel surface deformation nanostructuring. *Metal Science and Heat Treatment*, 2020, vol. 62, no. 1-2, pp. 61–69. EDN: [GFTTFR](https://www.edn.net/GFTTFR).
 11. Petrova L.G. Strengthening of austenitic steels and alloys due to forming of solid solution by nitriding. *Uprochnyayushchie tekhnologii i pokrytiya*, 2007, no. 4, pp. 9–17. EDN: [HZRRJT](https://www.edn.net/HZRRJT).
 12. Liu R.L., Wang S., Wei C.Y., Yan M.F., Qiao Y.J. Microstructure and corrosion behavior of low temperature carburized AISI 304 stainless steel. *Materials Research Express*, 2019, vol. 6, article number 066417. DOI: [10.1088/2053-1591/ab104c](https://doi.org/10.1088/2053-1591/ab104c).
 13. Savrai R.A., Skorynina P.A. Structural-phase transformations and changes in the properties of AISI 321 stainless steel induced by liquid carburizing at low temperature. *Surface and Coatings Technology*, 2022, vol. 443, article number 128613. DOI: [10.1016/j.surfcoat.2022.128613](https://doi.org/10.1016/j.surfcoat.2022.128613).
 14. Savrai R.A., Osintseva A.L. Effect of hardened surface layer obtained by frictional treatment on the contact endurance of the AISI 321 stainless steel under contact gigacycle fatigue tests. *Materials Science and Engineering: A*, 2021, vol. 802, article number 140679. DOI: [10.1016/j.msea.2020.140679](https://doi.org/10.1016/j.msea.2020.140679).
 15. Putilova E.A., Goruleva L.S., Zadvorkin S.M. Effect of friction treatment of the AISI 321 steel on changes in its hardness and magnetic characteristics. *Diagnostics, Resource and Mechanics of materials and structures*, 2022, no. 5, pp. 40–49. DOI: [10.17804/2410-9908.2022.5.040-049](https://doi.org/10.17804/2410-9908.2022.5.040-049).
 16. Tsujikawa M., Egawa M., Sone T., Ueda N., Okano T., Higashi K. Modification of S phase on austenitic stainless steel using fine particle shot peening steel. *Surface and Coatings Technology*, 2013, vol. 228, pp. S318–S322. DOI: [10.1016/j.surfcoat.2012.05.111](https://doi.org/10.1016/j.surfcoat.2012.05.111).
 17. Yarovchuk A.V., Doronina T.A., Tivanova O.V. The influence of deformation martensite on pitting resistance of 12H18N10T stainless steel. *Polzunovskiy almanakh*, 2007, no. 1–2, pp. 190–196. EDN: [NNYBSW](https://www.edn.net/NNYBSW).
 18. Skorynina P.A., Makarov A.V., Berezovskaya V.V., Merkushkin E.A., Chekan N.M. The influence of nanostructuring friction treatment on micromechanical and corrosive characteristics of stable austenitic chromium-nickel steel. *Frontier Materials & Technologies*, 2021, no. 4, pp. 80–88. DOI: [10.18323/2782-4039-2021-4-80-88](https://doi.org/10.18323/2782-4039-2021-4-80-88).
 19. Korshunov L.G., Sagaradze V.V., Chernenko N.L., Shabashov V.A. Friction-induced structural transformations of the carbide phase in hadfield steel. *The Physics of Metals and Metallography*, 2015, vol. 116, no. 8, pp. 823–828. DOI: [10.1134/S0031918X15080098](https://doi.org/10.1134/S0031918X15080098).
 20. Narkevich N.A., Mironov Y.P., Shulepov I.A. Structure, mechanical, and tribotechnical properties of an austenitic nitrogen steel after frictional treatment. *The Physics of Metals and Metallography*, 2017, vol. 118, no. 4, pp. 399–406. DOI: [10.1134/S0031918X17020090](https://doi.org/10.1134/S0031918X17020090).
 21. Neslušán M., Minárik P., Čep R., Uriček J., Trojan K., Ganev N., Trško L. Barkhausen noise emission of AISI 304 stainless steel originating from strain induced martensite by shot peening. *Journal of Materials Research and Technology*, 2022, vol. 20, pp. 748–762. DOI: [10.1016/j.jmrt.2022.07.107](https://doi.org/10.1016/j.jmrt.2022.07.107).
 22. Chen Xin, Gushev M., Balonis M., Bauchy M., Sant G. Emergence of micro-galvanic corrosion in plastically deformed austenitic stainless steels. *Materials and Design*, 2021, vol. 203, article number 109614. DOI: [10.1016/j.matdes.2021.109614](https://doi.org/10.1016/j.matdes.2021.109614).
 23. Balusamy T., Kumar S., Sankara Narayanan T.S.N. Effect of surface nanocrystallization on the corrosion behaviour of AISI 409 stainless steel. *Corrosion Science*, 2010, vol. 52, no. 11, pp. 3826–3834. DOI: [10.1016/j.corsci.2010.07.004](https://doi.org/10.1016/j.corsci.2010.07.004).
 24. Yin Songbo, Li D.Y., Bouchard R. Effects of the strain rate of prior deformation on the wear-corrosion synergy of carbon steel. *Wear*, 2007, vol. 263, no. 1-6, pp. 801–807. DOI: [10.1016/j.wear.2007.01.058](https://doi.org/10.1016/j.wear.2007.01.058).
 25. Hao Yun-wei, Deng Bo, Zhong Cheng, Jiang Yi-ming, Li Jin. Effect of surface mechanical attrition treatment on corrosion behavior of 316 stainless steel. *Journal of Iron and Steel Research International*, 2009, vol. 16, no. 2, pp. 68–72. DOI: [10.1016/S1006-706X\(09\)60030-3](https://doi.org/10.1016/S1006-706X(09)60030-3).
 26. Sun Jianlin, Tang Huajie, Wang Chenglong, Han Zhao, Li Shisen. Effects of alloying elements and microstructure on stainless steel corrosion: a review. *Steel Research International*, 2022, vol. 93, no. 5, article number 2100450. DOI: [10.1002/srin.202100450](https://doi.org/10.1002/srin.202100450).
 27. Kadowaki M., Saengdeejing A., Muto I. et al. First-principles analysis of the inhibitive effect of interstitial carbon on an active dissolution of martensitic steel. *Corrosion Science*, 2020, vol. 163, article number 108251. DOI: [10.1016/j.corsci.2019.108251](https://doi.org/10.1016/j.corsci.2019.108251).

СПИСОК ЛИТЕРАТУРЫ

1. Borgioli F. From austenitic stainless steel to expanded austenite-S phase: formation, characteristics and properties of an elusive metastable phase // *Metals*. 2020. Vol. 10. № 2. Article number 187. DOI: [10.3390/met10020187](https://doi.org/10.3390/met10020187).
2. Pradhan K.K., Matawale C.R., Murarka S. Analysis of erosion-corrosion resistance and various application in domestic and industrial field of stainless steel grade 304 // *International Journal of Research (IJR)*. 2015. Vol. 2. № 4. P. 807–811.
3. Wei Xinlong, Ling Xiang, Zhang Meng. Influence of surface modifications by laser shock processing on the acid chloride stress corrosion cracking susceptibility of AISI 304 stainless steel // *Engineering Failure Analysis*. 2018. Vol. 91. P. 165–171. DOI: [10.1016/j.engfailanal.2018.04.045](https://doi.org/10.1016/j.engfailanal.2018.04.045).

4. Костина М.В., Криворотов В.И., Костина В.С., Кудряшов А.Э., Мурадян С.О. Особенности химического состава и структурно-фазового состояния, обусловившие снижение коррозионной стойкости деталей из стали 18Cr–10Ni // Известия высших учебных заведений. Черная металлургия. 2021. Т. 64. № 3. С. 217–229. DOI: [10.17073/0368-0797-2021-3-217-229](https://doi.org/10.17073/0368-0797-2021-3-217-229).
5. Макаров А.В., Скорынина П.А., Осинцева А.Л., Юровских А.С., Саврай Р.А. Повышение трибологических свойств аустенитной стали 12X18H10T наноструктурирующей фрикционной обработкой // Обработка металлов (технология, оборудование, инструменты). 2015. № 4. С. 80–92. DOI: [10.17212/1994-6309-2015-4-80-92](https://doi.org/10.17212/1994-6309-2015-4-80-92).
6. Загибалова Е.А., Москвина В.А., Майер Г.Г. Влияние метода и температуры ионно-плазменной обработки на физико-механические свойства поверхностных слоев в аустенитной нержавеющей стали // Frontier Materials & Technologies. 2021. № 4. С. 17–26. DOI: [10.18323/2782-4039-2021-4-17-26](https://doi.org/10.18323/2782-4039-2021-4-17-26).
7. Balusamy T., Sankara Narayanan T.S.N., Ravichandran K., Park Il Song, Lee Min Ho. Influence of surface mechanical attrition treatment (SMAT) on the corrosion behaviour of AISI 304 stainless steel // Corrosion Science. 2013. Vol. 74. P. 332–344. DOI: [10.1016/j.corsci.2013.04.056](https://doi.org/10.1016/j.corsci.2013.04.056).
8. Wang Cong, Han Jing, Zhao Jiyun, Song Yuanming, Man Jiexiang, Zhu Hua, Sun Jiapeng, Fang Liang. Enhanced wear resistance of 316 L stainless steel with a nanostructured surface layer prepared by ultrasonic surface rolling // Coatings. 2019. Vol. 9. № 4. Article number 276. DOI: [10.3390/coatings9040276](https://doi.org/10.3390/coatings9040276).
9. Li Yang, Lian Yang, Jing Fengyu, He Tiantian, Zou Yun. Improvement in the tribological behaviour of surface-nanocrystallised 304 stainless steel through supersonic fine particle bombardment // Applied Surface Science. 2023. Vol. 627. Article number 157334. DOI: [10.1016/j.apsusc.2023.157334](https://doi.org/10.1016/j.apsusc.2023.157334).
10. Макаров А.В., Саврай Р.А., Скорынина П.А., Волкова Е.Г. Развитие методов поверхностного деформационного наноструктурирования сталей // Металловедение и термическая обработка металлов. 2020. № 1. С. 62–69. EDN: [RMDMCZ](https://www.edn.ru/RMDMCZ).
11. Петрова Л.Г. Упрочнение аустенитных сталей и сплавов за счет формирования твердого раствора при азотировании // Упрочняющие технологии и покрытия. 2007. № 4. С. 9–17. EDN: [HZRRJT](https://www.edn.ru/HZRRJT).
12. Liu R.L., Wang S., Wei C.Y., Yan M.F., Qiao Y.J. Microstructure and corrosion behavior of low temperature carburized AISI 304 stainless steel // Materials Research Express. 2019. Vol. 6. Article number 066417. DOI: [10.1088/2053-1591/ab104c](https://doi.org/10.1088/2053-1591/ab104c).
13. Savrai R.A., Skorynina P.A. Structural-phase transformations and changes in the properties of AISI 321 stainless steel induced by liquid carburizing at low temperature // Surface and Coatings Technology. 2022. Vol. 443. Article number 128613. DOI: [10.1016/j.surfcoat.2022.128613](https://doi.org/10.1016/j.surfcoat.2022.128613).
14. Savrai R.A., Osintseva A.L. Effect of hardened surface layer obtained by frictional treatment on the contact endurance of the AISI 321 stainless steel under contact gigacycle fatigue tests // Materials Science and Engineering: A. 2021. Vol. 802. Article number 140679. DOI: [10.1016/j.msea.2020.140679](https://doi.org/10.1016/j.msea.2020.140679).
15. Путилова Е.А., Горюлева Л.С., Задворкин С.М. Влияние поверхностной фрикционной обработка на твердость и магнитные характеристики стали AISI 321 // Diagnostics, Resource and Mechanics of materials and structures. 2022. № 5. P. 40–49. DOI: [10.17804/2410-9908.2022.5.040-049](https://doi.org/10.17804/2410-9908.2022.5.040-049).
16. Tsujikawa M., Egawa M., Sone T., Ueda N., Okano T., Higashi K. Modification of S phase on austenitic stainless steel using fine particle shot peening steel // Surface and Coatings Technology. 2013. Vol. 228. P. S318–S322. DOI: [10.1016/j.surfcoat.2012.05.111](https://doi.org/10.1016/j.surfcoat.2012.05.111).
17. Яровчук А.В., Доронина Т.А., Тиванова О.В. Влияние мартенсита деформации на стойкость к питтинговой коррозии нержавеющей стали 12X18H10T // Ползуновский альманах. 2007. № 1–2. С. 190–196. EDN: [NNYBSW](https://www.edn.ru/NNYBSW).
18. Скорынина П.А., Макаров А.В., Березовская В.В., Меркушкин Е.А., Чекан Н.М. Влияние наноструктурирующей фрикционной обработки на микромеханические и коррозионные свойства стабильной аустенитной хромоникелевой стали // Frontier Materials & Technologies. 2021. № 4. С. 80–88. DOI: [10.18323/2782-4039-2021-4-80-88](https://doi.org/10.18323/2782-4039-2021-4-80-88).
19. Коршунов Л.Г., Сагарадзе В.В., Черненко Н.Л., Шабашов В.А. Структурные превращения карбидной фазы в стали Гадфильда, инициированные фрикционным воздействием // Физика металлов и металловедение. 2015. Т. 116. № 8. С. 867–873. DOI: [10.7868/S0015323015080094](https://doi.org/10.7868/S0015323015080094).
20. Наркевич Н.А., Шулёпов И.А., Миронов Ю.П. Структура, механические и триботехнические свойства аустенитной азотистой стали после фрикционной обработки // Физика металлов и металловедение. 2017. Т. 118. № 4. С. 421–428. DOI: [10.7868/S0015323017020097](https://doi.org/10.7868/S0015323017020097).
21. Neslušán M., Minárik P., Čep R., Uriček J., Trojan K., Ganev N., Trško L. Barkhausen noise emission of AISI 304 stainless steel originating from strain induced martensite by shot peening // Journal of Materials Research and Technology. 2022. Vol. 20. P. 748–762. DOI: [10.1016/j.jmrt.2022.07.107](https://doi.org/10.1016/j.jmrt.2022.07.107).
22. Chen Xin, Gushev M., Balonis M., Bauchy M., Sant G. Emergence of micro-galvanic corrosion in plastically deformed austenitic stainless steels // Materials and Design. 2021. Vol. 203. Article number 109614. DOI: [10.1016/j.matdes.2021.109614](https://doi.org/10.1016/j.matdes.2021.109614).
23. Balusamy T., Kumar S., Sankara Narayanan T.S.N. Effect of surface nanocrystallization on the corrosion behaviour of AISI 409 stainless steel // Corrosion Science. 2010. Vol. 52. № 11. P. 3826–3834. DOI: [10.1016/j.corsci.2010.07.004](https://doi.org/10.1016/j.corsci.2010.07.004).
24. Yin Songbo, Li D.Y., Bouchard R. Effects of the strain rate of prior deformation on the wear-corrosion synergy of carbon steel // Wear. 2007. Vol. 263. № 1–6. P. 801–807. DOI: [10.1016/j.wear.2007.01.058](https://doi.org/10.1016/j.wear.2007.01.058).
25. Hao Yun-wei, Deng Bo, Zhong Cheng, Jiang Yi-ming, Li Jin. Effect of surface mechanical attrition treatment on corrosion behavior of 316 stainless steel // Journal of Iron and Steel Research International. 2009. Vol. 16. № 2. P. 68–72. DOI: [10.1016/S1006-706X\(09\)60030-3](https://doi.org/10.1016/S1006-706X(09)60030-3).
26. Sun Jianlin, Tang Huajie, Wang Chenglong, Han Zhao, Li Shisen. Effects of alloying elements and microstructure on stainless steel corrosion: a review // Steel Research International. 2022. Vol. 93. № 5. Article number 2100450. DOI: [10.1002/srin.202100450](https://doi.org/10.1002/srin.202100450).

27. Kadowaki M., Saengdeejing A., Muto I. et al. First-principles analysis of the inhibitive effect of interstitial carbon on an active dissolution of martensitic steel //

Corrosion Science. 2020. Vol. 163. Article number 108251. DOI: [10.1016/j.corsci.2019.108251](https://doi.org/10.1016/j.corsci.2019.108251).

Влияние фрикционной обработки и жидкостной цементации на сопротивление общей коррозии хромоникелевых аустенитных сталей

© 2023

Скорынина Полина Андреевна^{*1,3}, младший научный сотрудник
Макаров Алексей Викторович^{1,2,4}, доктор технических наук, член-корреспондент РАН,
заведующий отделом материаловедения и лабораторией механических свойств
Саврай Роман Анатольевич^{1,5}, кандидат технических наук,
заведующий лабораторией конструкционного материаловедения

¹Институт машиноведения имени Э.С. Горкунова Уральского отделения РАН, Екатеринбург (Россия)

²Институт физики металлов имени М.Н. Михеева Уральского отделения РАН, Екатеринбург (Россия)

*E-mail: skorynina@imach.uran.ru,
polina.skorynina@mail.ru

³ORCID: <https://orcid.org/0000-0002-8904-7600>

⁴ORCID: <https://orcid.org/0000-0002-2228-0643>

⁵ORCID: <https://orcid.org/0000-0001-9873-3621>

Поступила в редакцию 27.06.2023

Принята к публикации 17.11.2023

Аннотация: В настоящее время для повышения твердости, прочности и износостойкости термически неупрочняемых аустенитных хромоникелевых сталей применение нашли такие методы, как фрикционная обработка скользящим индентором и жидкостная цементация. Однако наряду с эффективным повышением механических характеристик применение указанных обработок может сопровождаться снижением коррозионной стойкости аустенитных сталей. Поэтому целесообразно исследовать влияние фрикционной обработки и жидкостной цементации на сопротивление общей коррозии Cr–Ni аустенитных сталей. В данной работе по методу восстановленного отпечатка определяли поверхностную микротвердость сталей 12X18H10T и AISI 321 после электролитического полирования, механического шлифования, фрикционной обработки и жидкостной цементации при температуре 780 °С. С применением сканирующей электронной микроскопии и оптической профилометрии изучали подвергнутые указанным обработкам поверхности сталей и определяли их шероховатость. Коррозионную стойкость стали исследовали при испытаниях на общую коррозию гравиметрическим методом. При испытаниях на общую коррозию установлено, что упрочняющая (до 710 HV 0,025) фрикционная обработка приводит к повышению скорости коррозии аустенитной стали 12X18H10T в сравнении с электрополированным состоянием (от $k_m=0,35$ г/(м²·ч) до $k_m=0,53–0,54$ г/(м²·ч)). Скорость коррозии шлифованной стали составляет $k_m=0,58$ г/(м²·ч), при этом механическое шлифование не обеспечивает значительного повышения микротвердости исследуемой стали (от 220 до 240 HV 0,025). Показано, что коррозионное поведение подвергнутой различным обработкам стали 12X18H10T определяется следующими факторами: наличием/отсутствием α' -мартенсита деформации в структуре, качеством сформированной поверхности и, по-видимому, дисперсностью сформированной структуры. Жидкостная цементация аустенитной стали AISI 321 приводит одновременно к повышению ее микротвердости до 890 HV 0,025 и некоторому росту коррозионной стойкости по сравнению с тонкой механической шлифовкой. Это связано с тем, что атомы внедрения углерода стабилизируют электронное строение железа (аустенита и мартенсита), тем самым повышая его коррозионную стойкость.

Ключевые слова: аустенитная хромоникелевая сталь; фрикционная обработка; жидкостная цементация; микротвердость; фазовый состав; шероховатость; коррозионная стойкость.

Благодарности: Авторы выражают глубокую благодарность за участие в работе доктору технических наук В.В. Березовской.

Работа выполнена в рамках государственных заданий ИМАШ УрО РАН по теме № АААА-А18-118020790148-1 и ИФМ УрО РАН по теме № 122021000033-2. Экспериментальные исследования выполнены на оборудовании ЦКП «Пластометрия» ИМАШ УрО РАН.

Статья подготовлена по материалам докладов участников XI Международной школы «Физическое материаловедение» (ШФМ-2023), Тольятти, 11–15 сентября 2023 года.

Для цитирования: Скорынина П.А., Макаров А.В., Саврай Р.А. Влияние фрикционной обработки и жидкостной цементации на сопротивление общей коррозии хромоникелевых аустенитных сталей // Frontier Materials & Technologies. 2023. № 4. С. 109–119. DOI: [10.18323/2782-4039-2023-4-66-10](https://doi.org/10.18323/2782-4039-2023-4-66-10).

Quantitative analysis of deformation texture and primary recrystallization after inclined rolling and annealing of the $(\text{Fe}_{83}\text{Ga}_{17})_{99}\text{B}_1$ magnetostrictive alloy

© 2023

Ivan R. Strizhachenko*¹, engineer

Irina V. Gervasyeva², Doctor of Sciences (Physics and Mathematics), leading researcher

Vasily A. Milyutin³, PhD (Physics and Mathematics), senior researcher

Denis I. Devyaterikov⁴, PhD (Physics and Mathematics), researcher

M.N. Mikheev Institute of Metal Physics of the Ural Branch of RAS, Yekaterinburg (Russia)

*E-mail: strizhachenko@imp.uran.ru

¹ORCID: <https://orcid.org/0009-0009-5217-230X>

²ORCID: <https://orcid.org/0000-0001-8928-1707>

³ORCID: <https://orcid.org/0000-0002-5808-3959>

⁴ORCID: <https://orcid.org/0000-0002-6909-7678>

Received 23.06.2023

Accepted 14.11.2023

Abstract: The Fe–Ga alloy is a promising magnetostrictive material thanks to of the optimal combination of functional properties and relatively low price due to the absence of rare-earth elements in the composition. To obtain the maximum magnetostriction in Fe–Ga polycrystals, it is necessary to create a crystallographic texture with a predominance of the <100> direction, since the tetragonal magnetostriction constant is the largest. Traditional methods of thermomechanical treatment do not lead to the formation of such a texture in a bcc alloy. In this paper, for the first time, the authors propose to use inclined rolling to increase the proportion of favorable texture components. Warm rolling with a deformation degree of 70 % was carried out at angles of 0, 30 and 90° to the direction of hot rolling. The deformation texture was examined using X-ray texture analysis and the texture and structure of the material after recrystallization was analyzed by electron backscatter diffraction (EBSD) on a scanning electron microscope. Quantitative texture analysis was carried out using the orientation distribution function (ODF) method using the ATEX software. The volume fraction of some texture components was calculated. The study shows that a significant change in the deformation textures and primary recrystallization occurs during rolling at an angle of 90°. The sample after such rolling contains the largest amount of the planar component {100}. The study identified a relationship between the texture of deformation and recrystallization in Fe–Ga: to increase the proportion of components with the <001> crystallographic direction during recrystallization, the presence of planar components {111} in the deformation texture is necessary, which is associated with the predominant growth of favorable components in the deformation matrix with such a texture.

Keywords: Fe–Ga alloy; $(\text{Fe}_{83}\text{Ga}_{17})_{99}\text{B}_1$ alloy; texture quantitative analysis; inclined rolling; primary recrystallization; magnetostriction.

Acknowledgments: The work was supported by the grant of the President of the Russian Federation for young scientists – PhDs (No. MK-344.2022.4) and within the state assignment of the Ministry of Science and Higher Education of the Russian Federation (code “Magnet”, No. 122021000034–9).

Electron microscopic studies were carried out at the Collaborative Access Center “Testing Center of Nanotechnology and Advanced Materials” of the M.N. Mikheev Institute of Metal Physics of the Ural Branch of RAS (Yekaterinburg, Russia).

The paper was written on the reports of the participants of the XI International School of Physical Materials Science (SPM-2023), Togliatti, September 11–15, 2023.

For citation: Strizhachenko I.R., Gervasyeva I.V., Milyutin V.A., Devyaterikov D.I. Quantitative analysis of deformation texture and primary recrystallization during inclined rolling and annealing of the $(\text{Fe}_{83}\text{Ga}_{17})_{99}\text{B}_1$ magnetostrictive alloy. *Frontier Materials & Technologies*, 2023, no. 4, pp. 121–128. DOI: 10.18323/2782-4039-2023-4-66-11.

INTRODUCTION

Alloys with high magnetostriction are widely used in the electrical industry. Actuators and linear motors, sound and ultrasound transducers, sensors for various purposes, devices for converting mechanical energy into electrical one, etc. are produced on their base. In recent years, Fe–Ga alloy, which has an optimal combination of properties and a much lower cost compared to the popular Fe–Dy–Tb alloy, is considered a promising replacement for traditional magnetostrictive materials [1]. For this reason, today a large number of studies on the Fe–Ga alloy have appeared. For example, methods to increase magnetostriction by creating an optimal phase composition, have been developed [2], phase transformations [3] and the reasons for

abnormally high magnetostriction in the alloy have been studied in detail [4]. The most common form of use of magnetostrictive alloys (and many other soft magnetic alloys) is sheets, which are separated from each other by an insulation layer and then assembled into positions of a given shape and size. Such configuration allows creating volumetric devices, that can operate under conditions of increased reversal magnetization frequencies without large eddy current losses, which is especially important in the context of many magnetostrictive devices.

To produce Fe–Ga alloy sheets, rolling deformation followed by recrystallization annealing is usually used. It is very important in the process of thermomechanical processing to create a certain crystallographic texture necessary to achieve the best properties (magnetostriction). In the case of Fe–Ga,

such texture is $\langle 100 \rangle // \text{RD}$ (rolling direction), at which the magnetostriction magnitude is maximum [5]. The problem is that the Fe–Ga alloy with a Ga content of up to 19 at. % (the first peak of the magnetostriction dependence on the composition [6]) used for rolling has a body-centered cubic (bcc) structure, in which it is quite difficult to obtain a large volume of grains with the $\langle 100 \rangle // \text{RD}$ orientation primary recrystallization. To achieve this goal, it is necessary to carry out a detailed study of the features of the formation of texture components, in the Fe–Ga alloy at various stages of thermomechanical treatment with varying modes. Such research has been actively conducted in recent years [7–9], but the problem has not yet been fully resolved. It is known that by selecting, rolling, and annealing modes, it is possible to increase significantly the content of the $\langle 100 \rangle // \text{RD}$ component in the final texture, but even in this case its proportion remains quite low [9; 10]. Moreover, in terms of engineering, rolling of the Fe–Ga alloy is complicated by its tendency to brittle fracture, so the binary alloy is often doped with a small amount of boron, which minimizes the problem [11]. There are studies demonstrating the possibility of creating a favourable texture with a predominance of the so-called Goss orientation (this is the name of the $\{110\}\langle 100 \rangle$ orientation), or an orientation close to it, due to secondary recrystallization, similar to the mechanism implemented in Fe–3%Si anisotropic electrical steel [12; 13]. However, this is a technologically difficult process, which requires, among other things, the introduction of additional inclusions to inhibit the normal growth of grains at certain annealing stages.

To solve the problem of creating a crystallographic texture, optimal for the formation of magnetic properties in the Fe–Ga alloys, further research is required, including the use of new non-standard approaches. One of such approaches is inclined rolling [14]. It consists in changing the angle of the cold rolling direction relative to the hot rolling direction. This allows making changes in the processes of grain nucleation and growth, which in some cases can lead to an increase in the amount of $\langle 100 \rangle$ orientation. Previously, this approach was used for Fe–Si bcc alloy rolling and showed its effectiveness [15–17]. Since this alloy is similar to Fe–Ga from the point of view of texture formation features, one can hope that inclined rolling will be effective in this case as well. Such experiments had not been carried out previously, so the idea of their implementation formed the basis of this paper.

To increase ductility and minimize the risk of fracture during rolling, an alloy doped with 1 at. % of boron, namely $(\text{Fe}_{83}\text{Ga}_{17})_{99}\text{B}_1$ was selected as a study material.

The purpose of this work is to study the influence of rolling at an angle on the crystallographic texture in the Fe–Ga alloy.

METHODS

An ingot of $(\text{Fe}_{83}\text{Ga}_{17})_{99}\text{B}_1$ composition (atomic percentages are used in the paper) was melted by induction in a protective argon atmosphere and poured into a copper mold using centrifugal casting. As was found earlier, such casting method allows reducing the number of pores in Fe–Ga ingots, and achieving a uniform distribution of chemical elements [18]. The addition of boron is intended to increase the ductility of the alloy, which will simplify the task of its

plastic deformation. A cylindrical ingot with a height of 50 mm and a diameter of 14 mm was cut into three equal parts across the long side. The blanks were forged to a thickness of 6 mm and hot rolled to a thickness of about 2.7 mm. Forging and hot rolling were carried out at a temperature of 1000 °C. Then, using an electric spark machine, rectangles 8 mm wide and 20 to 30 mm long were cut from the resulting sheets at different angles to the hot rolling direction (Fig. 1).

The samples were rolled in several passes on a double rolling mill heated to 350 °C before each pass to minimize the risk of cracking. The overall degree of deformation using warm rolling was 70 %. The deformation texture was studied using a PANalytical Empyrean Series 2 diffractometer. The pole figures of the samples were obtained in a configuration with a focusing polycapillary lens.

The sample was fixed on a measuring table with three degrees of freedom. An X-ray tube operating at the characteristic wavelength of $\text{CoK}\alpha$, $\lambda=1.789 \text{ \AA}$ served as the radiation source. Based on the experimental pole figures $\{110\}$, $\{200\}$ and $\{112\}$, Bunge orientation distribution functions (ODFs) were built using ATEX software¹. Using a specially created program, volume fractions of specified orientations $\{hkl\}\langle uvw \rangle \pm 10^\circ$ were obtained from ODF data for deformed samples, in the same way that it was implemented in our previous work [19].

Recrystallization annealing of deformed samples was carried out in vacuum at a temperature of 900 °C for 30 min. Sample preparation for structural studies was carried out by mechanical grinding, and electropolishing in a 90 % $\text{C}_2\text{H}_4\text{O}_2$ + 10 % HClO_4 solution. The structure and texture of the recrystallized samples were studied using the electron backscatter diffraction (EBSD) method, on a FEI Quanta 200 scanning electron microscope using an EDAX attachment. On recrystallized samples subjected to chemical polishing, a zone of the same area was scanned at a relatively low magnification of $\times 100$, which allows covering a larger number of grains and obtain better statistics. In total, using the EBSD method, an area of about 25 mm² was examined on each sample. Applying the TSL OIM Analysis program, the volume fractions of planes or directions in a plane, as well as the average grain diameter were determined.

RESULTS

Fig. 2 shows the ODF sections at an angle of $\varphi_2=45^\circ$ with relevant information.

The ODF 45° section (Fig. 2 a) presents the orientations most characteristic of the deformation of bcc materials. It can be observed that in all three variants of inclined rolling (Fig. 2 b–d), orientations with an octahedral plane $\{111\}$ parallel to the rolling plane (horizontal line at angle of $\Phi=54.7^\circ$) are predominantly present. Moreover, orientations with a cubic plane $\{100\}$ parallel to the rolling plane (upper side of the orientation cube at $\Phi=0^\circ$) occur with significantly greater intensity. In this case, in the sample rolled transverse to the rolling direction (Fig. 2 c), there are significantly more orientations with $\{111\}$ planes. The sum of the volume fractions of $\{111\}\langle 110 \rangle$ and $\{111\}\langle 112 \rangle$ in this sample is 6.9 %, and in samples rolled at angles of 0

¹ Beausir B., Fundenberger J.-J. *Analysis Tools for Electron and X-ray diffraction. ATEX-software*. URL: www.atex-software.eu.

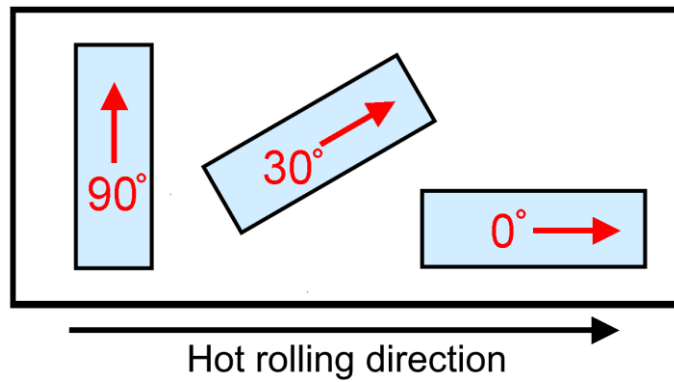


Fig. 1. The scheme of cutting samples from a hot-rolled sheet at different angles to the hot rolling direction

Рис. 1. Схема вырезания образцов из горячекатанного листа под разными углами по отношению к направлению горячей прокатки.
Горизонтальная стрелка внизу рисунка указывает направление горячей прокатки

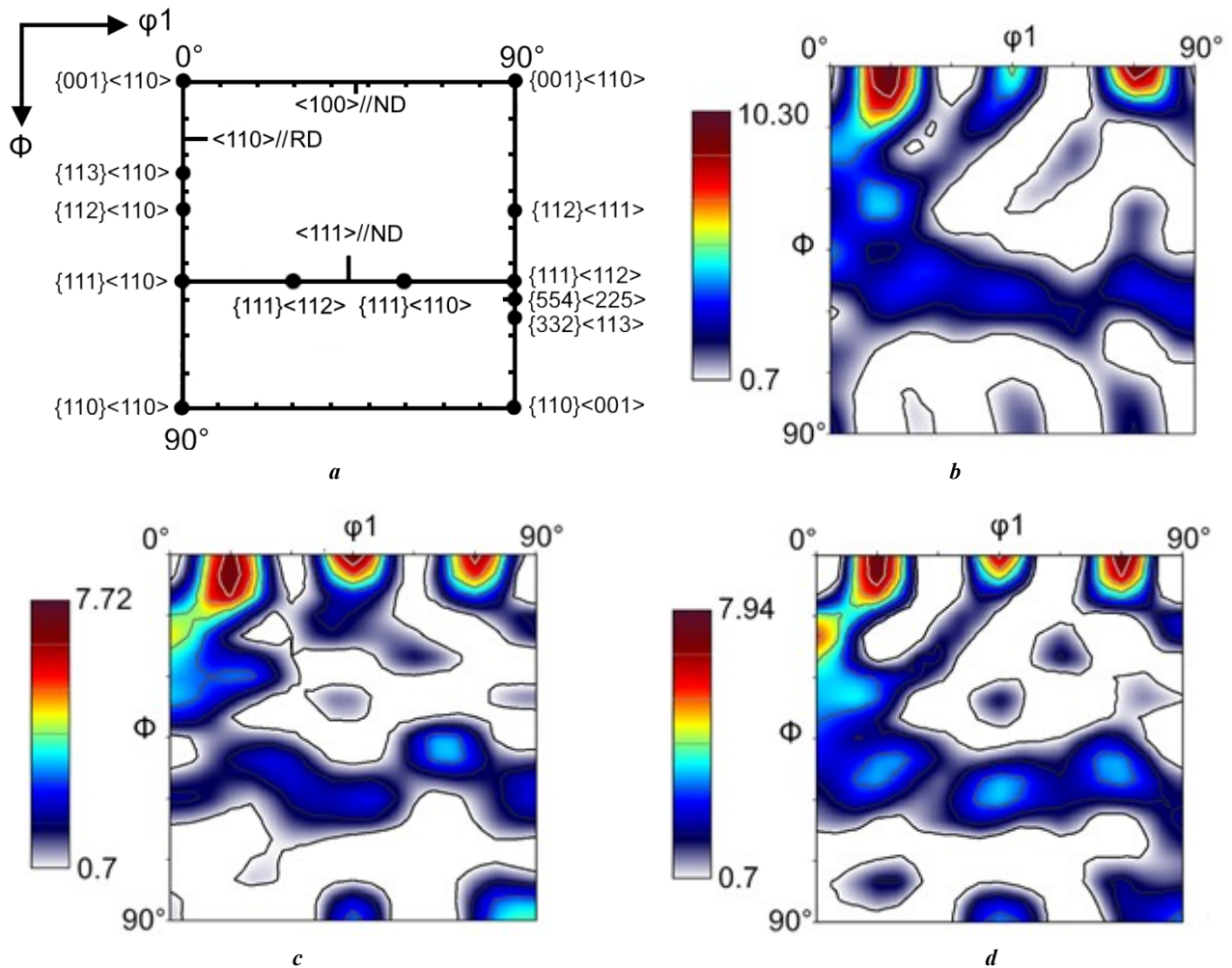


Fig. 2. The location of the most important orientations (at $\phi_2=45^\circ$) on the ODF specific to rolling and recrystallization of bcc metals (a) and ODF sections at $\phi_2=45^\circ$ for samples rolled at different angles to hot rolling direction: 0° (b); 30° (c); 90° (d)

Рис. 2. Положение наиболее важных ориентировок (при $\phi_2=45^\circ$) на ФРО, характерных для прокатки и рекристаллизации ОЦК-металлов (a) и сечения ФРО при $\phi_2=45^\circ$ для образцов, прокатанных под разными углами к направлению горячей прокатки: 0° (b); 30° (c); 90° (d)

and 30°, is 5.8 and 5.7 %, respectively. Moreover, the $\{111\}<132>$ orientation is clearly visible in this sample (7.1 %, which is higher than for other variants) (Fig. 2, Table 1). As for cubic orientations, their volume fraction is significantly higher than of octahedral ones, and is approximately the same in all studied samples. In addition, Fig. 2 b and 2 c show a Goss orientation $\{110\}<001>$ (lower right corner in the section), which, like cubic, is desirable for the formation of magnetic properties.

The study of recrystallized samples allows tracing the crystallographic texture evolution depending on the angle between cold and hot rolling. The recrystallization texture was studied by EBSD, since in this case the samples are less suitable for X-ray diffraction (XRD) studies. This is related to the fact that the grains of a certain orientation formed as a result of recrystallization are much larger in area than the cells in the deformation structure, which does not provide a good level of statistical sampling using the XRD method. The EBSD method makes it possible to analyze simultaneously the grain structure and crystallographic texture and suits well for the study of recrystallized samples. The results of the study by this method are shown in Fig. 3 in the form of fragments of orientation maps.

Upon visual analysis of the orientation maps, one can conclude that the sample rolled at an angle of 90°, contains a larger number of "red" grains, i. e., those in which the $\{100\}$ planes lie in the sheet plane. Of course, to make an unambiguous conclusion, it is necessary to carry out a detailed quantitative analysis of the content of one or another texture component in the texture of samples. The results of such an analysis for the deformation texture and recrystallization texture are given in Table 1. Since the predominant directions are of greatest importance in terms of the formation of the Fe–Ga functional properties, their analysis was carried out in recrystallized samples with a scattering of $\pm 15^\circ$.

It can be observed from Table 1 that the use of inclined rolling, significantly improves the texture of the samples in terms of the relation between the main crystallographic directions. Moreover, the effect when changing an angle between hot and warm rolling by 90° is more visible than by 30°. Compared to rolling along the hot rolling direction (0°), rolling at 90° leads to a twofold decrease in the undesired $<111> // RD$ orientation, and a significant increase in the fraction of $<100> // RD$. At the same time, the proportion of grains with $<110> // RD$ directions is unchanged under any of the studied rolling modes.

DISCUSSION

It is known that in the Fe–19%Ga alloy, the magnetostriction constant λ_{100} is maximal and is about 250 ppm. At the same time, λ_{110} is also quite high – about 150 ppm. Finally, λ_{111} is minimal and, according to various sources, varies from –20 to 0 [10]. To achieve high magnetostriction values in a polycrystalline sample, it is necessary to combine in its texture as many $<100>$ orientations as possible and as few $<111>$ orientations as possible, while the presence of $<110>$ is acceptable. The work revealed the influence of the angle between hot and warm rolling on the number of these orientations in the $(Fe_{83}Ga_{17})_{99}B_1$ alloy.

To identify the reasons for changes in the recrystallization texture of samples rolled at different angles, it is neces-

sary to analyze their deformation texture. Since the recrystallization annealing of all samples was carried out under identical conditions, it is the initial texture (in this case, the texture of the samples after final rolling), which is responsible for the observed phenomena. Changing the angle of the final rolling direction relative to the hot rolling direction is equivalent to rotating the sample around the normal direction (ND). This leads to changes in the rotation trajectories of various orientations, during plastic deformation. As can be observed, the deformation texture of a sample rolled transverse to the hot rolling direction contains significantly more $\{111\}$ planar orientations.

It is well known from the literature [20] that in the Fe–3%Si bcc alloy, the grains disordered around the $<110>$ axis by 27–35° have the boundaries of greatest mobility. This explains the growth of the $\{110\}<001>$ component into a matrix with a strong $\{111\}<112>$ orientation, during secondary recrystallization in electrical steel. Perhaps, in the Fe–Ga alloy, it is possible to find other favourable correlations for the growth of the $\{100\}<hkl>$ component into any of the components of the $\{111\}$ axial texture, for example, into the $\{111\}<321>$ orientation predominant in the variant with rolling at an angle of 90° (Fig. 2 c). This will be the subject of further research.

The orientation criterion although is the main one, but not the only one, for the growth of grains with a favourable $<100> // RD$ direction. It is also necessary to take into account the features of mesostructural elements, such as deformation bands, shear bands, and transition bands in the deformation structure. Moreover, an important role is played both by the relationship between the deformation texture components, and the distance between potential recrystallization nuclei with a certain orientation, as well as by other parameters. Therefore, identifying definite mechanisms responsible for the observed change in texture during recrystallization requires additional research. This work shows for the first time that rolling at an angle of 90° with respect to the hot rolling direction can be a promising tool for creating a favourable texture in a Fe–Ga alloy.

The authors studied samples cut at angles of 0, 30 and 90° relative to the hot rolling direction. There were no samples cut at other angles, such as 60°, due to technical limitations. All samples in the study were cut from the same ingot (to maintain equal experimental conditions for all samples). The size of the ingot and the hot-rolled sheets made from it did not allow cutting out another full-scale sample at an angle of 60°. It was not possible to reduce the size of the cut samples, since otherwise it would be problematic to carry out subsequent cold rolling. In connection with the prospects of the proposed approach, further research using other angles between the directions of hot and cold rolling, including 60°, is certainly necessary.

CONCLUSIONS

1. The $(Fe_{83}Ga_{17})_{99}B_1$ alloy melted by induction and cast using centrifugal casting, was successfully deformed by hot and warm rolling at different angles (0, 30, and 90°) to the hot rolling direction.

2. It is shown that the deformation texture after 70 % compression, alongside a noticeable amount of the $\{111\}$ planar component, contains a large number of cubic orientations that are atypical for the deformation texture of bcc

Table 1. Texture quantitative characteristics (volume fraction of components $\{hkl\}\langle uvw\rangle\pm 10^\circ$, % in deformation texture and volume fraction of directions $\langle uvw\rangle\pm 15^\circ$ in recrystallization texture) and average grain size after recrystallization
Таблица 1. Количественные характеристики текстуры (объемная доля компонент $\{hkl\}\langle uvw\rangle\pm 10^\circ$, % в текстуре деформации и объемная доля направлений $\langle uvw\rangle\pm 15^\circ$ в текстуре рекристаллизации) и средний размер зерна после рекристаллизации

Studied characteristics	An angle between cold and hot rolling directions, deg.		
	0	30	90
Rolling deformation			
{100}<001> orientation fraction	1.6	3.4	2.1
{100}<230> orientation fraction	7.1	8.9	8.0
{100}<120> orientation fraction	7.5	8.9	8.4
{110}<001> orientation fraction	2.6	2.0	1.5
{111}<112> orientation fraction	3.4	3.0	3.0
{111}<110> orientation fraction	2.4	2.7	3.9
{111}<132> orientation fraction	6.3	5.7	7.1
Recrystallization 900 °C, 30 min			
Grain size (by the cutting line), μm	123.6	99.3	129.0
Grain size (by average diameter), μm	149.2	130.3	153.2
Fraction of <100> // RD directions	15.3	18.9	24.4
Fraction of <110> // RD directions	15.6	15.5	15.9
Fraction of <111> // RD directions	7.8	5.7	3.5

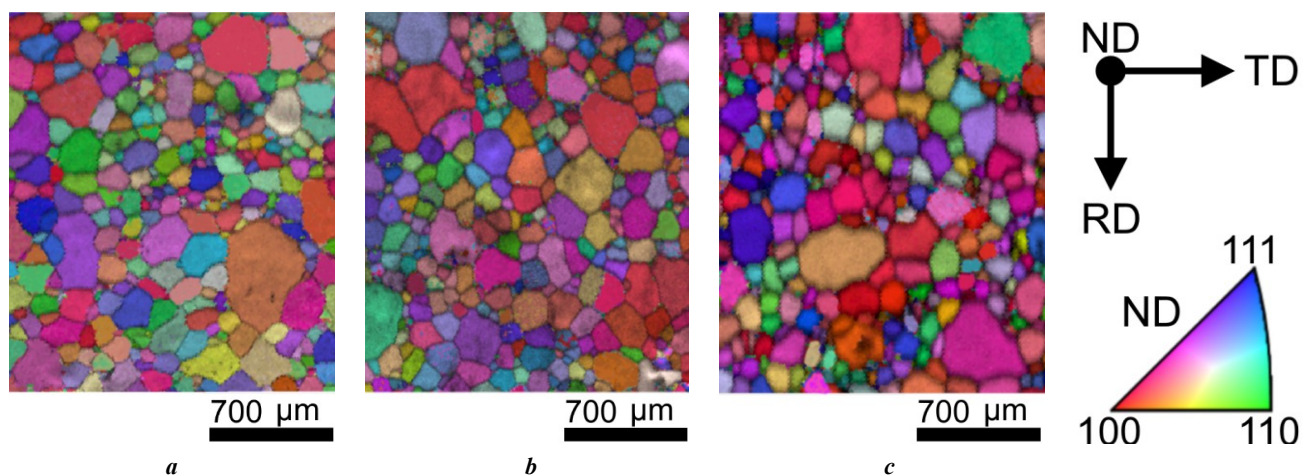


Fig. 3. Fragments of orientation maps EBSD obtained from recrystallized samples. Rolling at angles to the hot rolling direction: 0° (a), 30° (b), 90° (c).

Sample orientation during scanning: RD – rolling direction; ND – normal direction to a sheet; TD – transverse direction

Рис. 3. Фрагменты ориентационных карт EBSD, полученных с рекристаллизованных образцов. Прокатка под углами к направлению горячей прокатки: 0° (a), 30° (b), 90° (c).

Ориентация образцов при съемке: RD – направление прокатки; ND – направление нормали к листу; TD – поперечное направление

alloys. Rolling at an angle of 90° results in the largest amount of {111}<132> confined component within the {111} axial one.

3. It has been found that recrystallization annealing at 900 °C of samples rolled at an angle of 30 and 90° leads to a more favourable texture in terms of the formation of Fe–Ga properties, compared to traditional rolling (0°). The most visible effect is observed in the sample rolled at an angle of 90° to the hot rolling direction. This work shows for the first time that angular rolling is an effective tool to improve the primary recrystallization texture in Fe–Ga alloys.

REFERENCES

- Golovin I.S., Palacheva V.V., Mohamed A.K., Balagurov A.M. Structure and properties of Fe–Ga alloys as promising materials for electronics. *The Physics of Metals and Metallography*, 2020, vol. 121, no. 9, pp. 851–893. DOI: [10.1134/S0031918X20090057](https://doi.org/10.1134/S0031918X20090057).
- Zhang Yiqun, Gou Junming, Yang Tianzi, Ke Yubin, Ma Tianyu. Non-Equilibrium Time-Temperature-Transformation Diagram for Enhancing Magnetostriction of Fe–Ga Alloys. *Acta Materialia*, 2022, vol. 244, article number 118548. DOI: [10.1016/j.actamat.2022.118548](https://doi.org/10.1016/j.actamat.2022.118548).
- Mohamed A.K., Palacheva V.V., Cheverikin V.V. et al. Low-temperature metastable-to-equilibrium phase transitions in Fe–Ga alloys. *Intermetallics*, 2022, vol. 145, article number 107540. DOI: [10.1016/j.intermet.2022.107540](https://doi.org/10.1016/j.intermet.2022.107540).
- Gou Junming, Ma Tianyu, Qiao Ruihua, Yang Tianzi, Liu Feng, Ren Xiaobing. Dynamic precipitation and the resultant magnetostriction enhancement in [001]-oriented Fe–Ga alloys. *Acta Materialia*, 2021, vol. 206, article number 116631. DOI: [10.1016/j.actamat.2021.116631](https://doi.org/10.1016/j.actamat.2021.116631).
- Na Suok-Min, Flatau A.B. Single grain growth and large magnetostriction in secondarily recrystallized Fe–Ga thin sheet with sharp Goss (011)[100] orientation. *Scripta Materialia*, 2012, vol. 66, no. 5, pp. 307–310. DOI: [10.1016/J.SCRIPTAMAT.2011.11.020](https://doi.org/10.1016/J.SCRIPTAMAT.2011.11.020).
- Xing Q., Du Y., McQueeney R.J., Lograsso T.A. Structural investigations of Fe–Ga alloys: Phase relations and magnetostrictive behavior. *Acta Materialia*, 2008, vol. 56, no. 16, pp. 4536–4546. DOI: [10.1016/j.actamat.2008.05.011](https://doi.org/10.1016/j.actamat.2008.05.011).
- Qi Qingli, Li Jiheng, Mu Xing, Ding Zhiyi, Bao Xiaoqian, Gao Xuexu. Microstructure evolution, magnetostrictive and mechanical properties of (Fe₈₃Ga₁₇)_{99.9}(NbC)_{0.1} alloy ultra-thin sheets. *Journal of Materials Science*, 2020, vol. 55, pp. 2226–2238. DOI: [10.1007/s10853-019-04057-8](https://doi.org/10.1007/s10853-019-04057-8).
- Milyutin V.A., Gervasyeva I.V., Shishkin D.A., Beaunon E. Structure and texture in rolled Fe₈₂Ga₁₈ and (Fe₈₂Ga₁₈)₉₉B₁ alloys after annealing under high magnetic field. *Physica B: Condensed Matter*, 2022, vol. 639, article number 413994. DOI: [10.1016/j.physb.2022.413994](https://doi.org/10.1016/j.physb.2022.413994).
- Milyutin V.A., Gervasyeva I.V. Formation of crystallographic texture in Fe–Ga alloys during various types of plastic deformation and primary recrystallization. *Materials Today Communications*, 2021, vol. 27, article number 102193. DOI: [10.1016/j.mtcomm.2021.102193](https://doi.org/10.1016/j.mtcomm.2021.102193).
- Fu Q., Sha Y.H., Zhang F., Esling C., Zuo L. Correlative effect of critical parameters for η recrystallization texture development in rolled Fe₈₁Ga₁₉ sheet: Modeling and experiment. *Acta Materialia*, 2019, vol. 167, pp. 167–180. DOI: [10.1016/j.actamat.2019.01.043](https://doi.org/10.1016/j.actamat.2019.01.043).
- Li J.H., Gao X.X., Zhu J., Bao X.Q., Xia T., Zhang M.C. Ductility, texture and large magnetostriction of Fe–Ga-based sheets. *Scripta Materialia*, 2010, vol. 63, no. 2, pp. 246–249. DOI: [10.1016/j.scriptamat.2010.03.068](https://doi.org/10.1016/j.scriptamat.2010.03.068).
- He Zhenghua, Liu Jiande, Zhu Xiaofei, Zhai Xinya, Sha Yuhui, Hao Hongbo, Chen Lijia. Secondary recrystallization of {310}<001> texture and enhanced magnetostriction in Fe–Ga alloy thin sheet. *Journal of Material Research and Technology*, 2023, vol. 22, pp. 1868–1877. DOI: [10.1016/j.jmrt.2022.12.038](https://doi.org/10.1016/j.jmrt.2022.12.038).
- He Zhenghua, Zhai Xinya, Sha Yuhui, Zhu Xiaofei, Chen Sihao, Hao Hongbo, Chen Lijia, Li Feng, Zuo Liang. Secondary recrystallization of Goss texture in one-stage cold rolled Fe–Ga thin sheets via a large rolling reduction. *AIP Advances*, 2023, vol. 13, no. 2, article number 025035. DOI: [10.1063/9.0000407](https://doi.org/10.1063/9.0000407).
- Mehdi M., He Youliang, Hilinski E.J., Kestens L.A.I., Edrisy A. The evolution of cube ({001}<100>) texture in non-oriented electrical steel. *Acta Materialia*, 2020, vol. 185, pp. 540–554. DOI: [10.1016/j.actamat.2019.12.024](https://doi.org/10.1016/j.actamat.2019.12.024).
- Mehdi M., He Youliang, Hilinski E.J., Edrisy A. Effect of skin pass rolling reduction rate on the texture evolution of a non orientated electrical steel after inclined cold rolling. *Journal of Magnetism and Magnetic Materials*, 2017, vol. 429, pp. 148–160. DOI: [10.1016/j.jmmm.2017.01.020](https://doi.org/10.1016/j.jmmm.2017.01.020).
- Fang F., Lu X., Zhang Y.X., Wang Y., Jiao H.T., Cao G.M., Yuan G., Xu Y.B., Misra R.D.K., Wang G.D. Influence of cold rolling direction on texture, inhibitor and magnetic properties in strip-cast grain-oriented 3% silicon steel. *Journal of Magnetism and Magnetic Materials*, 2017, vol. 424, pp. 339–346. DOI: [10.1016/j.jmmm.2016.10.086](https://doi.org/10.1016/j.jmmm.2016.10.086).
- He Youliang, Hilinski E.J. Textures of non-oriented electrical steel sheets produced by skew cold rolling and annealing. *Metals (Basel)*, 2022, vol. 12, no. 1, article number 17. DOI: [10.3390/met12010017](https://doi.org/10.3390/met12010017).
- Milyutin V.A., Gervasyeva I.V., Davidov D.I., Nikiforova S.M. Centrifugal Casting of Fe₈₂Ga₁₈ Alloy as a Tool of Mechanical Properties Improvement. *Metallurgical and Materials Transactions A*, 2021, vol. 52, pp. 3684–3688. DOI: [10.1007/s11661-021-06348-9](https://doi.org/10.1007/s11661-021-06348-9).
- Gervasyeva I.V., Khlebnikova Yu.V., Makarova M.V., Dolgikh D.V., Suaridze T.R. Crystallographic texture of tape substrates for HTSC from Cu-40%Ni alloy with additives of refractory elements. *Journal of Alloys and Compounds*, 2022, vol. 921, article number 166156. DOI: [10.1016/j.jallcom.2022.166156](https://doi.org/10.1016/j.jallcom.2022.166156).
- Harase J., Shimizu R., Takahashi N. Mechanism of Goss Secondary Recrystallization in Grain Orientated Silicon Steel. *Texture and Microstructures*, 1991, vol. 14-18, pp. 679–684.

СПИСОК ЛИТЕРАТУРЫ

1. Головин И.С., Палачева В.В., Мохамед А.К., Балагуров А.М. Структура и свойства Fe–Ga сплавов – перспективных материалов для электроники // Физика металлов и металловедение. 2020. Т. 121. № 9. P. 937–980. DOI: [10.31857/s0015323020090053](https://doi.org/10.31857/s0015323020090053).
2. Zhang Yiqun, Gou Junming, Yang Tianzi, Ke Yubin, Ma Tianyu. Non-Equilibrium Time-Temperature-Transformation Diagram for Enhancing Magnetostriction of Fe–Ga Alloys // Acta Materialia. 2022. Vol. 244. Article number 118548. DOI: [10.1016/j.actamat.2022.118548](https://doi.org/10.1016/j.actamat.2022.118548).
3. Mohamed A.K., Palacheva V.V., Cheverikin V.V. et al. Low-temperature metastable-to-equilibrium phase transitions in Fe–Ga alloys // Intermetallics. 2022. Vol. 145. Article number 107540. DOI: [10.1016/j.intermet.2022.107540](https://doi.org/10.1016/j.intermet.2022.107540).
4. Gou Junming, Ma Tianyu, Qiao Ruihua, Yang Tianzi, Liu Feng, Ren Xiaobing. Dynamic precipitation and the resultant magnetostriction enhancement in [001]-oriented Fe–Ga alloys // Acta Materialia. 2021. Vol. 206. Article number 116631. DOI: [10.1016/j.actamat.2021.116631](https://doi.org/10.1016/j.actamat.2021.116631).
5. Na Suok-Min, Flatau A.B. Single grain growth and large magnetostriction in secondarily recrystallized Fe–Ga thin sheet with sharp Goss (011)[100] orientation // Scripta Materialia. 2012. Vol. 66. № 5. P. 307–310. DOI: [10.1016/J.SCRIPTAMAT.2011.11.020](https://doi.org/10.1016/J.SCRIPTAMAT.2011.11.020).
6. Xing Q., Du Y., McQueeney R.J., Lograsso T.A. Structural investigations of Fe–Ga alloys: Phase relations and magnetostrictive behavior // Acta Materialia. 2008. Vol. 56. № 16. P. 4536–4546. DOI: [10.1016/j.actamat.2008.05.011](https://doi.org/10.1016/j.actamat.2008.05.011).
7. Qi Qingli, Li Jiheng, Mu Xing, Ding Zhiyi, Bao Xiaoqian, Gao Xuexu. Microstructure evolution, magnetostrictive and mechanical properties of (Fe₈₃Ga₁₇)_{99,9}(NbC)_{0,1} alloy ultra-thin sheets // Journal of Materials Science. 2020. Vol. 55. P. 2226–2238. DOI: [10.1007/s10853-019-04057-8](https://doi.org/10.1007/s10853-019-04057-8).
8. Milyutin V.A., Gervasyeva I.V., Shishkin D.A., Beaugnon E. Structure and texture in rolled Fe₈₂Ga₁₈ and (Fe₈₂Ga₁₈)₉₉B₁ alloys after annealing under high magnetic field // Physica B: Condensed Matter. 2022. Vol. 639. Article number 413994. DOI: [10.1016/j.physb.2022.413994](https://doi.org/10.1016/j.physb.2022.413994).
9. Milyutin V.A., Gervasyeva I.V. Formation of crystallographic texture in Fe–Ga alloys during various types of plastic deformation and primary recrystallization // Materials Today Communications. 2021. Vol. 27. Article number 102193. DOI: [10.1016/j.mtcomm.2021.102193](https://doi.org/10.1016/j.mtcomm.2021.102193).
10. Fu Q., Sha Y.H., Zhang F., Esling C., Zuo L. Correlative effect of critical parameters for η recrystallization texture development in rolled Fe₈₁Ga₁₉ sheet: Modeling and experiment // Acta Materialia. 2019. Vol. 167. P. 167–180. DOI: [10.1016/j.actamat.2019.01.043](https://doi.org/10.1016/j.actamat.2019.01.043).
11. Li J.H., Gao X.X., Zhu J., Bao X.Q., Xia T., Zhang M.C. Ductility, texture and large magnetostriction of Fe–Ga-based sheets // Scripta Materialia. 2010. Vol. 63. № 2. P. 246–249. DOI: [10.1016/j.scriptamat.2010.03.068](https://doi.org/10.1016/j.scriptamat.2010.03.068).
12. He Zhenghua, Liu Jiande, Zhu Xiaofei, Zhai Xinya, Sha Yuhui, Hao Hongbo, Chen Lijia. Secondary recrystallization of {310}<001> texture and enhanced magnetostriction in Fe–Ga alloy thin sheet // Journal of Material Research and Technology. 2023. Vol. 22. P. 1868–1877. DOI: [10.1016/j.jmrt.2022.12.038](https://doi.org/10.1016/j.jmrt.2022.12.038).
13. He Zhenghua, Zhai Xinya, Sha Yuhui, Zhu Xiaofei, Chen Sihao, Hao Hongbo, Chen Lijia, Li Feng, Zuo Liang. Secondary recrystallization of Goss texture in one-stage cold rolled Fe–Ga thin sheets via a large rolling reduction // AIP Advances. 2023. Vol. 13. № 2. Article number 025035. DOI: [10.1063/9.0000407](https://doi.org/10.1063/9.0000407).
14. Mehdi M., He Youliang, Hilinski E.J., Kestens L.A.I., Edrisy A. The evolution of cube ({001}<100>) texture in non-oriented electrical steel // Acta Materialia. 2020. Vol. 185. P. 540–554. DOI: [10.1016/j.actamat.2019.12.024](https://doi.org/10.1016/j.actamat.2019.12.024).
15. Mehdi M., He Youliang, Hilinski E.J., Edrisy A. Effect of skin pass rolling reduction rate on the texture evolution of a non orientated electrical steel after inclined cold rolling // Journal of Magnetism and Magnetic Materials. 2017. Vol. 429. P. 148–160. DOI: [10.1016/j.jmmm.2017.01.020](https://doi.org/10.1016/j.jmmm.2017.01.020).
16. Fang F., Lu X., Zhang Y.X., Wang Y., Jiao H.T., Cao G.M., Yuan G., Xu Y.B., Misra R.D.K., Wang G.D. Influence of cold rolling direction on texture, inhibitor and magnetic properties in strip-cast grain-oriented 3% silicon steel // Journal of Magnetism and Magnetic Materials. 2017. Vol. 424. P. 339–346. DOI: [10.1016/j.jmmm.2016.10.086](https://doi.org/10.1016/j.jmmm.2016.10.086).
17. He Youliang, Hilinski E.J. Textures of non-oriented electrical steel sheets produced by skew cold rolling and annealing // Metals (Basel). 2022. Vol. 12. № 1. Article number 17. DOI: [10.3390/met12010017](https://doi.org/10.3390/met12010017).
18. Milyutin V.A., Gervasyeva I.V., Davidov D.I., Nikiforova S.M. Centrifugal Casting of Fe₈₂Ga₁₈ Alloy as a Tool of Mechanical Properties Improvement // Metallurgical and Materials Transactions A. 2021. Vol. 52. P. 3684–3688. DOI: [10.1007/s11661-021-06348-9](https://doi.org/10.1007/s11661-021-06348-9).
19. Gervasyeva I.V., Khlebnikova Yu.V., Makarova M.V., Dolgikh D.V., Suaridze T.R. Crystallographic texture of tape substrates for HTSC from Cu-40%Ni alloy with additives of refractory elements // Journal of Alloys and Compounds. 2022. Vol. 921. Article number 166156. DOI: [10.1016/j.jallcom.2022.166156](https://doi.org/10.1016/j.jallcom.2022.166156).
20. Harase J., Shimizu R., Takahashi N. Mechanism of Goss Secondary Recrystallization in Grain Orientated Silicon Steel // Texture and Microstructures. 1991. Vol. 14-18. P. 679–684.

Количественный анализ текстуры деформации и первичной рекристаллизации при угловой прокатке и отжиге магнитоотрицательного сплава (Fe₈₃Ga₁₇)₉₉B₁

© 2023

Стрижаченко Иван Романович^{*1}, инженер*Гервасьева Ирина Владимировна*², доктор физико-математических наук, ведущий научный сотрудник*Милютин Василий Александрович*³, кандидат физико-математических наук, старший научный сотрудник*Девятериков Денис Игоревич*⁴, кандидат физико-математических наук, научный сотрудник

Институт физики металлов имени М.Н. Михеева Уральского отделения РАН, Екатеринбург (Россия)

*E-mail: strizhachenko@imp.uran.ru

¹ORCID: <https://orcid.org/0009-0009-5217-230X>²ORCID: <https://orcid.org/0000-0001-8928-1707>³ORCID: <https://orcid.org/0000-0002-5808-3959>⁴ORCID: <https://orcid.org/0000-0002-6909-7678>

Поступила в редакцию 23.06.2023

Принята к публикации 14.11.2023

Аннотация: Сплав Fe–Ga является перспективным магнитоотрицательным материалом благодаря оптимальному сочетанию функциональных свойств и относительно низкой цены за счет отсутствия редкоземельных элементов в составе. Для получения максимальной магнитоотрицательности в поликристаллах Fe–Ga необходимо создавать кристаллографическую текстуру с преобладанием направления <100>, поскольку наибольшей является константа тетрагональной магнитоотрицательности. Традиционные методы термомеханической обработки не приводят к формированию такой текстуры в сплаве с ОЦК-решеткой. В работе впервые предложено использовать угловую прокатку с целью увеличения доли благоприятных текстурных компонент. Теплая прокатка со степенью деформации 70 % была реализована под углами 0, 30 и 90° по отношению к направлению горячей прокатки. Текстура деформации анализировалась с помощью рентгеновского текстурного анализа, а текстура и структура материала после рекристаллизации – методом дифракции обратно рассеянных электронов (EBSD) на сканирующем электронном микроскопе. Количественный анализ текстур проводился с помощью метода функции распределения ориентаций с использованием программного обеспечения ATEX. Количественно определена объемная доля некоторых компонент. Показано, что существенное изменение в текстурах деформации и первичной рекристаллизации происходит при прокатке под углом 90°. Образец после такой прокатки содержит наибольшее количество плоскостной компоненты {100}. Установлена зависимость между текстурой деформации и рекристаллизации в Fe–Ga: так, для повышения доли компонент с кристаллографическим направлением <001> при рекристаллизации необходимо присутствие в текстуре деформации плоскостных компонент {111}, что связано с преимущественным ростом благоприятных компонент в деформационной матрице с такой текстурой.

Ключевые слова: сплав Fe–Ga; сплав (Fe₈₃Ga₁₇)₉₉B₁; количественный анализ текстуры; угловая прокатка; первичная рекристаллизация; магнитоотрицательность.

Благодарности: Работа выполнена при поддержке гранта Президента Российской Федерации для молодых ученых – кандидатов наук (№ МК-344.2022.4) и в рамках государственного задания Министерства науки и высшего образования Российской Федерации (шифр «Магнит», № 122021000034–9).

Электронно-микроскопические исследования выполнены в Центре коллективного доступа Испытательного центра нанотехнологий и перспективных материалов Института физики металлов имени М.Н. Михеева Уральского отделения РАН (Екатеринбург, Россия).

Статья подготовлена по материалам докладов участников XI Международной школы «Физическое материаловедение» (ШФМ-2023), Тольятти, 11–15 сентября 2023 года.

Для цитирования: Стрижаченко И.Р., Гервасьева И.В., Милютин В.А., Девятериков Д.И. Количественный анализ текстуры деформации и первичной рекристаллизации при угловой прокатке и отжиге магнитоотрицательного сплава (Fe₈₃Ga₁₇)₉₉B₁ // Frontier Materials & Technologies. 2023. № 4. С. 121–128. DOI: 10.18323/2782-4039-2023-4-66-11.

OUR AUTHORS

Afanasyev Maksim Anatolyevich, researcher of the Research Institute of Advanced Technologies.
Address: Togliatti State University, 445020, Russia, Togliatti, Belorusskaya Street, 14.
E-mail: alexey.danyuk@gmail.com

Aryshenskiy Evgeny Vladimirovich, Doctor of Sciences (Engineering), Associate Professor, senior researcher of the Laboratory of Electron Microscopy and Image Processing, leading researcher.
Address 1: Siberian State Industrial University, 654007, Russia, Novokuznetsk, Kirov Street, 42.
Address 2: Academician S.P. Korolev Samara National Research University, 443086, Russia, Samara, Moskovskoye Shosse, 34.
E-mail: arishenskiy_ev@sibsiu.ru

Avtokratova Elena Viktorovna, PhD (Engineering), senior researcher.
Address: Institute for Metals Superplasticity Problems of RAS, 450001, Russia, Ufa, Stepan Khalturin Street, 39.
E-mail: avtkratova@imsp.ru

Brilevskiy Aleksandr Igorevich, junior researcher of the Research Institute of Advanced Technologies.
Address: Togliatti State University, 445020, Russia, Togliatti, Belorusskaya Street, 14.
E-mail: alexandrbril@yandex.ru

Bykova Tatyana Mikhailovna, PhD (Engineering), senior researcher.
Address: Institute of Engineering Science of the Ural Branch of RAS, 620049, Russia, Yekaterinburg, Komsomolskaya Street, 34.
E-mail: tatiana_8801@mail.ru

Danyuk Aleksey Valerievich, PhD (Physics and Mathematics), senior researcher of the Research Institute of Advanced Technologies.
Address: Togliatti State University, 445020, Russia, Togliatti, Belorusskaya Street, 14.
E-mail: alexey.danyuk@gmail.com

Denisov Vladimir Viktorovich, PhD (Engineering), Head of Laboratory of Beam-Plasma Surface Engineering.
Address: Institute of High Current Electronics SB of RAS, 634055, Russia, Tomsk, Prospekt Akademicheskiiy, 2/3.
E-mail: volodyadenisov@yandex.ru

Devyaterikov Denis Igorevich, PhD (Physics and Mathematics), researcher.
Address: M.N. Mikheev Institute of Metal Physics of the Ural Branch of RAS, 620108, Russia, Yekaterinburg, Sofya Kovalevskaya Street, 18.
E-mail: devidor@imp.uran.ru

Gervasyeva Irina Vladimirovna, Doctor of Sciences (Physics and Mathematics), leading researcher.
Address: M.N. Mikheev Institute of Metal Physics of the Ural Branch of RAS, 620108, Russia, Yekaterinburg, Sofya Kovalevskaya Street, 18.
E-mail: gervasy@imp.uran.ru

Golubev Roman Aleksandrovich, junior researcher, postgraduate student.
Address 1: Institute of Technical Acoustics of the National Academy of Sciences of Belarus, 210009, Republic of Belarus, Vitebsk, Prospekt Generala Ludnikova, 13.
Address 2: RUDN University (Peoples' Friendship University of Russia), 117198, Russia, Moscow, Miklukho-Maklai Street, 6.
E-mail: asdfdss.asdasf@yandex.ru

Golubkov Pavel Evgenievich, PhD (Engineering),
assistant professor of Chair “Information and Measuring Equipment and Metrology”.
Address: Penza State University,
440026, Russia, Penza, Krasnaya Street, 40.
E-mail: golpavpnz@yandex.ru

Ilyasov Rafis Raisovich, junior researcher.
Address: Institute for Metals Superplasticity Problems of RAS,
450001, Russia, Ufa, Stepan Khalturin Street, 39.
E-mail: diesel874@yandex.ru

Karamyshev Konstantin Yurievich, engineer
of the Laboratory of Precision Alloys and Intermetallic Compounds.
Address: M.N. Mikheev Institute of Metal Physics of the Ural Branch of RAS,
620108, Russia, Yekaterinburg, Sofya Kovalevskaya Street, 18.
E-mail: karamyshev@imp.uran.ru

Konovalov Sergey Valeryevich, Doctor of Sciences (Engineer), Professor,
Vice-rector for Science and Innovative Activities, chief researcher.
Address 1: Siberian State Industrial University,
654007, Russia, Novokuznetsk, Kirov Street, 42.
Address 2: Academician S.P. Korolev Samara National Research University,
443086, Russia, Samara, Moskovskoye Shosse, 34.
E-mail: konovalov@sibsiu.ru

Krishtal Mikhail Mikhailovich, Doctor of Sciences (Physics and Mathematics),
Professor, chief researcher of the Research Institute of Advanced Technologies.
Address: Togliatti State University,
445020, Russia, Togliatti, Belorusskaya Street, 14.
E-mail: krishtal@tltsu.ru

Kritchenkov Andrey Sergeevich, Doctor of Sciences (Chemistry), leading researcher.
Address 1: Institute of Technical Acoustics of the National Academy of Sciences of Belarus,
210009, Republic of Belarus, Vitebsk, Prospekt Generala Ludnikova, 13.
Address 2: RUDN University (Peoples' Friendship University of Russia),
117198, Russia, Moscow, Miklukho-Maklai Street, 6.
E-mail: platinist@mail.ru

Kritchenkov Ilya Sergeevich, PhD (Chemistry), senior researcher.
Address 1: Institute of Technical Acoustics of the National Academy of Sciences of Belarus,
210009, Republic of Belarus, Vitebsk, Prospekt Generala Ludnikova, 13.
Address 2: St. Petersburg State University,
199034, Russia, St. Petersburg, Universitetskaya Naberezhnaya, 7–9.
E-mail: ilya.kritchenkov@gmail.com

Krymsky Stanislav Vatslavovich, PhD (Engineering), Head of laboratory.
Address: Institute for Metals Superplasticity Problems of RAS,
450001, Russia, Ufa, Stepan Khalturin Street, 39.
E-mail: stkr_imspp@mail.ru

Lapshov Maksim Aleksandrovich, engineer.
Address: Academician S.P. Korolev Samara National Research University,
443086, Russia, Samara, Moskovskoye Shosse, 34.
E-mail: lapshov.m.syz@gmail.com

Makarov Aleksey Viktorovich, Doctor of Science (Engineering),
Corresponding Member of RAS, Head of Department of Materials Science,
Head of Laboratory of Mechanical Properties.
Address 1: Institute of Engineering Science of the Ural Branch of RAS,
620049, Russia, Yekaterinburg, Komsomolskaya Street, 34.
Address 2: M.N. Mikheev Institute of Metal Physics of the Ural Branch of RAS,
620108, Russia, Yekaterinburg, Sofya Kovalevskaya Street, 18.
E-mail: av-mak@yandex.ru

Makarov Vladimir Viktorovich, researcher
of the Laboratory of Non-ferrous Alloys, junior researcher.
Address 1: Academician S.P. Korolev Samara National Research University,
443086, Russia, Samara, Moskovskoye Shosse, 34.
Address 2: M.N. Mikheev Institute of Metal Physics of the Ural Branch of RAS,
620108, Russia, Yekaterinburg, Sofya Kovalevskaya Street, 18.
E-mail: makarov@imp.uran.ru

Malkin Kirill Aleksandrovich, laboratory assistant.
Address: Academician S.P. Korolev Samara National Research University,
443086, Russia, Samara, Moskovskoye Shosse, 34.
E-mail: malkin.ka@ssau.ru

Markushev Mikhail Vyacheslavovich, Doctor of Sciences (Engineering),
senior researcher, Head of laboratory.
Address: Institute for Metals Superplasticity Problems of RAS,
450001, Russia, Ufa, Stepan Khalturin Street, 39.
E-mail: mvmark@imsp.ru

Maslov Aleksey Andreevich, laboratory assistant of Chair of Mechanical Engineering.
Address: Ufa University of Science and Technology,
450076, Russia, Ufa, Zaki Validi Street, 32.
E-mail: alexey.maslov2011@gmail.com

Merson Dmitry Lvovich, Doctor of Sciences (Physics and Mathematics),
Professor, Director of the Research Institute of Advanced Technologies.
Address: Togliatti State University,
445020, Russia, Togliatti, Belorusskaya Street, 14.
E-mail: d.merson@tltsu.ru

Milyutin Vasily Aleksandrovich, PhD (Physics and Mathematics),
senior researcher.
Address: M.N. Mikheev Institute of Metal Physics of the Ural Branch of RAS,
620108, Russia, Yekaterinburg, Sofya Kovalevskaya Street, 18.
E-mail: v.a.milutin@gmail.com

Nazarov Almaz Yunirovich, PhD (Engineering),
assistant professor of Chair of Mechanical Engineering.
Address: Ufa University of Science and Technology,
450076, Russia, Ufa, Zaki Validi Street, 32.
E-mail: nazarov.ayu@ugatu.su

Nikolaev Aleksey Aleksandrovich, assistant
of Chair of Mechanical Engineering.
Address: Ufa University of Science and Technology,
450076, Russia, Ufa, Zaki Validi Street, 32.
E-mail: nikolaev.aleksej95@gmail.com

Pecherskaya Ekaterina Anatolyevna, Doctor of Sciences (Engineering),
Professor, Head of Chair "Information and Measuring Equipment and Metrology".
Address: Penza State University,
440026, Russia, Penza, Krasnaya Street, 40.
E-mail: peal@list.ru

Polunin Anton Viktorovich, PhD (Engineering),
leading researcher of the Research Institute of Advanced Technologies.
Address: Togliatti State University,
445020, Russia, Togliatti, Belorusskaya Street, 14.
E-mail: Anpol86@gmail.com

Polunina Alisa Olegovna, researcher of the Research Institute of Advanced Technologies.
Address: Togliatti State University,
445020, Russia, Togliatti, Belorusskaya Street, 14.
E-mail: a.cheretaeva@tltsu.ru

Pugacheva Nataliya Borisovna, Doctor of Sciences (Engineering),
Associate Professor, chief researcher.
Address : Institute of Engineering Science of the Ural Branch of RAS,
620049, Russia, Yekaterinburg, Komsomolskaya Street, 34.
E-mail: nat@imach.uran.ru

Ramazanov Kamil Nurullaevich, Doctor of Sciences (Engineering),
Head of Chair of Mechanical Engineering.
Address: Ufa University of Science and Technology,
450076, Russia, Ufa, Zaki Validi Street, 32.
E-mail: ramazanovkn@gmail.com

Rasposienko Dmitry Yuryevich, PhD (Engineering),
senior researcher of the Laboratory of Non-ferrous Alloys.
Address: M.N. Mikheev Institute of Metal Physics of the Ural Branch of RAS,
620108, Russia, Yekaterinburg, Sofya Kovalevskaya Street, 18.
E-mail: dmitrijrasp@gmail.com

Rubanik Vasily Vasilievich, Doctor of Sciences (Engineering),
corresponding member of the National Academy of Sciences of Belarus,
Associate Professor, Head of Laboratory of Metal Physics.
Address: Institute of Technical Acoustics of the National Academy of Sciences of Belarus,
210009, Republic of Belarus, Vitebsk, Prospekt Generala Ludnikova, 13.
E-mail: v.v.rubanik@tut.by

Rubanik Vasily Vasilievich Jr., Doctor of Sciences (Engineering),
Associate Professor, Director.
Address: Institute of Technical Acoustics of the National Academy of Sciences of Belarus,
210009, Republic of Belarus, Vitebsk, Prospekt Generala Ludnikova, 13.
E-mail: ita@vitebsk.by

Savrai Roman Anatolievich, PhD (Engineering),
Head of Laboratory of Constructional Material Science.
Address: Institute of Engineering Science of the Ural Branch of RAS,
620049, Russia, Yekaterinburg, Komsomolskaya Street, 34.
E-mail: ras@imach.uran.ru

Semenov Anatoly Dmitrievich, Doctor of Sciences (Engineering),
professor of Chair “Information and Measuring Equipment and Metrology”.
Address: Penza State University,
440026, Russia, Penza, Krasnaya Street, 40.
E-mail: sad-50@mail.ru

Senaeva Ekaterina Igorevna, junior researcher.
Address: Institute of Engineering Science of the Ural Branch of RAS,
620049, Russia, Yekaterinburg, Komsomolskaya Street, 34.
E-mail: nata5-4@yandex.ru

Shmakov Aleksandr Nikolaevich, leading researcher.
Address 1: Federal Research Center Boreskov Institute of Catalysis SB of RAS,
630090, Russia, Novosibirsk, Akademik Lavrentiev Prospekt, 5.
Address 2: Institute of High Current Electronics SB of RAS,
634055, Russia, Tomsk, Prospekt Akademicheskiiy, 2/3.
E-mail: highres@mail.ru

Sitdikov Oleg Shamilevich, PhD (Physics and Mathematics),
senior researcher.

Address: Institute for Metals Superplasticity Problems of RAS,
450001, Russia, Ufa, Stepan Khalturin Street, 39.

E-mail: sitdikov.oleg.1967@mail.ru

Skorynina Polina Andreevna, junior researcher.

Address: Institute of Engineering Science of the Ural Branch of RAS,
620049, Russia, Yekaterinburg, Komsomolskaya Street, 34.

E-mail: polina.skorynina@mail.ru

Strizhachenko Ivan Romanovich, engineer.

Address: M.N. Mikheev Institute of Metal Physics of the Ural Branch of RAS,
620108, Russia, Yekaterinburg, Sofya Kovalevskaya Street, 18.

E-mail: strizhachenko@imp.uran.ru

Valeev Irshat Shamilovich, PhD (Engineering), researcher.

Address: Institute for Metals Superplasticity Problems of RAS,
450001, Russia, Ufa, Stepan Khalturin Street, 39.

E-mail: valeevs@mail.ru

Valeeva Aigul Khammatovna, PhD (Engineering), researcher.

Address: Institute for Metals Superplasticity Problems of RAS,
450001, Russia, Ufa, Stepan Khalturin Street, 39.

E-mail: valeevs@mail.ru

НАШИ АВТОРЫ

Автократова Елена Викторовна, кандидат технических наук,
старший научный сотрудник.

Адрес: Институт проблем сверхпластичности металлов РАН,
450001, Россия, г. Уфа, ул. Степана Халтурина, 39.

E-mail: avtokratova@imsp.ru

Арышенский Евгений Владимирович, доктор технических наук, доцент,
старший научный сотрудник лаборатории электронной микроскопии
и обработки изображений, ведущий научный сотрудник.

Адрес 1: Сибирский государственный индустриальный университет,
654007, Россия, г. Новокузнецк, ул. Кирова, 42.

Адрес 2: Самарский национальный исследовательский университет
имени академика С.П. Королева,
443086, Россия, г. Самара, Московское шоссе, 34.

E-mail: arishenskiy_ev@sibsiu.ru

Афанасьев Максим Анатольевич, научный сотрудник
НИИ прогрессивных технологий.

Адрес: Тольяттинский государственный университет,
445020, Россия, г. Тольятти, ул. Белорусская, 14.

E-mail: alexey.danyuk@gmail.com

Брилевский Александр Игоревич, младший научный сотрудник
НИИ прогрессивных технологий.

Адрес: Тольяттинский государственный университет,
445020, Россия, г. Тольятти, ул. Белорусская, 14.

E-mail: alexandrbril@yandex.ru

Быкова Татьяна Михайловна, кандидат технических наук,
старший научный сотрудник.

Адрес: Институт машиноведения имени Э.С. Горкунова
Уральского отделения РАН,
620049, Россия, г. Екатеринбург, ул. Комсомольская, 34.

E-mail: tatiana_8801@mail.ru

Валеев Иршат Шамилович, кандидат технических наук,
научный сотрудник.

Адрес: Институт проблем сверхпластичности металлов РАН,
450001, Россия, г. Уфа, ул. Степана Халтурина, 39.

E-mail: valeevs@mail.ru

Валеева Айгуль Хамматовна, кандидат технических наук,
научный сотрудник.

Адрес: Институт проблем сверхпластичности металлов РАН,
450001, Россия, г. Уфа, ул. Степана Халтурина, 39.

E-mail: valeevs@mail.ru

Гервасьева Ирина Владимировна, доктор физико-математических наук,
ведущий научный сотрудник.

Адрес: Институт физики металлов имени М.Н. Михеева
Уральского отделения РАН,

620108, Россия, г. Екатеринбург, ул. Софьи Ковалевской, 18.

E-mail: gervasy@imp.uran.ru

Голубев Роман Александрович, младший научный сотрудник, аспирант.

Адрес 1: Институт технической акустики Национальной академии наук Беларуси,
210009, Республика Беларусь, г. Витебск, пр-т Генерала Людникова, 13.

Адрес 2: Российский университет дружбы народов,
117198, Россия, г. Москва, ул. Миклухо-Маклая, 6.

E-mail: asdfdss.asdasf@yandex.ru

Голубков Павел Евгеньевич, кандидат технических наук,
доцент кафедры «Информационно-измерительная техника и метрология».
Адрес: Пензенский государственный университет,
440026, Россия, г. Пенза, ул. Красная, 40.
E-mail: golpavpnz@yandex.ru

Данюк Алексей Валериевич, кандидат физико-математических наук,
старший научный сотрудник НИИ прогрессивных технологий.
Адрес: Тольяттинский государственный университет,
445020, Россия, г. Тольятти, ул. Белорусская, 14.
E-mail: alexey.danyuk@gmail.com

Девятериков Денис Игоревич, кандидат физико-математических наук,
научный сотрудник.
Адрес: Институт физики металлов имени М.Н. Михеева
Уральского отделения РАН,
620108, Россия, г. Екатеринбург, ул. Софьи Ковалевской, 18.
E-mail: devidor@imp.uran.ru

Денисов Владимир Викторович, кандидат технических наук,
заведующий лабораторией пучково-плазменной инженерии поверхности.
Адрес: Институт сильноточной электроники СО РАН,
634055, Россия, г. Томск, пр. Академический, 2/3.
E-mail: volodyadenisov@yandex.ru

Ильясов Рафис Раисович, младший научный сотрудник.
Адрес: Институт проблем сверхпластичности металлов РАН,
450001, Россия, г. Уфа, ул. Степана Халтурина, 39.
E-mail: diesel874@yandex.ru

Карамышев Константин Юрьевич, инженер
лаборатории прецизионных сплавов и интерметаллидов.
Адрес: Институт физики металлов имени М.Н. Михеева
Уральского отделения РАН,
620108, Россия, г. Екатеринбург, ул. Софьи Ковалевской, 18.
E-mail: karamyshev@imp.uran.ru

Коновалов Сергей Валерьевич, доктор технических наук, профессор,
проректор по научной и инновационной деятельности, главный научный сотрудник.
Адрес 1: Сибирский государственный индустриальный университет,
654007, Россия, г. Новокузнецк, ул. Кирова, 42.
Адрес 2: Самарский национальный исследовательский университет
имени академика С.П. Королева,
443086, Россия, г. Самара, Московское шоссе, 34.
E-mail: konovalov@sibsiu.ru

Критченков Андрей Сергеевич, доктор химических наук,
ведущий научный сотрудник.
Адрес 1: Институт технической акустики Национальной академии наук Беларуси,
210009, Республика Беларусь, г. Витебск, пр-т Генерала Людникова, 13.
Адрес 2: Российский университет дружбы народов,
117198, Россия, г. Москва, ул. Миклухо-Маклая, 6.
E-mail: platinist@mail.ru

Критченков Илья Сергеевич, кандидат химических наук,
старший научный сотрудник.
Адрес 1: Институт технической акустики Национальной академии наук Беларуси,
210009, Республика Беларусь, г. Витебск, пр-т Генерала Людникова, 13.
Адрес 2: Санкт-Петербургский государственный университет,
199034, Россия, г. Санкт-Петербург, Университетская наб., 7–9.
E-mail: ilya.kritchenkov@gmail.com

Криштал Михаил Михайлович, доктор физико-математических наук, профессор, главный научный сотрудник НИИ прогрессивных технологий.
Адрес: Тольяттинский государственный университет, 445020, Россия, г. Тольятти, ул. Белорусская, 14.
E-mail: krishtal@tltsu.ru

Крымский Станислав Вацлавович, кандидат технических наук, заведующий лабораторией.
Адрес: Институт проблем сверхпластичности металлов РАН, 450001, Россия, г. Уфа, ул. Степана Халтурина, 39.
E-mail: stkr_imsp@mail.ru

Лапшов Максим Александрович, инженер.
Адрес: Самарский национальный исследовательский университет имени академика С.П. Королева, 443086, Россия, г. Самара, Московское шоссе, 34.
E-mail: lapshov.m.syz@gmail.com

Макаров Алексей Викторович, доктор технических наук, член-корреспондент РАН, заведующий отделом материаловедения и лабораторией механических свойств.
Адрес 1: Институт машиноведения имени Э.С. Горкунова Уральского отделения РАН, 620049, Россия, г. Екатеринбург, ул. Комсомольская, 34.
Адрес 2: Институт физики металлов имени М.Н. Михеева Уральского отделения РАН, 620108, Россия, г. Екатеринбург, ул. Софьи Ковалевской, 18.
E-mail: av-mak@yandex.ru

Макаров Владимир Викторович, научный сотрудник лаборатории цветных сплавов, младший научный сотрудник.
Адрес 1: Самарский национальный исследовательский университет имени академика С.П. Королева, 443086, Россия, г. Самара, Московское шоссе, 34.
Адрес 2: Институт физики металлов имени М.Н. Михеева Уральского отделения РАН, 620108, Россия, г. Екатеринбург, ул. Софьи Ковалевской, 18.
E-mail: makarov@imp.uran.ru

Малкин Кирилл Александрович, лаборант.
Адрес: Самарский национальный исследовательский университет имени академика С.П. Королева, 443086, Россия, г. Самара, Московское шоссе, 34.
E-mail: malkin.ka@ssau.ru

Маркушев Михаил Вячеславович, доктор технических наук, старший научный сотрудник, заведующий лабораторией.
Адрес: Институт проблем сверхпластичности металлов РАН, 450001, Россия, г. Уфа, ул. Степана Халтурина, 39.
E-mail: mvmark@imsp.ru

Маслов Алексей Андреевич, лаборант кафедры технологии машиностроения.
Адрес: Уфимский университет науки и технологий, 450076, Россия, г. Уфа, ул. Заки Валиди, 32.
E-mail: alexey.maslov2011@gmail.com

Мерсон Дмитрий Львович, доктор физико-математических наук, профессор, директор НИИ прогрессивных технологий.
Адрес: Тольяттинский государственный университет, 445020, Россия, г. Тольятти, ул. Белорусская, 14.
E-mail: d.merson@tltsu.ru

Милютин Василий Александрович, кандидат физико-математических наук, старший научный сотрудник.

Адрес: Институт физики металлов имени М.Н. Михеева
Уральского отделения РАН,
620108, Россия, г. Екатеринбург, ул. Софьи Ковалевской, 18.
E-mail: v.a.milutin@gmail.com

Назаров Алмаз Юнирович, кандидат технических наук, доцент кафедры технологии машиностроения.

Адрес: Уфимский университет науки и технологий,
450076, Россия, г. Уфа, ул. Заки Валиди, 32.
E-mail: nazarov.ayu@ugatu.su

Николаев Алексей Александрович, ассистент кафедры технологии машиностроения.

Адрес: Уфимский университет науки и технологий,
450076, Россия, г. Уфа, ул. Заки Валиди, 32.
E-mail: nikolaev.aleksej95@gmail.com

Печерская Екатерина Анатольевна, доктор технических наук, профессор, заведующий кафедрой «Информационно-измерительная техника и метрология».

Адрес: Пензенский государственный университет,
440026, Россия, г. Пенза, ул. Красная, 40.
E-mail: peal@list.ru

Полунин Антон Викторович, кандидат технических наук, ведущий научный сотрудник НИИ прогрессивных технологий.

Адрес: Тольяттинский государственный университет,
445020, Россия, г. Тольятти, ул. Белорусская, 14.
E-mail: Anpol86@gmail.com

Полунина Алиса Олеговна, научный сотрудник НИИ прогрессивных технологий.

Адрес: Тольяттинский государственный университет,
445020, Россия, г. Тольятти, ул. Белорусская, 14.
E-mail: a.cheretaeva@tltsu.ru

Пугачева Наталия Борисовна, доктор технических наук, доцент, главный научный сотрудник.

Адрес: Институт машиноведения имени Э.С. Горкунова
Уральского отделения РАН,
620049, Россия, г. Екатеринбург, ул. Комсомольская, 34.
E-mail: nat@imach.uran.ru

Рамазанов Камиль Нуруллаевич, доктор технических наук, заведующий кафедрой технологии машиностроения.

Адрес: Уфимский университет науки и технологий,
450076, Россия, г. Уфа, ул. Заки Валиди, 32.
E-mail: ramazanovkn@gmail.com

Распосненко Дмитрий Юрьевич, кандидат технических наук, старший научный сотрудник лаборатории цветных сплавов.

Адрес: Институт физики металлов имени М.Н. Михеева
Уральского отделения РАН,
620108, Россия, г. Екатеринбург, ул. Софьи Ковалевской, 18.
E-mail: dmitrijrasp@gmail.com

Рубаник Василий Васильевич, доктор технических наук, доцент, член-корреспондент Национальной академии наук Беларуси, заведующий лабораторией физики металлов.

Адрес: Институт технической акустики Национальной академии наук Беларуси,
210009, Республика Беларусь, г. Витебск, пр-т Генерала Людникова, 13.
E-mail: v.v.rubanik@tut.by

Рубаник Василий Васильевич мл., доктор технических наук, доцент, директор.

Адрес: Институт технической акустики Национальной академии наук Беларуси,
210009, Республика Беларусь, г. Витебск, пр-т Генерала Людникова, 13.

E-mail: ita@vitebsk.by

Саврай Роман Анатольевич, кандидат технических наук,
заведующий лабораторией конструкционного материаловедения.

Адрес: Институт машиноведения имени Э.С. Горкунова

Уральского отделения РАН,

620049, Россия, г. Екатеринбург, ул. Комсомольская, 34.

E-mail: ras@imach.uran.ru

Семёнов Анатолий Дмитриевич, доктор технических наук,
профессор кафедры «Информационно-измерительная техника и метрология».

Адрес: Пензенский государственный университет,

440026, Россия, г. Пенза, ул. Красная, 40.

E-mail: sad-50@mail.ru

Сенаева Екатерина Игоревна, младший научный сотрудник.

Адрес: Институт машиноведения имени Э.С. Горкунова

Уральского отделения РАН,

620049, Россия, г. Екатеринбург, ул. Комсомольская, 34.

E-mail: nata5-4@yandex.ru

Ситдиков Олег Шамилович, кандидат физико-математических наук,
старший научный сотрудник.

Адрес: Институт проблем сверхпластичности металлов РАН,

450001, Россия, г. Уфа, ул. Степана Халтурина, 39.

E-mail: sitdikov.oleg.1967@mail.ru

Скорынина Полина Андреевна, младший научный сотрудник.

Адрес: Институт машиноведения имени Э.С. Горкунова

Уральского отделения РАН,

620049, Россия, г. Екатеринбург, ул. Комсомольская, 34.

E-mail: polina.skorynina@mail.ru

Стрижаченко Иван Романович, инженер.

Адрес: Институт физики металлов имени М.Н. Михеева

Уральского отделения РАН,

620108, Россия, г. Екатеринбург, ул. Софьи Ковалевской, 18.

E-mail: strizhachenko@imp.uran.ru

Шмаков Александр Николаевич, ведущий научный сотрудник.

Адрес 1: Федеральный исследовательский центр

«Институт катализа им. Г.К. Борескова СО РАН»,

630090, Россия, г. Новосибирск, пр. Академика Лаврентьева, 5.

Адрес 2: Институт сильноточной электроники СО РАН,

634055, Россия, г. Томск, пр. Академический, 2/3.

E-mail: highres@mail.ru

On the cover: Light-field image of the Al_{0.3}Mg₁Si_{0.3}Sc_{0.15}Zr alloy microstructure after annealing at (440 °C, 8 h) + (500 °C, 0.5 h) + (180 °C, 5 h). Author of the photo: V.V. Makarov, researcher of the Laboratory of Non-ferrous Alloys (M.N. Mikheev Institute of Metal Physics of the Ural Branch of RAS, Yekaterinburg, Russia).

На обложке: Светлопольное изображение микроструктуры сплава Al_{0,3}Mg₁Si_{0,3}Sc_{0,15}Zr после отжига по режиму (440 °C, 8 ч) + (500 °C, 0,5 ч) + (180 °C, 5 ч). Автор фото: В.В. Макаров, научный сотрудник лаборатории цветных сплавов (Институт физики металлов имени М.Н. Михеева Уральского отделения РАН, Екатеринбург, Россия).